

**TRANSMISSION ELECTRON MICROSCOPY STUDY OF  
ADVANCED MAGNETIC SENSOR FILMS**

**By Susan Jane Tara Murdoch**

Submitted for the degree of Doctor of Philosophy

University of Glasgow, Department of Physics and Astronomy

© S.J.T. Murdoch September 2001

ProQuest Number: 13818894

All rights reserved

INFORMATION TO ALL USERS

The quality of this reproduction is dependent upon the quality of the copy submitted.

In the unlikely event that the author did not send a complete manuscript and there are missing pages, these will be noted. Also, if material had to be removed, a note will indicate the deletion.



ProQuest 13818894

Published by ProQuest LLC (2018). Copyright of the Dissertation is held by the Author.

All rights reserved.

This work is protected against unauthorized copying under Title 17, United States Code  
Microform Edition © ProQuest LLC.

ProQuest LLC.  
789 East Eisenhower Parkway  
P.O. Box 1346  
Ann Arbor, MI 48106 – 1346



12399  
copy 1

**CONTENTS**

**Contents ..... i**  
**Acknowledgements ..... v**  
**Declaration..... vi**  
**Summary ..... vii**

**Chapter 1 Magnetism and Magnetic Recording ..... 1-26**

1.1 Introduction ..... 1  
1.2 Ferromagnetism..... 1  
1.3 Energy ..... 4  
1.3.1 Exchange energy ..... 4  
1.3.2 Anisotropy energy ..... 5  
1.3.3 Magnetostatic energy ..... 6  
1.3.4 Zeeman energy ..... 7  
1.3.5 Total energy..... 7  
1.3.6 Magnetic Domains ..... 8  
1.3.7 Domain Walls..... 9  
1.4 Hysteresis ..... 11  
1.5 Magnetisation reversal processes ..... 13  
1.5.1 Reversible..... 13  
1.5.2 Irreversible ..... 14  
1.6 Magnetoresistance..... 14  
1.6.1 Anisotropic Magnetoresistance ..... 15  
1.6.2 Giant Magnetoresistance ..... 16  
1.7 Spin valves ..... 18  
1.8 Magnetic Recording and Sensors..... 21  
1.8.1 Introduction ..... 21  
1.8.2 Magnetoresistive heads ..... 23  
1.8.3 Giant magnetoresistive heads..... 25  
1.9 Outline of thesis ..... 26

## **Chapter 2 Transmission Electron Microscopy – Instrumentation and Techniques..... 27-51**

2.1	Introduction.....	27
2.2	Electron microscopy.....	27
2.2.1	Electron gun .....	27
2.2.2	EM column.....	31
2.2.3	Image capture .....	33
2.2.4	JEOL 1200EX and 2000FX .....	34
2.2.5	Philips CM20 .....	35
2.3	Microstructural information .....	35
2.3.1	Bright and dark field imaging .....	36
2.3.2	Diffraction patterns .....	36
2.4	Magnetic imaging.....	40
2.4.1	Electron beam and specimen interaction.....	40
2.4.2	Fresnel Imaging.....	42
2.4.3	Foucault imaging.....	45
2.4.4	Low Angle Diffraction.....	47
2.4.5	Differential Phase Contrast .....	48
2.5	In-situ applied magnetic fields .....	49

## **Chapter 3 Growth and Fabrication of Specimens..... 52-62**

3.1	Introduction .....	52
3.2	Si <sub>3</sub> N <sub>4</sub> membrane substrates .....	52
3.3	Deposition of films.....	57
3.4	Bulk characterisation of magnetic films .....	58
3.5	Patterned elements .....	59
3.5.1	Electron beam lithography .....	59
3.5.2	Liftoff Process .....	62

**Chapter 4 Microstructure of Magnetic Films..... 63-79**

4.1 Introduction ..... 63

4.2 Permalloy – Ni<sub>80</sub>Fe<sub>20</sub> ..... 63

4.3 Microstructure of NiFe ..... 64

4.4 Microstructure of NiFe grown on Ta underlayer ..... 70

4.5 Microstructure of NiFeRe ..... 75

4.6 Microstructure of spin-valve stacks ..... 77

4.7 Summary ..... 79

**Chapter 5 Magnetisation Reversal of Single-layer NiFe and AMR Stacks  
..... 80-93**

5.1 Introduction ..... 80

5.2 Reversal mechanisms of NiFe single layer ..... 80

5.2.1 Easy axis..... 81

5.2.2 Hard axis ..... 85

5.3 Reversal mechanisms of AMR materials ..... 87

5.3.1 Easy Axis ..... 89

5.3.2 Hard Axis ..... 91

**Chapter 6 Free Layer Reversal of a Spin-valve with Crossed Anisotropy  
..... 94-118**

6.1 Introduction ..... 94

6.2 Crossed Anisotropy Geometry ..... 95

6.3 Free layer reversal mechanism as a function of applied field orientation  
..... 96

6.4 Comparisons of reversal mechanisms with modelled results of Labrune  
..... 105

6.5 Free layer reversal mechanism as a function of specimen temperature  
..... 106

6.6 Analysis and comparisons..... 117

**Chapter 7 Spin-valve Stacks with Varying Layer Thicknesses .....119-132**

7.1 Introduction ..... 119

7.2 Variation of seed layer thickness ..... 120

7.3 Variation of Cu layer thickness..... 124

7.4 Variation of Ru layer thickness..... 126

7.5 Variation of NiMn layer thickness ..... 129

7.6 Analysis and comparisons..... 131

**Chapter 8 Patterned Elements of Spin-valve Material.....133-170**

8.1 Introduction ..... 133

8.2 Pattern designs ..... 135

8.3 Behaviour of small patterned elements of spin-valve material ..... 138

8.3.1 Dependence on aspect ratio for rectangular elements..... 139

8.3.2 Dependence on element end shape ..... 152

8.4 Analysis..... 170

**Chapter 9 Conclusions and Further Work .....171-176**

9.1 Introduction ..... 171

9.2 Conclusions ..... 171

9.2.1 Ch 4 Microstructure ..... 171

9.2.2 Ch 5 Magnetisation of NiFe and AMR materials ..... 172

9.2.3 Ch 6 and Ch 7 Magnetisation of spin-valve materials ..... 173

9.2.4 Ch 8 Patterned elements of spin-valve material..... 174

9.3 Future work on continuous films ..... 175

9.4 Future work on patterned spin-valves ..... 175

**References..... 177-180**

## ACKNOWLEDGEMENTS

There are many people whom I have to thank for their assistance and support over the past 4 years. Firstly I would like to thank Prof. John Chapman, for his encouragement as my supervisor, and also for providing the TEM facilities as head of the Solid State Physics research group. Also to Prof C.D.W. Wilkinson for providing access to the e-beam and photolithography facilities in the department of Electronic Engineering at the University of Glasgow.

Thanks to Seagate Technology, for the CASE Award support for my project. Deposition of the specimens used throughout this project was carried out by staff at both the Springtown, Northern Ireland, and Normandale, Minnesota plants.

Thanks to Dr. Katherine Kirk and Dr. Peter Aitchison for training me in the lithography and microscopy techniques used throughout, and for assistance on the microscopes; Dr Stephen McVitie, my secondary supervisor, for useful discussions; Dr Pat Nicholson and Dr Sam McFadzean for keeping the computers and equipment working. My appreciation to all other members of the SSP group for their friendship over the years, and for helping keep life interesting.

I would like to thank everyone at Seagate Springtown R&D department who welcomed me during my summer placement; also to my new friends and colleagues at Seagate for their encouragement during the writing up process.

Finally, and especially, many thanks to Mum and Dad, for your endless love and support.

## **DECLARATION**

This thesis is a record of experimental work which I carried out by myself during the period 1997 – 2000 in the Department of Physics and Astronomy at the University of Glasgow. The work described herein is my own, with the exception of the bulk of the specimen depositions, which were carried out by staff at the Seagate Technology facilities in Springtown, Northern Ireland, and Normandale, Minnesota.

Some of the work described in this thesis can be found in the paper:

S.J.T. Murdoch, J.N. Chapman, T.G. Pokhil, S. Mao, E.S. Murdock, J. Appl. Phys., 87, 9, 4945 (2000), Transmission electron microscopy study of thermal effects on the free-layer reversal of a crossed-anisotropy spin valve.

## SUMMARY

This thesis begins with an overview of the phenomenon of ferromagnetism and the theory of magnetic data recording in Chapter 1. The basic concepts of ferromagnetism and antiferromagnetism are described, along with the different energy contributions which determine the properties and characteristics of ferromagnetic materials. The chapter then concludes with the introduction of the important application of spin-valves as sensor materials. Chapter 2 then goes on to introduce the instrumentation and experimental techniques adopted for the transmission electron microscopy investigations in this study. The magnetic imaging modes of Lorentz microscopy are discussed, along with the methods used to apply controllable magnetic fields in-situ within the TEM. Chapter 3 describes the fabrication of electron transparent substrates suitable for TEM investigations. It then goes on to discuss the deposition and preparation of the magnetic films of interest, including electron beam lithography patterning. In chapter 4 the physical microstructure of a selection of magnetic materials is considered. Grain size and texturing are investigated for a range of different materials of interest. Chapter 5 looks at the magnetisation reversal of single-layer NiFe films and AMR stacks. Hard and easy axis reversal behaviour of these films is investigated as a prelude to the investigation of more complex multi-layer sensor films. In chapter 6, the free-layer reversal mechanism of spin-valve material is investigated as a function of applied field orientation, and then as a function of specimen temperature. Chapter 7 investigates how the properties of a spin-valve stack vary when selected layer thicknesses are altered. This shows the importance of optimisation of a spin-valve stack, considering the properties of each layer in turn. Chapter 8 considers the reversal behaviour of micron-sized patterned elements of spin-valve material. Elements of different shapes, aspect ratios and orientation relative to the biasing direction are considered. Finally chapter 9 discusses the conclusions which can be drawn from this work, and finishes by considering some possible further work which would extend the investigations carried out here.

## Chapter 1 Magnetism and Magnetic Recording

### 1.1 Introduction

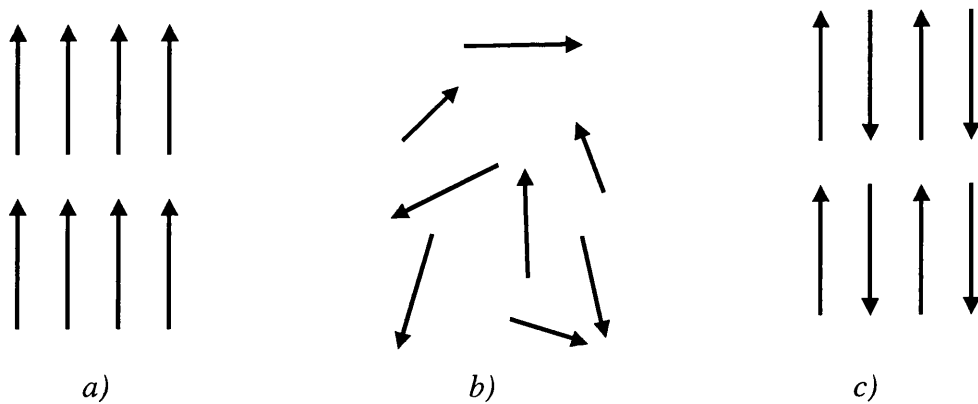
This chapter begins by describing the basic concepts of ferromagnetism and antiferromagnetism, and discussing the different magnetic energy contributions which determine the properties and characteristics of ferromagnetic materials. Magnetic hysteresis and magnetisation reversal processes are next discussed, followed by the introduction of magnetoresistance. Giant magnetoresistance (GMR) is of particular interest, in the context of spin-valves. Spin-valves are multilayer magnetic films, which exhibit GMR. The chapter then concludes with an overview of magnetic recording and the important application of spin-valves as sensor materials.

### 1.2 Ferromagnetism

A material is said to be a ferromagnet if, in the absence of an external applied field, it possesses a spontaneous non-zero magnetic moment. Ferromagnetism can be exhibited by transition metals and their alloys, rare earths and some oxides such as  $\text{CrO}_2$ .

Magnetic materials contain magnetic moments originating from two possible sources: orbital angular momentum, and spin angular momentum due to electron spin. Iron, cobalt and nickel are ferromagnetic transition metal elements; their magnetic moments can be attributed largely to spin angular momentum from unpaired electrons in the 3d shell (classically it is said that the orbits are fixed in space, or locked into the “crystal fields”). When this is the case, the orbital angular momentum is said to be “quenched”. In the case of rare earth metals at room temperature, the atomic magnetic moment is due to both the orbital and spin angular momentum components from the 4f electrons. The crystal fields are significant for many properties of the rare earth atoms, but they are not strong enough to quench the orbital momentum.

In all ferromagnetic materials, below a critical temperature known as the Curie temperature,  $T_C$ , the atomic magnetic moments are aligned almost perfectly parallel to one another due to a strong positive interaction between neighbouring electron spins. This is shown schematically in figure 1.1(a) below. Weiss first described this [1], when he postulated that each magnetic moment can be assumed to be acted upon by a molecular field proportional to the magnetisation of its environment. This means that, should a local parallel alignment of moments appear at any place in the lattice, a molecular field will be produced, which in turn will promote further alignment of the magnetic moments. As the temperature increases, however, thermal agitation disturbs the alignment of the spins resulting in a loss of the magnetic ordering at  $T_C$ . At this point the magnetic moments become randomly oriented in the absence of an applied field and the material is said to have become paramagnetic. Figure 1.1(b) shows the random orientations of magnetic moments in a paramagnet. Even in the presence of an applied field, only a weak positive interaction of the magnetic moments is observed in paramagnetic materials.



*Figure 1.1 Schematic arrangements of electron spins within a) ferromagnetic, b) paramagnetic, c) antiferromagnetic materials*

Heisenberg [2] accounted for the molecular field by proposing a quantum mechanical interaction known as the exchange interaction, acting between pairs of electrons. The Pauli exclusion principle [3] states that the total wave function for

an atom must be asymmetric. This means that no two electrons may have exactly the same set of quantum numbers. When considering that the electronic wave function is the product of the spatial and spin components, it follows that the electron distributions for parallel and antiparallel configurations are different. These configurations therefore have different electrostatic (Coulomb) energies, so that the exchange interaction can be regarded as an alignment of the electron spins in order to lower the electrostatic energy of the system.

In this discussion, it should be noted that the electrons are assumed to be localised at their respective atoms. This “localised” model works well in the case of rare earth metals and ferromagnetic oxides where the unpaired electrons responsible for magnetism are in the inner 4f shells of the atoms and so are constrained to their individual atoms. In the case of transition metals such as Fe, Co and Ni, the 3d electrons are more exposed, with their wave functions overlapping with those of neighbouring atoms. In this case, the 3d electrons can be thought of as spreading into a sea of electrons as the 3d energy levels are perturbed and spread to form an energy band. This concept leads to the “itinerant” or “band” theory of ferromagnetism [4] which includes the ability to explain non-integral values of atomic magnetic moments and to predict some aspects of the magnetic behaviour of the 3d metals and alloys. It should be noted that it is extremely difficult to make fundamental calculations based on the itinerant model, and in many cases interpretations of magnetic properties are still more often made on the basis of the localised electron model.

The exchange interaction results in an alignment of the electron spins in order to lower the electrostatic energy of the system.

$$E_{ex} = -J(r_{ij})\underline{s}_i \cdot \underline{s}_j \quad 1.1$$

Here  $E_{ex}$  is the exchange energy for two interacting electron spins  $s_i$  and  $s_j$  separated by a distance  $r_{ij}$  and  $J(r_{ij})$  is the exchange integral. For cases where  $J > 0$ , this leads to the phenomenon of ferromagnetism, whereas for  $J < 0$  antiferromagnetism results.

Below a temperature known as the Néel temperature certain materials such as Cr, Mn, MnO and NiO exhibit antiparallel alignment of magnetic moments in adjacent atom planes. This is known as antiferromagnetism, and the net magnetic moment is zero. This is shown schematically in figure 1.1(c).

### 1.3 Energy

The magnetic configuration of a magnetic material corresponds to a minimum in the overall potential energy, which is made up of several magnetic energy contributions. Here, we consider each energy term in turn, then go on to discuss the total magnetic potential energy and how minimising this can lead to the formation of magnetic domains and domain boundaries within a magnetic solid.

#### 1.3.1 Exchange Energy

The exchange energy as described above, is responsible for the spontaneous alignment of atomic magnetic dipoles in a ferromagnet. When considering a finite volume of magnetic material, it is usually only necessary to consider interactions between nearest neighbour electron spins, and so the exchange energy can be described by:

$$E_{ex} = A \int_V [(\nabla \alpha)^2 + (\nabla \beta)^2 + (\nabla \gamma)^2] dV \quad 1.2$$

where  $\alpha$ ,  $\beta$  and  $\gamma$  are the directional cosines of the magnetic vector and  $A$  is the exchange constant of the material, defined for cubic materials as

$$A = \frac{kJS^2}{a} \quad 1.3$$

$k$  is a constant depending on the crystalline structure (1 for simple cubic structures, 2 for body-centred cubic, 4 for face-centred cubic),  $a$  is the lattice constant and  $S$  is the spin magnetic moment of the atom.

### 1.3.2 Anisotropy Energy

When, in the absence of an applied field, the magnetisation vector within a magnetic material has preferred directions, the material is said to be anisotropic. The preferred directions are referred to as the easy axes and are aligned along particular crystallographic directions. Any deviation of the magnetisation vector away from an easy axis results in an increase in the magnetocrystalline anisotropy energy, which has its maximum along a hard axis.

For hexagonal or uniaxial crystals such as Co, the c-axis corresponds to the easy axis, and the anisotropy energy is described as

$$E_a = \int_V [K_1(1 - \gamma^2) + K_2(1 - \gamma^2)^2] dV \quad 1.4$$

where  $K_1$  and  $K_2$  are the first two anisotropy constants of the material, and  $\gamma$  is the direction cosine of the magnetisation from the hexagonal or c-axis.

For cubic crystals, such as Fe, the [100] directions are the easy axes. Then the anisotropy energy becomes

$$E_a = \int_V [K_1(\alpha^2\beta^2 + \alpha^2\gamma^2 + \beta^2\gamma^2) + K_2\alpha^2\beta^2\gamma^2] dV \quad 1.5$$

where  $\alpha$ ,  $\beta$  and  $\gamma$  are the direction cosines. For most transition metals,  $K_1 \gg K_2$  and so the anisotropy energy can be approximated to a single term. Co is an exception where this is not true over the temperature range up to  $T_c$ .

When the magnetic material of interest is micro-polycrystalline, the anisotropy direction varies locally from one crystallite to the next. This gives a random contribution to the local easy axis direction and results in local variations in the direction of the magnetisation vector. This phenomenon is known as magnetisation ripple [5].

Permalloy ( $\text{Ni}_{80}\text{Fe}_{20}$ ) is a polycrystalline, random alloy in which the composition gives close to zero magnetocrystalline anisotropy. It is known as an isotropic material and has no preferred easy or hard directions. For such materials, it is possible to induce an anisotropy during processing of thin films, either by deposition in the presence of an applied field, or annealing in an applied field at a temperature below  $T_C$ . The applied magnetic fields need only be large enough to saturate the film in the field direction. This induced anisotropy is due to preferential ordering of pairs of atoms within an overall disordered alloy [6]. Atom pairs orient themselves preferentially within the lattice so as to minimise their energy during deposition in a magnetic field. Similarly, during a magnetic anneal, some reordering of the atoms occurs. This ordering is retained after cooling within the magnetic field, leading to an induced anisotropy.

### 1.3.3 Magnetostatic Energy

There is a magnetostatic contribution to the energy of a magnetic system, which arises from the interactions between magnetic “free poles”. These can be generated within the volume of a magnetic material or at its surface if there is a divergent component of magnetisation. The free poles or magnetic charges give rise to both an external stray field, and an internal field known as the demagnetising field  $H_d$ , which is in the opposite sense to the magnetisation.  $H_d$  can be described in terms of an integral over the volume and surface of the source as follows:

$$\underline{H}_d(\underline{R}) = \frac{1}{4\pi} \int_V \frac{-\nabla \cdot \underline{M}}{R^2} dV + \frac{1}{4\pi} \int_S \frac{\underline{M} \cdot \underline{n}}{R^2} dS \quad 1.6$$

where  $\underline{R}$  is the position vector for the point at which the charge is evaluated and  $\underline{n}$  is the outward pointing unit vector normal to the surface.  $\nabla \cdot \underline{M}$  is the magnetic volume charge and  $\underline{M} \cdot \underline{n}$  is the magnetic surface charge. Only for the case of a uniformly magnetised ellipsoid is this integral straightforward to evaluate, and the demagnetisation field will be uniform. In general cases the integral has no simple analytical form.

The magnetostatic energy contribution from the interaction of the magnetic “free poles” takes the form:

$$E_m = -\frac{1}{2}\mu_0 \int_V \underline{M} \cdot \underline{H}_d dV \quad 1.7$$

#### 1.3.4 Zeeman Energy

When an external magnetic field is applied to the specimen, the magnetic moments within the specimen tend to align with the external applied field. The Zeeman energy term which describes this interaction takes the form

$$E_z = -\mu_0 \int_V \underline{M} \cdot \underline{H} dV \quad 1.8$$

where  $\underline{H}$  is the external applied field.

#### 1.3.5 Total Energy

The total potential energy of a magnetic system depends on all of the above-mentioned energy components. In different circumstances, one or other may dominate the magnetic behaviour.

$$E_{total} = E_{ex} + E_a + E_m + E_z \quad 1.9$$

The magnetic configuration of the system at any time will correspond to a minimum of the total energy. In a fully demagnetised state a magnetic system will correspond to a global energy minimum, but when the system has not been demagnetised the remanent state may only be a local minimum. Thus the energy of the system depends on what fields have been applied to it previously. This dependence of the magnetic state on the sample history is known as hysteresis and is dealt with in section 1.4.

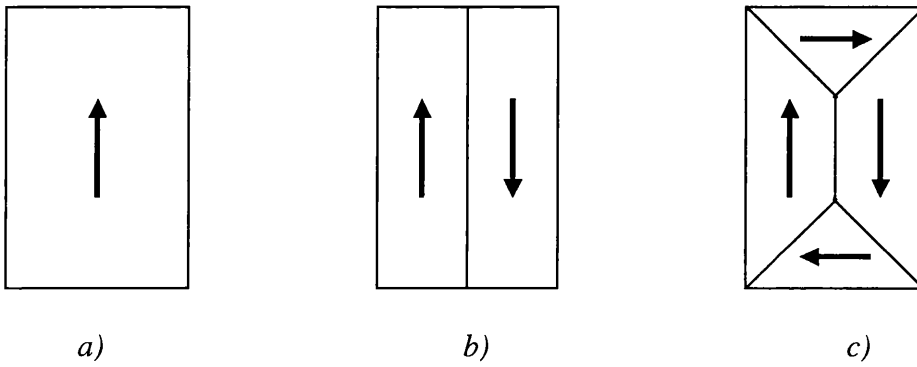
### 1.3.6 Magnetic Domains

The net magnetisation of a ferromagnetic material is usually less than the total saturation magnetisation, and can take any value between  $-M_s$  and  $+M_s$  depending on the magnetic history of the specimen. To account for this, the concept of magnetic domains – local areas of aligned magnetisation, was introduced [7]. This assumes that there are many different areas of locally aligned magnetisation within a specimen, each with a different magnetisation direction. Depending on the history of the specimen, the orientations of magnetisation in neighbouring domains may be random or partially aligned. These different orientations result in an overall lowering of the net magnetisation of the specimen.

The boundaries between adjacent domains are known as domain walls, regions across which the magnetisation rotates smoothly between the directions of magnetisation in each domain. The structure of domain walls is considered further in the next section.

Domain structure has been shown [8] to depend on the different magnetic energy contributions. Formation of domains is favoured if there is an energy saving going from a saturated state with high magnetostatic energy to a domain configuration with lower total energy. Figure 1.2 shows three possible domain configurations for the simple case of a small rectangular element of ferromagnetic material.

When the element contains only a single domain, as in fig 1.2a), magnetic charges form at the edges and a large magnetostatic energy contribution results. This magnetostatic contribution can be reduced by the element splitting into two domains with magnetisations in opposite directions as in fig 1.2b). Here the magnetic charges at the edges are less than in the single-domain case, but still lead to a significant magnetostatic energy. Figure 1.2.c) shows a configuration where “closure” domains are formed, completing a loop of flux within the element. In this case there are no free magnetic charges at the edges, and there is no stray field outside of the element. Depending on the energy associated with the walls (see next section), this configuration can be energetically more favourable than a) and b) as the magnetostatic energy contribution goes to zero.



*Figure 1.2 Possible domain configurations for a small rectangular element  
a) single domain, b) two-domain, c) flux-closure*

### 1.3.7 Domain Walls

The boundaries between magnetic domains are known as domain walls. The magnetisation vector rotates smoothly across the domain wall from the direction in one domain to that in the next. The different ways in which the vector can rotate across the wall leads to the formation of three different basic types of domain wall. These are known as Néel walls [9], Bloch walls [10], and cross-tie

walls [11], shown schematically in figure 1.3. In a Néel wall, fig 1.3a), the magnetisation vector rotates within the plane of the thin film. In a Bloch wall the magnetisation vector rotates out of the plane of the film as shown in fig 1.3.b). In some cases a cross-tie wall can form, which is an intermediate structure containing both Néel-type and Bloch-type regions as shown in fig 1.3.c). The thickness of the film strongly affects the type of domain wall which forms. Figure 1.4 shows the expected wall type in NiFe as a function of film thickness. From this, it can be seen that Néel walls are the favoured structure for NiFe films of thickness  $\leq 40\text{nm}$ .

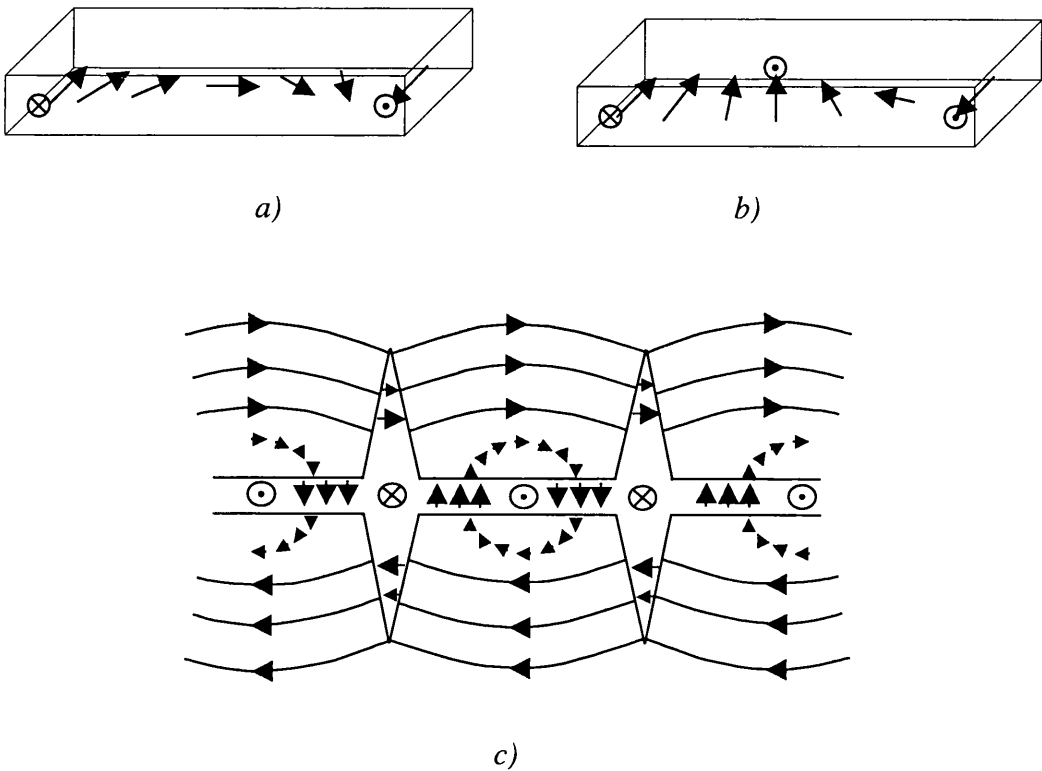


Figure 1.3 a) Néel wall, b) Bloch wall, c) cross-tie wall

The rotation of the magnetisation vector through a domain wall results in contributions to the exchange energy, anisotropy energy, and sometimes also the magnetostatic energy. The energy associated with a domain wall is a combination

of previously introduced energies, however in some cases it is valid to consider it as a separate energy term  $E_{wall}$ .

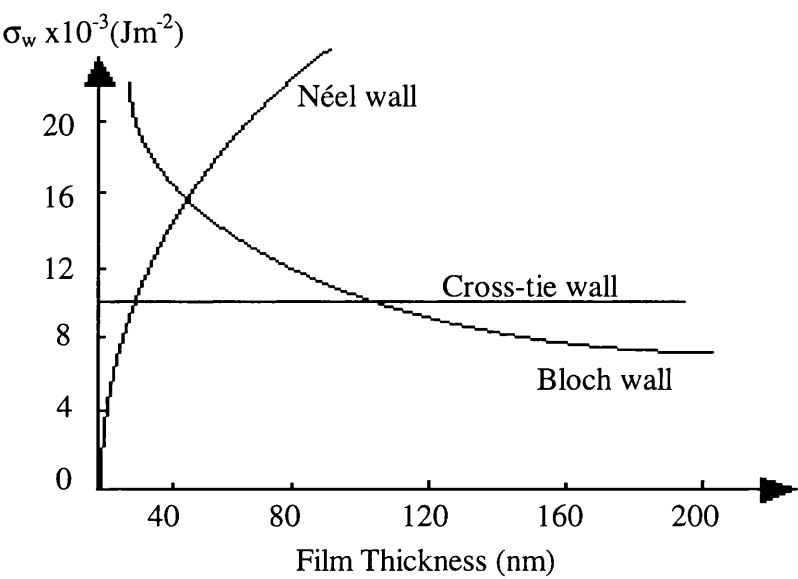


Figure 1.4 Phase diagram showing expected domain wall type as a function of NiFe thickness [12]

## 1.4 Hysteresis

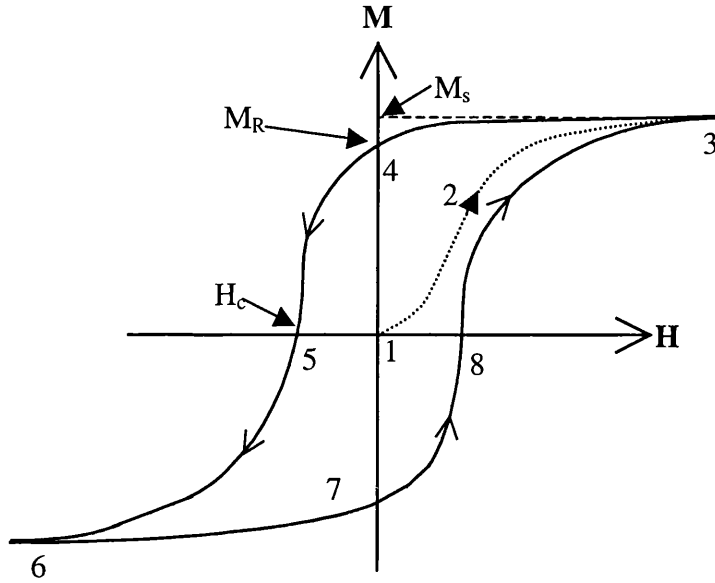


Figure 1.5 Example of a hysteresis loop for a ferromagnetic material

Figure 1.5 shows an example of a hysteresis loop for a ferromagnetic material. This describes how the overall magnetisation  $M$  of a sample varies with applied field  $H$ . If the specimen begins from a completely demagnetised state, then at zero applied  $H$  the orientations of individual domains are random, and the net magnetisation is zero, as indicated by point (1) in fig 1.5. When a positive magnetic field is applied, the magnetisation follows the initial magnetisation curve (1→2). As  $H$  is increased further, the magnetisation of the sample goes towards saturation ( $M_s$ ) at point (3). As the sample is magnetised from (1)→(3), the randomly oriented magnetic vectors throughout align towards the applied field direction. This occurs by a combination of magnetisation rotation and domain wall motion until saturation is reached and perfect alignment of  $M$  along the direction of  $H$  is achieved. From this point, if the applied field strength is reduced, the magnetisation will not decrease along (3→2→1) but follows the curve along (3→4→5→6). Point (4) is known as the remanent magnetisation  $M_r$ , the magnetisation which is present at  $H=0$ . Here, there is still partial alignment of the

magnetisation along the applied field direction. It is the existence of the remanent magnetisation which causes the magnetic state of any sample to be dependent on its history. From this point, as the field  $H$  is applied in the negative direction, the magnetisation decreases and reaches zero at point (5), the coercive field  $H_c$ . As the applied field in the negative direction becomes greater, the magnetisation approaches saturation in the negative direction at point (6). From here, decreasing the negative field and applying a positive field traces the curve from (6→7→8→3), reaching saturation in the positive direction once again. Cycling the field would continue to trace the loop as before.

Hysteresis is the phenomenon where the forward and reverse parts of the loop do not coincide. The behaviour of the system on application of an applied field depends on the direction in which the magnetisation of the system was most recently saturated.

The saturation magnetisation  $M_s$  is an intrinsic property of the ferromagnetic material of interest.  $M_r$  and  $H_c$ , however, can be varied for the same material by use of different deposition or processing techniques. These three parameters together define the shape of the hysteresis loop, and must all be taken into account when considering a material for a particular application.

## 1.5 Magnetisation reversal processes

When a magnetic film is subjected to an external magnetic field, the magnetisation of the film will tend to align with the applied field direction. This can be achieved by different mechanisms, falling into two categories: reversible and irreversible.

### 1.5.1 Reversible

A magnetisation process can be described as reversible if by reversing the direction of the applied magnetic field at any point in the cycle, the system will

return by the same path. Thus, cycling the applied field in opposite directions will cause the system to retrace the same set of intermediate states forward and backward. Such a cycle displays no hysteresis, the path followed having no dependence on choice of starting point but only on the direction of applied field.

A magnetisation reversal which takes place only by rotation of the magnetisation within a single domain to align with the applied field, is an example of a reversible process. Applying the same field in the opposite direction would cause the magnetisation to rotate in the opposite direction to align with the new applied field.

### **1.5.2 Irreversible**

An irreversible process means that the path of reversal undergone by the system depends not only on the direction and magnitude of the field applied, but also on the previous history of the specimen, in particular the immediately preceding field applied.

A magnetisation reversal process which takes place with formation and motion of domain walls will be irreversible, as whenever domain walls move beyond a small reversible range, they make irreversible jumps to new positions. These irreversible domain wall jumps are the origin of hysteresis in soft magnetic materials. These jumps are also a source of noise, termed Barkhausen noise, in magnetic recording systems.

## **1.6 Magnetoresistance**

Ferromagnetic materials undergo a change in electrical resistance in the presence of an applied field, which is dependent on the direction and magnitude of the field  $H$ . This is known as the magnetoresistance effect, and was first discovered in 1857 by William Thompson [13], who later became Lord Kelvin. It is only in more recent years that this effect has been utilised in magnetic sensors.

Magnetoresistance is a general term describing the variation of resistance with magnetic field. It covers several different phenomena, including anisotropic magnetoresistance (AMR) and giant magnetoresistance (GMR) which are considered here, as well as other phenomena now being investigated such as colossal magnetoresistance (CMR) and tunnelling magnetoresistance (TMR).

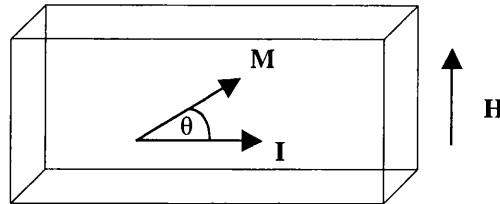
### 1.6.1 Anisotropic Magnetoresistance

The anisotropic magnetoresistance effect is the term used to describe the intrinsic physical property of ferromagnetic materials discovered by Thomson, where the electrical resistance changes in the presence of an applied magnetic field.

In a thin film of magnetic material, as used for magnetic sensor purposes, the magnetisation direction is within the plane of the film, due to demagnetising fields. In a thin film, single-domain state, the AMR effect can be described in straightforward terms [14]. Figure 1.6 shows an element of ferromagnetic material, used as an AMR sensor. When the angle between the magnetisation  $M$ , and the sense current  $I$  is  $\theta$ , the electrical resistance  $R$  is given by:

$$R = R_0 + \Delta R \cos^2 \theta \quad 1.10$$

where  $R_0$  is the fixed part, and  $\Delta R$  is the maximum value of the variable part of the resistance.



*Figure 1.6 AMR effect in a single-domain thin film element*

A plot of the variable part of the resistance for a soft magnetic material such as permalloy versus the angle of the magnetisation is shown in figure 1.7. It can be seen that the maximum value of the variable part occurs when the magnetisation is parallel to the current, where  $\theta=0$ . This curve has inflection points at  $\pm 45^\circ$ , where the change in resistance for a small change in magnetisation angle is nearly linear, and also has the greatest sensitivity. Hence, it is desirable for use as a sensor for the magnetisation of the material to be biased at  $45^\circ$  to the current direction. Different methods are used to achieve this in AMR heads, and are introduced in section 1.8.2.

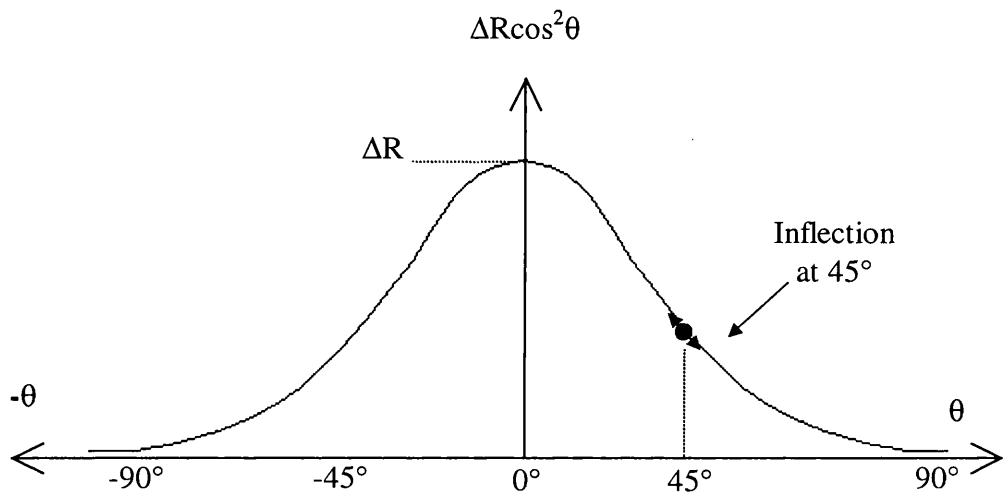


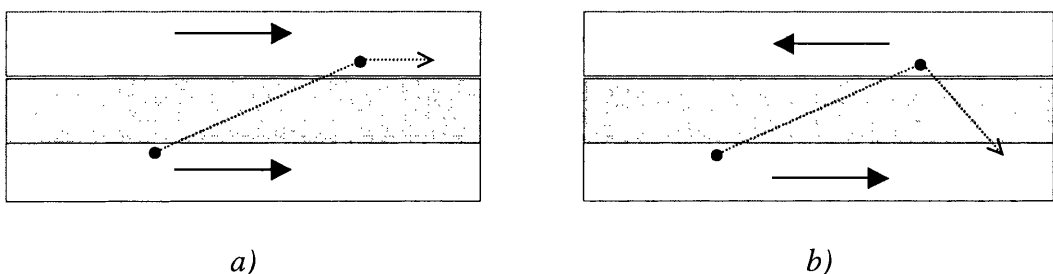
Figure 1.7 Magnetoresistance change vs. angle  $\theta$

### 1.6.2 Giant Magnetoresistance

Giant Magnetoresistance (GMR) was discovered in 1988 by Baibich et al. [15]. There are different types of structures which display giant magnetoresistance; granular materials, where a ferromagnetic material is suspended in a non-magnetic matrix, multilayers of ferromagnetic materials separated by non-magnetic spacer materials, and spin-valves, a more complex multilayer structure described in the

next section. The physical origins of the giant magnetoresistance are different to those of anisotropic magnetoresistance.

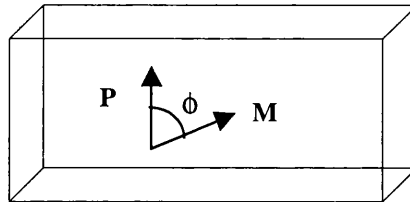
GMR results from spin-dependent scattering of conduction electrons at the interfaces between ferromagnetic and non-magnetic layers. In order to minimise energy, the majority of the conduction electrons within the ferromagnetic layers orient their spins parallel to the magnetisation. This is known as spin-polarisation. When an electric field is applied, the spin-polarised electrons accelerate until they encounter a scattering centre. Figure 1.8 shows the two possible cases which can arise when a spin-polarised electron is scattered so that it crosses the non-magnetic spacer layer of a spin-valve type structure. Provided that the non-magnetic spacer layer thickness is less than the spin relaxation length of the material, the conduction electron will arrive at the interface of the other ferromagnetic layer still carrying its original spin orientation. Figure 1.8(a) shows the case when the ferromagnetic layers have parallel magnetisation directions. The arriving conduction electron enters the ferromagnetic layer with very low probability of scattering, as its spin orientation matches the majority spins of that layer. This is the low resistance state. However, when the magnetisations of the two ferromagnetic layers are aligned anti-parallel as seen in figure 1.8(b), the majority of spin-polarised electrons encounter strong scattering at the interface, as their spins do not match the majority spins in the next layer. This strong scattering results in the high resistance state of the system.



*Figure 1.8 Spin-dependent scattering across non-magnetic spacer layer*  
a) parallel magnetisations – little scattering,  
b) anti-parallel magnetisations – strong scattering

## 1.7 Spin-valves

Spin-valves are a class of magnetic multilayer materials, which utilise the giant magnetoresistive effect. Spin-valve materials are now widely in use as magnetic sensors, and the majority of the work reported in this thesis is based on spin-valve materials. A basic spin valve consists of two ferromagnetic layers separated by a non-magnetic spacer layer, where one of the ferromagnetic (FM) layers is in contact with an antiferromagnetic (AF) material. The FM layer in contact with the AF is known as the “pinned” layer as the AF effectively fixes the direction of the magnetisation in this layer. The other FM layer is weakly coupled to the pinned layer through the spacer layer, but in an applied field is able to move its magnetisation direction to align with the applied field. This is known as the “free” layer. The resistance of the entire spin-valve structure is dependent on the angle  $\phi$  between the pinning direction  $P$  and the magnetisation direction of the free layer  $M$  as shown in figure 1.9. Thus the low resistance state for a spin-valve is when the free layer magnetisation lies parallel to that in the pinned layer, as is the case in the absence of an applied field. The high resistance state is when the free layer magnetisation lies anti-parallel to that of the free layer.



*Figure 1.9 Angle  $\phi$  between pinning direction and free layer magnetisation in a spin-valve*

A large number of variations in the materials used, layer thicknesses and arrangements in spin-valve structures are in existence, many more combinations are possible. The position of the AF layer at the top or bottom of the stack gives rise to top- and bottom- spin-valves. Positioning an AF at both the top and bottom of a stack gives what is known as a dual spin-valve. These different arrangements are indicated in figure 1.10.

Layers of other materials are often incorporated into spin valve stacks; as a seed layer to control grain growth; as a protective capping layer; or within the stack to improve different magnetic or electrical properties of the overall stack.

Increasingly, structures known as synthetic antiferromagnets (SAF's) are being included in spin valve stacks in place of the single pinned layer to improve the stability of the pinning effect. A SAF consists of two ferromagnetic layers separated by an extremely thin ( $\leq 1\text{nm}$ ) non-magnetic spacer, often Ruthenium, as shown in fig 1.11. The pinned layer is in contact with the AF, and there is a strong antiferromagnetic coupling across the thin spacer layer, which causes the magnetisation direction in the reference layer to lie antiparallel to that in the pinned layer. The pinning effect achievable by using a SAF structure like this in a spin-valve is much stronger and more stable than is possible using a single pinning layer in contact with the antiferromagnetic material.

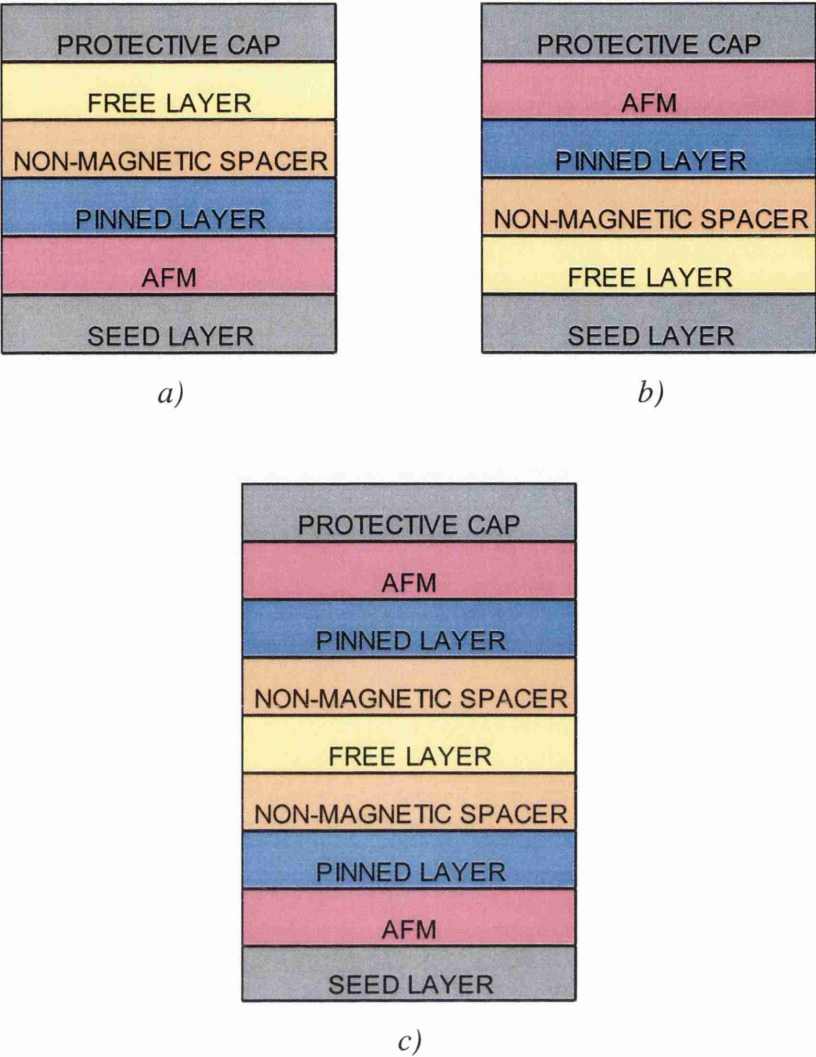


Figure 1.10 Schematic structures of spin-valve stacks  
a) bottom spin-valve, b) top spin-valve, c) dual spin-valve

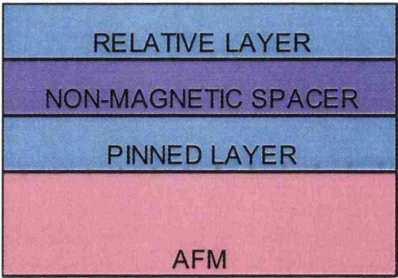


Figure 1.11 Schematic of SAF structure

## **1.8 Magnetic Recording and Sensors**

### **1.8.1 Introduction**

Magnetic data storage is of critical importance today, as the volumes of information being stored increase each year at an exponential rate. This section introduces some of the fundamentals of magnetic data storage technology, particularly digital data storage.

Initially, magnetic recording was developed using a single inductive coil as both a read and write head. Great improvements have been made over recent years in the read part of the head with the advent of magnetoresistive and giant magnetoresistive sensors. However, the writer part of a magnetic recording head is still based on an inductive coil used to apply fields to the recording media to write information.

The writer is shown schematically in figure 1.12, and is made up of 3 parts: the core, the coil and the write-gap. The write current is passed through the coil, which is wound round the magnetic core, and induces a magnetic flux within the core. The write-gap permits the magnetic flux circulating in the core to fringe out and intercept the recording media, causing it to become locally magnetised. Due to hysteresis, the ferromagnetic material of the media retains its magnetisation direction, and hence the information, after the write current is switched off. It is the stray fields emanating from transitions between written bits in the media which must be sensed by the reader part of the head in order to retrieve the stored information.

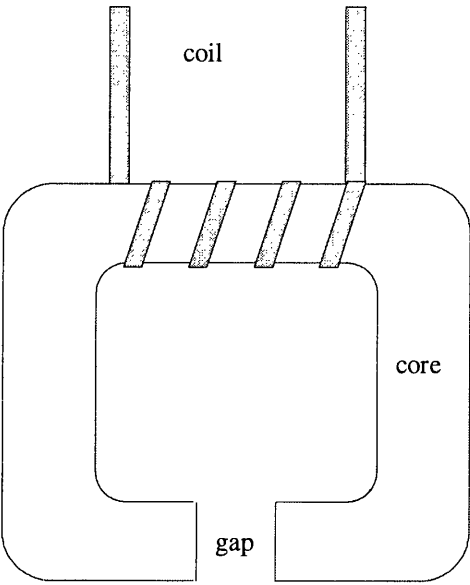


Figure 1.12 Write head structure

In inductive heads, the reading process is essentially the writing process in reverse. The core provides a flux closure path for the stray fields emanating from the media, and this then induces an output signal current in the coil, given by Faraday’s Induction Law. This law states that the induced e.m.f. in the coil circuit is equal to the rate of change of the flux linking the circuit,

$$V = -N \frac{d\phi}{dt} \tag{1.11}$$

where  $V$  is the induced e.m.f. in the coil,  $N$  is the number of turns and  $\phi$  is the magnetic flux.

Today’s thin film technology has allowed the writer structure to be deposited in layers, enabling smaller dimensions of the pole tips, and so achieving higher fringing fields from the write-gap. This is necessary since higher areal bit density requires media with higher coercivity to constrain the magnetisation in the written bit. The higher coercivity media in turn requires a greater flux from the write-gap

in order to magnetise the media and record the information. Another advantage of thin film heads is that the higher permeability achievable permits high frequency operation, giving faster writing speeds.

1.8.2 Magnetoresistive Heads

Magnetoresistive read heads [16], utilise the magnetoresistive effect as described in section 1.6, to sense those components of the stray fields from transitions between adjacent written bits of information on the recording media which lie in the plane of the sensor. Figure 1.13 represents the layout of an AMR head, showing the AMR sensor, the inductive writer part, and the lower shield. The bottom pole of the writer forms the upper shield for the sensor, with both shields acting to protect the sensor from extraneous stray fields from bits other than that to be read.

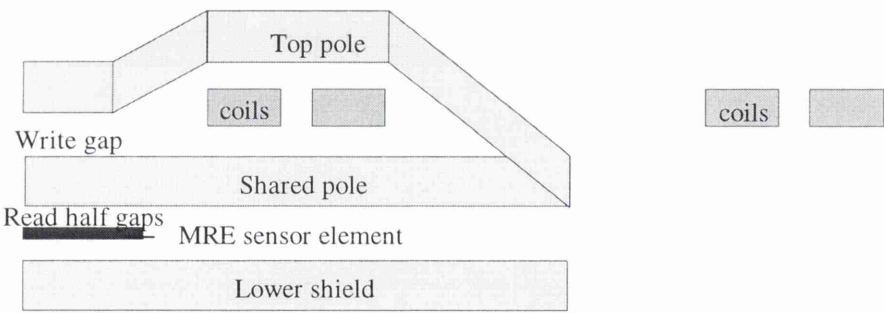


Figure 1.13 Layout of an AMR head

A simple AMR sensor can be made from a single layer of permalloy, which can be single domain, with the magnetisation lying within the plane of the film. It is desirable to have the magnetisation of the sensor biased to 45° from the sense current direction, as previously discussed in section 1.6.1. This can be achieved in a number of different ways, including permanent magnet biasing, where a permanent magnet is placed in contact with the sensor to apply a small field perpendicular to the sense current as shown in figure 1.14. Another method of biasing an AMR sensor is by the use of a soft adjacent layer (SAL). The SAL

vertical biasing arrangement is shown in figure 1.15. Here a low-coercivity, high permeability magnetic material is placed adjacent to the AMR material. The current flowing in the MR material produces a vertical magnetic field, and hence vertical magnetisation in the SAL. This magnetisation in the SAL then causes a magnetostatic interaction with the MR layer to produce a vertical biasing field as required. Other methods of biasing AMR heads are in use, including the Barber-pole system [17], which uses the current to produce the bias; and exchange biasing [refs], which depends on contact between the AMR material and another magnetic material (ferro- or anti-ferro-).

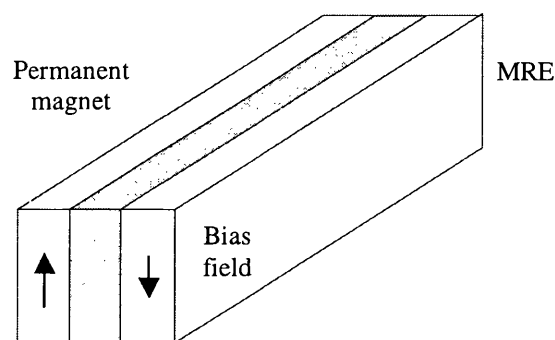


Figure 1.14 Permanent magnet biasing of an AMR sensor

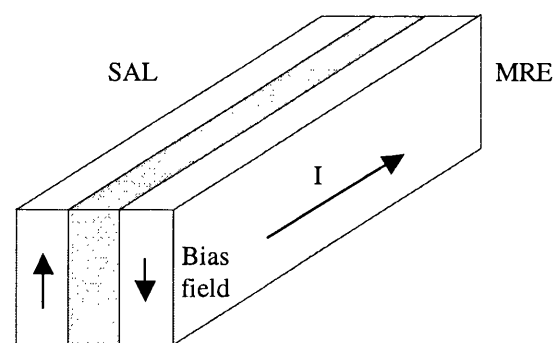


Figure 1.15 SAL biasing of an AMR sensor

AMR heads have largely been superseded in recent years by GMR heads in hard disc drive (HDD) applications, however they are still in use for many tape storage systems.

1.8.3 Giant Magnetoresistive Heads

Giant magnetoresistive (GMR) heads use spin-valve or GMR multilayer structures as sensors, in order to give a greater output amplitude signal than more basic AMR heads. The structure of a spin-valve head is shown schematically in figure 1.16. The writer part and the shielding arrangement is largely the same as for an AMR head as shown above in fig 1.13, although variations exist.

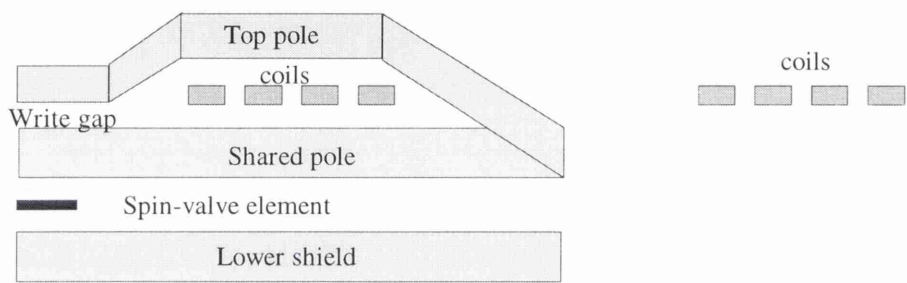


Figure 1.16 Layout of a GMR spin-valve head

There are several advantages in using GMR over AMR based sensor devices. Perhaps the main advantage is that spin-valve heads are capable of better low-field sensitivity than AMR heads [18,19]. Also, the complicated biasing systems adopted in the AMR case as described above are not necessary in spin-valve heads. The presence of the pinned layer, as well as the use of various processing techniques such as sputter deposition in the presence of an alignment field, and magnetic annealing, can control the orientation of the free layer magnetisation in the absence of an applied field.

## 1.9 Outline of Thesis

In Chapter 2 of this thesis, follows a description of the instrumentation and experimental techniques adopted for the transmission electron microscopy investigations. Chapter 3 goes on to describe the fabrication of electron transparent substrates suitable for TEM investigations and the growth of the magnetic films of interest. In Chapter 4 we consider the physical microstructure of the magnetic materials investigated.

Chapter 5 goes on to discuss the magnetic behaviour of some single-layer ferromagnetic films, and also materials used as AMR sensors. Chapter 6 looks at a set of spin-valves and their magnetic response as a function of applied field orientation and specimen temperature. Chapter 7 considers the effects of changing the thicknesses of different layers within a particular spin-valve stack. Chapter 8 looks at patterned elements of spin-valve material, considering the effects of shape, size and aspect ratio.

Finally, Chapter 9 discusses the conclusions drawn from this work, and goes on to consider some further work on the subject of spin-valves which would be of potential interest.

## **Chapter 2 Transmission Electron Microscopy – Instrumentation and Techniques**

### **2.1 Introduction**

The electron microscope is a versatile tool, which gives rise to a variety of different experimental techniques. This chapter provides a summary of the equipment and techniques used in this study. The methods described herein make up a small subset of the available techniques.

### **2.2 Transmission Electron Microscopy**

The transmission electron microscope can be considered in the most basic terms as analogous to a conventional optical microscope. The most obvious difference is that while an optical microscope uses a beam of light to illuminate the specimen, the electron microscope uses a beam of electrons. The magnetic lenses and the vacuum systems necessary make electron microscopes much more complex in their construction and operation however. Here, an introduction is given to some of the features of an electron microscope. This is by no means a complete treatment of the subject, but should give a summary of the key features of an electron microscope [1,2].

The electron microscopes within the Solid State Physics labs at the University of Glasgow which have been used for this work are the JEOL 1200EX and 2000FX, and the Philips CM20. Therefore, in the following descriptions, particular attention is paid to aspects of these instruments.

#### **2.2.1 Electron gun**

The electron gun provides the source of electrons within an electron microscope. The most common system for production of a beam of electrons uses thermionic emission from a heated tungsten filament. The “hairpin” of tungsten wire acts as

the cathode, heated to ~2800K and held at a high negative potential with respect to the anode and the rest of the microscope. Thermionically emitted electrons from the filament are accelerated rapidly towards the anode and form a high energy beam which is emitted through a circular hole in the anode into the microscope column. This is the system adopted in the JEOL microscopes used in this work.

The thermionic gun is adequate for many purposes, but the resultant beam is of limited brightness. The brightness is defined as the beam current density per unit solid angle; therefore it gives a measure of the number of electrons per second, which can be directed at a given area of specimen. For a thermionic gun the brightness  $B$  is given by:

$$B = 2 \times 10^5 TV \exp\left(-\frac{\phi}{kT}\right) \quad 2.1$$

Where  $T$  is the temperature of the filament in K,  $V$  is the potential at which it is held,  $\phi$  is the thermionic work function of the filament material, and  $k$  is the Boltzmann constant.

The brightness can be increased somewhat by replacing the tungsten filament, which has a work function of 4.5eV, with a LaB<sub>6</sub> crystal which has a work function of 3.0eV.

If still higher brightness is required, a field emission gun (FEG) can be used. This is comprised of a sharp tungsten needle with an oxide coating, frequently zirconia (ZrO<sub>2</sub>), which is subjected to a high electric field. Electrons can leave the surface by tunnelling without requiring the energy to overcome the work function, so many more electrons can be drawn from a piece of tungsten than by thermionic emission, giving higher brightness by a factor of a thousand or more. FEG sources also have the advantages over thermionic sources of smaller electron energy spread (0.6-1.2eV), smaller source size (~6nm virtual source size) and higher

coherence. These benefits are important for Lorentz imaging where it is important that the electron source is not only bright and small, but also that the angle subtended by it is significantly less than the Lorentz deflection angle ( $\sim 0.1\text{ mrad}$ ) (see section 2.4.1).

Figure 2.1 shows schematically the field emission gun within the Philips CM20 [3], which is used for a large portion of the work in this study. This gun, which is optimised for high current and stability, contains the field emitter source, and extraction anode and an electrostatic gun lens. The extraction anode provides the extraction voltage in the range 1.0 to  $\approx 6.0\text{ keV}$  that controls electron emission from the tip from a few  $\mu\text{A}$  to  $\approx 250\mu\text{A}$ . In order to maintain tip lifetime, without compromising usable beam brightness, the extraction voltage is usually set to provide an electron emission of  $\approx 100\mu\text{A}$ . The 3-element electrostatic gun lens focuses the electron beam to its initial crossover and provides an initial acceleration of the beam to around  $40\text{ keV}$ . Several accelerator anodes then increase the electron energies up to  $200\text{ keV}$  in the case of the CM20.

FEG guns require much higher vacuum conditions than thermionic guns, so that the emitter region is pumped by an ion-getter pump to a vacuum of  $5 \times 10^{-7}\text{ Pa}$ , and the accelerator region is separately pumped by another ion-getter pump to a vacuum of  $10^{-6}\text{ Pa}$ . This separation of source and accelerator prevents small bursts of gas disturbing the electron emission. This type of gun configuration [4] provides very low chromatic aberration and produces a very coherent electron beam of high brightness from a small virtual source size.

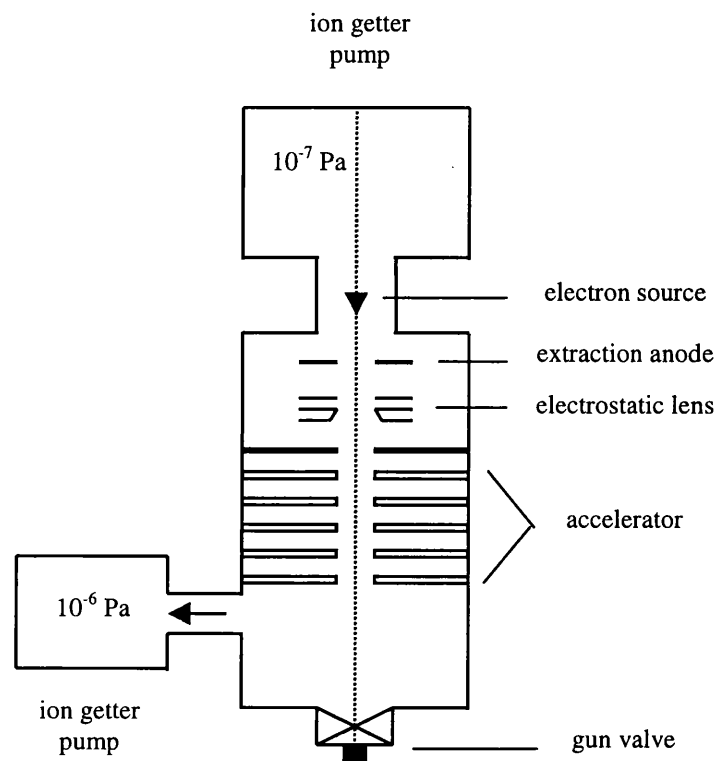


Figure 2.1 Field emission gun (FEG) used in the Philips CM20

### 2.2.2 TEM column

The electron microscope column encloses the path of the electron beam from the gun to the image-viewing screen. A series of electromagnetic lenses are positioned along the column, which focus the beam onto the specimen and then transfer the image formed to the viewing screen or image capture device. The entire column, with the exception of the lens coils, is held in a vacuum of approximately  $10^{-5}$  Pa. The layout of the column in the Philips CM20 is shown in figure 2.2.

The first lenses to affect the electron beam after it leaves the gun assembly are the two condenser lenses. The first of these acts to demagnify the electron source, determining the electron spot size at the specimen. The second of the condenser lenses controls the angular convergence of the beam, determining the spot size of the beam as it is projected onto the specimen. The beam then encounters the condenser aperture, the first of the selectable apertures in the column, which defines the electron probe. For this reason it is particularly crucial that it is accurately aligned with the optical axis of the microscope. Different sizes of aperture are available in the range 10 to 200 $\mu$ m with a smaller aperture producing a beam with higher coherence and smaller convergence angle.

In standard electron microscopes, which have not been modified for magnetic imaging, the specimen is situated within the main imaging lens, known as the objective lens. This lens focuses the electron beam to produce a diffraction pattern near its back focal plane, and as in optical microscopy, it is this lens which determines the final resolution of the microscope. Lenses in electron microscopy use a vertical magnetic field of up to 1T to converge the electron beam. When imaging magnetic materials this field severely perturbs or destroys the magnetic structure of interest. One possible solution to investigate magnetic properties of a specimen is to leave the objective lens unexcited and use the post-specimen lenses to focus the image. This gives only low resolution, and so is not satisfactory for many magnetic studies.

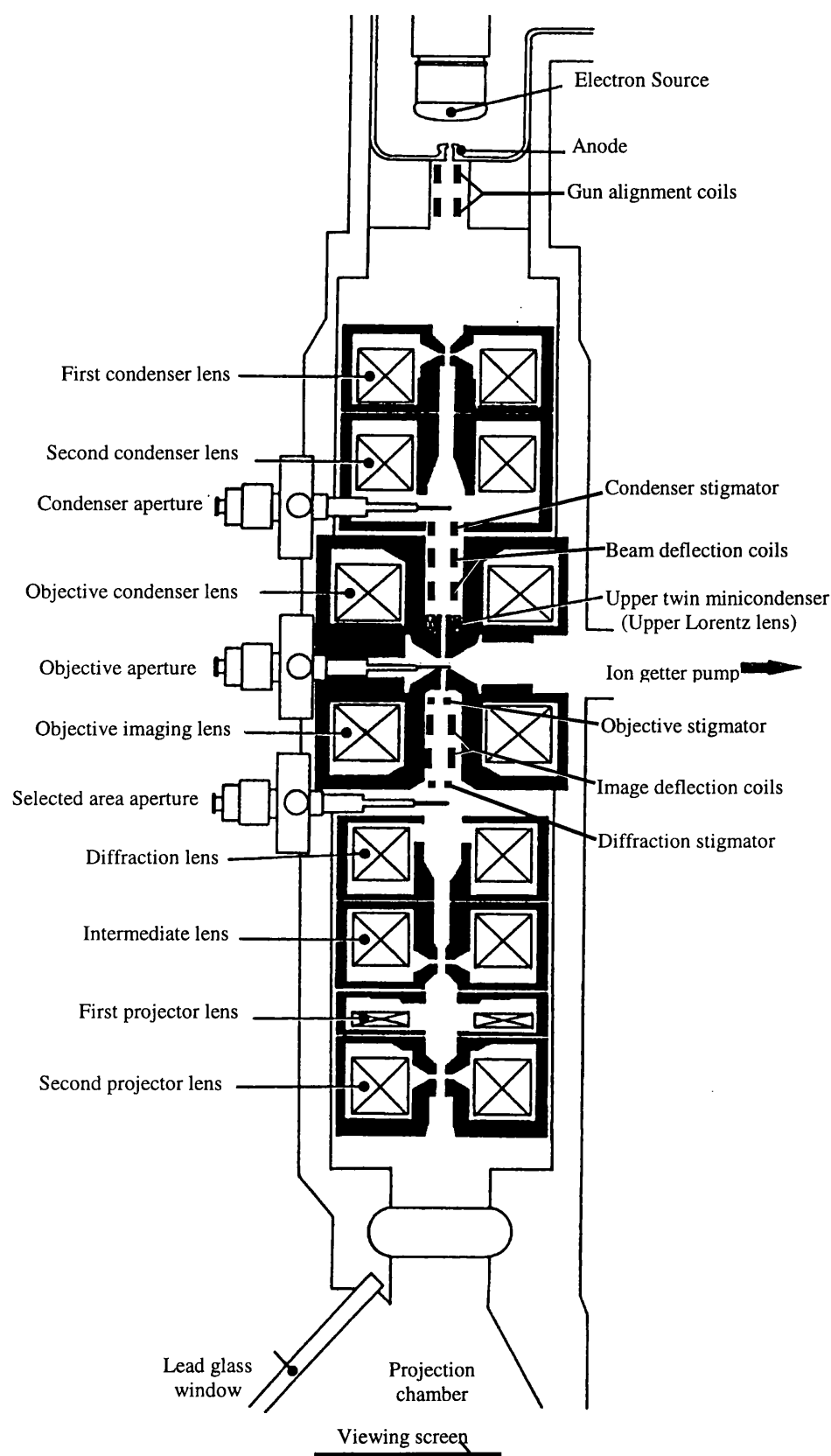


Figure 2.2 EM column in the Philips CM20

In order to enable high resolution studies of magnetic structures, highly modified objective lenses have been used. In the JEOL 2000FX the original objective lens is replaced with a split pole-piece lens to provide a field-free region around the specimen [5].

In the Philips CM20 a split objective lens remains, and an additional pair of mini lenses (known as the Lorentz lenses) are included above and below the objective pole-pieces. When magnetic materials are studied, these Lorentz lenses can be used individually or together to provide focussing without the use of the objective lens, leaving the specimen in a field-free area [6].

The objective aperture, situated near the back focal plane of the objective lens, is used to generate diffraction contrast or to enable Foucault imaging (see section 2.4.3, and can be moved in and out from the beam path. Below the objective lens system is the selected area aperture, which can be inserted into the beam path to allow diffraction patterns to be collected from specific regions of the specimen.

In the standard imaging mode of conventional transmission electron microscopy (CTEM), the image formed by the objective lens is then magnified and projected onto the viewing screen or image capture device, by a set of intermediate and projector lenses. These post-specimen lenses can also be adjusted in order to project the back focal plane of the objective lens onto the viewing screen, revealing the diffraction pattern of the specimen.

### **2.2.3 Image capture**

When the desired image or diffraction pattern is obtained, the data must be somehow recorded. The electron microscope can be fitted with various devices to collect images. Of these, photographic plates are the traditional method, which offer very good resolution and sensitivity but require time-consuming preparation and development processes. Video cameras allow real-time observation of time-dependent effects, but have poor signal to noise ratios in comparison with

micrographs. In more recent years slow-scan CCD cameras have become popular, as they allow high resolution digital images to be collected quickly and without the inconvenience of photographic processing. Also, during lengthy experiments, the number of images recorded is only limited by the storage capacity of the CCD controlling computer, instead of the 50 or so photographic plates which can typically be accommodated within the camera chamber of an electron microscope.

The choice of image capture method for any particular experiment depends which type of data the operator desires. In the Philips CM20 used in the majority of the experiments in this work, all three options of image capture are available, adding to the versatility of the system.

#### **2.2.4 JEOL 1200EX and 2000FX**

The JEOL 1200EX and 2000FX [5] used in this work are conventional transmission electron microscopes (CTEMs). The 1200EX is a standard CTEM and has been used in this work primarily for observations of the physical microstructure of thin films. The objective lens system in this microscope has not been modified for magnetic investigations, and so specimens' magnetic microstructure is altered after insertion in the 1200EX. The magnifications used range from a few hundred times to 400kx, allowing physical structure to be studied on nm scale.

The 2000FX was also used for some of the physical microstructure observations, but this microscope has been specially modified for investigation of magnetic specimens. It has been fitted with a two-part objective pole-piece so that the specimen is contained in a field-free region. This means that the magnetic field from the objective lens does not affect the specimen while within the TEM. It is preferable therefore to carry out physical microstructure investigations on magnetically-sensitive materials within this microscope rather than in the 1200EX. Indeed, depending on conditions required, it is often convenient to carry out microstructural investigations within the same experimental session as in-situ

magnetisation investigations. A specially-designed specimen holder with magnetising coils on either side allows that the specimen can be imaged either in zero field, or with the application of a controllable field (see section 2.5).

### **2.2.5 Philips CM20**

The Philips CM20 microscope [6], which was used for the majority of the magnetising experiments described within this work, has been extensively modified for the purposes of specialised magnetic imaging techniques. The addition of a pair of lenses, known as the Lorentz twin lenses, which sit above and below the objective lens pole pieces, enables the microscope to be operated without the objective lens being active, providing a field-free environment for the specimen. Alternatively, the twin lenses can be used as the focusing lenses with the objective lens being partially excited to provide a controllable vertical magnetic field in the specimen region. Thus by tilting the specimen away from horizontal, a component of the vertical field is brought into the plane of the specimen (see section 2.5).

The CM20 is a FEG (S)TEM microscope, equipped for a range of different experimental techniques. The scanning mode enables differential phase contrast magnetic imaging (see section 2.4.5), which is used in investigating small patterned elements (Chapter 8).

Although the CM20 has been extensively modified to optimise its magnetic imaging capabilities, it also retains versatility and can be used for a number of analytical techniques such as electron energy loss spectroscopy (EELS). These techniques are the subject of much research, but are not used in this study.

## **2.3 Microstructural Information**

Electron microscopy can yield a variety of information on the physical microstructure of materials. In this study only a brief investigation of the physical

structure of the magnetic thin films of interest has been carried out (Chapter 4). Hence, only those techniques adopted are described here.

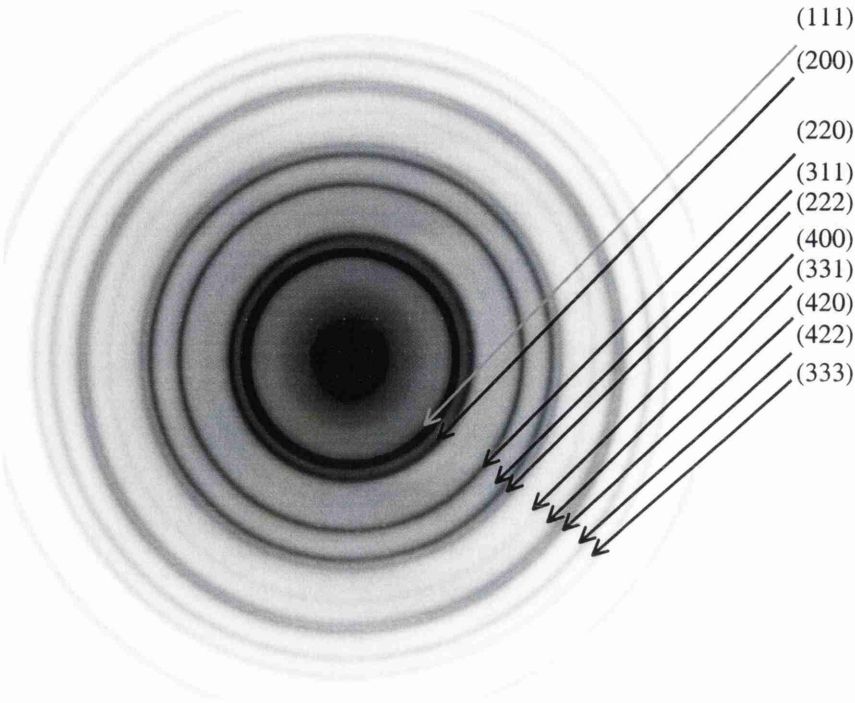
### 2.3.1 Diffraction Patterns

Diffraction patterns are obtained by adjusting the post-specimen lenses to project the back focal plane of the objective lens onto the viewing screen or image capture device. For polycrystalline specimens, as were all of the films in this study, the diffraction pattern appears as a set of concentric rings. Each ring is formed by electrons which have been scattered by a particular set of crystal planes in the many small crystallites. Figure 2.3 shows a diffraction pattern for NiFe, indexed to show which planes give rise to particular rings. Indexing diffraction patterns becomes more complex as multi-layer films are considered.

Diffraction patterns taken with the specimen tilted away from horizontal can indicate any texturing in the film. Figure 2.4 shows a pair of diffraction patterns obtained for Ta / NiFe with the specimen a) horizontal and b) tilted through 30°. Intensity variations within the (200) and (220) rings of NiFe in 2.4b) show that there is texturing present in the [111] direction in the NiFe due to the presence of the Ta underlayer. Single layer NiFe films do not show this effect.

### 2.3.2 Bright and Dark field imaging

The simplest mode of operation of a transmission electron microscope is known as bright field imaging, where the beam of electrons is transmitted through the specimen and brought to a focus at the imaging plane. Inserting the objective aperture removes some of the scattered components from the beam and improves the contrast of the image. In this mode, the physical microstructure of the specimen can be observed at high resolution. Figure 2.5a shows a typical bright field image of a NiFe thin film specimen, revealing the polycrystalline structure.



*Figure 2.3 Diffraction pattern of NiFe*

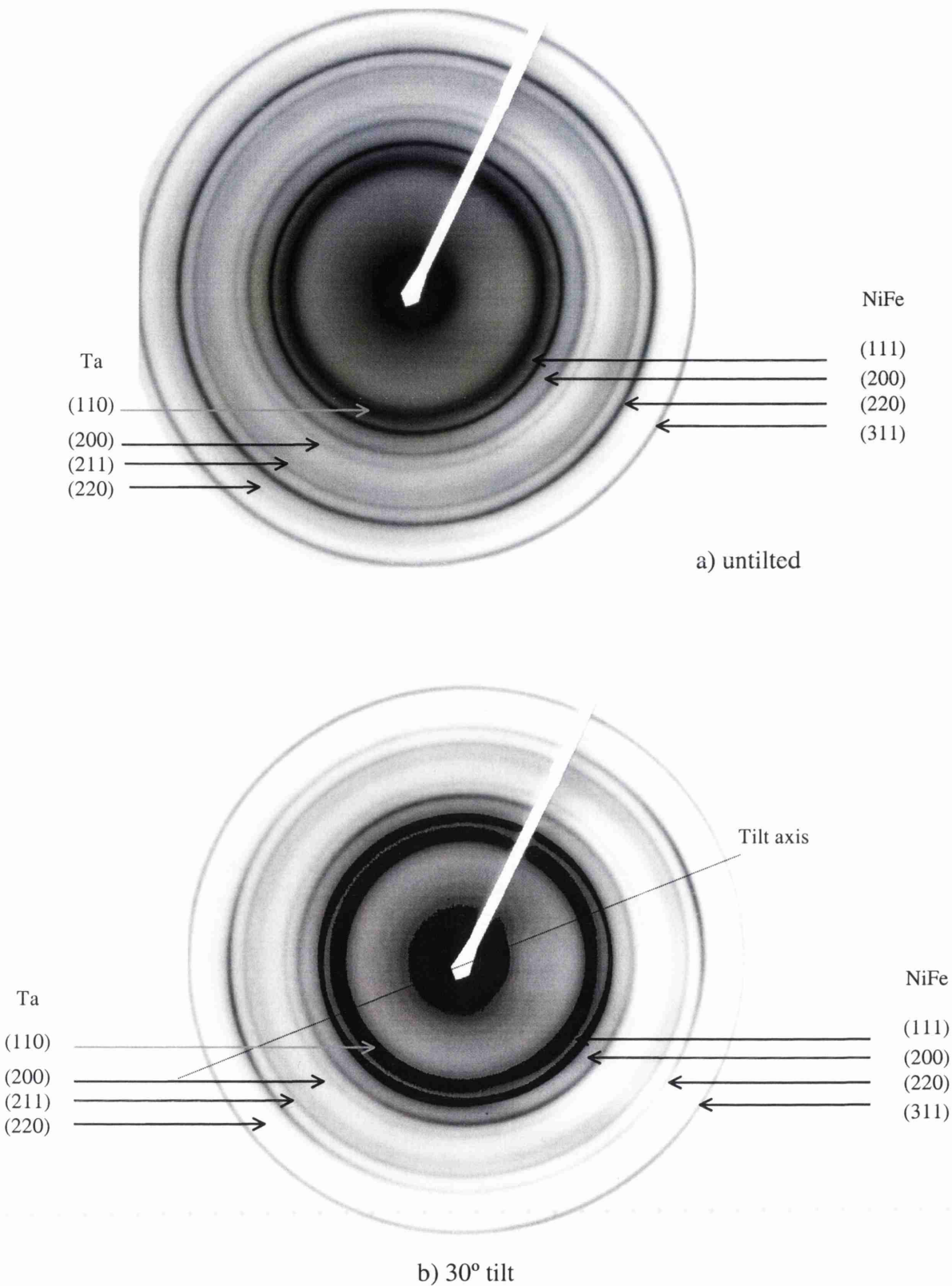
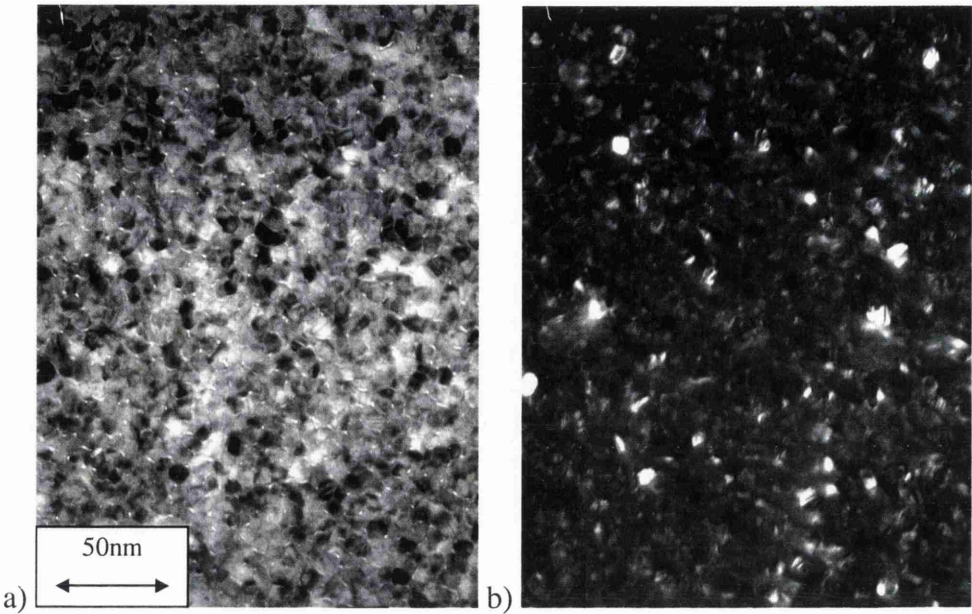


Figure 2.4 Diffraction patterns Ta/NiFe taken with a) specimen horizontal, b) specimen tilted through 30°



*Figure 2.5 Grain structure of 40nm NiFe shown in a) bright field image,  
b) dark field image*

Dark field imaging is achieved by the insertion of the objective aperture in the back focal plane to select “information” from part of a particular diffraction ring (for polycrystalline specimens) or spot (for single crystals). Figure 2.5b shows a dark field image of the same specimen obtained by selecting a segment of the (111) diffraction ring. The regions which appear bright in this image are small crystallites which are oriented to excite certain (111) reflections. Images like these enable estimates of individual grain sizes within the films.

## 2.4 Magnetic Imaging

The set of techniques used in the TEM for observation of magnetic contrast are known collectively as Lorentz microscopy, as these techniques all utilise the Lorentz interaction of a beam of electrons with a magnetic field [7]. A brief explanation of this Lorentz interaction is presented, before describing the principal magnetic imaging techniques which have been used in this work.

### 2.4.1 Electron beam and specimen interaction

A parallel electron beam, incident on a magnetic thin film, experiences a Lorentz deflection through an angle  $\beta$  given by:

$$\beta_x(x, y) = \frac{e\lambda}{h} \int_{-\infty}^{+\infty} B_y(x, y, z) dz \quad 2.2$$

where  $B_y(x, y, z)$  is the y-component of magnetic induction at point (x,y,z),  $e$  the electronic charge,  $\lambda$  the electronic wavelength and  $h$  is Planck’s constant. Here the z direction is the optic axis, perpendicular to the film, and x and y directions are in the plane of the film. This arrangement is shown schematically in figure 2.6.

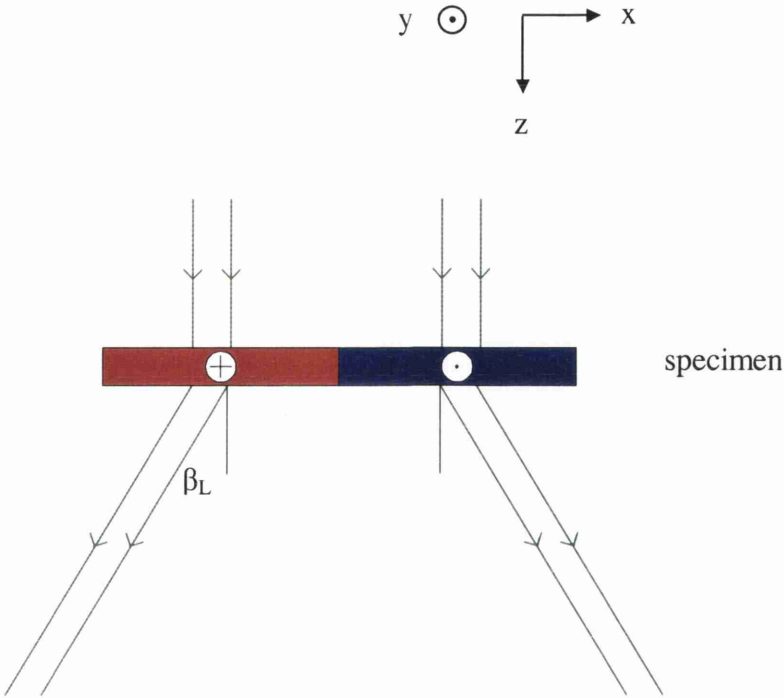


Figure 2.6 Schematic of Lorentz deflection

Assuming that the film is of a constant thickness  $t$ , uniform magnetisation, and there is no stray field emanating from the film, then this becomes:

$$\beta = \frac{eB_s \lambda t}{h} \tag{2.3}$$

where  $B_s$  is the saturation induction,  $B_s = \mu_0 M_s$ . The Lorentz deflection angle ( $\sim 0.1 \text{ mrad}$ ) is significantly smaller than the first Bragg angle ( $\sim 10^{-2} \text{ rad}$ ) of a typical magnetic material.

### 2.4.2 Fresnel imaging

Fresnel imaging is a mode of Lorentz microscopy where magnetic contrast is obtained by defocusing the imaging lens to reveal domain walls as narrow bright and dark bands. Figure 2.7 shows a cross-sectional view through a thin ferromagnetic film containing magnetic domains of opposite directions of magnetisation into and out of the plane of the page. This illustrates how the Lorentz deflection causes divergences and convergences of the electron beam at the boundaries of magnetic domains. By slightly defocusing the image forming lens the object plane is now slightly above or below the specimen plane, revealing bright and dark contrast where the convergences and divergences of the electron beam occur. This contrast is highly dependent on the defocus value and can be inverted by moving the imaging lens from over-focused to under-focused. Figure 2.8 is an example of a Fresnel image from a 20nm NiFe specimen, showing convergent and divergent domain walls.

Magnetisation ripple [8], observed in Fresnel images, is the effect whereby small variations in the magnetisation direction within a domain cause variations in contrast which appear orthogonal to the mean magnetisation direction in that area. Observation of magnetisation ripple contrast thus enables a qualitative assessment of magnetic domain structures by deducing the axis in which the magnetisation lies. It is not possible to determine which sense the magnetisation direction lies, however, from magnetisation ripple alone.

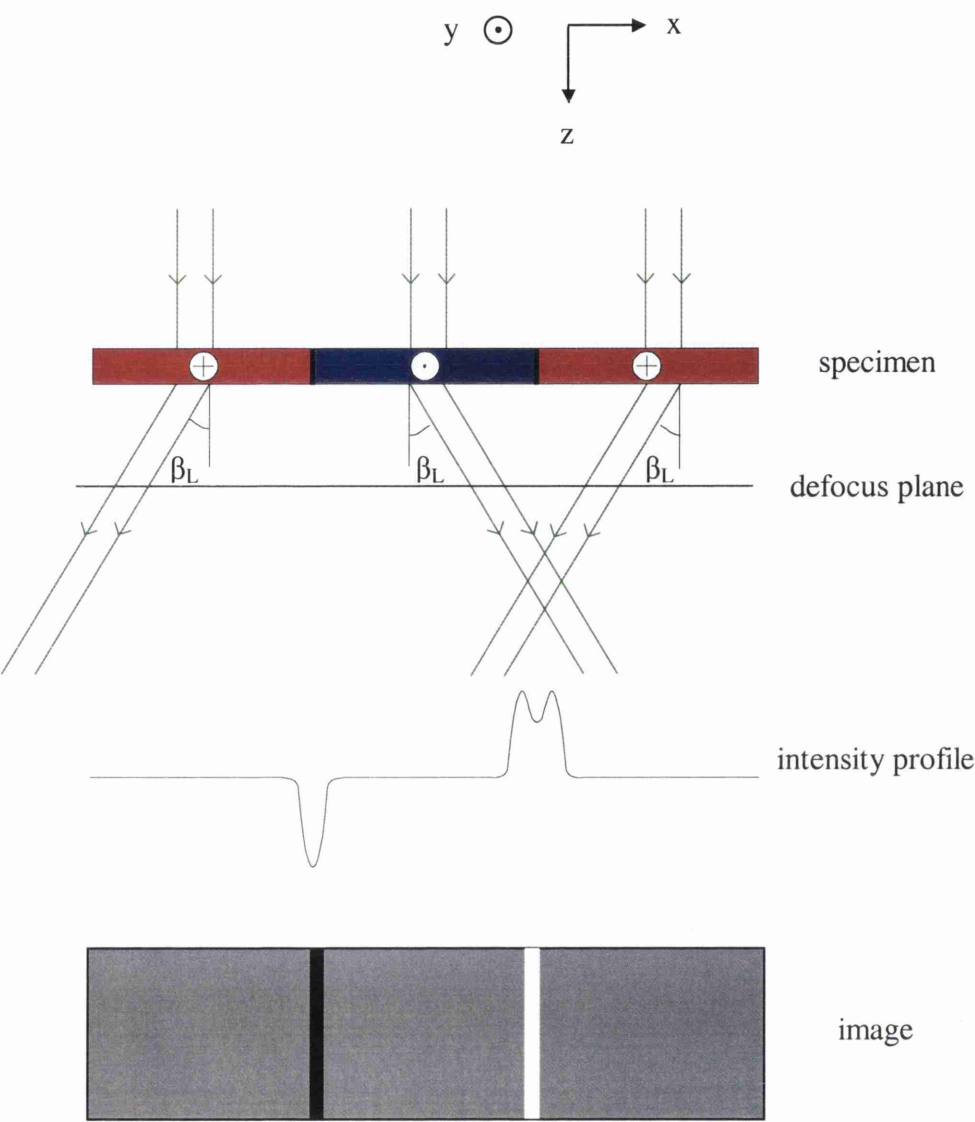
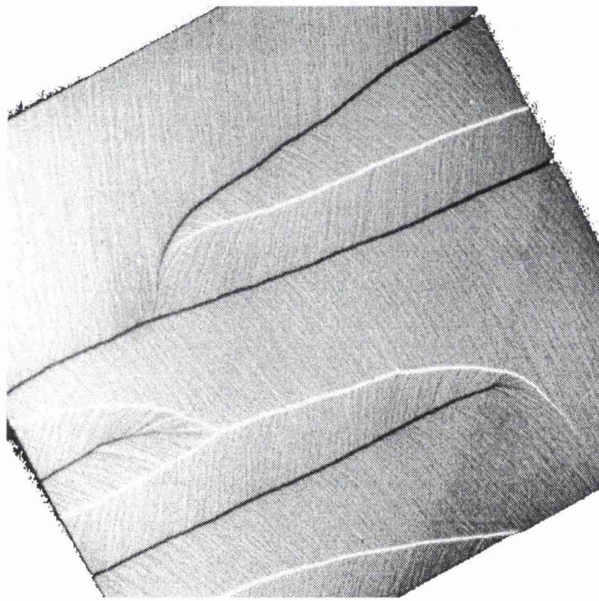


Figure 2.7 Schematic of Fresnel image formation

Fresnel is the simplest of the magnetic imaging techniques to implement, and can give high contrast at domain walls. For these reasons it is often convenient to operate in Fresnel mode, and much of the work reported here has been carried out using Fresnel imaging. However, the defocus of the imaging lens in order to provide the magnetic contrast also provides difficulties. It is this defocus which limits the resolution available, making Fresnel imaging particularly unsuitable for observation of small patterned elements, and prevents simple comparisons of magnetic structure with topography. Also, it is difficult to deduce any quantitative information from Fresnel images as the very nature of the defocus technique makes precise measurements of contrast intensity or of location within the specimen impractical.



*Figure 2.8 Fresnel image of NiFe showing convergent (bright) and divergent (dark) domain walls*

### 2.4.3 Foucault imaging

Foucault imaging is another standard mode of Lorentz microscopy, so it is mentioned here briefly although it has not been implemented in the experimental work described in later chapters. This mode utilises the fact that electrons passing through a given domain are deflected by the same angle and so are all focused at the same point near the back focal plane of the image forming lens. Figure 2.9 shows schematically the microscope configuration for Foucault imaging. When the objective aperture, situated near the back focal plane, is aligned in such a way as to block out those electrons which arise from a particular domain then this domain has zero intensity in the image. Domains with magnetisation in the opposite sense have the strongest intensity in the image, while domains with all other directions of magnetisation have intermediate grey levels. The positioning of the objective aperture can be manipulated in order to show contrast in different directions. It is standard procedure to collect at least two images with orthogonal mapping directions. This technique is relatively simple to implement, and does not suffer from the poor resolution of Fresnel, being an in-focus mode. It is vulnerable, however, to large variations in intensity due to difficulties with the mechanical alignment of the objective aperture.

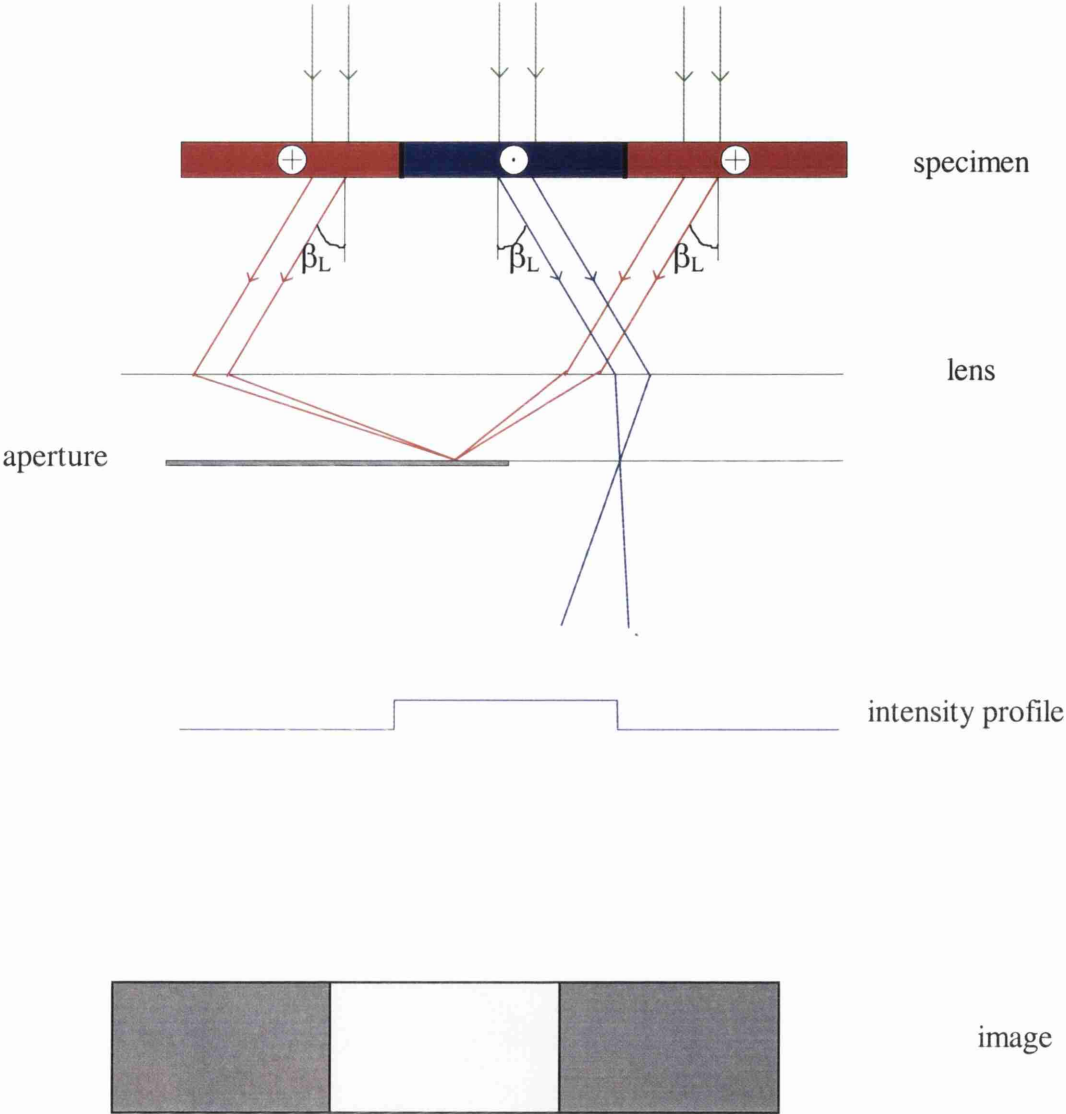
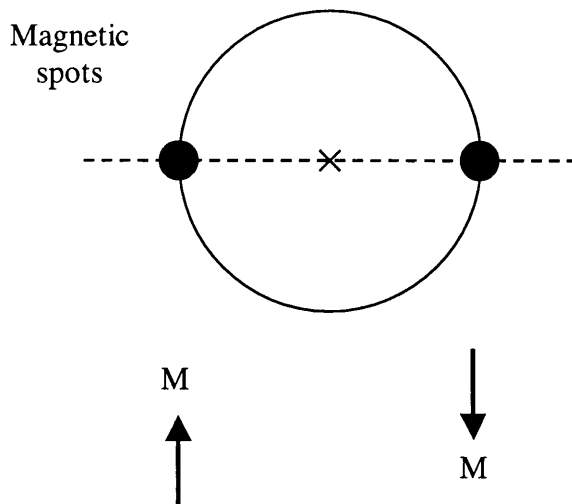


Figure 2.9 Schematic of Foucault image formation

#### 2.4.4 Low Angle Diffraction

As discussed in the previous section referring to Foucault imaging, all electrons which pass through a given domain are deflected by the same angle and so are focused at the same point near the back focal plane of the image forming lens. In the mode of low angle diffraction, the post-specimen lenses are set in such a way as to project this plane onto the viewing screen or detector. This is of interest in magnetic studies when the central spot, which is unscattered by the crystal lattice is considered. Long camera lengths ( $\sim 50\text{m}$ ) are used to magnify this central spot since the deflection angles which affect the central spot are small ( $\sim 0.1\text{mrad}$ ). In a sample containing several domains, the Lorentz deflections split the central unscattered spot into several sub-spots each corresponding to a different direction of magnetic induction in the specimen. The intensity of the spots is indicative of the relative fractions of induction in the specimen having a direction perpendicular to a line joining the spot to the undeflected beam position. This is illustrated in Figure 2.10

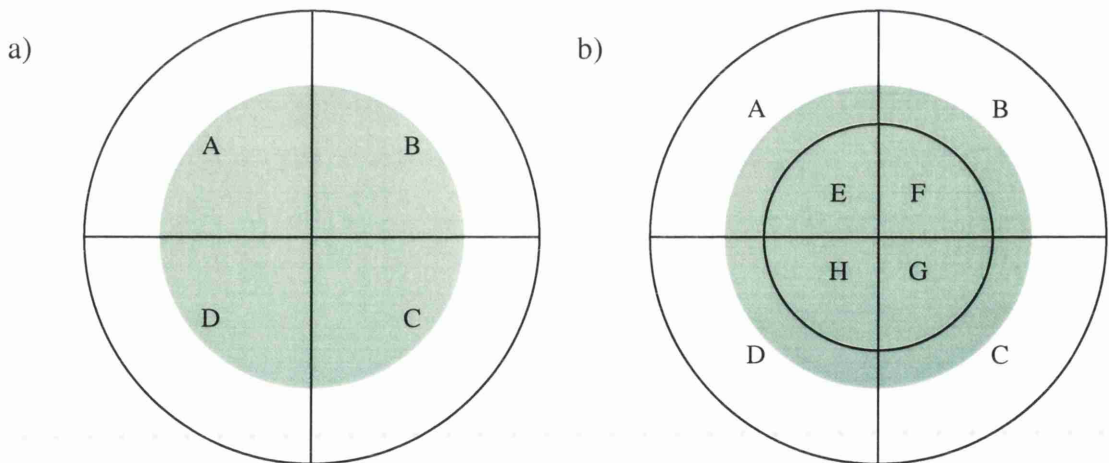


*Figure 2.10 Schematic illustration of a low angle diffraction pattern, with representation of magnetisation directions giving rise to each spot*

### 2.4.5 Differential Phase Contrast

Differential Phase Contrast is different from the other magnetic imaging modes mentioned above in that it is a scanning transmission electron microscopy (STEM) technique. This technique requires a quadrant detector, and contrast is achieved by taking the difference between signals from opposite segments []. Quantitative micromagnetic information can be obtained from this technique.

There is an inherent problem, however, that the data obtained from a real specimen contains both magnetic and non-magnetic components, such as physical microstructure and crystalline potentials, which can conceal magnetic structure. It is the zero order beam which is used in this technique, achieved by increasing the magnification such that the diffraction rings due to physical microstructure lie well outside the area subtended by the detector and so do not affect the data collected. The spatial frequency of the crystalline potential contrast is often significantly greater than that of the magnetic contrast. Hence, by preferentially detecting the lower frequency components of the image, it is possible to increase the relative magnetic signal. This can be achieved by the use of an 8 segment detector. Figure 2.11 shows the detector which is fitted in the Philips CM20.



*Figure 2.11 a) standard 4-segment detector, b) 8-segment detector used for differential phase contrast (DPC) imaging in the Philips CM20*

Only the parts of the electron distribution which are involved in the overlap between the scattered and unscattered beams carry information in a difference signal. This overlap is at the edge of the unscattered cone for the lower frequency magnetic components. Hence, by collecting difference signals from the outer annular segments, we reduce the higher frequency data gathered and the lower frequency magnetic components of the image are preferentially detected. This technique has been developed extensively for the study of magnetic materials [13-15].

When implementing this imaging technique, one important consideration is the value of  $\kappa$  [16], defined as the ratio of the inner annulus  $K_i$  of the detector to the radius of the bright field cone  $K_a$ . This should be set close to 1 so that the bright field cone impinges only slightly onto the outer four quadrants. The post specimen lenses can be adjusted to alter  $\kappa$  as the beam reaches the detector.

## 2.5 In-situ applied magnetic fields

Within the JEOL 2000FX, the modification of the split objective pole-piece means that the specimen is contained in a field-free space. In order to apply a magnetic field to the specimen, a specially designed specimen holder is used which has small coils situated on either side of the specimen, Figure 2.12 [17]. By applying a variable current through these coils, a controlled field is applied in the plane of the specimen. The specimen can also be rotated within the rod to control the relative alignment with respect to the applied field. This magnetic field also affects the electron beam, however, introducing a deflection away from the centre of the column. This can be counteracted by using the beam tilt controls within the microscope. For modest fields (<100 Oe), this causes little distortion to the final image. When higher fields are applied using this method, the large angle through which the beam must be tilted in order to counteract this deflection, introduces a significant degree of astigmatism into the image. This astigmatism, seen as streaking in the image, can in turn be counteracted by use of the stigmator coils, but this can cause difficulties for the operator.

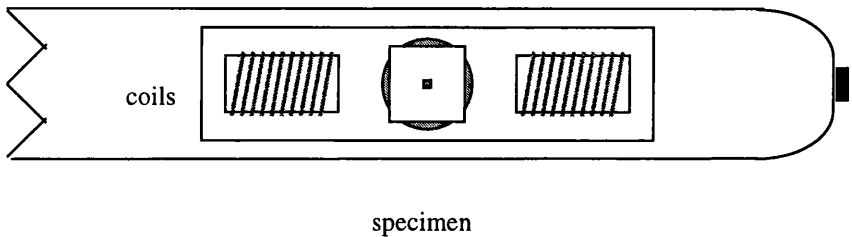


Figure 2.12 Specimen holder with magnetising coils for use in JEOL 2000FX

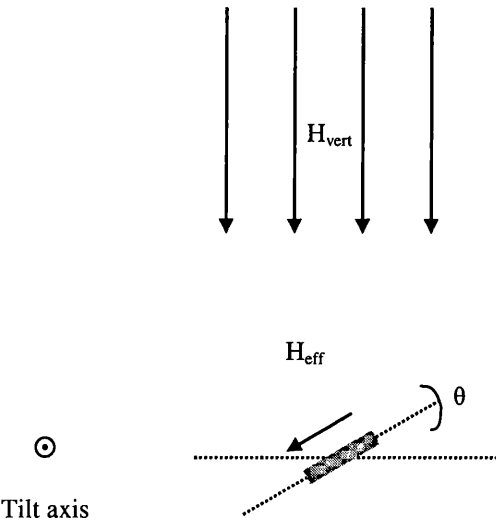


Figure 2.13 In-situ application of magnetic field in Philips CM20

The system adopted in the Philips CM20 for the application of magnetic fields to the specimen is quite different, Figure 2.13 [18]. This utilises the modification of including “twin” lenses above and below the main objective lens. When the objective lens is not excited, the focussing action can be provided by either or both of the twin lenses, and the specimen encounters only very small remanent fields. When however the objective lens is partially excited, the specimen encounters the vertical magnetic field from the objective lens. When a thin film specimen is held in the standard horizontal position, this vertical field is perpendicular to the plane of the specimen. So, for a thin film specimen whose magnetisation tends to remain oriented within the plane, this can be effectively considered as zero applied field in the plane of the specimen. When the specimen is tilted through an angle of  $\theta^\circ$  away from the horizontal, however, the specimen encounters a component of the vertical field within the plane of the specimen given by

$$H_{eff} = H_{vert} \sin \theta \quad 2.4$$

Thus, keeping the current in the objective lens constant, the effective in-plane field encountered by the specimen can be controlled by altering the angle through which the specimen rod is tilted. This method avoids the beam deflection problem of using a magnetising stage on the specimen holder, and also allows the application of very large fields (up to thousands of Oe).

The use of a vertical applied field will always affect a specimen of finite thickness, even though the magnetisation directions in a thin film will lie preferentially in the plane of the film. A film of finite thickness will have some sensitivity to field components perpendicular to the plane, with the effect of lowering the fields at which domain walls form in comparison to the equivalent horizontal field. In thicker films, this can also increase the probability of formation of vortex states.

## Chapter 3 Growth and Fabrication of Specimens

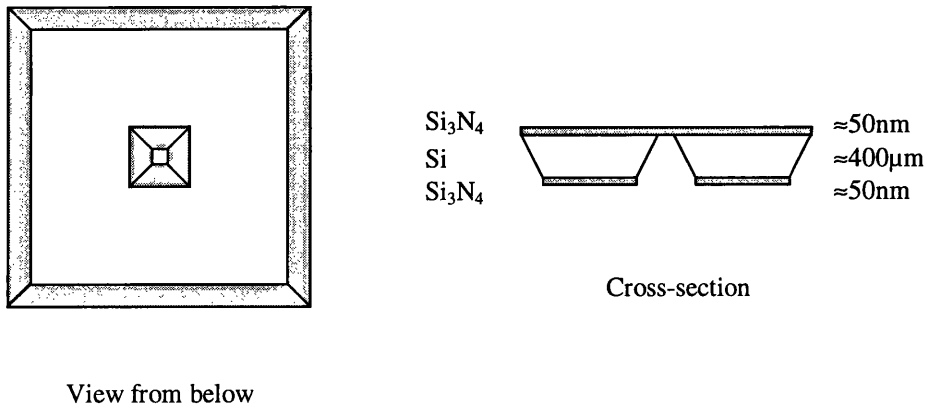
### 3.1 Introduction

This chapter describes the methods of preparation of specimens suitable for investigation in the TEM. The main requirement for TEM specimens is that they be thin enough to be electron-transparent. For magnetic thin films this means that the film must be supported on a substrate which allows electrons to pass through the area of interest, while remaining robust enough to withstand handling. For this purpose,  $\text{Si}_3\text{N}_4$  membrane window substrates supported on Si are fabricated. These membrane substrates can be used to support continuous film specimens, or further processing can be carried out to produce small patterned elements of the magnetic film of interest. The techniques described here were used in the preparation of specimens for this study.

### 3.2 $\text{Si}_3\text{N}_4$ membrane substrates

The first stage in the preparation of specimens for use in the TEM is the fabrication of suitable substrates to support the magnetic thin film of interest. These substrates are fabricated using the facilities in the Department of Electronics and Electrical Engineering at the University of Glasgow. The substrates are  $2 \times 2 \text{ mm}^2$  of Si covered with a thin layer of  $\text{Si}_3\text{N}_4$ . At the centre of the substrate a  $100 \times 100 \mu\text{m}^2$  window is back-etched to leave only the  $\text{Si}_3\text{N}_4$  membrane, as shown in fig 3.1 below [1-2].

Three-inch Si (100) wafers of thickness  $\approx 400 \mu\text{m}$  coated on both sides with an amorphous layer of  $\text{Si}_3\text{N}_4$  of approximately 50nm are obtained from the Edinburgh Microfabrication Facility at the University of Edinburgh. These wafers are the basis from which the membrane window substrates are fabricated.



*Figure 3.1 2x2mm<sup>2</sup> membrane window substrate for TEM*

Before processing begins, each face of the wafer is protected by the application of a layer of photoresist (Shipley S1818) spun onto the surface at 4000rpm for 30s then baked at 90°C for 30min. This forms a protective layer of resist of thickness 1.8µm. The smooth, shiny top surface which is to form the membrane of the substrate is coated first as it is crucial this does not become scratched. When both faces are protected in this way, the wafer is scribed into quarters, parallel to the [110] direction as indicated by flats on the wafer, using a diamond stylus.

The quarter-wafers are then cleaned using an ultrasonic bath, three times in acetone for 2min each, to remove the protective photoresist, and rinsed three times for 2 min each in turn in acetone, methanol and RO (reverse osmosis) water, before being dried with nitrogen.

The front face of each cleaned quarter-wafer is then spun with Shipley S1805 photoresist at 4000rpm for 30s, and baked at 90°C for 30 min. This again protects the shiny top face from damage. The back face is similarly spun with S1805 resist and baked to form a coating of 0.5µm. A mask aligner is used to align the required mask, in this case for the back face as shown in fig 3.2, with the Si [110] direction. The photoresist is then exposed using the 394nm wavelength UV radiation from a mercury lamp for 4s. This defines the membrane windows and

the cleavage grooves required. The exposed photoresist is then developed for 75s using Microposit Developer diluted 1:1 with RO water, rinsed in RO water and blown dry. At this stage the developed pattern can be checked using an optical microscope with a yellow filter to prevent further exposure of the resist.

The patterned photoresist acts as a mask when the back surface undergoes  $\text{CHF}_3$  reactive ion etching (RIE or “dry” etching) in the BP80 RIE system. This removes the SiN layer from the exposed area of the pattern, revealing the Si below.

The back face of each quarter-wafer is then wet-etched for 45 min in a reflux apparatus in boiling sodium hydroxide solution (20% NaOH in RO water at  $112 \pm 1^\circ\text{C}$ ). The sodium hydroxide selectively etches the Si [100] at a rate of  $5.5 \mu\text{m min}^{-1}$  creating pyramidal cavities and grooves, while leaving the SiN intact. On removal from the boiling alkali solution, the wafer is again rinsed in RO water and blown dry. This first wet-etch stage is not intended to back-etch completely to form the SiN membranes, but thins the Si in these regions sufficiently that IR radiation can pass through. The etch depth can be checked using an optical microscope, and should be 200-250  $\mu\text{m}$  from the wafer bottom face to the base of the pyramid trunk.

After cleaning in acetone, methanol and RO water in turn, without the use of ultrasonics as the cleavage grooves now make the wafer more fragile, and being blown dry, the front face can now be patterned. The smooth, shiny front face of the wafer is spun with S1805 photoresist at 4000rpm for 30s and baked at  $90^\circ\text{C}$  for 30min as before. An IR sensitive TV camera on the mask aligner is then used to align the appropriate mask for the front face (shown in fig 3.3) with the already patterned back face by back illumination. With this apparatus, the pattern etched into the back of the quarter-wafer is visible and can be accurately aligned with the mask for the front face. The photoresist on the front face is then exposed for 4s with UV light, and the exposed resist is developed for 75s in a 1:1 solution of Microposit Developer and RO water, rinsed and dried as before. The patterned photoresist on the front face acts as a mask as the front face is  $\text{CHF}_3$  dry-etched to remove the SiN from the patterned areas.

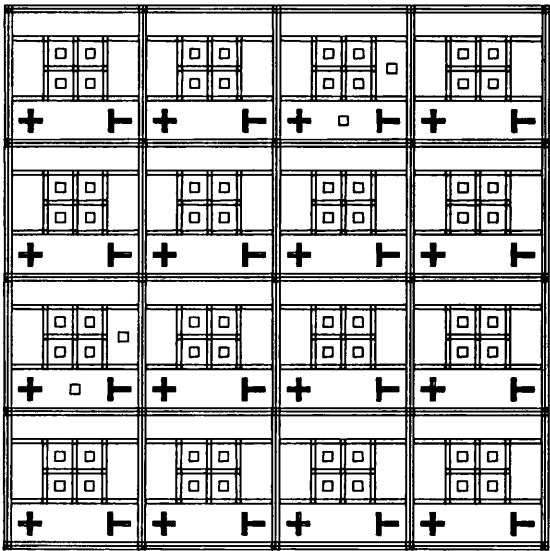


Figure 3.2 Mask used for bottom face in fabrication of TEM substrates

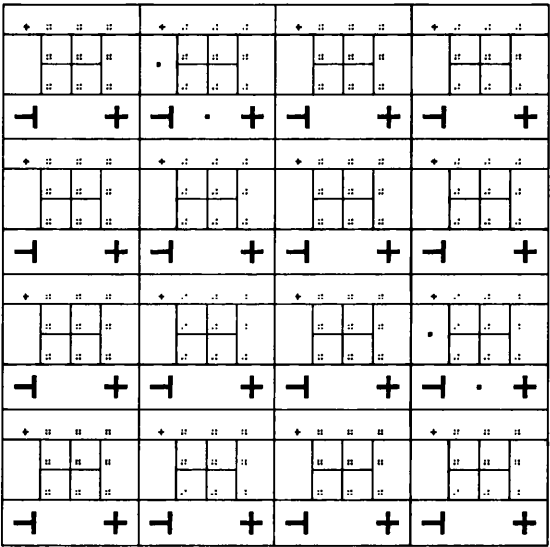
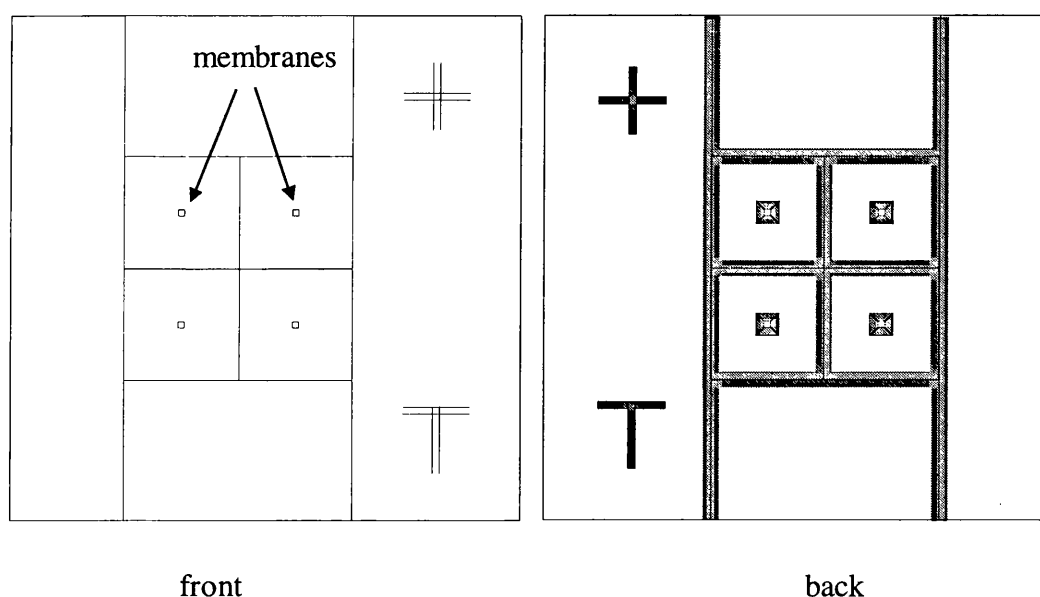


Figure 3.3 Mask used for top face in fabrication of TEM substrates

The quarter-wafer is then wet-etched again in boiling sodium hydroxide solution, using the same conditions as in the previous wet etch stage, but for a shorter time  $\approx 30$  min. The etching of the back face continues as the shallower cleavage grooves and markings on the top face are formed. When this wet etch stage is complete, the substrates are very fragile and must be handled with great care as they are removed from the alkali, rinsed in RO water and gently dried. The substrates are then cleaved along the grooves into  $9 \times 9 \text{ mm}^2$  blocks, each containing 4  $2 \times 2 \text{ mm}^2$  membrane substrates with a handling frame, shown in figure 3.4. These blocks have alignment markers, and are now ready to undergo electron beam lithography patterning of small elements (see section 3.5).



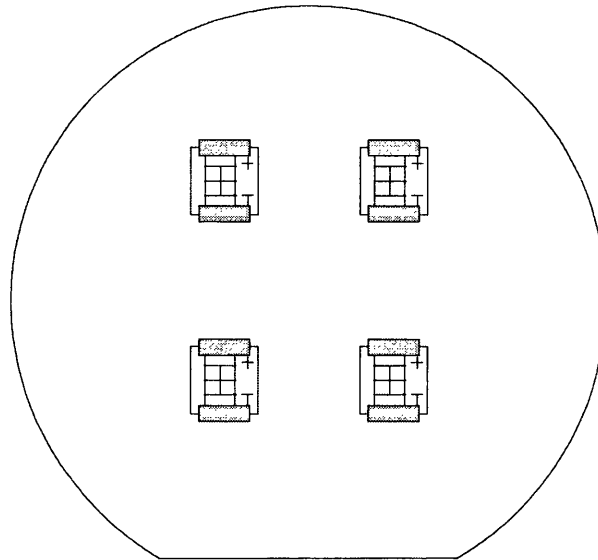
*Figure 3.4  $9 \times 9 \text{ mm}^2$  substrate block*

The curved shape of the quarter-wafers, along with inevitable processing flaws, means that not all of the  $9 \times 9 \text{ mm}^2$  blocks produced are suitable for electron beam lithography, being of irregular shape or having damaged markers. These can be used to provide continuous film TEM specimens, by having the film of interest deposited directly onto them, either as blocks or after cleaving into individual  $2 \times 2 \text{ mm}^2$  membrane substrates.

### 3.3 Deposition of Films

The magnetic thin films of interest are sputter-deposited on a commercial physical vapour deposition (PVD) apparatus. This was carried out by staff at Seagate Technology's wafer fabrication facilities in Minneapolis and in Springtown, Northern Ireland.

The commercial deposition equipment is not designed for substrates as small or fragile as the membrane specimens used. Therefore it is necessary to attach the specimens to a three-inch Si wafer using Kapton tape, an adhesive tape which is cleanroom compatible and can also withstand annealing temperatures of the order of 300°C. The specimens must be carefully aligned with the flats on the wafer so that the magnetic directions are known (fig 3.5). Once the specimens are securely attached to the Si wafer, the wafer can be used in the deposition equipment the same as standard wafers.



*Figure 3.5 4  $9 \times 9 \mu\text{m}^2$  substrate blocks attached to 3" Si wafer for deposition*

The deposition systems used contain a number of different metal targets, from which material is deposited onto the substrates. This means that multi-layer structures such as spin-valves can be deposited layer by layer in a single processing step without breaking vacuum.

For spin-valve materials, it is necessary to anneal the specimen in order to fix the pinning direction of the antiferromagnetic material. The wafer is heated in a dry N<sub>2</sub> atmosphere, held within a magnetic field, to above the Curie temperature of the antiferromagnet (for NiMn ~300°C). The chamber is maintained at this temperature for a period of a few hours and then cooled down to ambient temperature before the wafers are removed. The annealing fields used can range from a few hundred Oe up to the order of Tesla, depending on the stack structure. Spin-valves including SAF structures (see section 1.7) require higher annealing fields in order to overcome the AF coupling between layers. Different annealing parameters such as temperature, time and field must be optimised for each type of stack to give the required properties.

### **3.4 Bulk characterisation of magnetic films**

After the deposition of magnetic films, monitor wafers deposited along with the TEM specimens undergo bulk characterisation measurements in the Seagate labs to ensure the properties of the material are as required. Different pieces of metrology equipment are used to measure various properties of the materials and here a brief description is given of some of the main techniques used.

A probe-mapping tool known as a Prometrix uses a 4-point probe to measure the electrical sheet resistance of the metal film at different points. When the properties of the metal film are known, these wafer maps can be used to indicate any irregularities in the layer thickness, or variations across the wafer. This method is used to measure each individual layer material, as well as complete spin-valve stacks.

The Looper uses two sets of inductive coils to measure the B-H transfer curve of the wafer. One set of coils is used to apply a varying magnetic field to the wafer placed within, while the other set of coils sense the resultant change in magnetic induction within the film. This method measures the magnetic response of the film across the entire wafer at once. The resultant curve can then be compared with a standard set of parameters for each type of material deposited, to check the response is as expected.

The Phasemetrics apparatus is a wafer mapping system, which has magnetic pole-pieces situated around a 4-point probe so that a varying magnetic field can be applied to a small area of the film while monitoring the electrical resistance. This gives a direct measurement of the magnetoresistive response of the film at each point across the wafer. The resulting maps show clearly any variations in magnetic properties across the wafer.

### **3.5 Patterned elements**

While continuous film specimens give useful information on the behaviour of a magnetic material, a better indication of the behaviour of sensors is given by investigating elements of the approximate dimensions used in devices. For this purpose, electron beam lithography and lift-off techniques are used to define patterns of small elements of magnetic film on the membrane substrates.

#### **3.5.1 Electron beam lithography**

Electron beam lithography is carried out in the Ultra Small Structures Lab. (USSL) in the Department of Electronics and Electrical Engineering at the University of Glasgow. The  $9 \times 9 \text{ mm}^2$  substrate blocks, produced as described in section 3.2, are firstly cleaned in acetone, methanol and isopropyl alcohol (IPA) in turn and blown dry with nitrogen. A double layer of PMMA (polymethylmethacrylate) resist is then spun onto the substrate using an aluminium holder to support the fragile substrate on the vacuum chuck (fig 3.6).



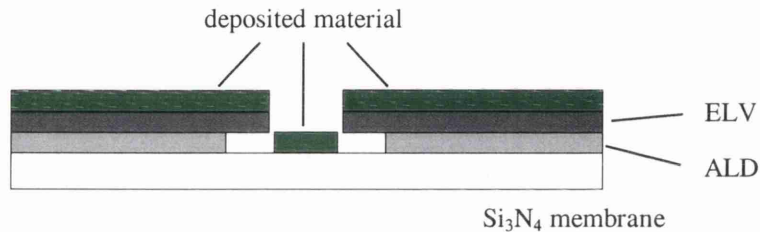
*Figure 3.6  $9 \times 9 \mu\text{m}^2$  block in Al holder for spinning of PMMA*

PMMA is a polymer, available in different molecular weights. It is sensitive to an electron beam, which breaks the long carbon chains, and so is used as an e-beam resist. An inherent edge roughness in electron beam lithography, in the range 5-10nm [3], is due to the statistical process of polymer chain breakdown and the distribution of the molecules in solution.

In the USSL lab, two brands of PMMA resist are in general use; Elvecite, known as ELV, and Aldrich, known as ALD. These have different molecular weights, ALD being lower than ELV, and thus having a higher sensitivity to the electron beam. Both types of PMMA are diluted with ortho-xylene for use. The lower the percentage of PMMA, the higher the solvent content, and thus the thinner the resulting polymer layer on the substrate after spinning and baking. For the scale of patterns used in this work 2.5% solutions of each are selected.

The first layer of PMMA resist to be spun onto the substrate is 2.5% ALD, spun at 3000rpm for 60s and then baked at  $180^\circ\text{C}$  for 1h to drive off the solvent. After allowing the substrate to cool upon removal from the oven, the second PMMA layer of 2.5%ELV is spun at 5000rpm for 60s and baked at  $180^\circ\text{C}$  for a further  $1\frac{1}{2}$  to 2h. The double layer of resist is used because the difference in sensitivities of

the two brands leads to an undercut profile in the resist, as shown in fig 3.7. This improves the final lift-off stage of patterning after the deposition of the specimen film. In general, electron beam lithography tends to result in a slight undercut profile even with the use of single layer resist, as multiple scattering of electrons in solids leads to spreading of the beam. Therefore, the area of PMMA which is exposed increases with the thickness of the resist and, depending on the material, the thickness of the substrate [4]. The membrane substrates used in this work are very thin, and the layers of resist used are thin, thus reducing this undercut effect. So by choosing a double layer resist, an undercut profile can be achieved, enhancing the quality of lift-off.



*Figure 3.7 undercut PMMA profile*

The patterns to be written onto the substrate are designed using a computer programme called WaveMaker, known as WAM. These WAM files are converted using other programmes (CATS and BELLE) into a form suitable for the beamwriter. The converted patterns are then transferred to a Leica-Cambridge beamwriter, which exposes the PMMA using 100kV electrons with a spot size of 12nm. The alignment marks defined in the fabrication of the substrate blocks are used to align the patterns over the membrane windows. The exposed patterns are then developed in a 3:1 IPA-MIBK (methyl isobutyl ketone) solution at 23°C for 35s, rinsed in IPA and carefully blown dry. The pattern can be checked in an optical microscope, and is now ready for the magnetic film of interest to be deposited as described in section 3.3.

### 3.5.2 Lift-off process

Standard lift-off techniques are used to remove the excess metal from the pattern after deposition. The samples are soaked in acetone, which can be gently warmed in a water bath to speed up the procedure if necessary. The acetone dissolves the unexposed PMMA resist and with it removes the metal film on top. This leaves isolated elements of metal over the membrane according to the pattern used. While still soaking in acetone, the samples can be checked in a low magnification optical microscope, to ensure the excess metal has been removed. The samples are rinsed in methanol then in IPA and blown dry, before being cleaved into individual  $2 \times 2 \text{ mm}^2$  specimens suitable for the TEM.

It is important to note that the PMMA resist is baked at a temperature of  $180^\circ\text{C}$ , but temperatures significantly higher than this can damage the polymer structure. This means that when preparing patterned specimens of spin-valve materials, the metal lift-off stage must be carried out before the annealing at  $300^\circ\text{C}$ . This poses potential problems as the annealing field must be high enough to overcome the demagnetising fields in the patterned elements. The size and orientation of each element relative to the annealing field determine the effectiveness of the annealing process.

Before lift-off of the excess material can be carried out, the substrate blocks must carefully be removed from the Si wafers used to support them during deposition. The lift-off is carried out as usual, and once the substrates are dried, they must then be reattached to the Si wafer, taking great care to maintain the same alignment as before. The wafer can then be annealed, and the substrates removed and cleaved into individual  $2 \times 2 \text{ mm}^2$  specimens.

Finally, before the patterned specimens can be used in the TEM, an evaporator is used to coat them with a thin layer of amorphous carbon. This forms a conductive coating in order to prevent electrical charging of the specimen in the electron beam, since the metal elements are isolated on an insulating  $\text{Si}_3\text{N}_4$  membrane. The preparation of the specimens is now complete, and they are ready for TEM investigation.

## Chapter 4 Microstructure of Magnetic Films

### 4.1 Introduction

In this chapter, the physical microstructure of some of the magnetic films investigated in this study is considered. Physical microstructure such as grain size in polycrystalline films, and the presence of texturing can have significant effects on the magnetic behaviour of specimens. The investigations of physical microstructure were carried out on the JEOL 1200 TEM using bright and dark field imaging techniques, and electron diffraction patterns (see Chapter 2).

### 4.2 Permalloy – $\text{Ni}_{80}\text{Fe}_{20}$

Permalloy is the name given to an alloy of nickel and iron with the approximate relative proportions 80:20. This material forms the basis of many magnetoresistive sensor multilayers [1-3]. With nickel and iron in these proportions the magnetostriction in the film can be reduced to close to zero. Magnetostriction is the effect whereby the physical dimensions of a magnetic material change in the presence of an applied field. It is important that this is controlled in magnetic sensor materials, to prevent unnecessary instabilities in devices. Some of the important properties of permalloy are listed in figure 4.1 below:

Composition range	Ni 80-85%, Fe 15-20%
Saturation magnetisation $4\pi M_s$	12,500 G
Electrical resistivity $\rho$	20 $\mu\Omega\text{cm}$
Thermal coefficient of resistivity	0.3%/°C
Magnetocrystalline anisotropy $K$	0 for $\text{Ni}_{82}\text{Fe}_{18}$
Magnetostrictive coefficient $\lambda$	0 for $\text{Ni}_{82}\text{Fe}_{18}$

*Figure 4.1 Some important properties of permalloy*

### 4.3 Microstructure of NiFe

Single layer specimens of NiFe with thicknesses 14nm, 20nm and 40nm were deposited at the Seagate Springtown plant. Figure 4.2 shows TEM images of the 14nm NiFe specimen deposited on a 25nm SiN membrane. Figure 4.2a) is a bright field image in which the small differently shaded areas represent differently oriented crystallites. Figure 4.2b) is a dark field image taken by selecting only a segment of the (111) ring of the diffraction pattern. The parts which appear bright in this image are small crystallites which are oriented to excite those (111) reflections which pass through the aperture.

Images like these show the grain structure of the film, allowing estimates of average grain size to be made. These estimates of average grain size were made by measuring the dimensions of a selection (>20) of individual grains in each image. Their dimensions were then averaged for at least two images (one bright field and one dark field) of each specimen. From these images an estimate of the average grain size for this film was made to be  $5.1 \pm 0.7$  nm.

Figure 4.3 shows bright and dark field images of the 14nm NiFe specimen deposited on a 55nm membrane, having an estimated average grain size of  $5.3 \pm 0.5$ nm. Figure 4.4 shows images of the 20nm NiFe specimen on a 25nm membrane, with an estimated average grain size of  $5.6 \pm 0.6$ nm. Figure 4.5 shows images of the 20nm NiFe specimen on 55nm membrane, with an estimated average grain size of  $6.0 \pm 0.9$ nm. Figure 4.6 shows images of the 40nm NiFe specimen grown on a 55nm membrane. This specimen has an estimated grain size of  $6.9 \pm 0.8$ nm. These sets of images show that the average crystallite size within the films increases with the thickness of the NiFe film, as has been observed previously [4]. Also, it appears that for the same thickness of NiFe film, the average crystallite size is very slightly larger for the sample grown on the thicker membrane. This may indicate that the thicker membrane is possibly smoother, improving the crystal growth of deposited films.

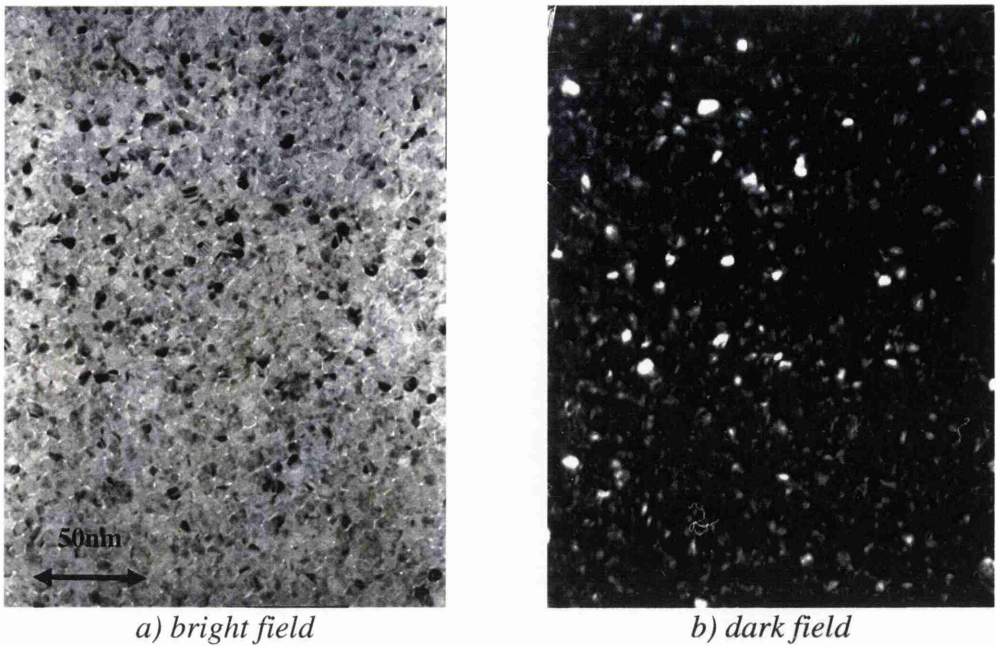


Figure 4.2 TEM images of 14nm NiFe on 25nm membrane

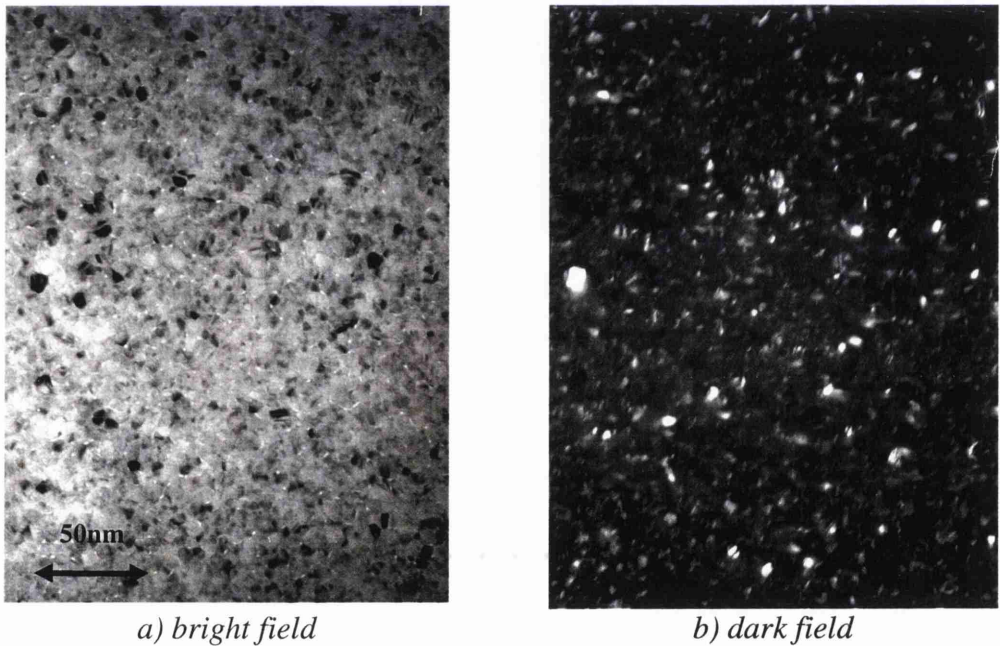
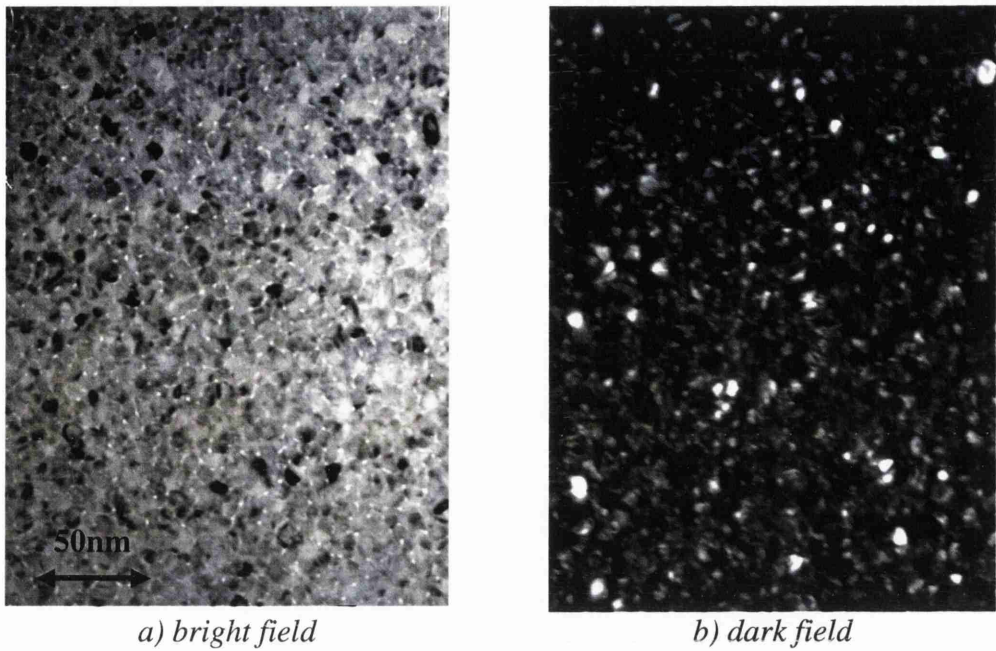
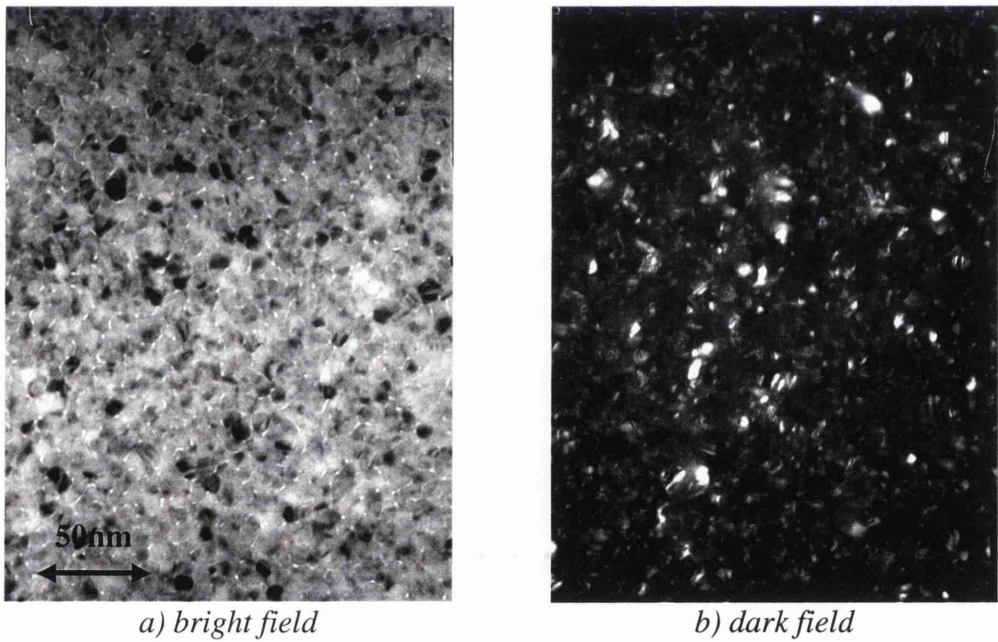


Figure 4.3 images of 14nm NiFe on 55nm membrane



*a) bright field*  
*b) dark field*  
*Figure 4.4 TEM images of 20nm NiFe on 25nm membrane*



*a) bright field*  
*b) dark field*  
*Figure 4.5 TEM images of 20nm NiFe on 55nm membrane*

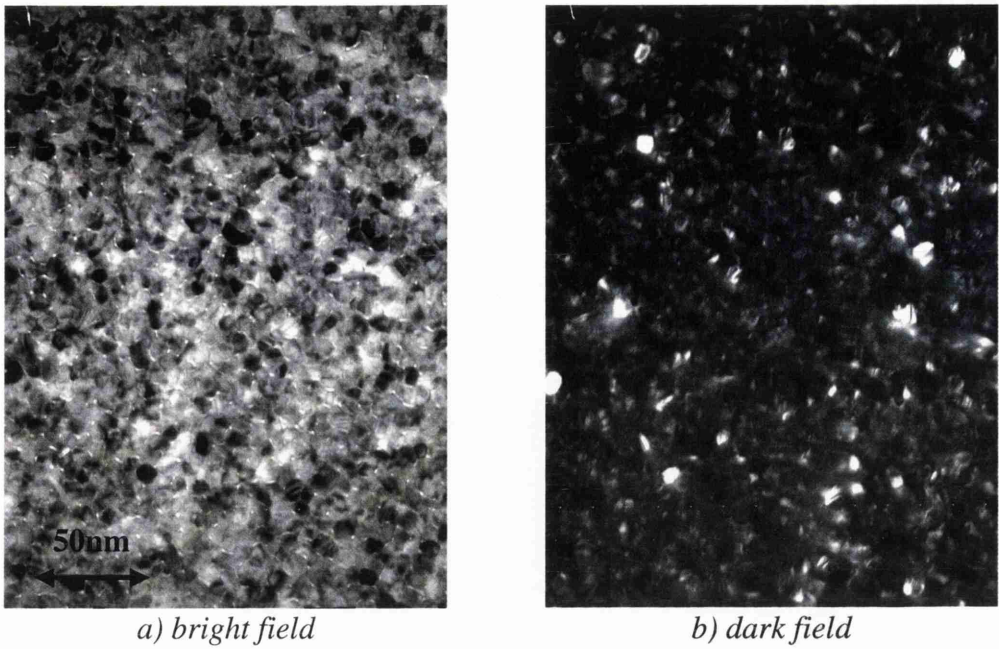


Figure 4.6 TEM images of 40nm NiFe on 55nm membrane

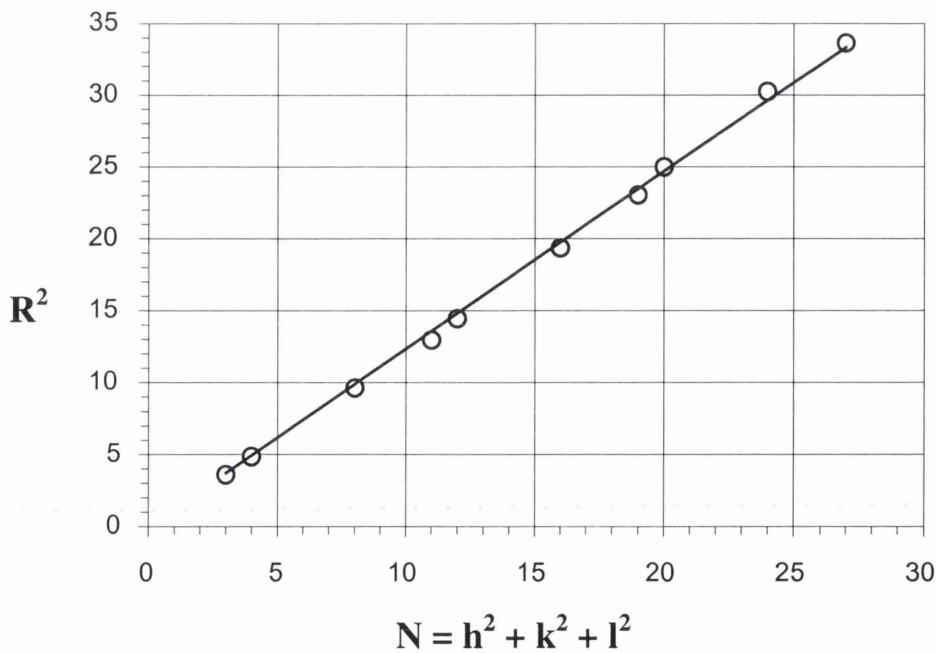
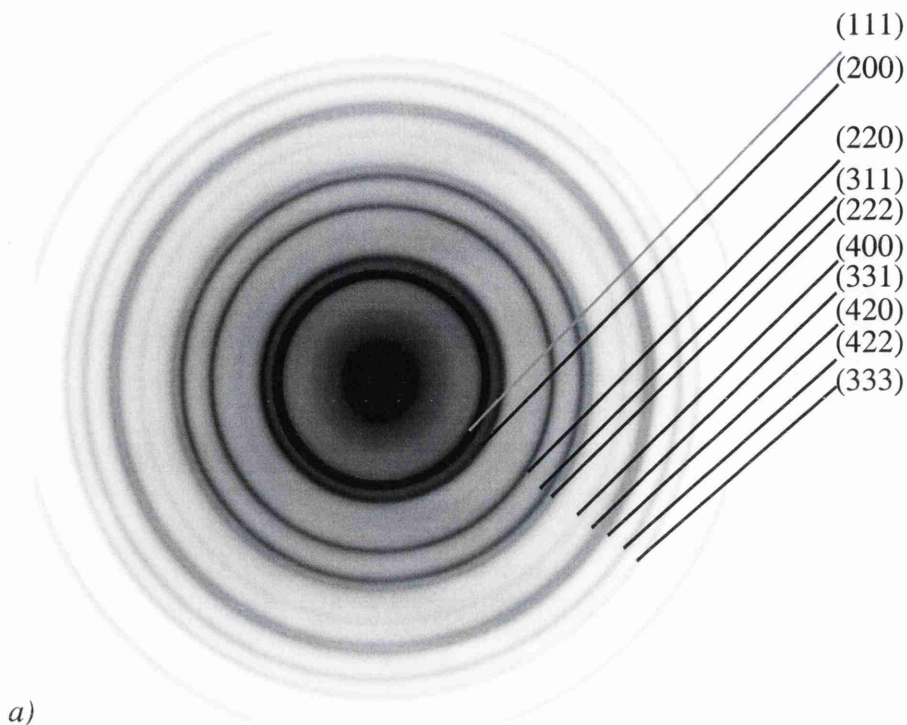


Figure 4.7 a) Indexed diffraction pattern for 40nm NiFe  
b) graphical method used for indexing

For polycrystalline films the electron diffraction pattern appears as a set of concentric rings (see Chapter 2). Each ring is formed by electrons which have been scattered by a particular set of crystal planes in the many small crystallites. Figure 4.7a) is an indexed diffraction pattern for the 40nm NiFe film imaged in figure 4.6. Figure 4.7b) shows the graphical method used to index the diffraction pattern.

For any given magnification of a ring diffraction pattern, the square of the radius  $R$  of each ring can be plotted against a set of integers  $N$ . Using the small angle approximation  $\sin \theta \approx \theta$  we find that

$$R^2 \propto \sin^2 \theta \approx \theta^2 \propto h^2 + k^2 + l^2 \quad 4.1$$

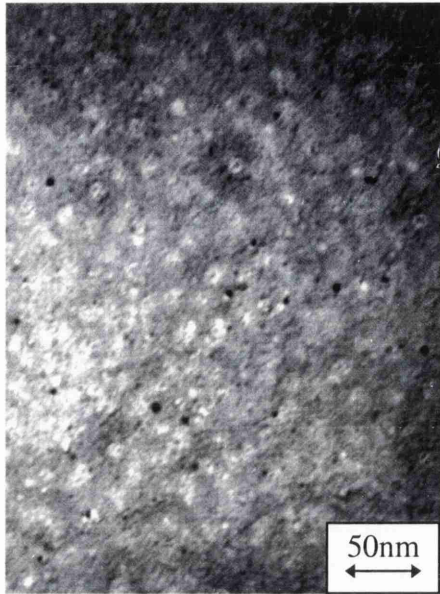
where  $N=(h^2+k^2+l^2)$ . Hence, by finding the set of integers  $N$  which allows the plot of  $R^2$  versus  $N$  to be linear, we can then deduce the indices  $(h, k, l)$  of the set of crystal planes which give rise to each diffraction ring.

#### 4.4 Microstructure of NiFe grown on Ta underlayer

Seed layers are commonly used to tailor the physical microstructure of thin magnetic films. Tantalum is a material which is often used for this purpose, to control the orientational growth of a NiFe film.

Single layer Ta specimens of thicknesses 7.5nm and 10nm deposited at Seagate Springtown are considered. Figure 4.8a) shows a bright field image, and figure 4.8b) shows a dark field image of the 7.5nm Ta specimen. Figure 4.8c) shows the electron diffraction pattern of this specimen. The diffraction rings are somewhat diffuse, indicating that the film does not have a well defined crystal structure. This is in agreement with the fact that the images show crystallites many of which are much smaller than 5nm.

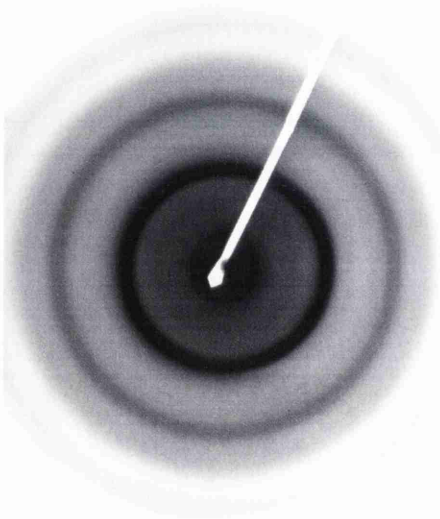
Figure 4.9 shows images and an electron diffraction pattern for the 10nm Ta specimen. The images show that there are more larger crystallites of the order of 6nm present in this film than in the 7.5nm Ta, but there are still many smaller than this. The diffraction pattern shows a better (but not well-) defined ring diffraction pattern than that of the 7.5nm Ta film, which indicates that a better defined crystal structure forms in the thicker film. This diffraction pattern is indexed using the same graphical technique as before, showing that it has a body centred cubic structure. The ring pattern is still somewhat broadened however, so a film which is thicker than this might have a better defined structure.



*a) bright field*



*b) dark field*



*c) diffraction pattern*

*Figure 4.8 a) bright field, b) dark field images,  
c) diffraction pattern for 7.5nm Ta film*

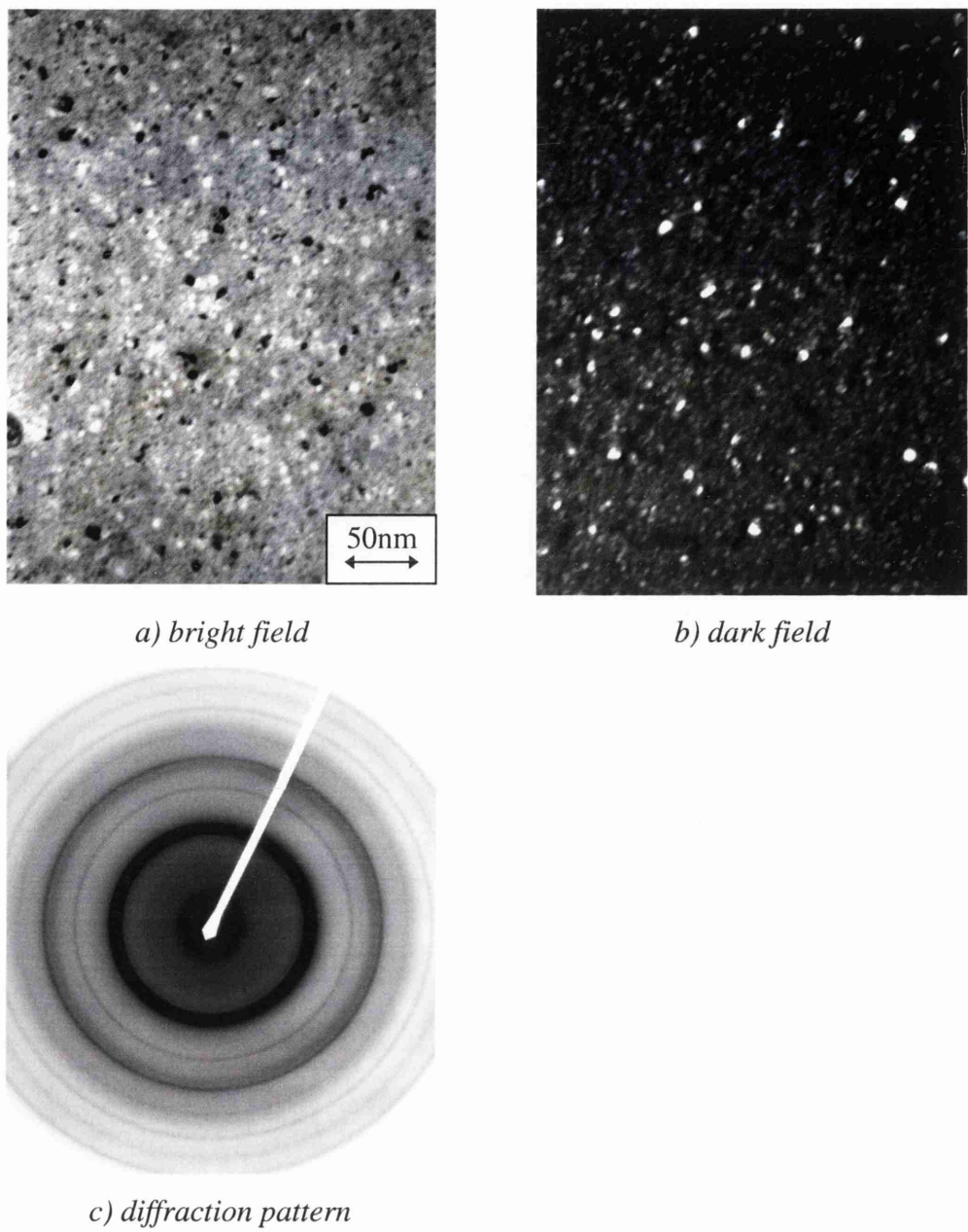


Figure 4.9 a) *bright field*, b) *dark field* images,  
c) *diffraction pattern* for 10nm Ta film

A specimen of 20.5nm NiFe grown over a 10nm Ta seed layer was also deposited at Seagate Springtown. Figure 4.10a) shows a bright field image, and figure 4.10b) shows a dark field image of this specimen. An estimate of the average crystallite size in this film is  $6.0 \pm 0.8 \text{ nm}$ , which is larger than that for the 20nm NiFe specimens without seed layer. Figures 4.10c) and d) show electron diffraction patterns taken c) with the specimen held horizontal within the TEM, and d) with the specimen tilted through an angle of  $30^\circ$ . These diffraction patterns are more complex than the others seen so far, as they are each a superposition of the diffraction patterns of the Ta and NiFe layers of the specimen. The indexing shows how individual rings can be ascribed to particular planes in each material. Diffraction patterns taken with the specimen tilted away from horizontal indicate any texturing in the film. Intensity variations seen within the (200) and (220) rings of NiFe in Figure 4.9d), the pattern taken at  $30^\circ$  tilt, show that there is texturing in the [111] direction in the NiFe due to the presence of the Ta underlayer [5]. Single layer permalloy films do not show this effect.

It is desirable in the manufacture of sensor devices to have a degree of texturing present in the film, as this has the effect of lowering the in-plane crystalline anisotropy of the film. Texturing introduced by the presence of a seed layer, in combination with the small ( $\sim 30 \text{ Oe}$ ) applied field during deposition, creates sufficient ordering of the crystallites to give an induced magnetic anisotropy across the entire film. This induced in-plane anisotropy gives lower dispersion within the film, and also enables the fields applied during post-deposition annealing processes to have a greater effect.

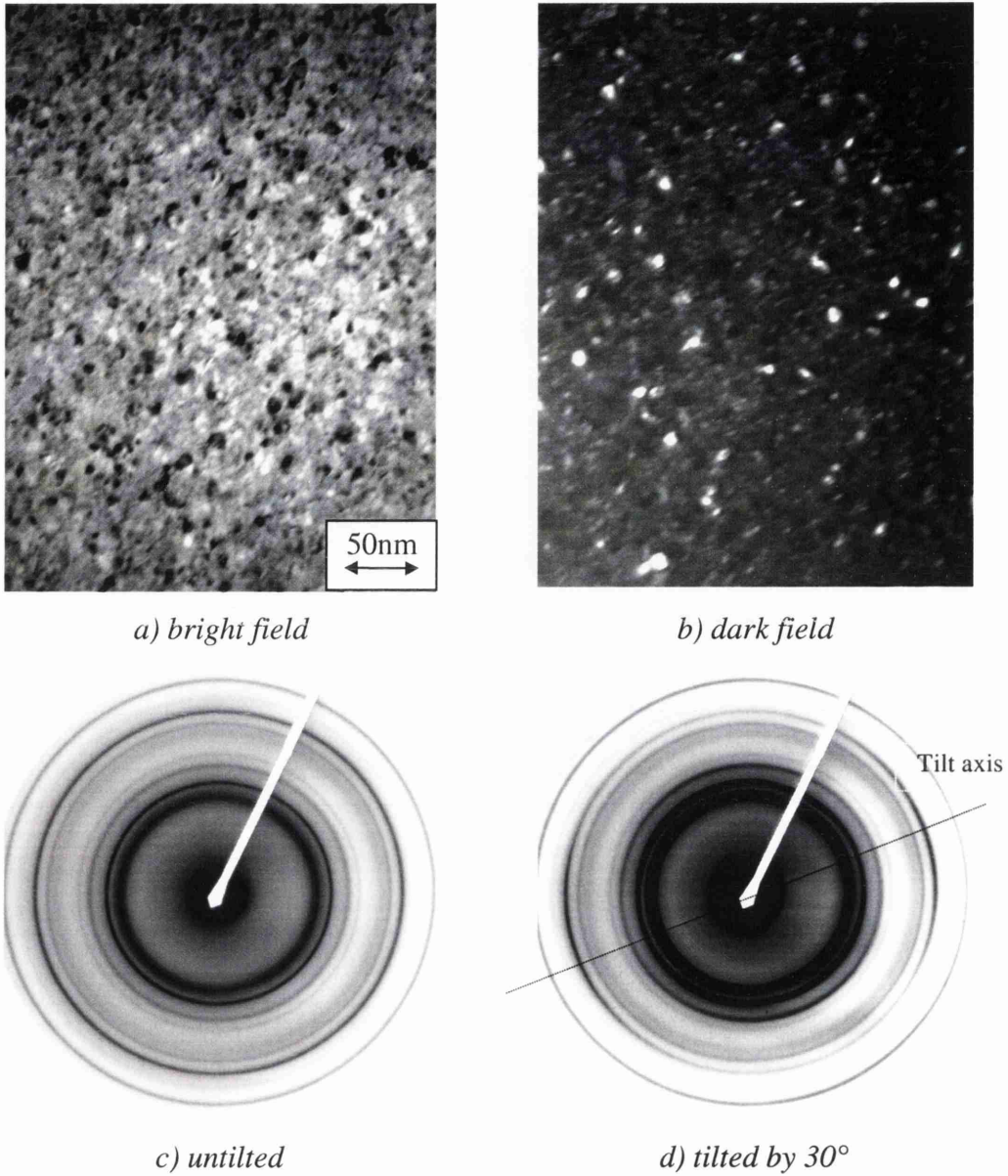


Figure 4.10 a) bright field, b) dark field images for 10nm Ta / 20.5nm NiFe  
diffraction patterns with specimen c) untilted, d) tilted by 30°

#### 4.5 Microstructure of NiFeRe

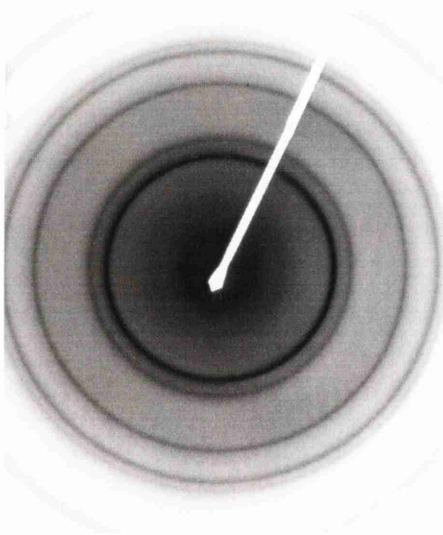
Addition of Rhenium to NiFe to form NiFeRe reduces the anisotropic magnetoresistance. This material is then used in AMR sensors as the soft adjacent layer (SAL) material. Figure 4.11 shows a) bright field and b) dark field images of a specimen of 11nm NiFeRe grown directly on the SiN membrane. It can be seen clearly from the bright field image that there are a number of cracks within the film, possibly caused by the inclusion of Re into the fcc lattice of NiFe. The larger size of the Re atom is likely to exert a strain within the NiFe lattice causing the film to crack and produce this effect. These cracks do not show in the dark field image as they do not diffract the electron beam. The average grain size was measured to be  $5.5 \pm 0.8\text{nm}$ . This is larger than that for the 14nm NiFe specimen. Figure 4.11c) shows an electron diffraction pattern, with the characteristic ring pattern for a face-centred cubic system, as for NiFe without the addition of Re. No evidence is seen of any texturing in the film.



*a) bright field*



*b) dark field*



*c) diffraction pattern*

*Figure 4.11 a) bright field, b) dark field images,  
c) diffraction pattern for 11nm NiFeRe*

#### 4.6 Microstructure of spin-valve stacks

Spin-valve stacks contain many more layers than the other specimens considered thus far. The physical microstructure is therefore more complex than for single- or two-layer films.

Spin-valve material of composition substrate / proprietary seed layer / 30Å NiFe / 250Å NiMn / 10Å NiFe / 20Å Co / 31Å Cu / 12.5Å Co / 50Å NiFe was deposited at Seagate Minneapolis. Figure 4.12 shows a) bright field and b) dark field images of this specimen. From these, the average crystallite size was estimated to be  $14 \pm 6$  nm. There is a large spread in grain size, and since the spin-valve structure has several different layers, this estimate gives only a rough guide. It is important to remember that TEM images always represent a projection through the entire thickness of the film, so that different possible grain sizes in different layers cannot be easily resolved. For thin films, however, a general assumption is made that the crystallite growth is columnar in fashion, with each layer adopting the grain boundaries from the layer below.

Figure 4.12c) and d) are electron diffraction patterns taken c) with the specimen held horizontal within the TEM, and d) with the specimen tilted through an angle of 45°. As the tilt angle was increased, the diffraction pattern observed changed noticeably. The marked intensity variations within the rings, and the splitting of the rings indicates that there is a high degree of [111] texture in the NiFe layer, due to the Ta underlayer.

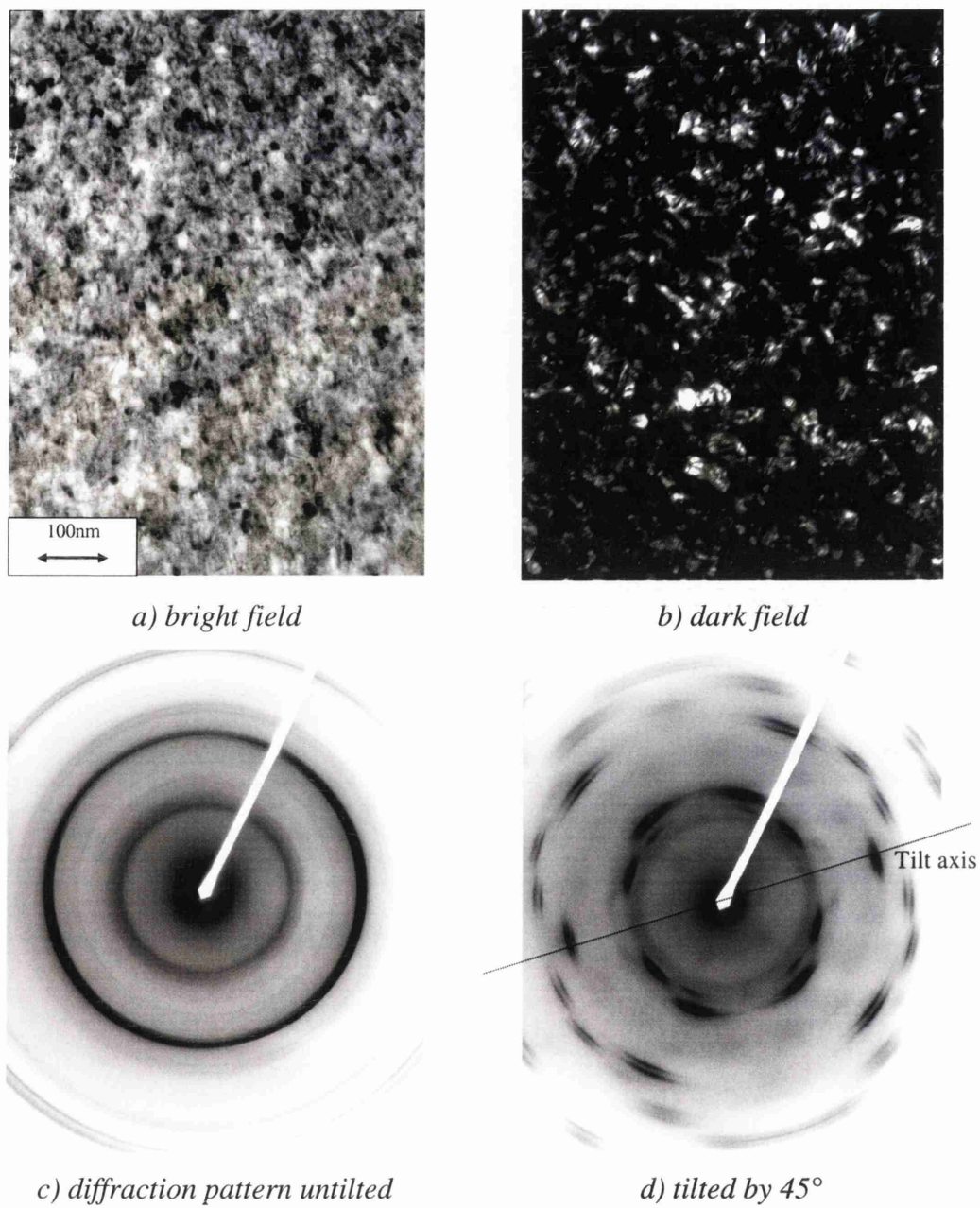


Figure 4.12 a) bright field, b) dark field images for spin-valve material  
diffraction patterns with specimen c) untilted, d) tilted by 45°

4.7 Summary

Microstructural investigations have been carried out for each of the continuous film specimens as described. The results are summarised in the table shown in figure 4.13 below.

From these results it can be seen that the average grain size in a single layer film increases with the thickness of the film deposited. This corresponds with previous findings [4]. There does appear to be a slight increase in grain size from the 20nm NiFe single layer to the 20.5nm NiFe with Ta underlayer. This is assumed to be due to the presence of the seed layer, and not the slightly differing thickness of the NiFe. There is a large spread in grain size for the spin-valve structure. Since this has several different layers, the estimate provides only a rough guide. Only the double-layer sample of Ta / NiFe and the spin-valve structure exhibit texturing.

sample	membrane	av.grain size nm	±	texture
14nm NiFe	25nm	5.1	0.7	none
14nm NiFe	55nm	5.3	0.5	none
20nm NiFe	25nm	5.6	0.6	none
20nm NiFe	55nm	6.0	0.9	none
40nm NiFe	55nm	6.9	0.8	none
7.5nm Ta	35nm	<5		none
10nm Ta	35nm	6.0	1.2	none
11nm NiFeRe	35nm	5.5	0.8	none
10nm Ta / 20.5nm NiFe	35nm	6.0	0.8	[111]
spin-valve	35nm	14.0	6.0	[111]

Figure 4.13 Table summarising physical microstructure results

## **Chapter 5 Magnetisation Reversal of Single-Layer NiFe and AMR Stacks**

### **5.1 Introduction**

One of the main materials used in magnetoresistive sensors is permalloy, the Ni/Fe alloy with approximate composition  $\text{Ni}_{80}\text{Fe}_{20}$ . Some of the important physical properties of permalloy were discussed in Chapter 4. This Chapter considers the magnetisation reversal behaviour of NiFe films as single layers, and as components in anisotropic magnetoresistive (AMR) multilayer sensor materials.

The magnetisation reversal mechanisms of single-layer permalloy films have been the subject of various different studies [eg. 1,2]. These experiments are repeated here using Seagate deposited films as a starting point for the understanding of more complex multilayer systems.

In this Chapter, both hard and easy axis magnetisation reversal mechanisms of simple NiFe films are considered, along with NiFe films grown on a Ta seed layer to control the crystal structure. The properties of NiFe can be altered, by the addition of a small amount of rhenium, in order to reduce the magnetoresistive effect for use as the SAL layer in AMR sensors. Magnetisation reversal of a single layer film of this NiFeRe material is also considered here. Finally, the magnetisation reversal of a complete AMR multilayer structure is considered.

### **5.2 Reversal mechanisms of NiFe single layer**

In order to understand the behaviour of more complex magnetic multi-layer systems, it is important to begin with an understanding of the main component materials. Thus, NiFe single-layer films give a good starting point for the understanding of many magnetic sensor stacks.

This section considers the magnetic behaviour of Seagate deposited single layer films, as an introduction to reversal mechanism investigations of more complex multilayer structures.

### 5.2.1 Easy axis

The easy axis of a soft magnetic film defines the preferred directions for the magnetisation to lie. Thus, if a field is applied along the easy axis, opposite to the magnetisation direction, the magnetisation will reverse by a rapid switching as the applied field is increased.

A magnetisation reversal cycle of a 40nm NiFe film was carried out with the applied field along the easy axis. Observations of Fresnel contrast were made during the experiment, but images were not recorded. As the field was decreased from the positive direction to zero field the dispersion in the film was seen to increase slightly. As the applied field increased in the opposite direction, an abrupt switch in the magnetisation direction occurred by the rapid formation of a single domain wall parallel with the easy axis of the film, which then swept across the whole film. After this switching, the dispersion in the film was seen to be much less, as the magnetisation direction across the entire film aligned with the applied field.

NiFe is often grown on a seed layer to control the grain growth and the texturing in the film, as seen in Chapter 4. Figure 5.1 shows a sequence of Fresnel images taken from the easy axis reversal of a 7.5nm Ta / 12nm NiFe specimen. Starting with the magnetisation oriented in the negative direction, when the field is increased in the positive direction, the dispersion increases before switching occurs at 2.5 Oe. Upon switching, a single wall parallel to the field direction crosses the specimen, but was not captured in these images. There is also a decrease in the ripple contrast observed on switching, and some small features are formed, denoted 'b' in the figure. The contrast continues to decrease as the field is increased to 9 Oe, and these features become less prominent ('c' on the figure).

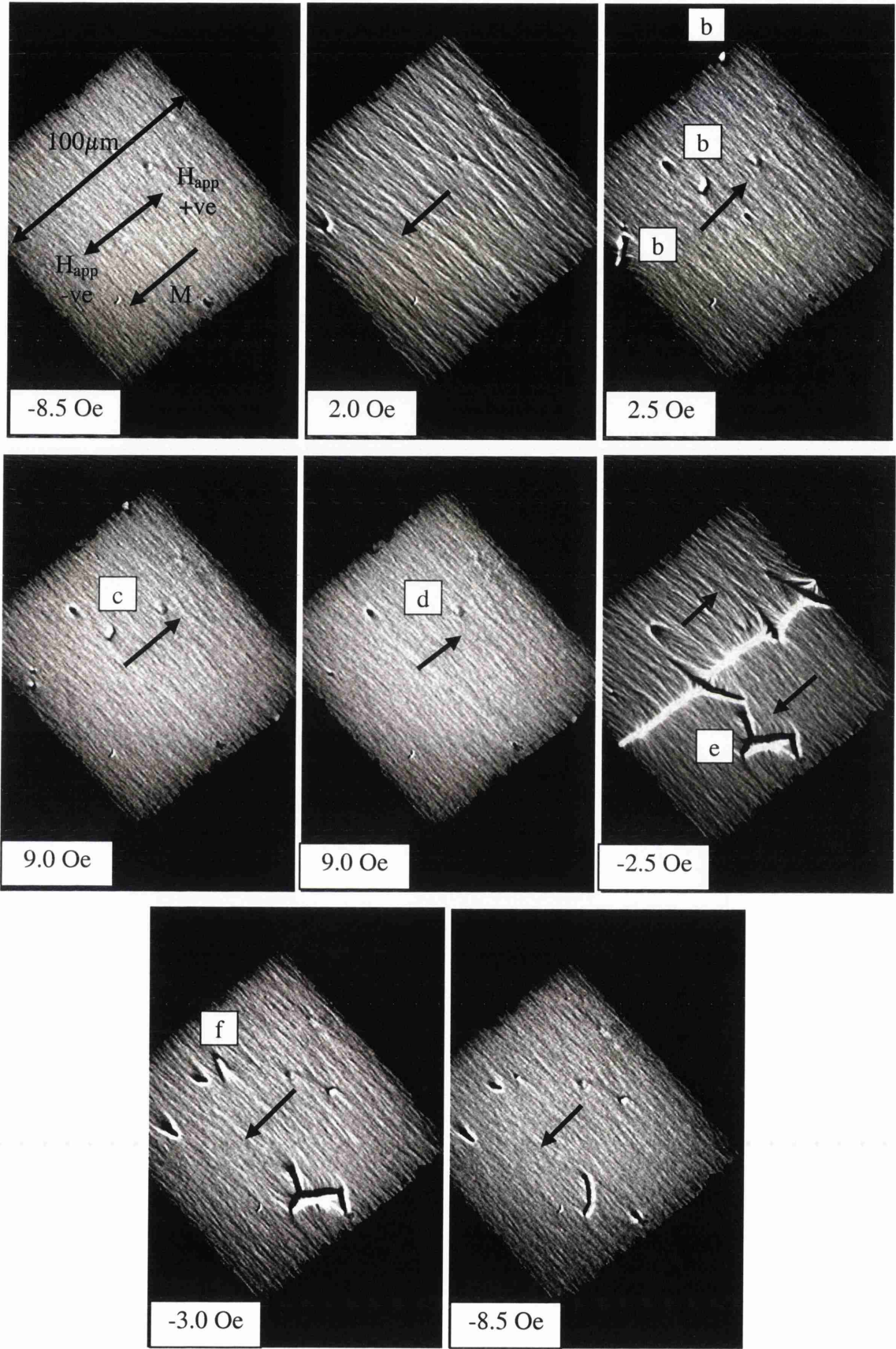


Figure 5.1 Easy axis magnetisation reversal of 7.5nm Ta / 12nm NiFe

The applied field is increased further to  $\approx 25$  Oe but this is not shown in the images. When the field is returned from 25 Oe to 9 Oe, some of the small remaining features have been eliminated ('d' on the figure). On relaxation of the field to zero and increase in the negative direction, the dispersion is seen to increase before switching occurs at -2.5 Oe. Here, the wall crossing the specimen is captured in an image, which shows more wall features have been formed, marked as 'e'. The black/white contrast of the features seen previously is inverted in polarity after switching (eg. 'f' on the figure), showing that the reversal has indeed occurred. As the field is increased further, the ripple contrast observed decreases and some of the features disappear, as seen in the final image of the sequence. This agrees with the reversal mechanism with applied field along the easy axis for a NiFe film without seed layer, as above.

Figure 5.2 shows a sequence of Fresnel images from a reversal for an 11nm NiFeRe specimen, as used for the SAL in an AMR sensor, with the field applied close to the easy axis. The dark areas in all of the images are pieces of debris which have become attached to the specimen. These appear to have no appreciable effect on the magnetic behaviour, merely obscuring a portion of the specimen from view. As the field is relaxed from negative and increased in the positive direction, the dispersion increases, the magnetisation direction begins to rotate clockwise, and some low-angle domain walls form before switching occurs at 1.0 Oe. The wall which sweeps across the specimen on switching is captured in the image. After switching, the magnetisation direction rotates through a small angle to align with the applied field, and the dispersion decreases. When the applied field is relaxed from positive and increases in the negative direction, there is again an increase in dispersion and some anti-clockwise rotation of magnetisation direction before switching occurs at just beyond -1.0 Oe. This rotation confirms that the applied field direction is not exactly coincident with the easy axis. The wall which crosses on switching is not captured in an image here, but the decrease in dispersion seen indicates that switching has occurred. After switching, the dispersion decreases as the magnetisation direction continues to rotate through a small angle to align with the applied field.

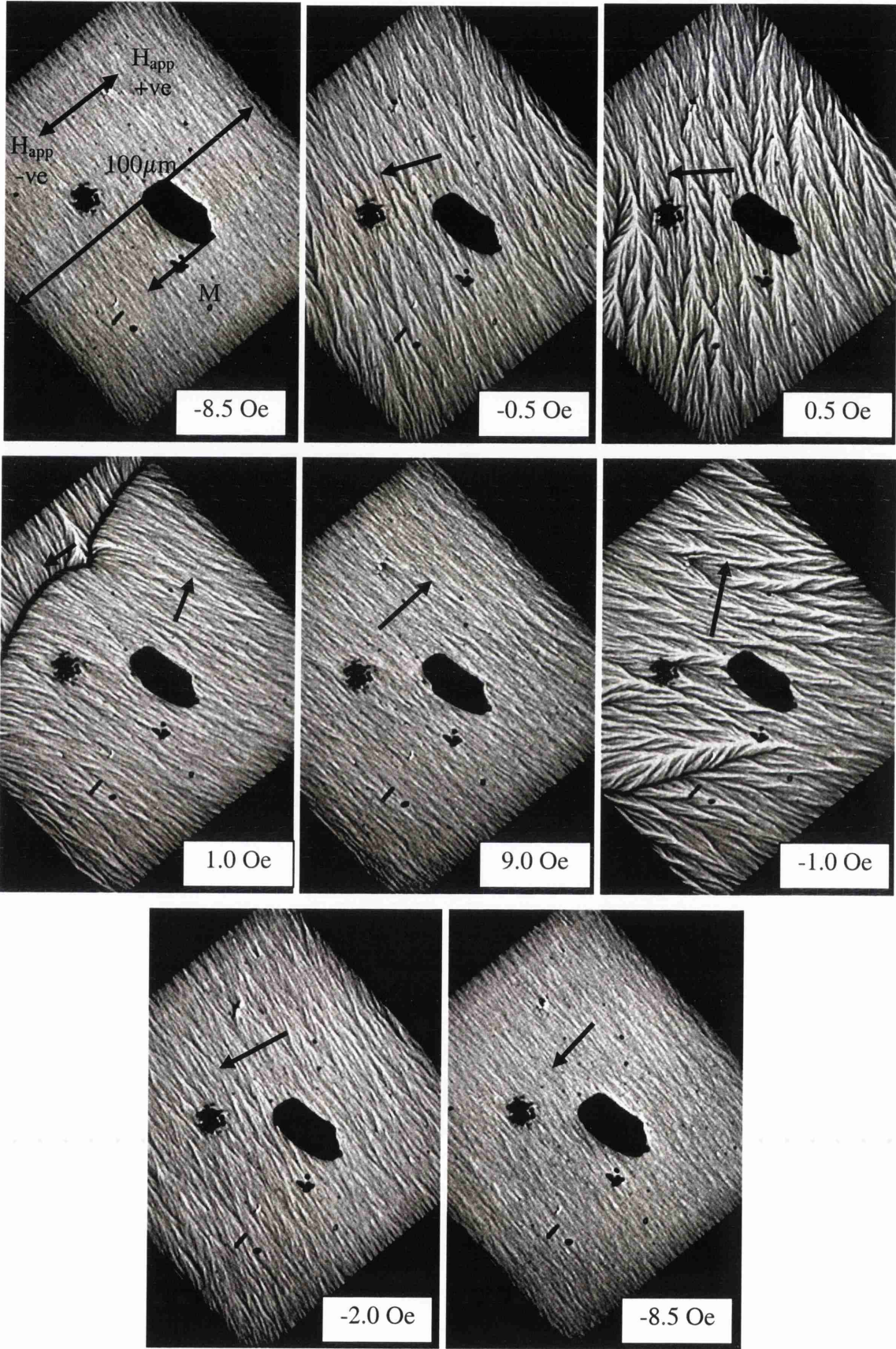


Figure 5.2 Near-easy axis magnetisation reversal of 11nm NiFeRe film

The mechanisms by which all of these soft magnetic films reverse with applied field along the easy axis are essentially the same. However, the field at which the switching of magnetisation direction occurs is affected by the thickness of the film, for identical materials. Figure 5.3 shows a table of switching field values measured in this way for different thicknesses of single layer NiFe both with and without the presence of a Ta underlayer to enhance (111) texturing, and also for the NiFeRe film. The switching field required for the 14nm NiFe film is smaller than that for the 40nm NiFe film as would be expected. These fields are small due to the soft magnetic nature of the films and are difficult to measure precisely.

Film	Easy axis switching field Oe
14nm NiFe	$2.5 \pm 0.5$
40nm NiFe	$3.5 \pm 0.5$
11nm NiFeRe	$2 \pm 1$
7.5nm Ta/12nm NiFe	$2.5 \pm 1$
10nm Ta/20.5nm NiFe	$4 \pm 1$

*Figure 5.3 Easy axis switching fields for magnetic films studied*

### 5.2.2 Hard axis

The hard axis of a soft magnetic material with uniaxial anisotropy, such as permalloy, is simply defined as the direction orthogonal to the easy axis. When the magnetisation within a film starts from a single domain state where the magnetisation is aligned along the easy direction, a field applied along the hard axis causes coherent rotation of the magnetisation towards the applied field direction.

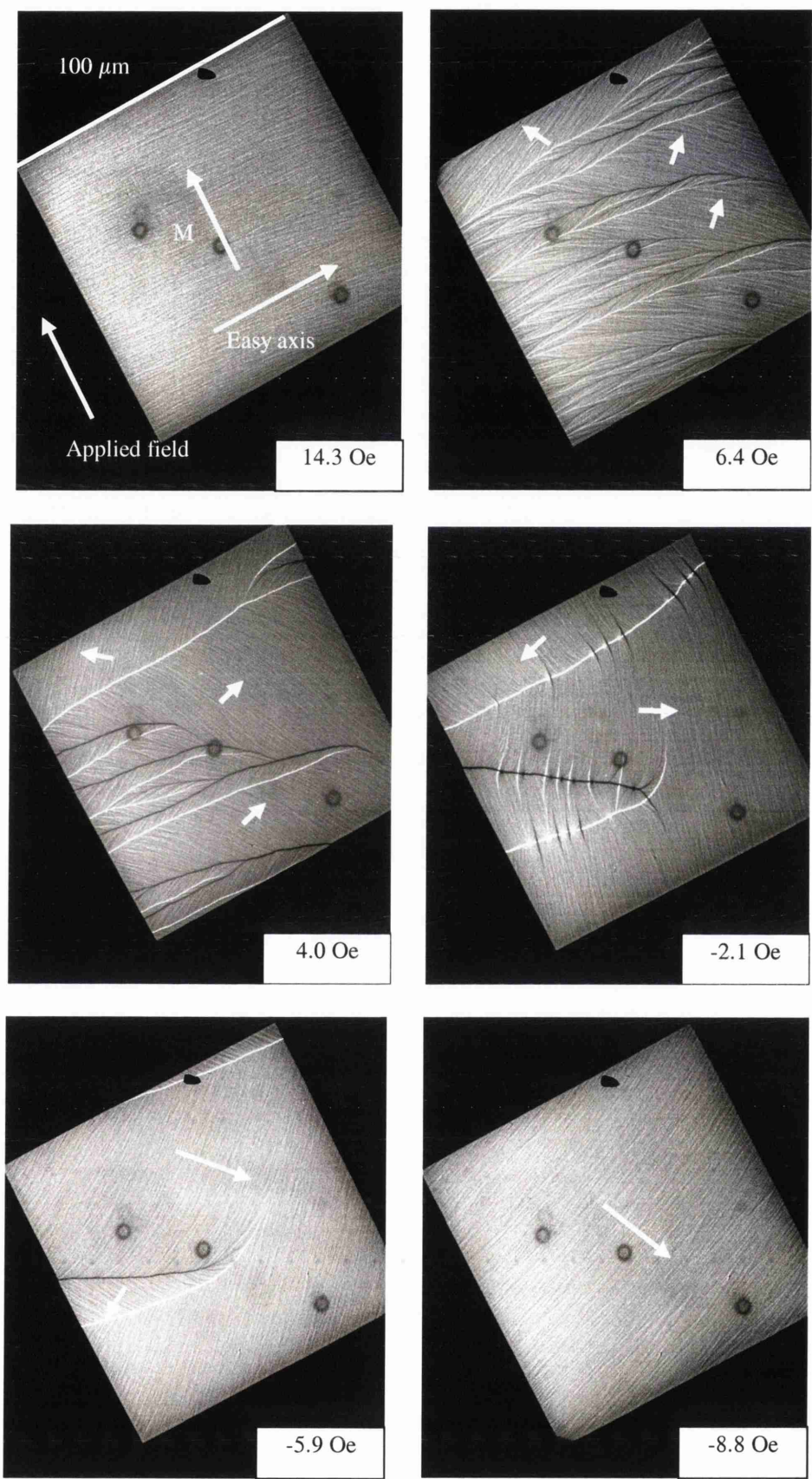


Figure 5.4 Hard axis magnetisation reversal of 40nm NiFe film

Figure 5.4 shows a series of Fresnel images taken during a magnetisation reversal sequence of a specimen of 40nm NiFe film with the applied field along the hard axis. Initially the applied field is reduced from saturation in the positive direction of the hard axis of the film, as marked on the figure. It can be seen that there is some increase in the dispersion of the film, observed as an increase in the contrast of magnetic ripple as the film magnetisation reduces from saturation. As the applied field is decreased, the magnetisation in different areas of the film begins to rotate in opposite directions towards the two easy directions. This has the effect of splitting the film into elongated domains, with walls perpendicular to the direction of applied field. Around zero field, the magnetisation in each domain lines up along the easy directions of the film, and the dispersion in the film is seen to reduce. The walls remain stationary over a range of field and become higher angle before cross-tie features can be seen to form. This is expected given the thickness of the film (see Chapter 1). As the field is increased in the negative direction, the magnetisation continues to rotate to align with the applied field direction, and the domain walls disappear.

NiFe films of different thicknesses, with and without a Ta seed layer, all displayed very similar hard axis reversal mechanisms except that the thickest film, 40nm, was the only one where cross-tie walls formed.

When the field is applied at any intermediate angle between the hard and easy axes, the magnetisation reversal is a combination of the rotation and switching mechanisms seen here. The exact mechanism of magnetisation reversal for a NiFe film is therefore dependent on the applied field angle relative to the easy axis.

### 5.3 Reversal mechanisms of AMR materials

A simple magnetic multilayer structure used as an AMR sensor material was also investigated. The composition of the specimen is: SiN substrate / Ta / 11nm NiFeRe / 7.5nm Ta / 12nm NiFe / 10nm Ta, as shown schematically in figure 5.5. In this structure, the NiFe layer is the sensor material, and the NiFeRe layer acts

as the soft adjacent layer (SAL) used to bias the magnetisation direction of the sensor relative to the sense current (see Chapter 1). The different Ta layers have different purposes, the first acts as a seed layer to control the texturing of the films, the second acts as a non-magnetic spacer layer to decouple the NiFeRe and the NiFe layers, and the final Ta layer acts as a protective capping layer to prevent corrosion or damage to the sensor structure during further processing.

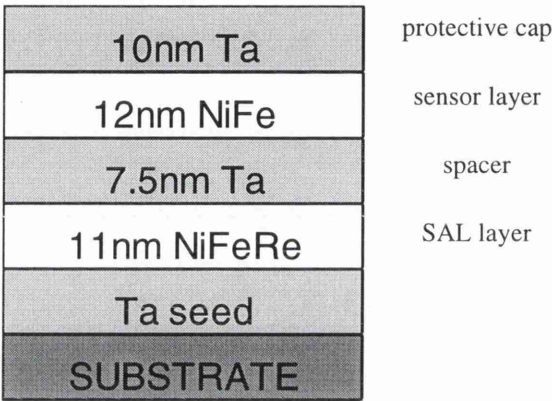


Figure 5.5 Schematic structure of AMR sensor stack

The biasing effect of the SAL is entirely dependent on the presence of an electrical current passing through patterned elements of the material, and so is not seen in this continuous film investigation of the SAL / MRE sensor structure. However, it is still of interest to compare the magnetic behaviour of the continuous film sensor stack to that of the single layer NiFe films investigated previously.

### 5.3.1 Easy axis

Figure 5.6 shows a sequence of Fresnel images taken during a magnetisation cycle of a continuous film specimen of the MRE/SAL AMR sensor structure described above. The applied field is close to the easy axis.

There is a hole in the film at the corner of the specimen, which appears as a white patch on the images. This was presumably formed by the shadowing action of some piece of debris present during deposition of the film which later fell off leaving the gap. The hole seems to have some effect on the formation of domain walls locally, but it does not appear to dominate the overall reversal mechanism.

From the start of the sequence, small remaining wall features, denoted by ‘g’ on the figure, are present from the specimen’s previous magnetic history. As the field is relaxed from negative and increased in the positive direction, these features grow and merge to form the reversal wall. Other wall segments begin to form at  $\approx 1.5$  Oe before switching occurs at 2.5 Oe. The wall crossing the specimen on switching is not captured in these images, but the black/white contrast of the small wall features is inverted (‘h’ on the figure), indicating that the magnetisation direction has been reversed. These features fade as the applied field is increased to 9 Oe, and then mostly disappear as the field is increased to  $\approx 25$  Oe, which is not shown in these images, and returned to 9 Oe. When the field is relaxed from positive and increased in the negative direction, the contrast of the magnetisation ripple increases, and some small walls (‘i’ on the figure) begin to form around the hole in the film before switching occurs at -0.5 Oe. Again the wall associated with switching is not captured in an image, but the black/white contrast of the remaining features is inverted (‘j’ on the figure), indicating that reversal has occurred. New walls (‘k’) have formed at the hole which then disappear as the negative field is increased.

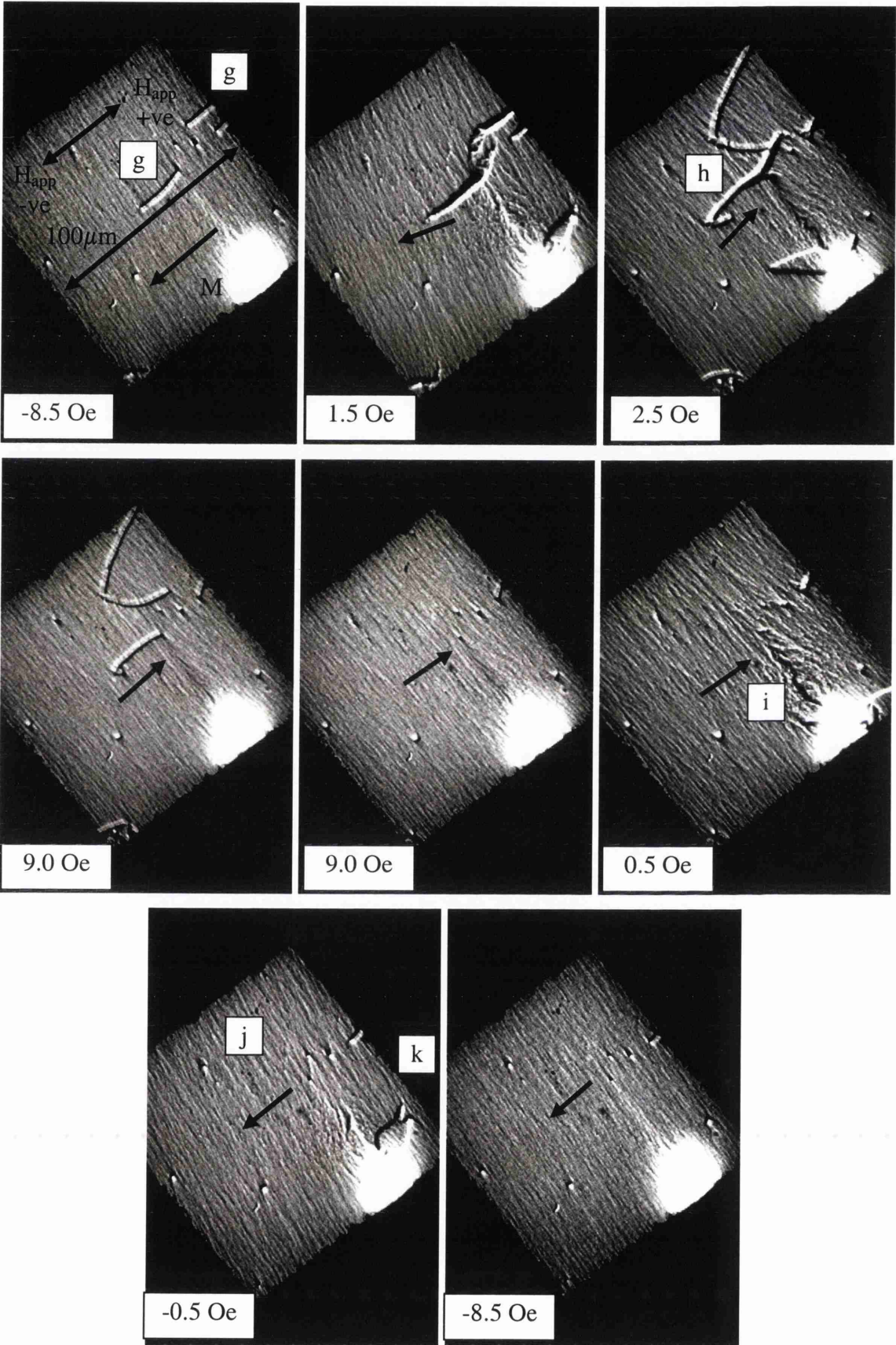


Figure 5.6 Near easy axis reversal of AMR sensor stack

### 5.3.2 Hard Axis

A near-hard axis magnetisation experiment was carried out for the same MRE/SAL specimen as used in the previous section. Figure 5.7 shows a series of Fresnel images from this reversal. The reversal in this case was seen to occur largely by rotation of the magnetisation direction. The rotation was fairly smooth, with the formation of a small number of domain walls, mainly low-angle, nucleated by the hole in the corner of the specimen. By measuring the mean direction of magnetisation ( $\theta$ ) in each of the full sequence of 51 Fresnel images taken during this experiment (only a selection of which are shown), a plot of  $\cos(\theta)$  versus the applied in-plane field component was constructed. This is shown in figure 5.8. This plot is a representation of the hysteresis curve for the specimen with field applied close to the hard axis, and shows no jumps in mean magnetisation direction and no hysteresis. This experimental curve agrees generally with the expected shape of a hard-axis hysteresis curve.

The magnetisation reversal processes seen here in the AMR sensor material are similar to those in the single layer NiFe specimens. The specimen is behaving as if it were a single layer of soft magnetic material. The two magnetic layers in the structure appear to act cooperatively, as if they were a single layer of soft magnetic material. The biasing effect of the soft adjacent layer (SAL) structure is entirely dependent on the presence of an electrical current passing through patterned elements of the multilayer film. Hence, it could not be expected to observe any biasing effect in this sheet film study.

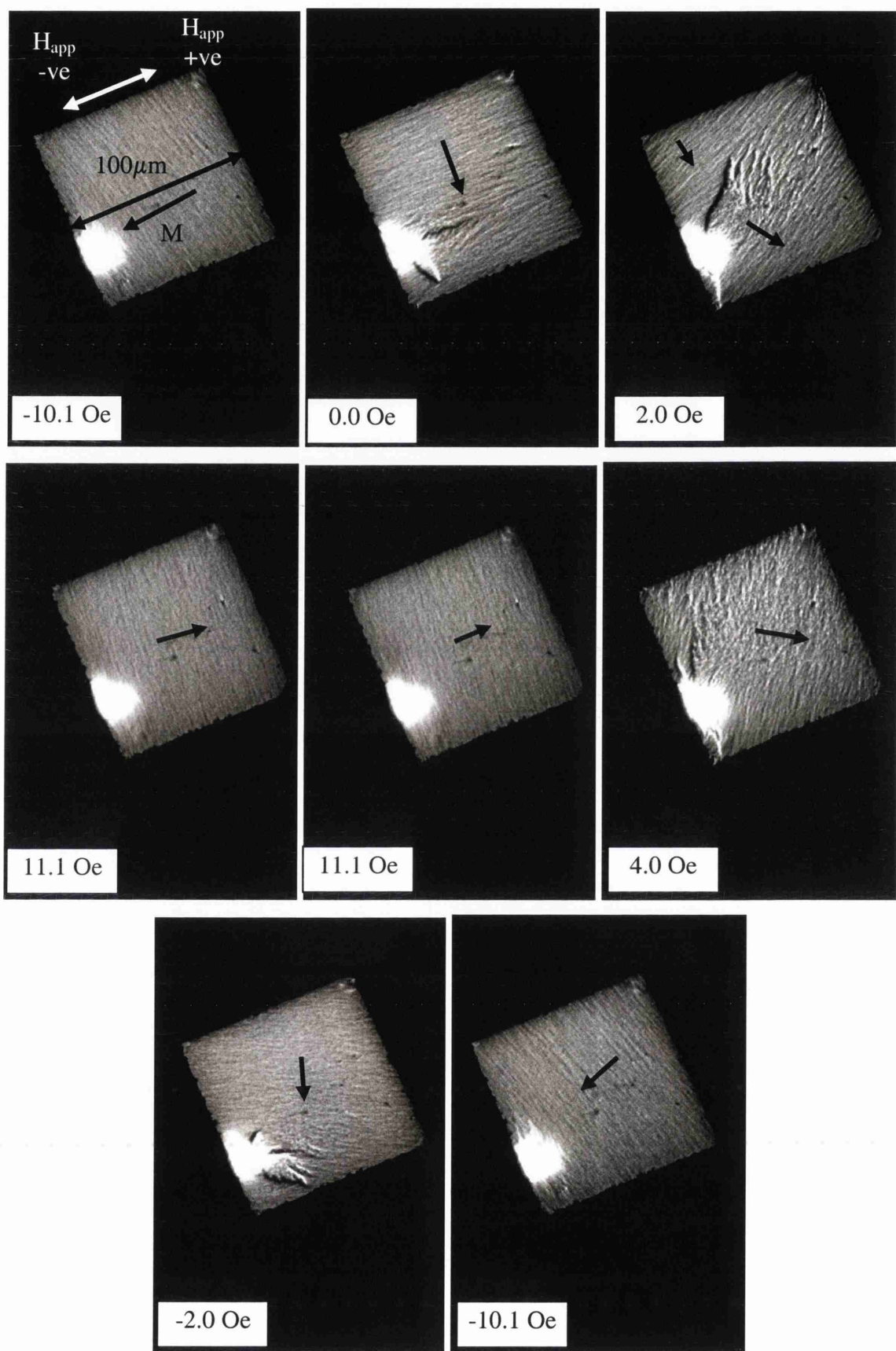


Figure 5.7 Near hard axis reversal for AMR sensor film

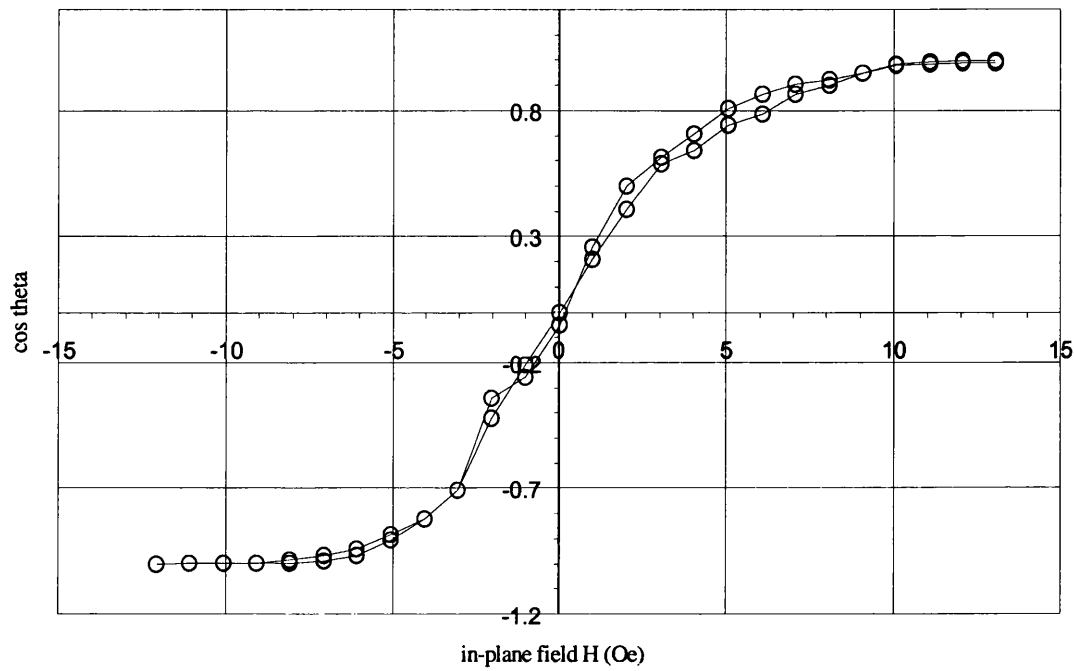


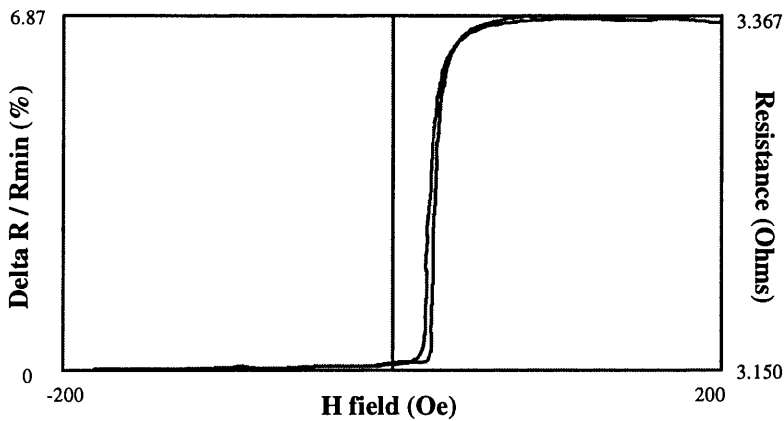
Figure 5.8 Near hard axis loop deduced from Fresnel images of AMR material

## Chapter 6 Free layer Reversal of a Spin-valve with Crossed Anisotropy

### 6.1 Introduction

The reversal of the free layer magnetisation is one factor which determines the suitability for sensor operation of a spin-valve material. In this Chapter, a particular spin-valve material with the crossed-anisotropy geometry is considered. The composition of the spin-valve material under investigation is substrate / seed / 30Å NiFe / 250Å NiMn / 10Å NiFe / 20Å Co / 31Å Cu / 12.5Å Co / 50Å NiFe. An extra layer of Cobalt is added on either side of the Cu spacer layer as this is less miscible than Ni with Cu. Interfacial mixing leads to deterioration of the stack performance over time, and lower overall GMR.

The magnetoresistance of a spin-valve film is proportional to  $(1 - \cos \phi)$ , where  $\phi$  is the angle between the pinning direction and the mean magnetisation direction in the free layer [1]. By measuring the angle  $\phi$  between the mean direction of magnetisation in the free layer and the pinning direction, as deduced from the magnetic contrast, in each of a sequence of Fresnel images, a plot of  $(1 - \cos \phi)$  versus the applied in-plane field component can be made and compared with a measured MR/H curve, shown for this material in figure 6.1.



*Figure 6.1 Measured MR/H curve for spin-valve material*

This assumes uniform magnetisation over the specimen, or low levels of dispersion and magnetisation ripple. When a number of magnetic domains are present, with different directions of magnetisation, this technique cannot be used to construct a plot of  $MR/H$ . In these cases, an estimate of the magnetisation directions in each domain must be treated separately.

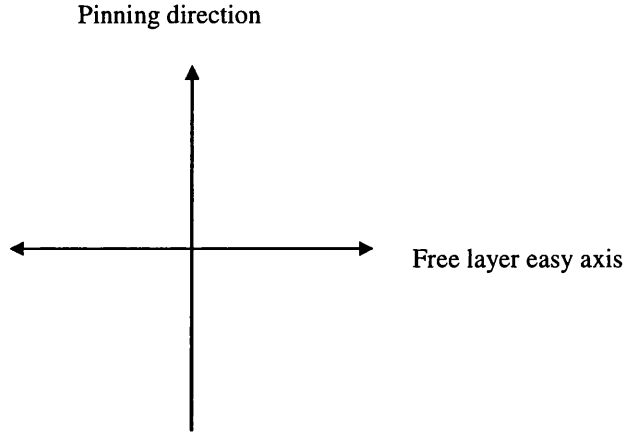
The slight horizontal offset in the free layer minor loop as shown in figure 6.1 is due to the ferromagnetic coupling between the pinned layer and the free layer across the copper spacer. This coupling is much less strong than the pinning effect of the AFM on the pinned layer, so that the free layer will typically reverse in fields of the order of Oe, while the pinned layer begins to reverse only in fields in the range of hundreds to thousands of Oe.

## 6.2 Crossed Anisotropy Geometry

Spin-valve materials can be processed in such a way that the easy axis of the free layer can have different orientations relative to the pinning direction of the pinned layer. These can be parallel, orthogonal, or canted to subtend any angle in between [2].

The spin-valve materials investigated in this work all have the crossed anisotropy geometry, where the easy axis of the free layer and the pinning direction are close to orthogonal. This can be achieved by rotation of the wafer substrate through  $90^\circ$  between the deposition of the different layers in the spin-valve stack or by annealing in orthogonal directions (see Chapter 3).

The schematic layout of the crossed anisotropy geometry is shown in figure 6.2. This geometry is chosen as it gives improved sensitivity  $\Delta R/\Delta H$  than the parallel arrangement, and also lessens the hysteresis effect observed.



*Figure 6.2 crossed anisotropy geometry*

### **6.3 Free layer reversal mechanism as a function of applied field orientation**

Magnetising cycles were carried out in the Philips CM20 with the applied field at different orientations relative to the pinning direction of the spin-valve. The directions chosen were anti-parallel to the pinning direction, and at angles of  $175^\circ$  and  $135^\circ$  away from the pinning direction of the spin-valve material.

The interpretation of all of these images relies on physical insight into the behaviour of thin magnetic films. The technique of Lorentz microscopy provides a projection through all layers of a multi-layer film, yet inferences can be made as to which individual layer gives rise to contrast within the image when the fields applied are known.

Figure 6.3 shows a sequence of Fresnel images taken during a magnetising cycle with the specimen aligned such that the applied field is anti-parallel to the pinning direction. In figure 6.3 a), at zero applied field, the free layer is in a single domain state with the magnetisation aligned with the pinning direction. As the field is increased, the dispersion can be seen to increase as the ripple contrast becomes stronger. Low-angle domain walls begin to form approximately perpendicular to

the applied field direction, as the magnetisation direction in different regions of the film rotates in opposite senses towards the easy axis of the free layer. These walls increase in angle as the magnetisation directions continue to rotate, splitting the sample into elongated domains. Figure 6.4 shows schematically how these elongated domains form as increasing the applied field overcomes the ferromagnetic coupling between the pinned layer and free layer, and the free layer magnetisation rotates towards the two easy directions.

Thereafter these domain walls decrease in angle as the magnetisation directions in each region continue to rotate to align with the applied field. The blue arrows shown in figure 6.4 show how the magnetisation within each domain rotates towards the applied field direction. The mobility of these domain walls is very low, as the rotation of magnetisation directions on either side do not apply any torque, which would lead to wall motion. Hence these walls do not disappear on increase of the applied field to  $\approx 100$  Oe where the magnetisation direction within each domain is aligned with the applied field, but they remain in position and develop some  $360^\circ$ -like characteristics. As the anti-parallel applied field is relaxed, the dispersion increases within each domain and the walls become higher in contrast as the magnetisation directions within the domains rotate back in opposite senses towards the easy axis of the free layer. The domain walls break up and disappear as the anti-parallel field is relaxed further, leaving small sections of  $360^\circ$  walls remaining. Figure 6.5 shows how these  $360^\circ$  walls are formed when the applied field is decreased from large positive applied field and increased in the negative direction.

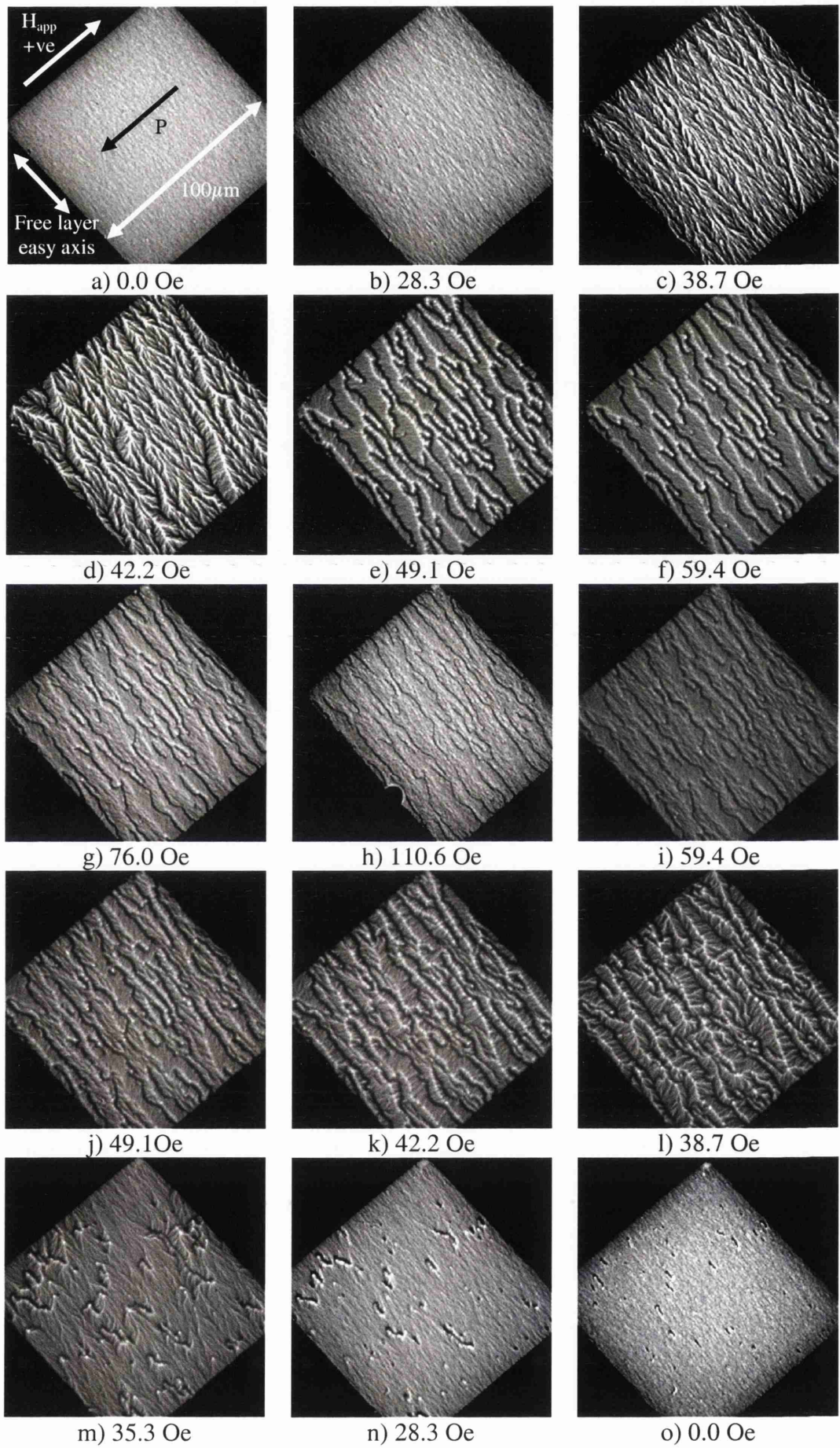


Figure 6.3 Free layer reversal with field applied antiparallel to pinning direction

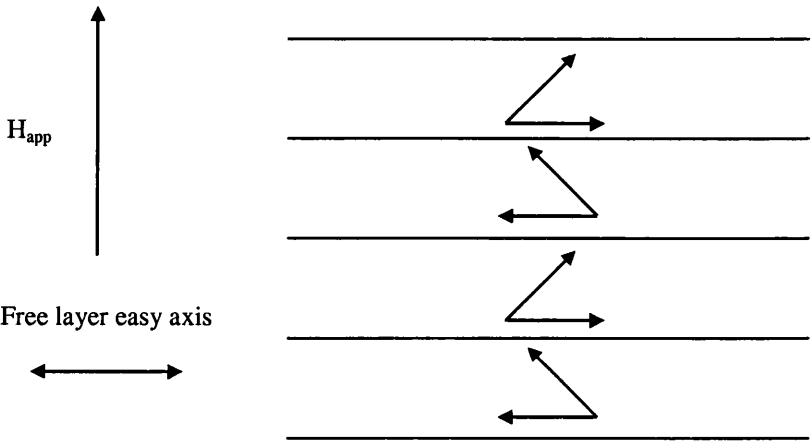


Figure 6.4 elongated domains form with field applied anti-parallel to pinning direction

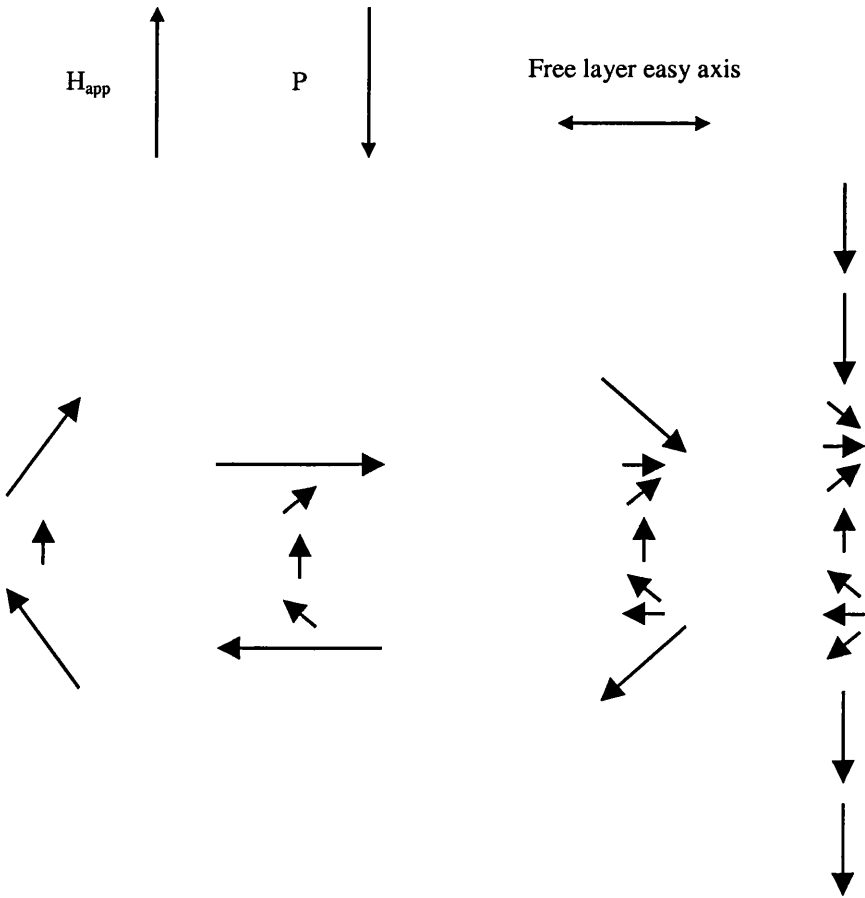


Figure 6.5 Formation of 360° walls with field applied anti-parallel to pinning direction

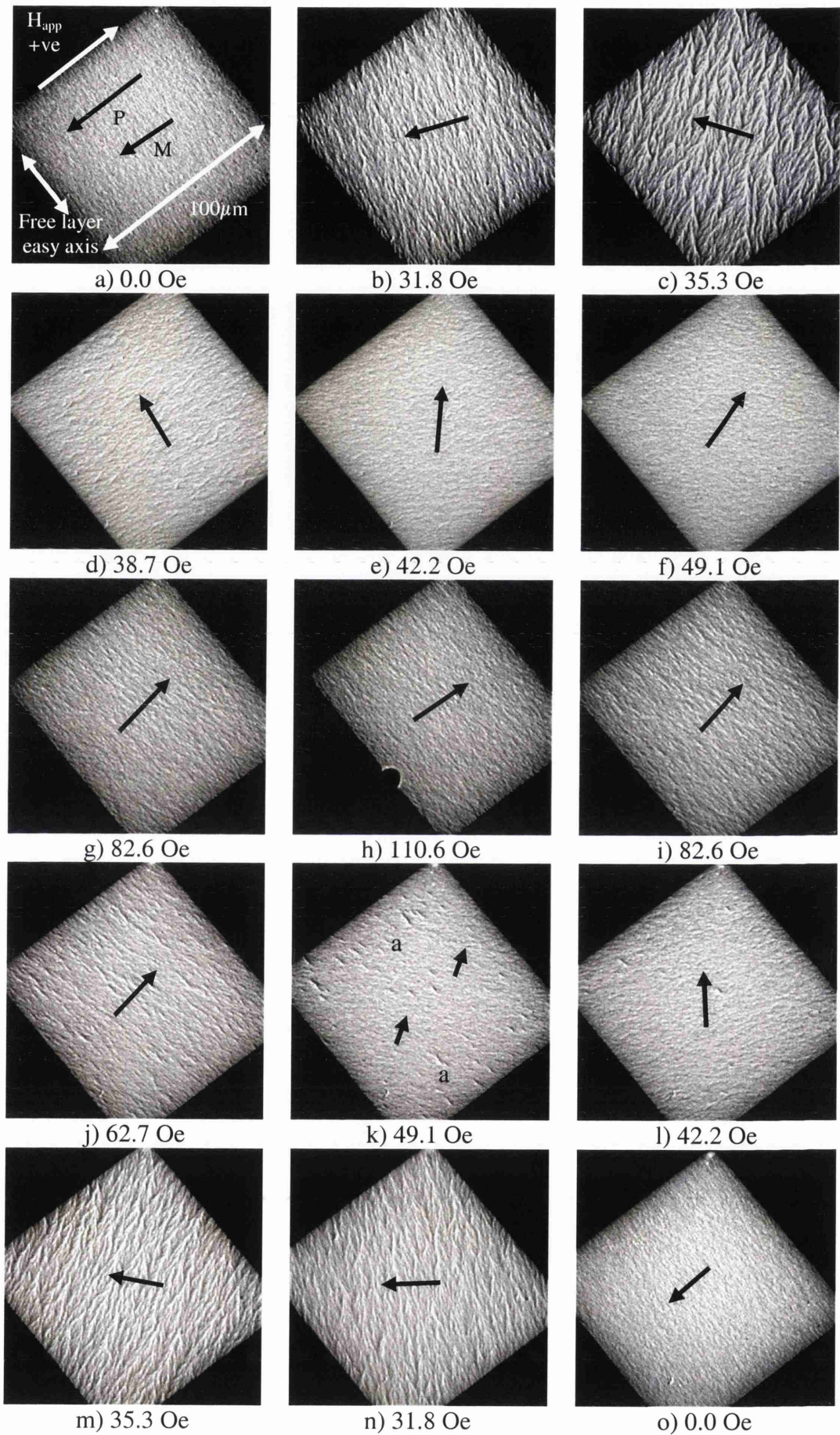


Figure 6.6 Free layer reversal with field applied at 175° to pinning direction

Figure 6.6 shows a sequence of Fresnel images taken with the applied field at an angle of  $175^\circ$  to the pinning direction. It can be seen from the images that the reversal mechanism is quite different from above. As the field is increased in the positive direction as shown on the figure, the magnetisation direction of the film begins to rotate in a clockwise sense, with increasing dispersion and formation of low-angle walls as the magnetisation is pulled away from the pinning direction, until there is a slight “jump” to align with the easy axis of the free layer at  $\approx 38$  Oe. After this jump there is a decrease in the contrast observed, and the magnetisation direction then continues to rotate more slowly to align with the applied field direction. As the applied field is reduced, the magnetisation direction begins to rotate in the opposite sense towards the easy axis of the free layer. Some small features appear, denoted by ‘a’ on the figure, but disappear before the rapid “jump” in magnetisation direction between 42.2 Oe and 35.3 Oe. Immediately after this jump there is an increase in the contrast observed, which then decreases as the magnetisation direction rotates more quickly to align with the pinning direction. This resembles a mode B reversal mechanism using the terminology of Labrune et al. [3]. Labrune classifies spin valve free layer reversal mechanisms into three modes A, B and C. Mode A corresponds to a switching mechanism where the uniaxial anisotropy dominates, with abrupt jumps to reach equilibrium positions. In mode B, switching largely occurs by coherent rotation of magnetisation with a small discontinuity. Mode C then corresponds to reversal by pure rotation without hysteresis. The mode adopted depends on the angle at which field is applied, as well as the strength of the coupling between the free layer and the pinned layer.

A plot of  $(1 - \cos \phi)$  versus  $H$ , constructed from this sequence of Fresnel images, is shown in figure 6.7. This shows an asymmetry in the curve as it slows before reaching the plateau, echoing the shape of the measured MR/ $H$  curve supplied by Seagate, which was shown in figure 6.1.

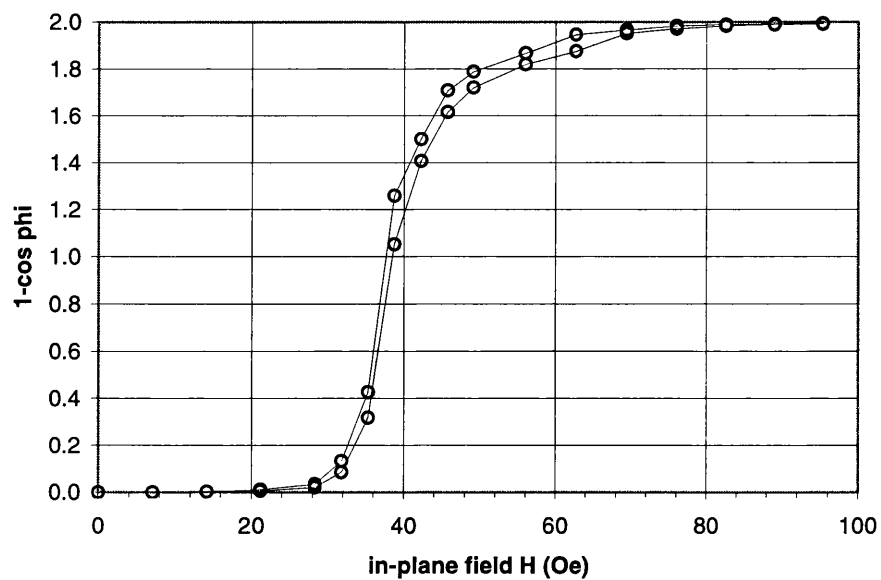
Figure 6.8 shows a sequence of Fresnel images taken with the applied field at an angle of  $135^\circ$  to the pinning direction. Here we see that the reversal occurs by a

smooth, coherent rotation of magnetisation direction of the whole film. As the applied field is increased in the positive direction as shown on the figure, the magnetisation direction begins to rotate towards the closest easy direction and there is a slight increase in ripple contrast. The ripple contrast decreases when the magnetisation direction is aligned with the easy axis at  $\approx 49$  Oe, and remains low as the magnetisation direction continues to rotate to align with the applied field. When the applied field is relaxed, the rotation in the opposite sense is again smooth and regular, with a slight increase in ripple contrast after the magnetisation direction has passed the easy axis. This resembles a mode C reversal mechanism using the terminology of Labrune et al [3].

When the field is applied at different directions relative to the pinning direction, we see that different values of applied field are required to overcome the pinning field so that the free layer magnetisation lies along the easy axis. This is shown schematically in figure 6.9. By simple geometry, the field applied at an angle  $\theta$  to the pinning direction must be such that the component of field acting anti-parallel to the pinning direction is equal to the pinning field  $H_p$  in order to overcome the pinning effect.

$$H_{app} \cos \theta = H_p \quad 6.1$$

Hence, the case where  $\theta \approx 135^\circ$  requires a field of  $\approx 49$  Oe to overcome the pinning, and the case where  $\theta \approx 175^\circ$  requires a field of only  $\approx 38$  Oe. This assumes that the applied field component perpendicular to the pinning direction has little or no effect on the free layer magnetisation.



*Figure 6.7 plot of free layer reversal with field applied at 175° to pinning direction*

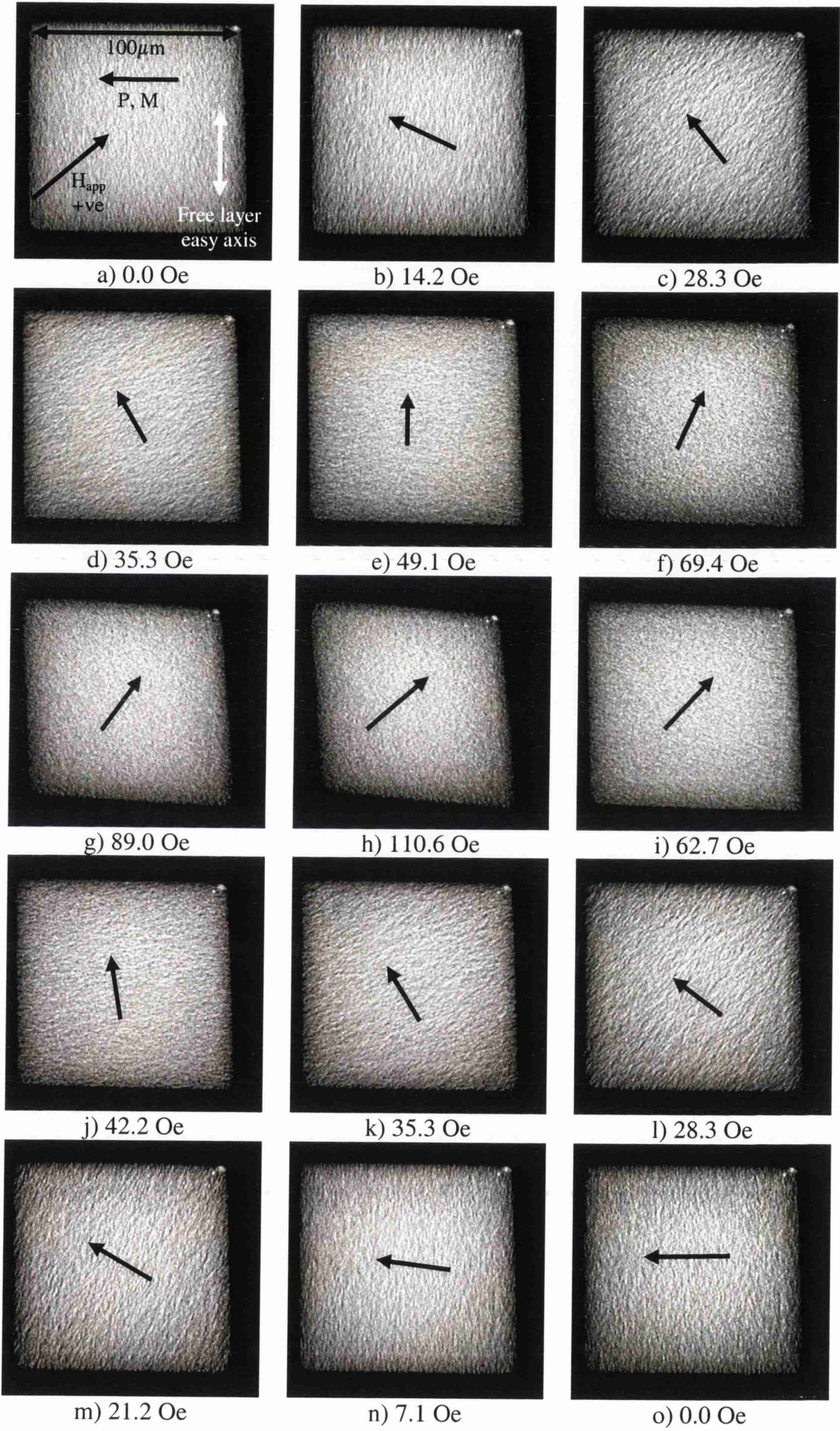


Figure 6.8 free layer reversal with field applied at 135° to pinning direction

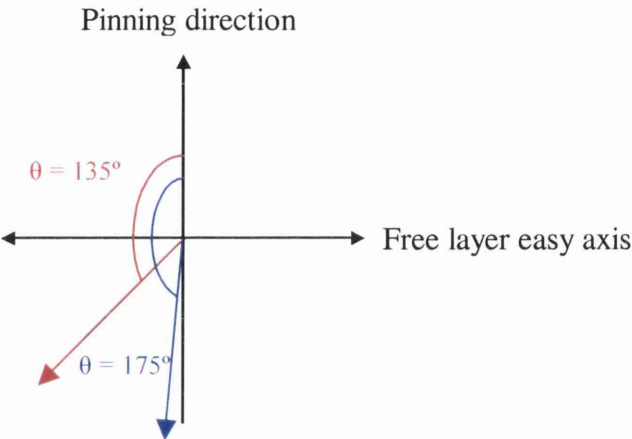


Figure 6.9 Applying field at different orientations relative to pinning direction

**6.4 Comparison of reversal mechanisms with modelled results of Labrune**

The experiments described above have shown above that the room temperature magnetisation reversal mechanism of the free-layer of a spin-valve with crossed-anisotropy depends strongly on the direction at which the field is applied. We see that the formation of complex domain structures can be avoided simply by ensuring that the applied field is rotated a few degrees away from lying anti-parallel to the pinning direction. However, the presence of the small jump in the magnetisation reversal when the applied field is at  $175^\circ$  to this direction could imply that the pinning direction and the easy axis may not be exactly orthogonal. This deduction is made from comparison with modelled results by Labrune at al [3].

From the phase diagram given by Labrune, it seems that for the case of exact orthogonality a pure rotation mechanism is expected with the field at all orientations for spin-valves where the coupling between the free- and pinned-layers is as strong as is the case here. Alternatively an explanation for the small jump may lie in the fact that, in real films, some dispersion of magnetisation is

inevitable whilst the single-parameter model of Labrune assumes complete uniformity of magnetisation throughout. It should also be noted that the model provides no guidance in cases where domain processes dominate the reversal process as was the case when the applied field was anti-parallel to the pinning direction.

## **6.5 Free layer reversal mechanism as a function of specimen temperature**

Magnetising experiments with fields applied at a few degrees from anti-parallel to the pinning direction were carried out with the specimen at room temperature, then heated in-situ within the TEM (see Chapter 2) to 100°C, 200°C and 280°C, and then cooled back down to room temperature.

The temperatures quoted are those obtained from a thermocouple mounted in the specimen rod. The exact temperature of the  $\text{Si}_3\text{N}_4$  membrane specimen may vary slightly from this quoted value, and will be partly dependent on the level of thermal contact between the specimen and the holder.

Figure 6.10 shows a sequence of Fresnel images taken during a magnetising cycle with field applied at 175° to the pinning direction, and the specimen maintained at room temperature, or more correctly at the ambient temperature within the TEM column. As was seen in the previous section, the free layer reversal at room temperature begins with increasing dispersion, which develops into low-angle walls by 35.3Oe. As the field is not applied directly anti-parallel to the pinning direction of the spin-valve film, the free layer magnetisation then aligns preferentially with one easy axis. Some 360° domain walls can be seen to form in 6.10 e), as shown schematically in figure 6.11. These are different from the 360° wall segments which formed previously seen in figure 6.5.

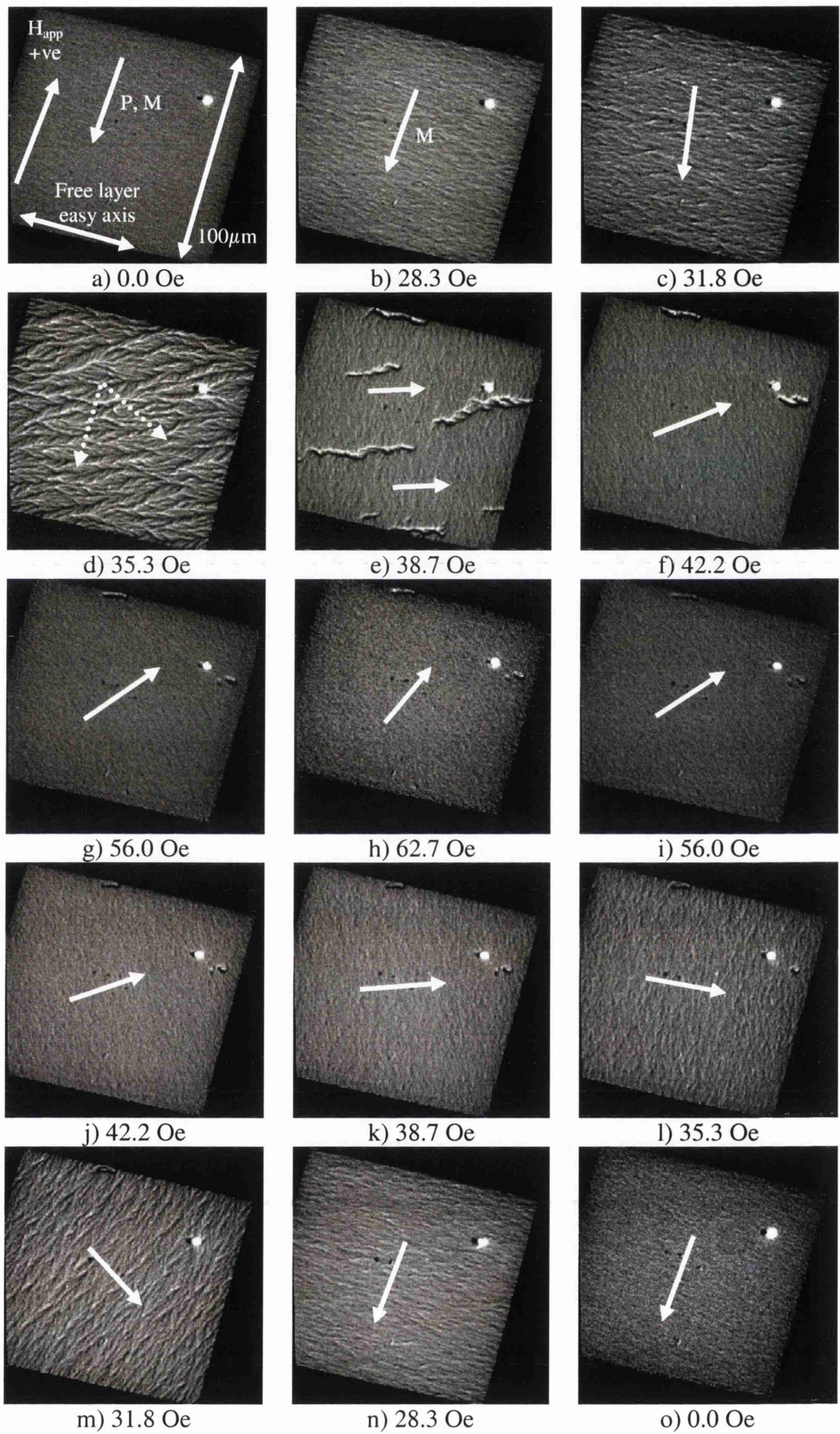
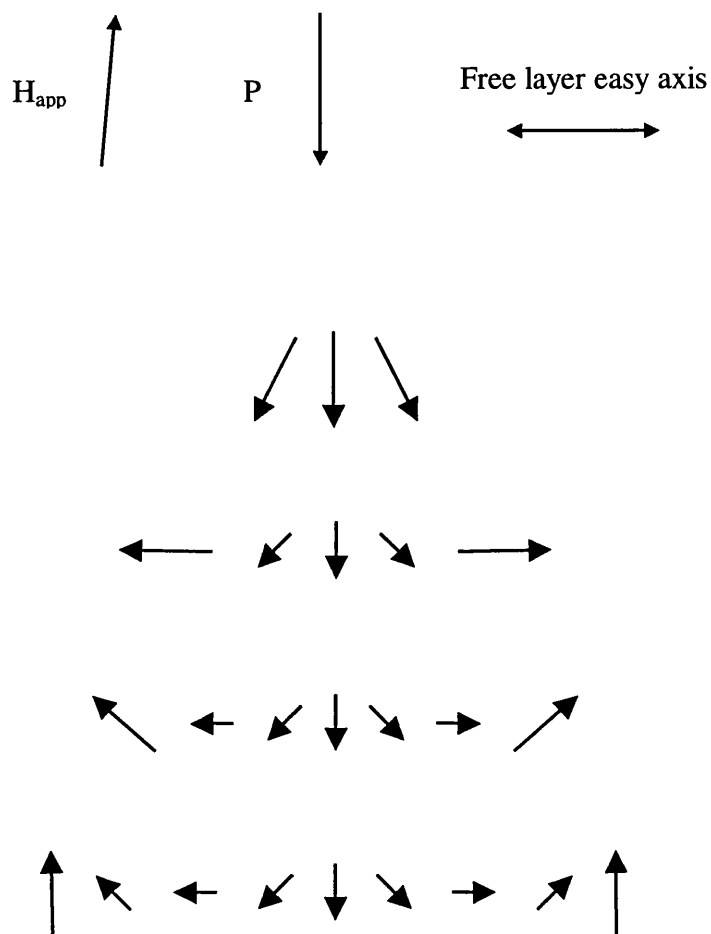


Figure 6.10 Free layer reversal with specimen at room temperature



*Figure 6.11 formation of 360° walls with field applied at 175° to pinning direction with specimen at room temperature*

These walls are mostly annihilated by 42.2Oe, where only a small number of 360° wall segments remain. These remain immobile as the bulk magnetisation direction continues to rotate smoothly towards the applied field direction, which it has not quite aligned with upon reaching 62.7Oe. The field was then increased to ~100Oe and again reduced to 62.7. The magnetisation direction rotates smoothly back towards the same easy direction as the applied field is reduced, reaching it at 35.3Oe. Upon further reduction of the field, dispersion in the film increases as the magnetisation direction moves past the easy axis of the film, then decreases as the magnetisation aligns with the pinning direction once again.

A plot of  $(1-\cos \phi)$  versus  $H$ , constructed from this sequence of Fresnel images, is shown in figure 6.12. This agrees with the plot seen in figure 6.7 taken under similar conditions, and also with the shape of the measured MR/H curve supplied by Seagate which was shown in figure 6.1.

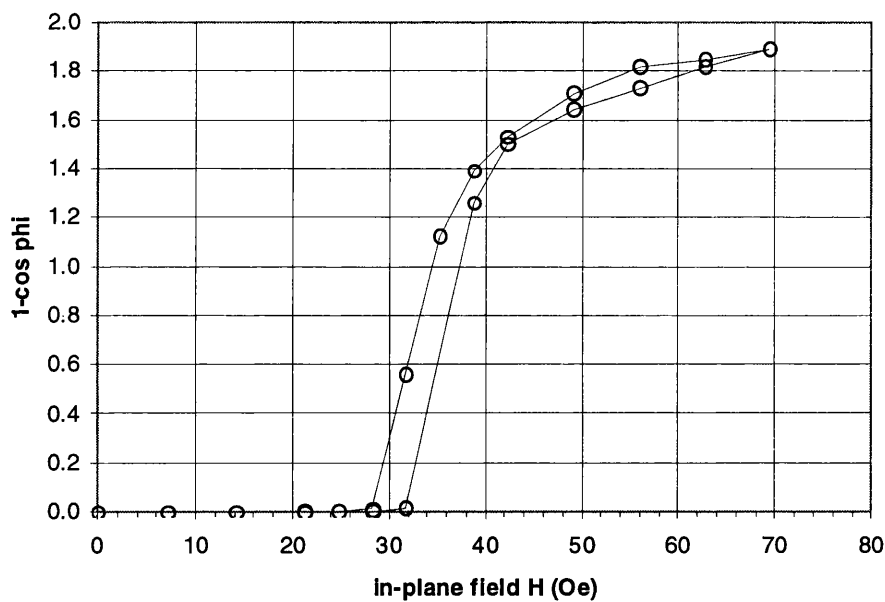


Figure 6.12 plot of free layer reversal with specimen at room temperature

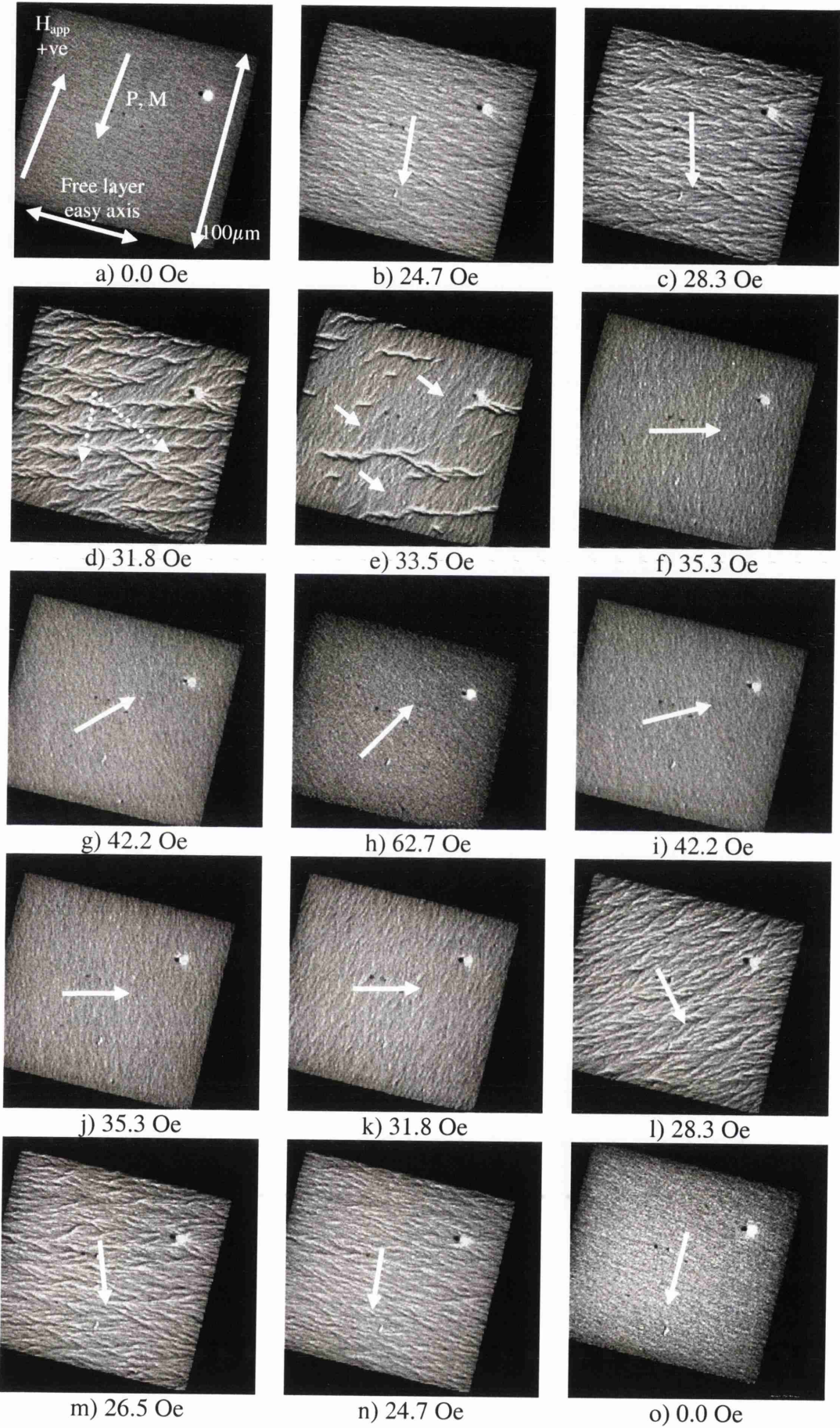
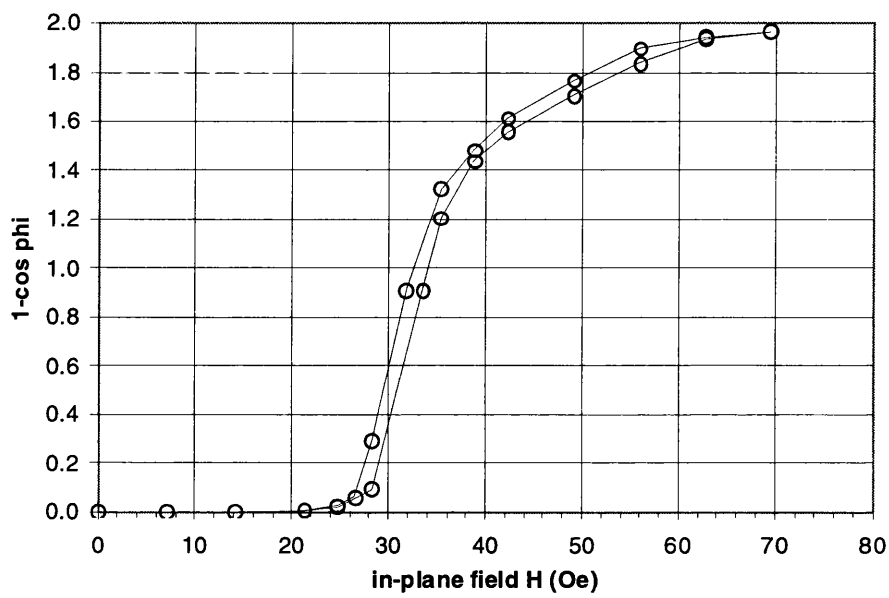


Figure 6.13 free layer reversal with specimen heated to 100°C

Figure 6.13 shows a sequence of Fresnel images taken with applied field at the same orientation as above, and the specimen heated in-situ in the TEM to 100°C. Figure 6.14 shows the  $(1-\cos \phi)$  versus  $H$  plot constructed from the image sequence. It can be seen from the Fresnel images and the plot, that the reversal mechanism is similar to that at room temperature, with equivalent stages reached at very slightly lower field values. The  $(1-\cos \phi)$  versus  $H$  plot also corresponds with that taken at room temperature and shows the asymmetry seen in the MR/H curve.



*Figure 6.14 plot of free layer reversal with specimen heated to 100 °C*

Figure 6.15 shows a sequence of Fresnel images taken with the specimen heated in-situ in the TEM to 200°C. The images show that the free layer reversal begins similarly to before, with increasing dispersion and formation of low-angle walls. Once again, equivalent stages are reached at lower fields, although the mean magnetisation tends to rotate towards the opposite easy direction from before. Some domains, with low mobility, remain stationary as the bulk magnetisation direction continues to rotate smoothly towards the applied field direction. However by 49.1 Oe, before the magnetisation has aligned with the applied field, some new contrast is evident. This is likely to be due to the “pinned layer” beginning to reverse, as the elevated temperature decreases the field necessary to overcome the coupling between the NiMn antiferromagnet and the “pinned layer”. This interpretation of what is happening relies on physical insight into the behaviour of thin magnetic films. The technique of Lorentz microscopy provides a projection through all layers of a multi-layer film, yet inferences can be made as to which individual layer gives rise to contrast within the image.

This contrast increases, presumably due to the dispersion in the “pinned layer” increasing by 56.0 Oe, but when the field is increased to ~100 Oe and then reduced to 49.1 Oe, this “pinned layer” contrast is greatly reduced. We take this to indicate that the magnetisation direction in the “pinned layer” has been reversed. Also, the remaining features after the field is reduced from ~100Oe show white-over-black contrast, the inverse of the black-above-white contrast seen as the field was increased. These features remain stationary, increasing in contrast while the mean magnetisation direction rotates smoothly towards the easy axis as the field is reduced. The dispersion in the free layer increases as the mean magnetisation direction passes the easy axis at 28.3Oe. Then, at 21.2Oe, there is a complex system of low-angle walls and the domain wall features believed to be in the “pinned layer”, as the magnetisation directions of the free layer and the “pinned layer” undergo a rapid change as they tend to revert to the original pinning direction. Many of the domain walls are annihilated after this point, as further reduction of the applied field allows both layers to align with the original pinning direction.

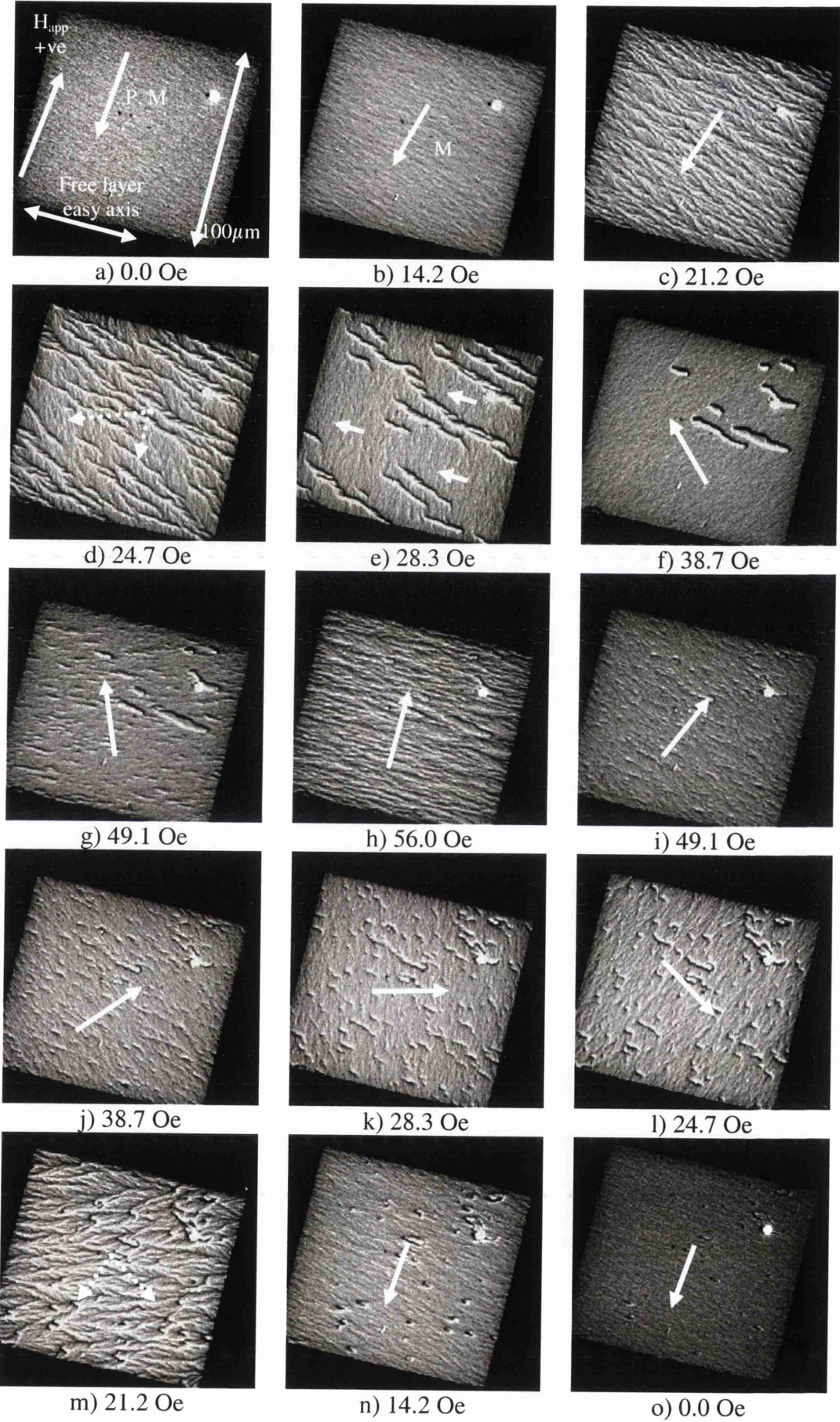


Figure 6.15 free layer reversal with specimen heated to 200°C

Figure 6.16 shows a sequence of Fresnel images taken with the specimen heated further in-situ in the TEM to 280°C. The Néel temperature of NiMn is ~380°C, and so heating to this temperature would not be expected to result in a complete break down of the AF behaviour. Even so, the behaviour seen in this sequence is quite different from that seen at 200°C. The free layer reversal occurs mainly by rotation, with a slight increase in dispersion, and the formation of some low-angle walls. These low-angle walls have disappeared by 31.8Oe where the magnetisation direction is aligned with the easy axis. After this point the magnetisation direction rotates smoothly to 56.0Oe. The effect seen at 200° C in the “pinned layer” does not appear, however until the field has been increased to ~100 Oe and returned to 56.0 Oe. The “pinned layer” contrast then is quite strong, suggesting that the “pinned layer” magnetisation has been reversed by the increase of applied field to ~100Oe. Many of these small domains remain as the field is reduced further and the mean magnetisation direction of the free layer can be seen to rotate smoothly. After 31.8Oe, where the mean magnetisation is aligned with the easy axis, the contrast of the mean magnetisation of the free layer increases and some of the small domain features in the “pinned layer” disappear. When the applied field is reduced further, the magnetisations in both the free layer and the “pinned layer” align with the original pinning direction.

After these cycles were carried out, the specimen was allowed to cool to the ambient temperature of the TEM. Another magnetising cycle was carried out, and figure 6.17 shows the sequence of Fresnel images. The behaviour seen in this case is significantly different to that seen before at room temperature. The free layer reversal occurs by rotation, with increased dispersion, but without the formation of domain walls as seen before heating. Also, by 62.7Oe the mean magnetisation direction has not rotated so far towards the applied field direction as seen in the room temperature cycle before heating. After the applied field was increased to ~100 Oe and reduced to 62.7 Oe, contrast similar to that seen at 200°C and 280°C but not seen previously at room temperature, was evident. Much of this, believed to be associated with the “pinned layer”, remained as the free layer magnetisation rotated back towards the pinning direction, leaving remanent features at zero field.

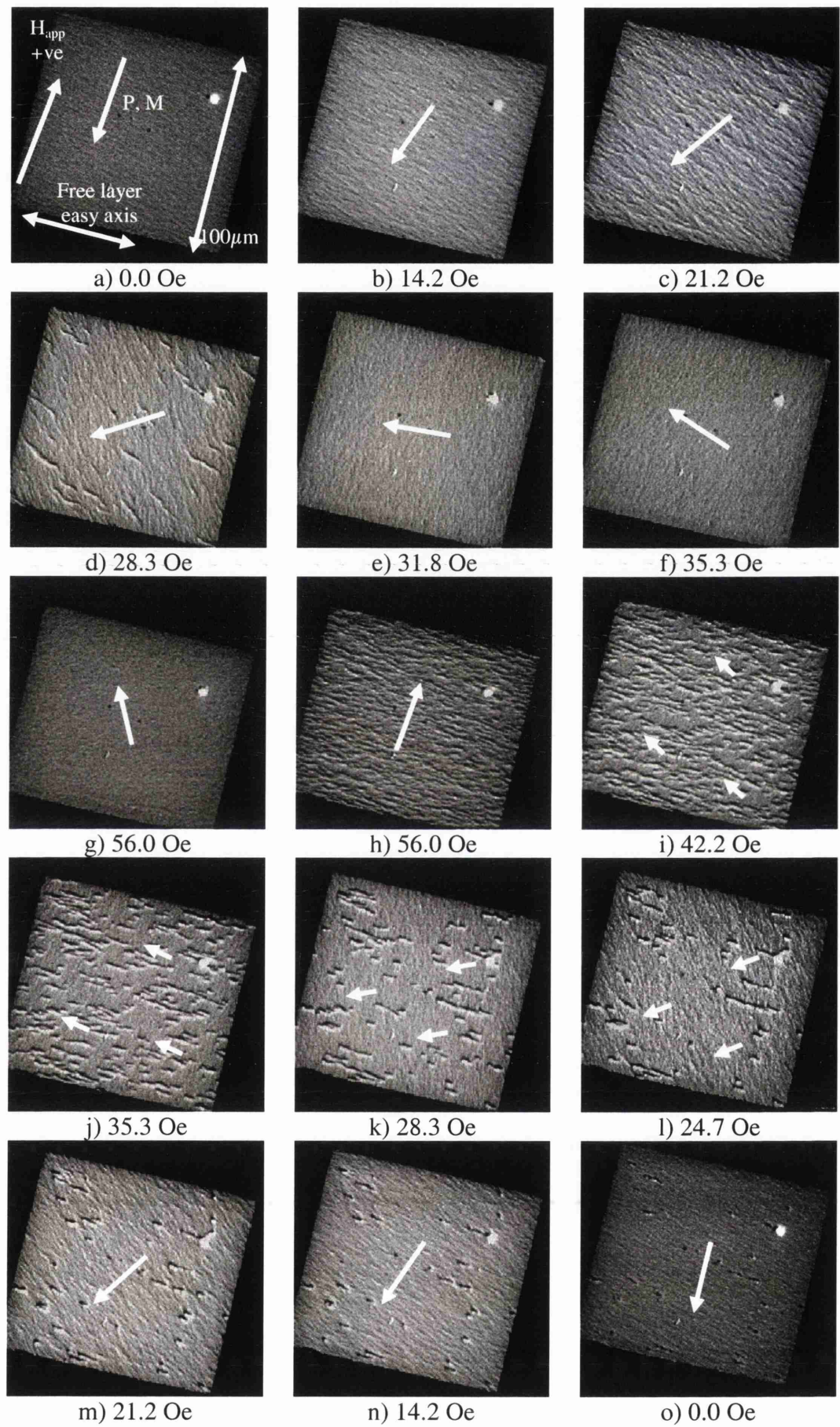


Figure 6.16 free layer reversal with specimen heated to 280°C

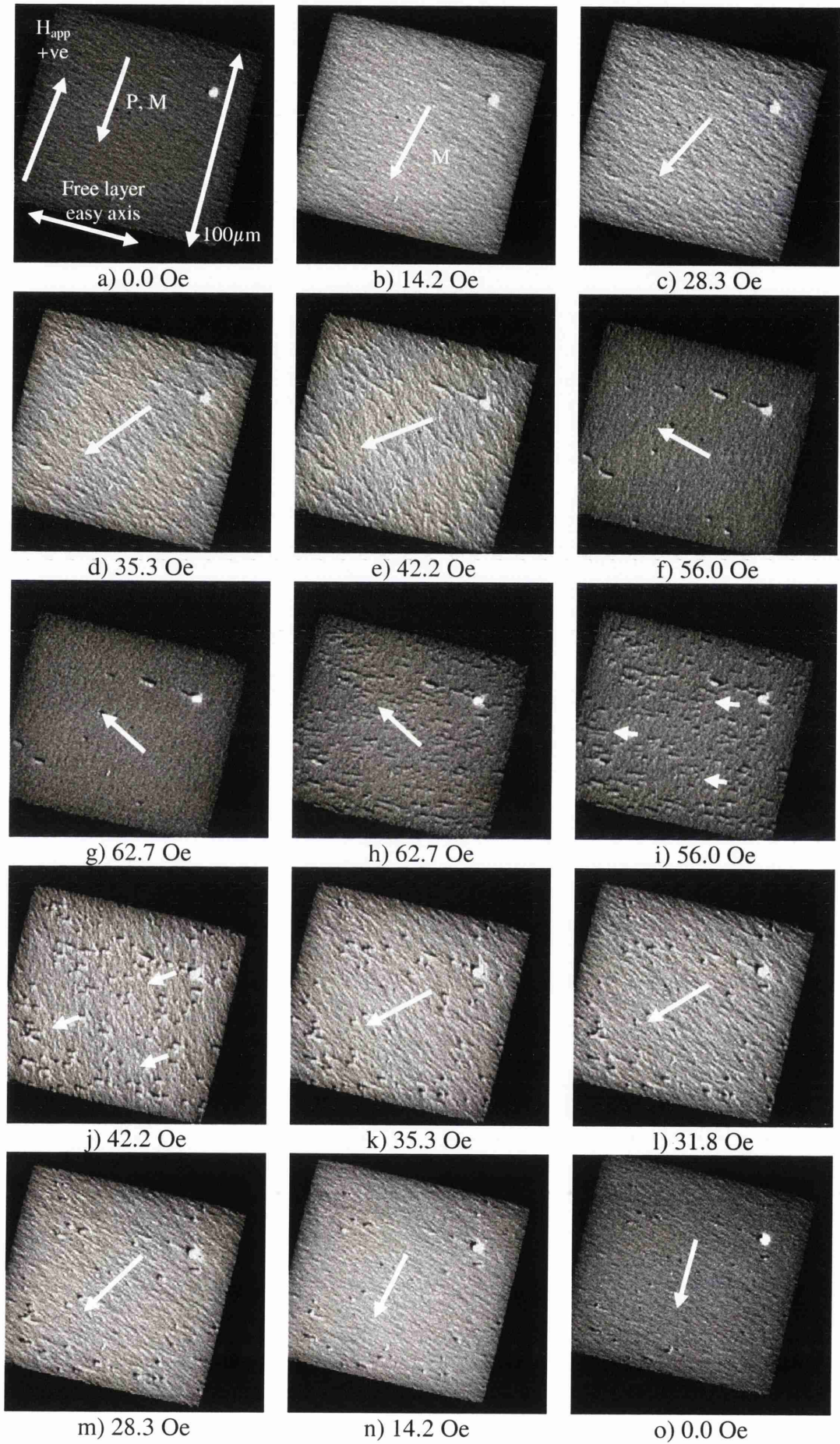


Figure 6.17 free layer reversal with specimen recooled to room temperature

The  $(1-\cos \phi)$  versus  $H$  plot constructed from this sequence (figure 6.18) illustrates the difference in behaviour compared to that taken at room temperature before heating. The steady gradient of the plot reflects the relatively smooth rotation of magnetisation direction, in contrast to the rapid change in magnetisation direction seen before heating.

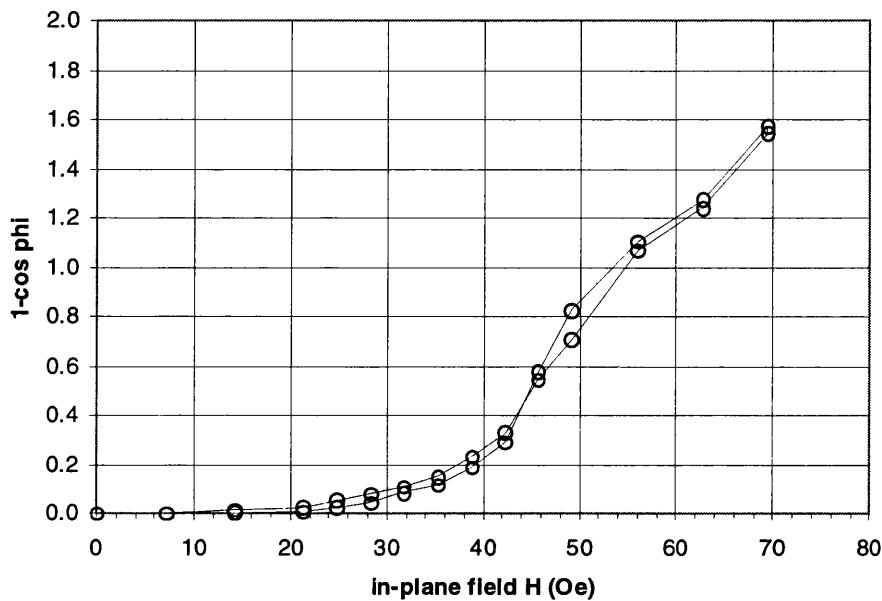


Figure 6.18 plot of free layer reversal with specimen recooled to room temperature

6.6 Analysis and comparisons

The free-layer reversal of the spin-valve was seen to be affected only slightly at temperatures up to 100°C but at temperatures >200°C the behaviour changed markedly. Magnetic structures which appeared when the reversal of the free-layer was almost complete were attributed to the onset of reversal in the pinned-layer. Furthermore, the changes that occurred at elevated temperature proved irreversible in that when the specimen was re-cooled to room temperature, the original behaviour was not recovered.

Analysis of the full image sequences (from which the selected images shown were extracted) can yield very useful quantitative information on how the magnetoresistance varies with field. The orientation of the free-layer magnetisation can be determined from each image and hence we have a measure of the angle,  $\phi$ , between the magnetisation vectors in the free- and pinned-layers. Given that the MR of a spin-valve is proportional to  $(1 - \cos \phi)$ , we can make plots of MR as a function of field for each sequence. The advantage of using this method to determine MR characteristics is that associated with each datum is an image showing precisely the magnetisation distribution in the sample at that point.

More detailed knowledge of the exchange bias pinning field, the anisotropy fields in each layer and the inter-layer coupling strength would have enabled micromagnetic modelling of the system for comparison with this experimental data. This would provide a useful addition to aid the understanding of the micromagnetic behaviour of such complex systems. In particular, modelling would help in interpreting the physical change in the NiMn layer upon heating.

## Chapter 7 Spin-Valve Stacks with Varying Layer Thicknesses

### 7.1 Introduction

This Chapter investigates the effects of changing selected layer thicknesses on the properties of a particular spin-valve structure. This spin-valve structure is a top spin-valve (TSV), which contains a synthetic antiferromagnet (SAF) structure as described in section 1.7. The SAF structure [1-4] was introduced to improve the stability of the pinning effect available from a single pinned layer. The standard composition of the selected spin-valve stack is shown schematically in figure 7.1 below. The layers whose thicknesses were varied in the following experiments are indicated by red lettering.

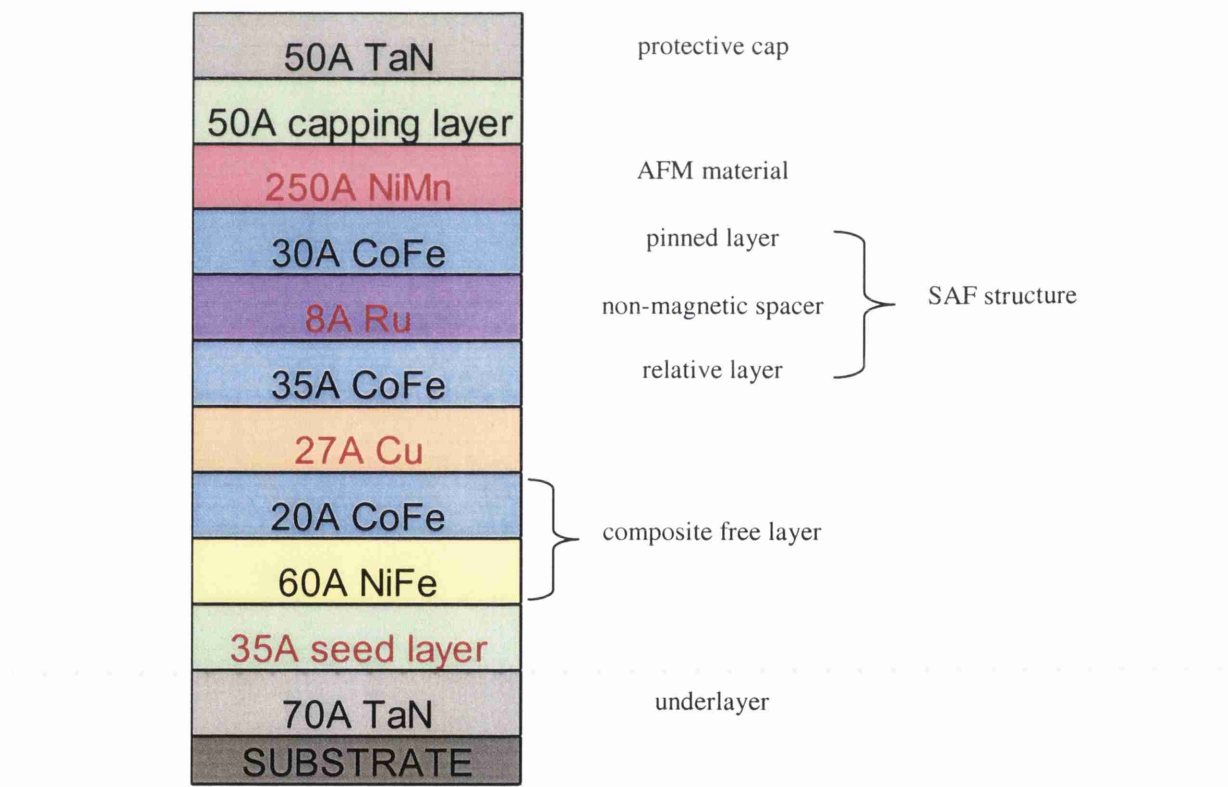


Figure 7.1 Standard spin-valve structure with red lettering showing layer thicknesses varied

The experiments described in this Chapter were carried out during a three-month summer placement at Seagate Technology's Springtown plant. The different magnetic films were deposited on 4.5" square AlTiC wafer substrates, using commercial sputter deposition systems.

These wafers were all annealed within a magnetic field after deposition in order to set the pinning direction of the NiMn AFM. After the annealing step, the wafers then underwent characterisation measurements using some of the metrology equipment described in Chapter 3.

## 7.2 Variation of seed layer thickness

Various materials can be used as "seed" layers on which magnetic sensor films can be grown. These seed layers can alter the growth of subsequent layers, affecting microstructural properties such as their crystal orientation and grain size. The proprietary seed layer material adopted by Seagate Technology in this spin-valve structure has the effect of increasing the grain size in the subsequent layers, as well as controlling the texturing to the [111] crystal orientations.

A set of wafers was deposited with spin-valve stacks identical apart from differing seed layer thicknesses. The thicknesses were 25, 30, 35, 40, 45Å, with 35Å being the thickness used in the standard structure.

Figure 7.2 shows a plot of  $dR/R$ , the magnetoresistance ratio, averaged across each wafer, as a function of the seed layer thickness. From this it can be seen that the MR ratio increases sharply from 5.8% at 30Å seed to 8.3% at 35Å seed. Above and below these thicknesses, there is a slower change in  $dR/R$  with seed layer thickness. This would suggest that 35Å is the minimum thickness desirable for the seed layer.

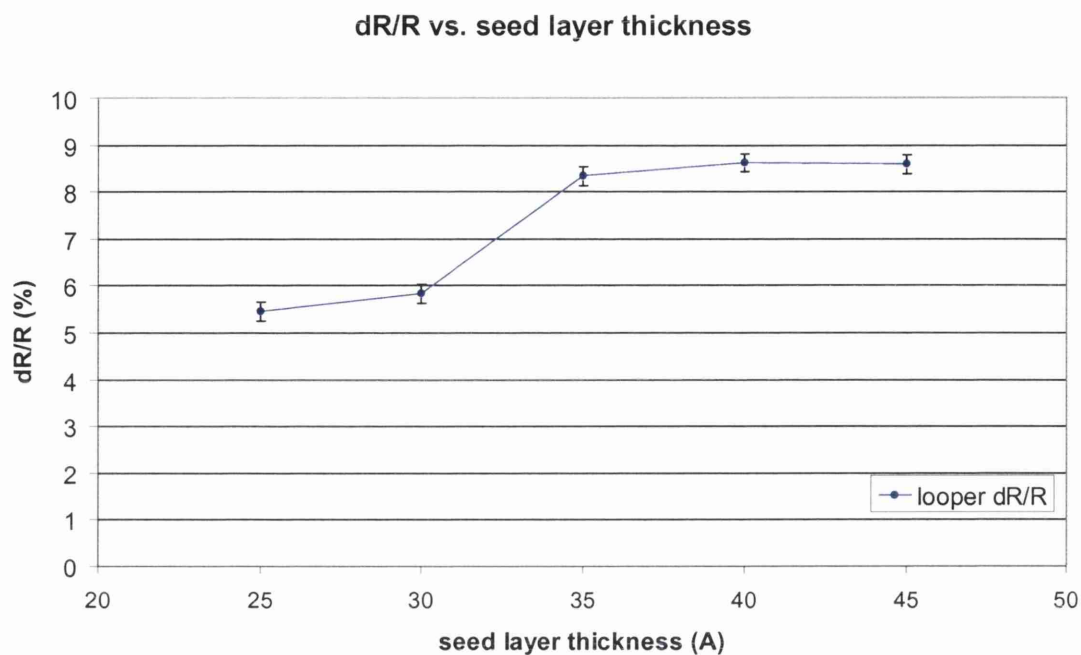


Figure 7.2 plot of dR/R vs. seed layer thickness

The effective pinning offset field,  $H_p$ , is another important parameter for a spin-valve. This is defined as the horizontal shift in the free layer minor loop due to the ferromagnetic coupling between the pinned and the free layers as shown in figure 7.3. For a spin-valve operating in a sensor device, it is important that the  $H_p$  is a positive-valued field of the order of a few Oe, and that this is uniform over a wafer, and stable throughout the lifetime of the sensor. Figure 7.4 shows a plot of  $H_p$ , as a function of seed layer thickness. This shows that  $H_p$  increases with thinner seed layers, and that below 35Å seed layer, this increases from 3.8Oe to 5.6Oe at 30Å. This change in  $H_p$  with seed layer thickness is likely to be due to the decrease in interface roughness with thicker seed layer films. This would indicate that 35Å is the thinnest seed layer desirable to achieve a  $H_p$  consistently below 5Oe, while maintaining a dR/R of over 8%.

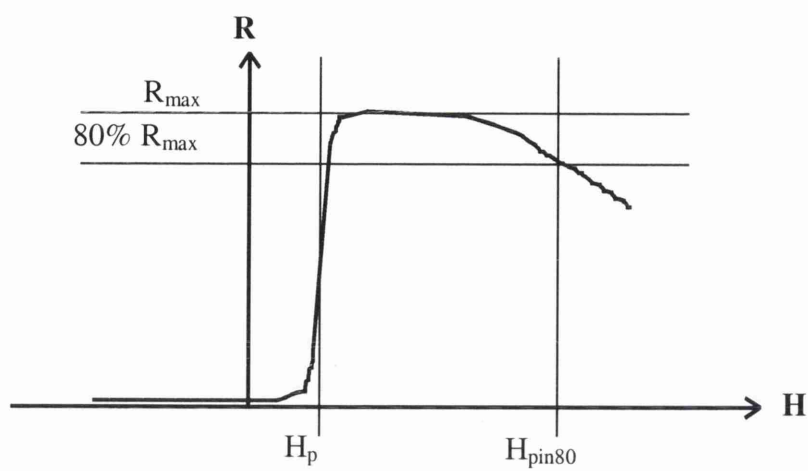


Figure 7.3 Schematic of spin-valve MR loop

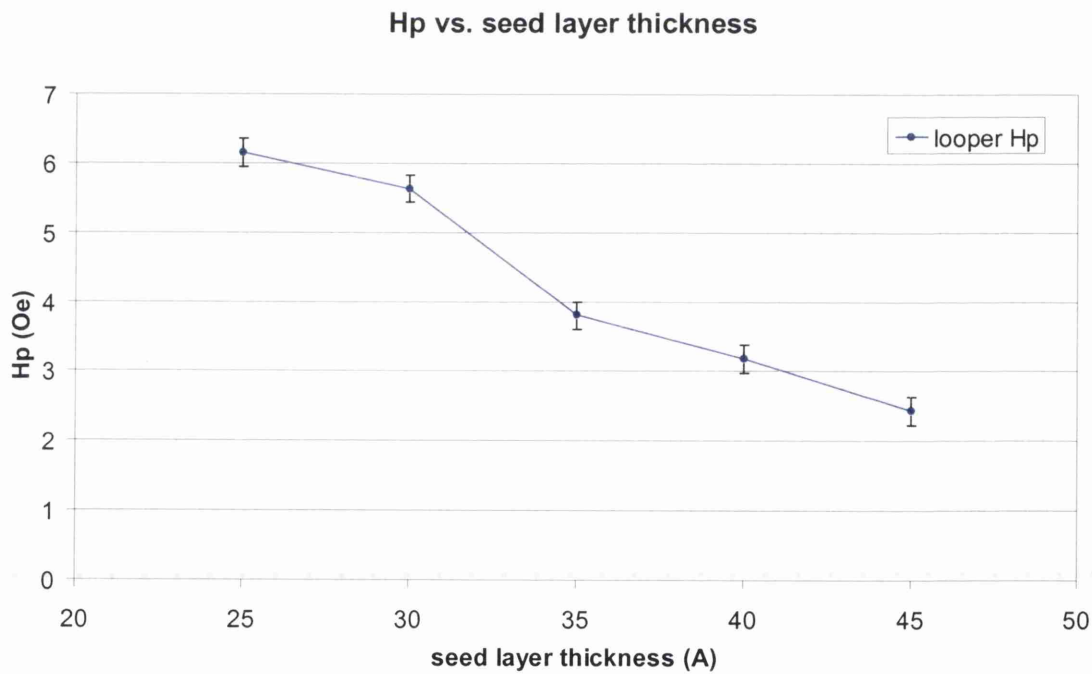
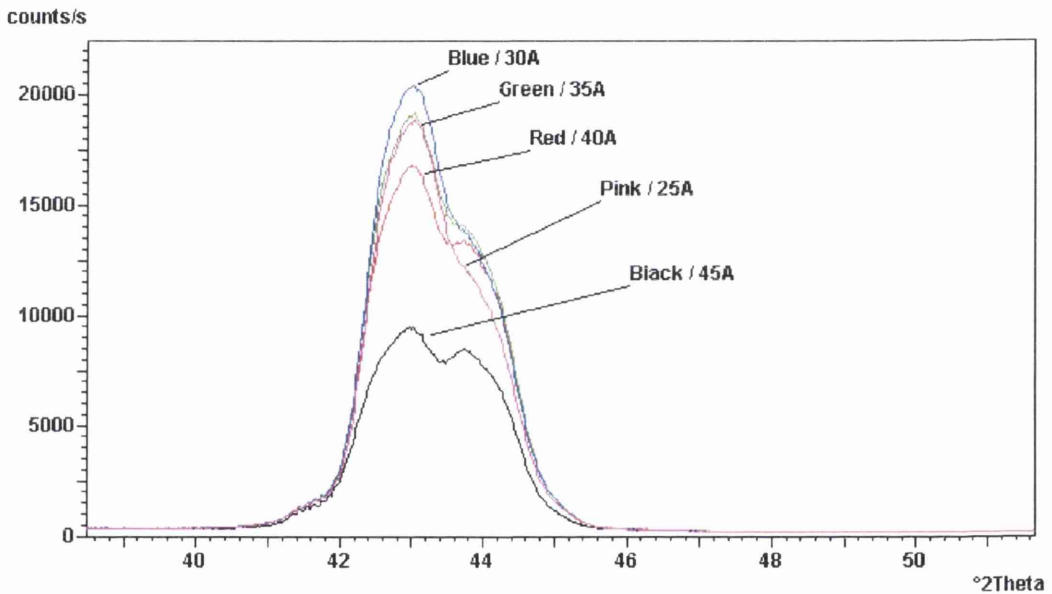


Figure 7.4 plot of  $H_p$  vs. seed layer thickness

Alison Bell of Seagate Springtown R&D carried out x-ray diffraction (XRD) measurements on these wafers, in order to ascertain what differences in the crystalline structure of the spin-valve might arise from the different thicknesses of seed layer. Figure 7.5 shows the XRD spectra obtained from this set of wafers around the NiFe (111) peak. There are differences in the peak intensities between the films with different seed layer thicknesses, suggesting differences in the level of texturing. There is not, however, any peak broadening apparent between the films, indicating that there is no appreciable change in grain size from one film to the next.



*Figure 7.5 XRD spectra of spin-valves with different seed layer thicknesses*

From this, it can be deduced that the presence of a seed layer of a minimum thickness to ensure uniform layer coverage, controls the crystalline growth of a spin-valve film, improving the magnetic properties. Beyond this minimum value, however, it does not seem that there is much to benefit from further increasing the seed layer thickness. It must be noted, however, that the spin-valve structure investigated here is of the top spin-valve (TSV) type, where the AF material sits at the top of the stack. For BSV or indeed DSV type stacks where the AF is in closer contact with the seed layer, structural effects from different seed layer thicknesses may have a greater effect on the magnetic pinning.

### 7.3 Variation of Cu layer thickness

The thickness of the Cu spacer layer separating the relative layer (see figure 7.1), or the pinned layer in a simple spin-valve without SAF, from the free layer in a spin-valve structure has an important effect on the overall performance. If the Cu layer is too thick, current shunting can occur, where the electrons flow preferentially in the low-resistance Cu. This reduces the likelihood of spin-dependent scattering events in the higher resistance magnetic layers, and so limits the change in resistance available. If the Cu layer is too thin however, the coupling between the free and relative layers can become too strong, so that the free layer magnetisation is no longer able to rotate to align with a moderate applied field.

A set of wafers was deposited with the standard spin-valve stack as above, with Cu thicknesses of 25, 27, 29, and 31 Å; 27 Å being the standard. Figure 7.6 shows a plot of  $dR/R$  versus Cu thickness. It can be seen that there is little effect on the  $dR/R$  of the stack with Cu thickness, only a small increase with thinner Cu layers. This is likely to be due to increased current shunting in the thicker Cu layers.

Figure 7.7 shows a plot of  $H_p$  versus Cu thickness, and it can be seen that  $H_p$  remains fairly stable at around 4.5-5 Oe for each of the Cu thicknesses considered here.

From this data, it can be seen that changing from the standard Cu layer thickness of 27 Å by a few Å in either direction gives no substantial benefit, either in  $dR/R$  output or in exchange field. It would seem that the standard thickness in use is close to the optimum value for this stack. This may be beneficial from a production point of view in that a slight variation in the Cu thickness across a wafer or from wafer to wafer will not give rise to significant changes in performance.

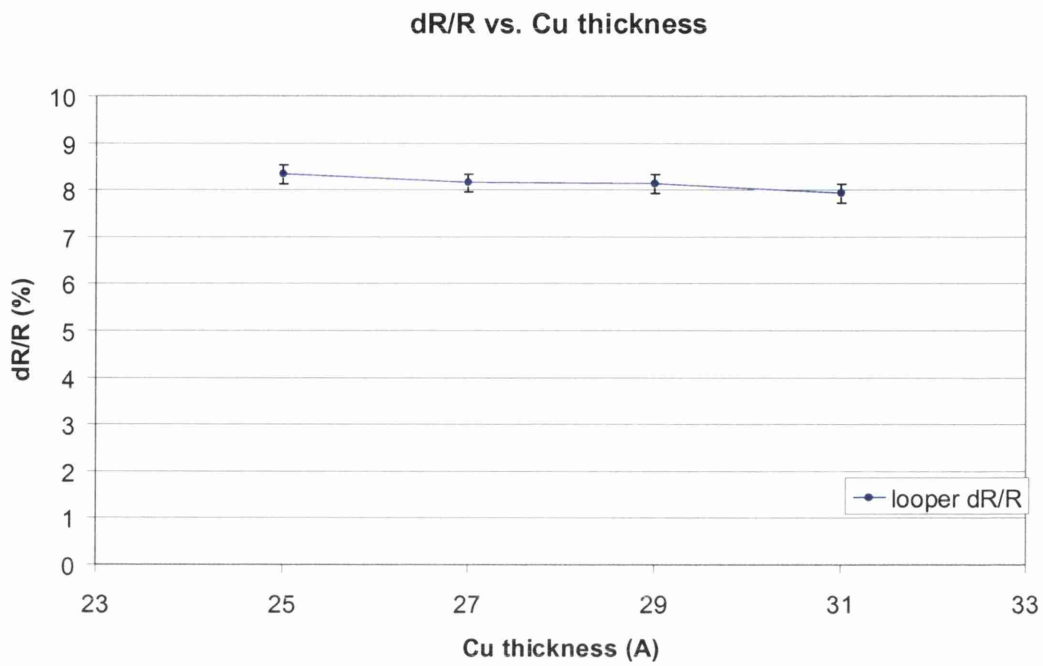


Figure 7.6 plot of  $dR/R$  vs. Cu layer thickness

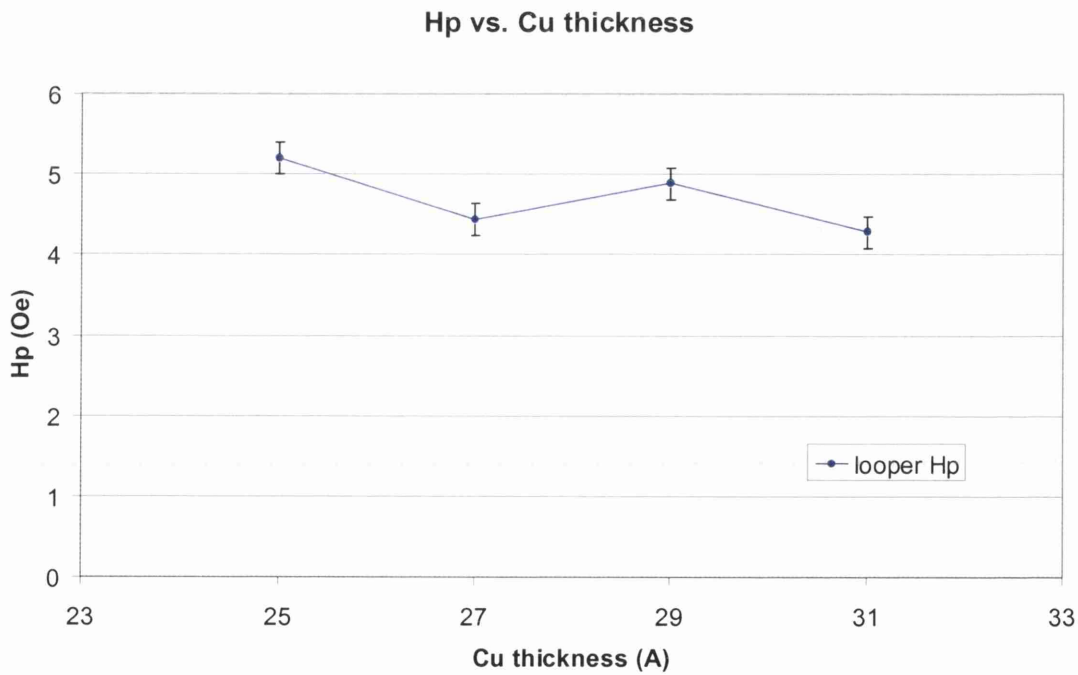


Figure 7.7 plot of  $H_p$  vs. Cu layer thickness

## 7.4 Variation of Ru layer thickness

The thickness of the Ru spacer layer separating the pinned layer from the relative layer in the SAF portion of the spin valve controls the RKKY coupling [5] between these layers. It is important that the Ru thickness is such that the magnetisation of the relative layer has a strong anti-ferromagnetic coupling to that of the pinned layer. This constrains the Ru layer thickness to the range 6-12Å. It is also important that such a thin layer can be deposited in such a way that it is both smooth and uniform across the wafer.

A set of wafers was deposited with the standard spin-valve structure as above, with Ru thicknesses of 6, 7, 8, 9 and 10Å; 8Å being the standard thickness. Figure 7.8 shows a plot of  $dR/R$  versus Ru thickness for these wafers. It can be seen that  $dR/R$  decreases from 8.0% with 6Å Ru to a minimum of 7.0% at 9Å Ru. It then recovers somewhat to 7.9% at 10Å Ru. At such thin layer thicknesses as these, the inherent grain roughness in the film is of the same order or larger than the difference of 1Å between films. This means that differences between the stacks may be less distinguishable.

Figure 7.9 shows a plot of  $H_p$  versus Ru thickness. This plot shows an increase in  $H_p$  from 4.5Oe at 7Å to 5.6Oe at 8Å, then levelling off at 5.2Oe for 9 and 10Å Ru. The values of  $H_p$  over this range of Ru layer thickness are all low enough to be acceptable for spin-valve performance.

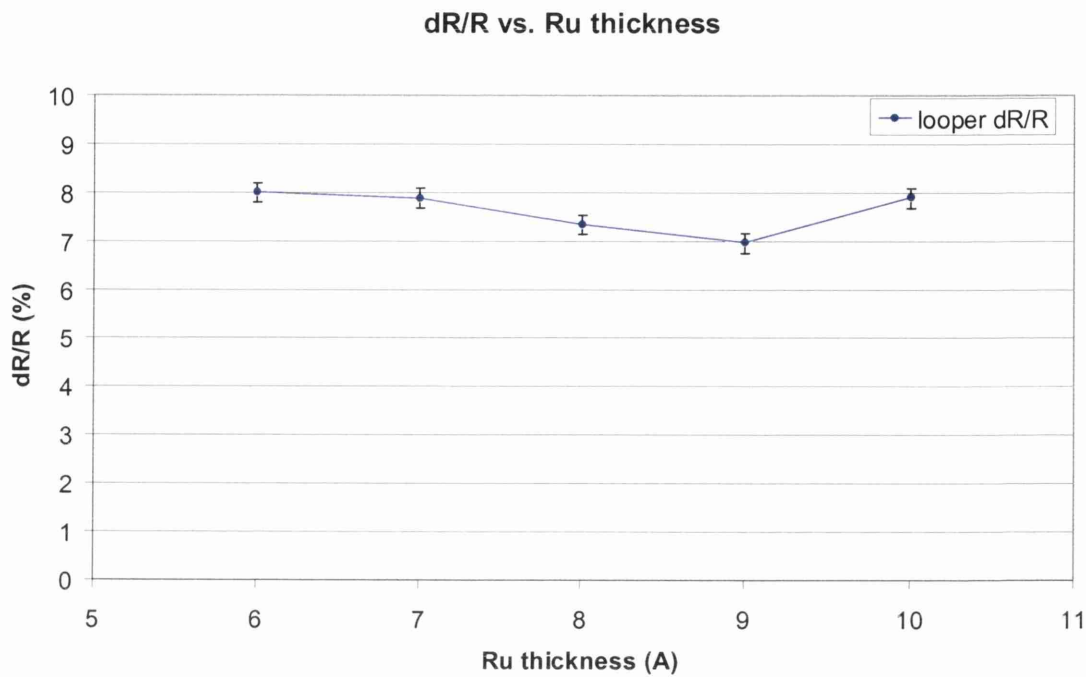


Figure 7.8 plot of  $dR/R$  vs. Ru layer thickness

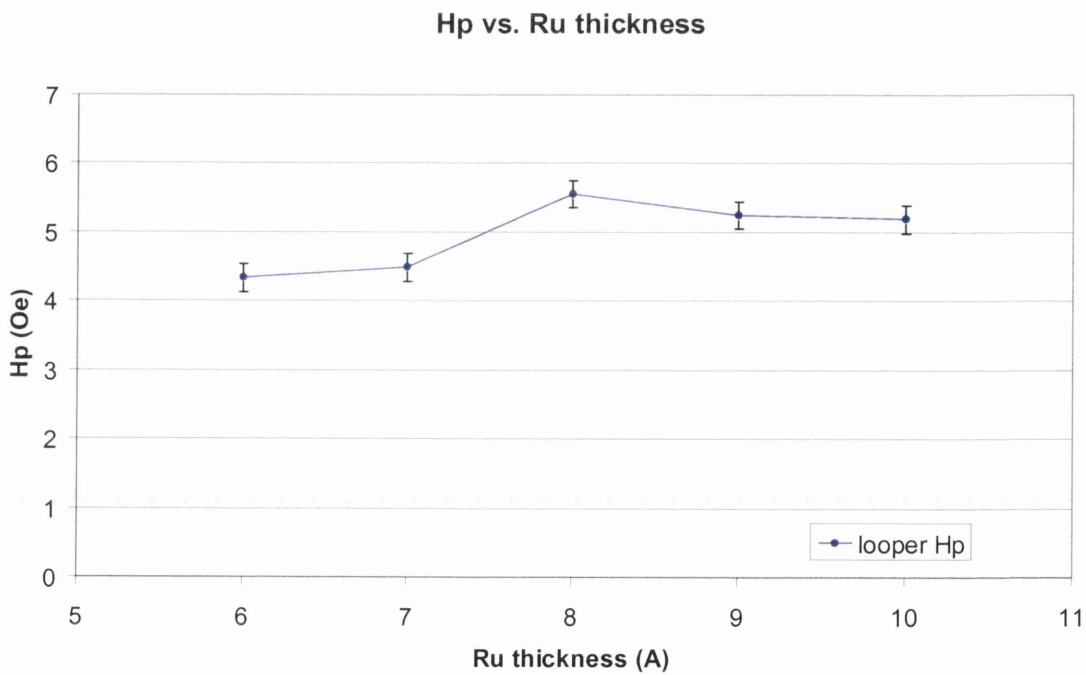


Figure 7.9 plot of  $H_p$  vs. Ru layer thickness

The high field pinning of a spin-valve can be quantified as  $H_{pin80}$ , as shown in figure 7.3. This is defined as the field at which the resistance has dropped to 80% of the saturation value, and is another important characteristic for a spin-valve. The higher this figure, the more stable the spin-valve stack. Figure 7.10 shows a plot of  $H_{pin80}$  versus Ru thickness, where it can be seen that the pinning drops dramatically from 1750 Oe at 6Å Ru, to 950 Oe at 7Å, then recovers and levels off at around 1400 Oe. This would indicate that changing to a thinner Ru layer of say 6Å could make improvements in stability of the SAF structure.

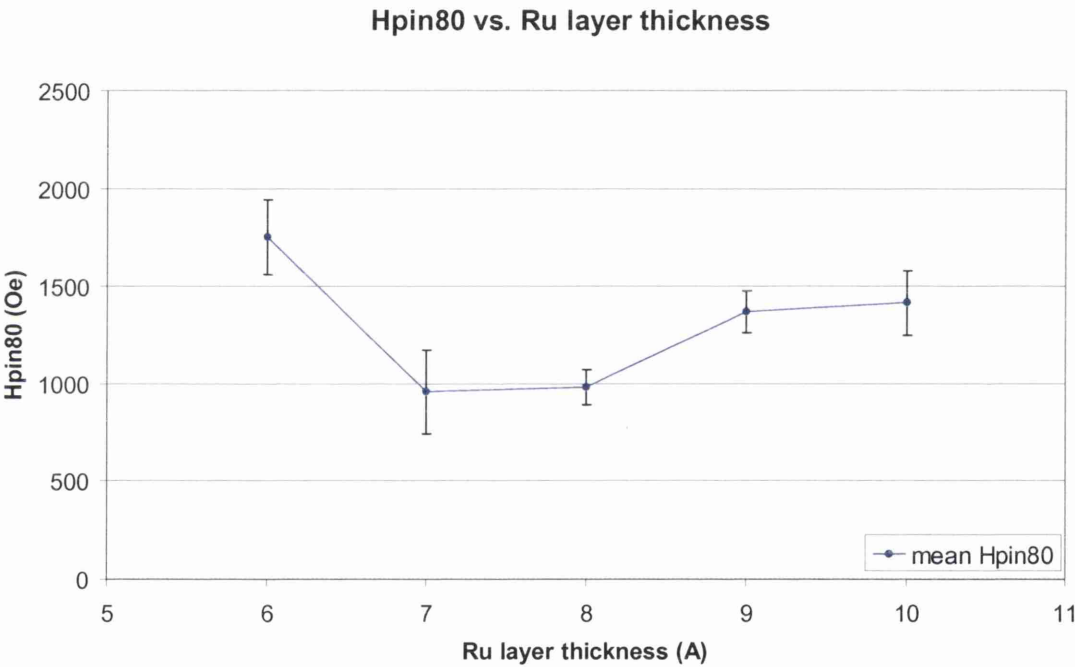


Figure 7.10  $H_{pin80}$  vs. Ru layer thickness

## 7.5 Variation of NiMn layer thickness

The antiferromagnetic material in a spin-valve, in this case NiMn, has the purpose of pinning the magnetisation of the pinned layer. Antiferromagnetic materials have a critical thickness  $t_c$ , above which they display stable antiferromagnetism. Layers of thicknesses below the  $t_c$  for a particular deposition process are not suitable for use in spin-valves.

In general, a thicker AF layer will produce a stronger pinning effect, however it is also desirable to reduce the thickness of the AF pinning layer, in order to maintain a total stack thickness thin enough to be accommodated within the shield to shield spacing of a complete head.

A set of spin-valve films was deposited with the same standard structure as above, with NiMn thicknesses of 150, 200, 250, 300, and 350Å; 250Å being the standard. Figure 7.11 is a plot of  $dR/R$  versus NiMn layer thickness, and this shows that  $dR/R$  remains fairly stable at around 8% over the range of thickness considered. Figure 7.12 is a plot of  $H_p$  versus NiMn layer thickness, and this also remains stable at close to 4Oe over the range. Figure 7.13 is a plot of  $H_{pin80}$  versus NiMn layer thickness. This shows that  $H_{pin80}$  changes little over the range of NiMn thickness, increasing slightly from 1370Oe at 150Å NiMn to 1415Oe at 200Å, then falling off to a value of 1310Oe by 350Å.

From this, it can be seen that a decrease in NiMn layer thickness to 150 or 200Å, lowering the overall stack thickness, would cause no loss in pinning stability, while maintaining a high  $dR/R$  performance and low exchange field.

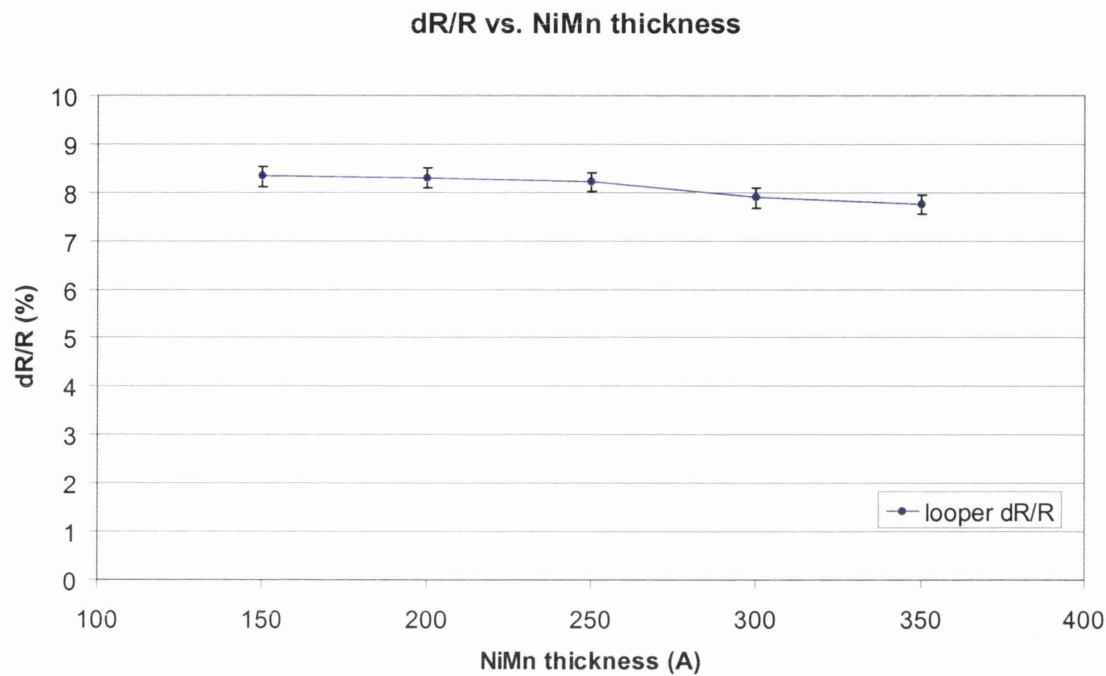


Figure 7.11 plot of  $dR/R$  vs. NiMn layer thickness

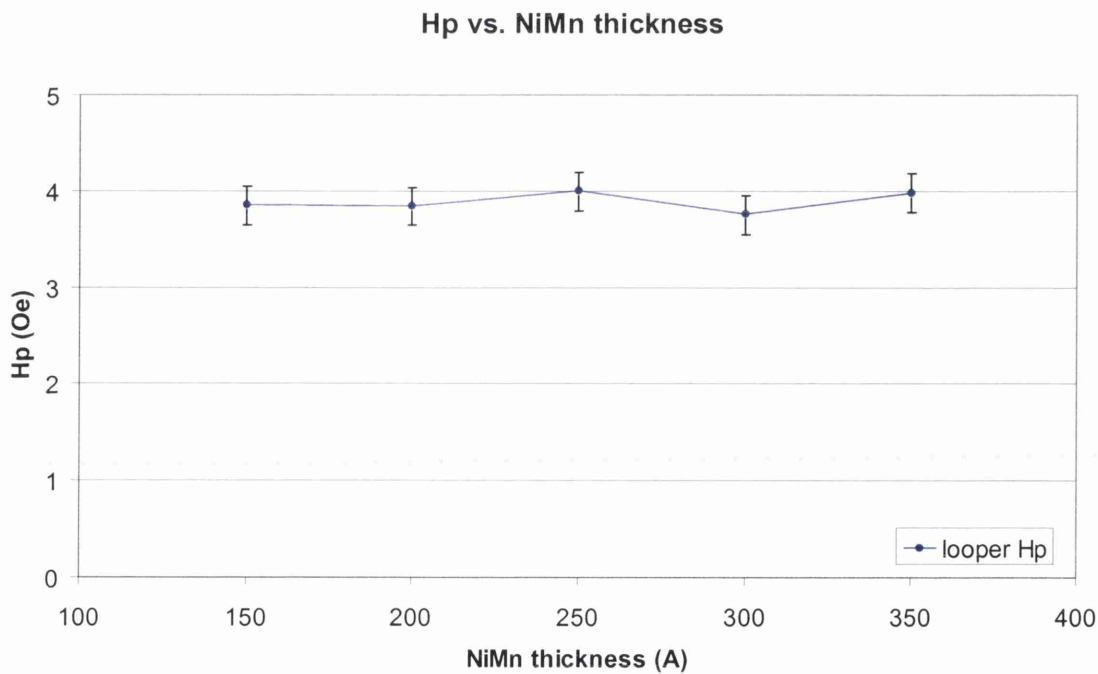
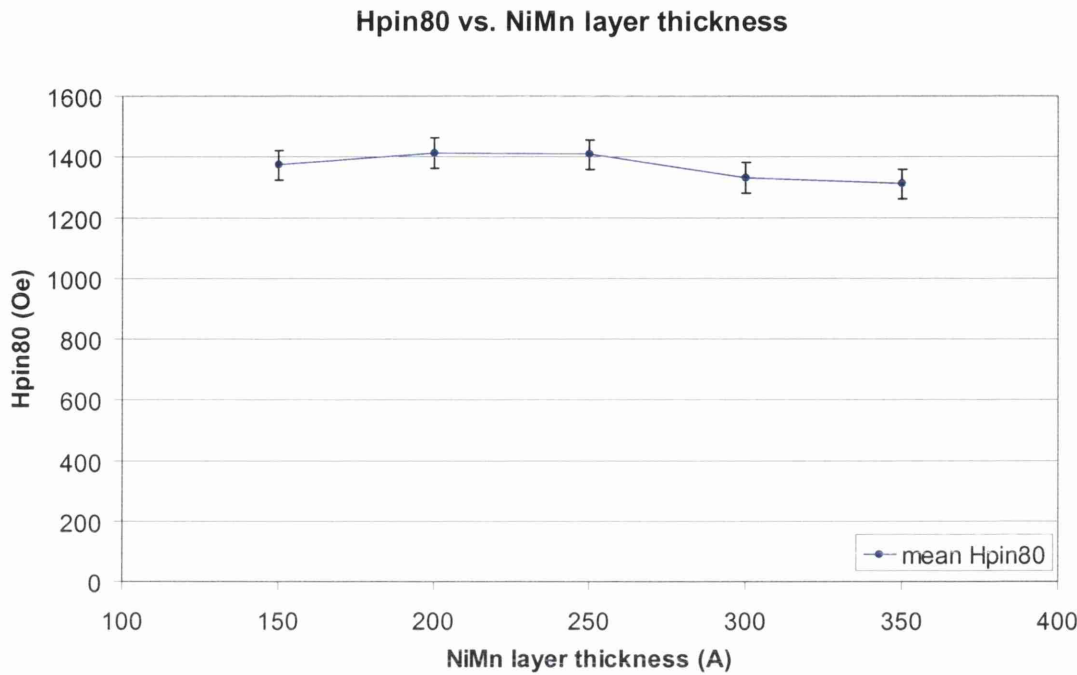


Figure 7.12 plot of  $H_p$  vs. NiMn layer thickness



*Figure7.13 plot of  $H_{pin80}$  vs. NiMn layer thickness*

**7.6 Analysis and comparisons**

The studies described in this Chapter demonstrate the importance of optimising the performance of a spin-valve structure by adjusting individual layer thicknesses within the stack. Other factors also influence the properties of a spin-valve stack, including the exact deposition parameters, as well as post-deposition processing such as annealing.

We have seen here that the seed layer adopted for a spin-valve stack has an important effect in controlling the crystal growth of the entire structure. This results in an increase in the dR/R of this stack for seed layer thicknesses of 35Å and above. There is no benefit therefore in changing from the 35Å layer in the standard stack, as a thinner layer would give a drop in dR/R output and give little improvement.

The Cu layer thickness of 27Å in the standard stack also appears to be close to optimum for this stack. Over the range of thicknesses considered, no overall improvement in  $dR/R$  and  $H_p$  could be seen.

Thinning the Ru layer thickness from 8Å in the standard stack to 6Å could give an improvement in high field pinning stability. However, this benefit could only be exploited if the deposition process was able to give smooth, uniform coverage of such a thin film.

Thinning the NiMn AF layer from 250Å in the standard stack to 200Å would enable the overall stack thickness to be reduced, while maintaining good  $dR/R$  performance. The high field pinning would also benefit slightly, without affecting the exchange field.

Overall, it can be seen that some improvements in this spin-valve stack are possible by changing the layers selected in this study. In order to optimise a spin-valve stack fully, however, each layer must be considered. As the properties of any one layer within a stack are altered, this can then have an effect on the interaction between the other layers. Finally, it is important to remember that any benefits demonstrated in a spin-valve at sheet film level must next be verified for device-sized patterned elements before an altered structure can be adopted into device builds.

## Chapter 8 Patterned Elements of Spin-valve Material

### 8.1 Introduction

Magnetic sensors within devices have considerably smaller dimensions than the continuous film specimens considered so far in this thesis. Indeed, sensors within devices have well-defined shapes, usually rectangular, and are patterned to dimensions in the sub-micron range.

The sensor element forms only a small part of the overall recording head, which is built at wafer level in plants such as Seagate Springtown. Thus the methods used for patterning the sensor in a device must be compatible with manufacturing equipment and large volume processes. These include ion milling etch processes to remove excess material during the wafer build, and lapping to grind back the edge of the head structure. These processes are different from those available within the University of Glasgow facilities, and indeed are not suitable for easy preparation of TEM specimens. Instead, electron-beam lithography and lift-off techniques as described in Chapter 3 are used to allow for relatively straightforward preparation of TEM specimens with an array of isolated spin-valve elements.

This Chapter investigates some of the properties of small patterned elements of spin-valve material produced by electron beam lithography (see Chapter 3). The spin-valve stack used in these experiments has the same composition as the standard spin-valve investigated in Chapter 7. This structure is shown in figure 8.1. The e-beam patterning was carried out in the department of Electrical and Electronic Engineering at the University of Glasgow, as described in Chapter 3. The films were then deposited at Seagate Springtown, and lift-off process was carried out prior to magnetic annealing to set the pinning of the AF material.

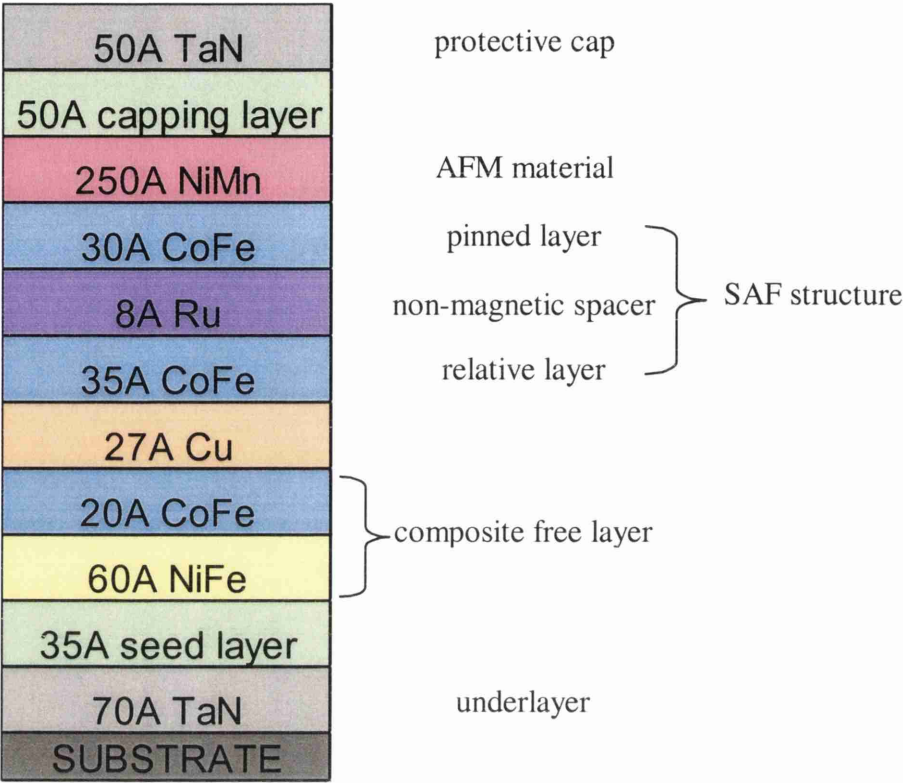


Figure 8.1 Standard spin-valve structure used for patterned elements

## 8.2 Pattern designs

Different pattern layouts were designed, in order to incorporate elements of varied sizes, shapes, and orientations relative to the pinning direction. These pattern designs were prepared for writing to the specimens as described in Chapter 3.

The patterns were designed such that each specimen when prepared contains a variety of different shapes and sizes of elements, at different orientations relative to the bias direction. Hence, one good specimen allows a range of different experiments to be carried out. Figure 8.2 shows a pattern of rectangular elements, which was designed by Dr. Katherine Kirk, used for some initial experiments in this study. Figure 8.3 shows an original pattern design, which incorporates elements with round, pointed and trapezoid end-shapes in addition to rectangular elements and larger blocks. Within each of these pattern designs used, only a small selection of the available elements has been considered in this study.

When designing patterns to be deposited with magnetic materials, it is important to remember that interactions between neighbouring elements can occur depending on their relative spacing. Stray fields emanate from a magnetic element to a distance similar to the element's width, and this can lead to coupling interactions between elements located closer together. For these experiments, effectively isolated elements were required, so the patterns were designed with spaces between elements of approximately 1.5x the element width.

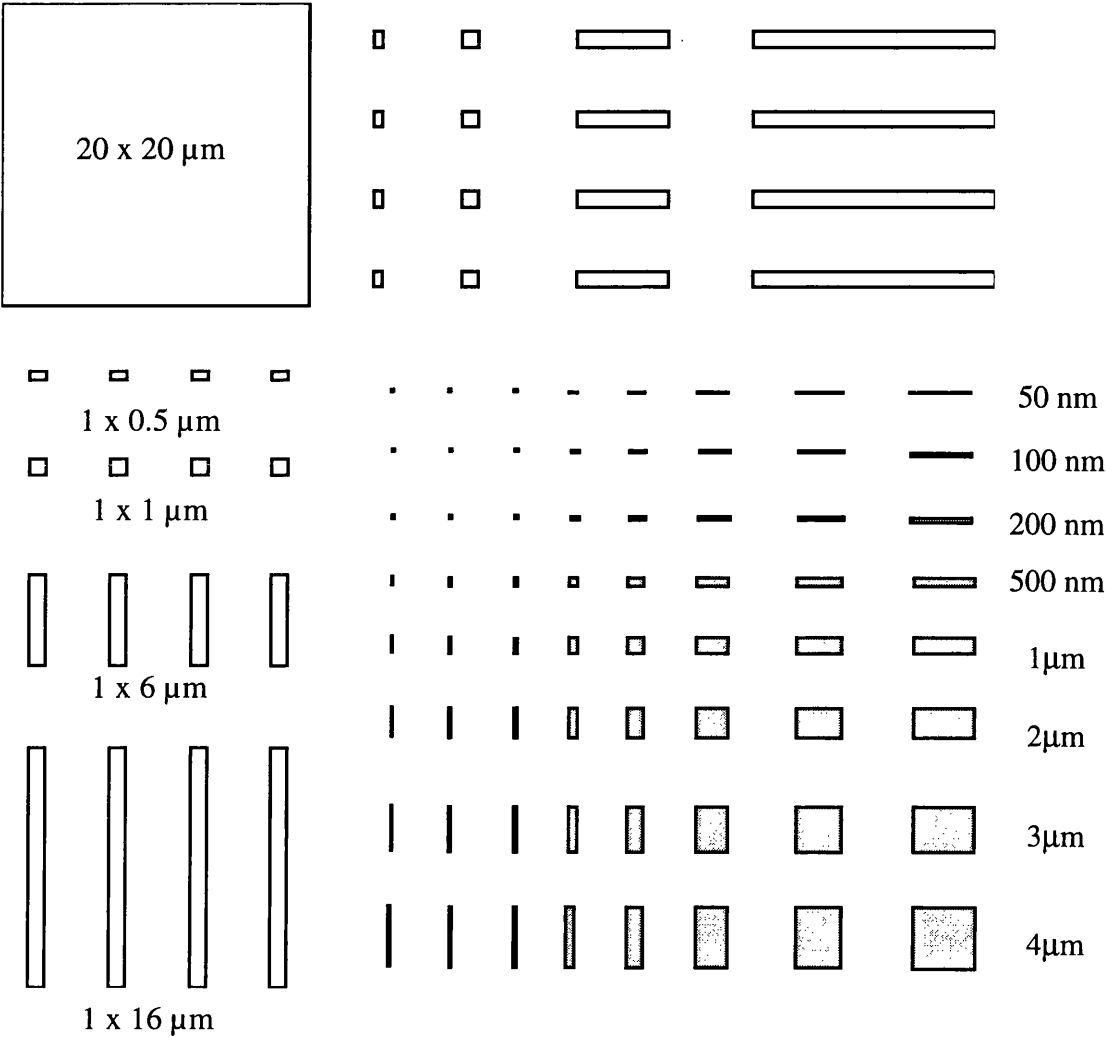


Figure 8.2 Standard rectangles pattern designed by Dr. K.J. Kirk

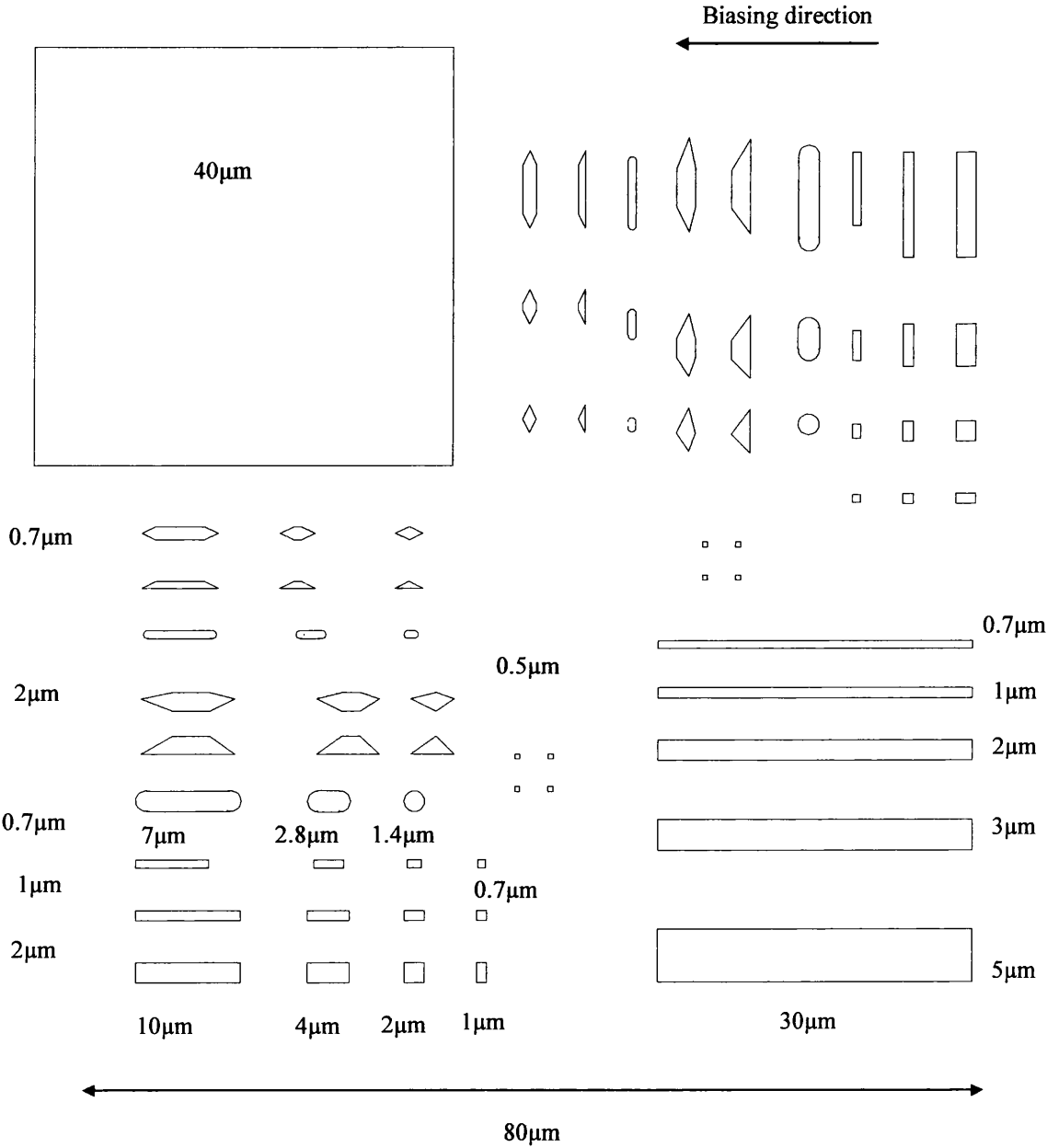


Figure 8.3 Pattern with varied end-shapes

8.3 Behaviour of small patterned elements of spin-valve material

The magnetic behaviour of an element of magnetic material is controlled to a large extent by the demagnetising fields associated with the element’s size, shape and aspect ratio. In the case of spin-valves, the orientation of the element relative to the biasing direction also has an effect on its behaviour in an applied field. Here a number of different elements of similar dimensions are investigated, having different aspect ratios, end shapes and orientations relative to the spin-valve biasing direction.

When a spin-valve containing a synthetic anti-ferromagnet (SAF) structure is patterned, the coupling between the two ferromagnetic layers within the SAF is set. Figure 8.4 illustrates how the pinned layer magnetisation follows that of the anti-ferromagnetic material at the interface between the two. The magnetisation in the relative layer is then coupled to the pinned layer across the non-magnetic spacer layer (often Ru) to form the SAF. It is convenient to consider the SAF as if it were a single pinned layer, so that the pinning direction  $H_p$  as discussed in the following investigations is actually the effective pinning experienced at the free layer of the spin-valve and not the true pinning direction at the pinned layer.

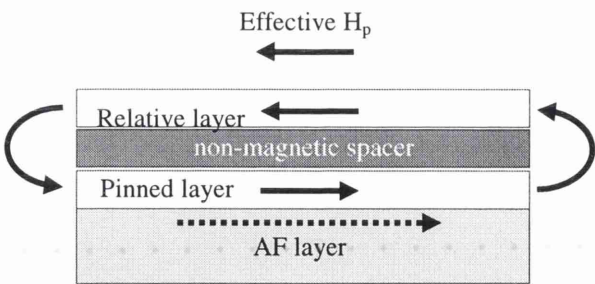


Figure 8.4 Magnetisation in the SAF structure of a patterned spin-valve element

### 8.3.1 Dependence on aspect ratio of rectangular elements

In this section, we consider rectangular elements of the same length  $4\mu\text{m}$ , with aspect ratios of 2:1 and 4:1 respectively. For each aspect ratio, there are elements oriented with the long axis both parallel and perpendicular to the biasing direction.

Here, differential phase contrast (DPC) imaging is adopted as Fresnel imaging cannot achieve sufficient resolution to investigate patterned elements in the micron to sub-micron range. DPC is an in-focus imaging technique, and so is far better suited to the study of small elements. In DPC imaging, the contrast in each image is sensitive to magnetic components along a single axis. In order to present a complete picture of the magnetisations within a specimen, a pair of images of orthogonal sensitivities is considered at each stage.

Interpreting DPC images, similarly as for Fresnel images, is somewhat subjective and relies on physical insight into the behaviour of magnetic thin films. With DPC however, observing the stray field contrast around patterned elements allows determination of magnetisation direction, not just the axis in which it lies. This means that magnetisation reversal can be detected even when no domain wall formation or motion is apparent. Indeed, the stray field contrast in a DPC image can often give more indication of the state of magnetisation than the domain contrast within the element.

Figure 8.5 shows a set of DPC images taken during a magnetisation reversal sequence of a  $2 \times 4\mu\text{m}^2$  rectangular spin-valve element where the long axis is perpendicular to the biasing direction of the spin-valve. The double-headed arrows in the first images of the sequence indicate the axis of magnetisation to which the contrast in each image is sensitive. Here, the left-hand column of images is sensitive to vertical components of magnetisation; the central column of images to horizontal components, and the right-hand column shows schematic representations of the magnetisation directions at selected stages in the reversal. The numbers in each row indicate the applied field value in Oe.

Thus, it can be seen that as the field is relaxed from negative values (parallel to the biasing direction), small domains begin to form at the long edges of the element. These edge domains increase in size, and the magnetisation direction in the central region rotates until at zero applied field (d) a near flux closure pattern of domains has formed. The shape anisotropy at this point has overcome the coupling between the relative layer and the free layer, as only a small portion of the element has its magnetisation aligned with the pinning direction. From this point, as the applied field increases in the opposite direction to the spin-valve biasing, the domain at the right hand side of the element grows in size while the magnetisation within this domain rotates clockwise to align with the applied field. Fig 8.5f) shows the point at which the reversal is nearing completion with only a modest variation in magnetisation direction, most pronounced towards the top of the element. Increasing the applied field further reduces the dispersion in magnetisation direction, thus reducing the contrast which can be seen at (g) where the magnetisation is constant across the element. The stray fields, seen on the images as bright and dark regions outside the element, can be seen to have reversed in black-white contrast.

Reducing the applied field from this maximum value, the contrast is seen to increase as more dispersion develops in the magnetisation direction. Edge domains begin to form and grow until at zero applied field (i) there is again a near flux-closure domain structure similar to that seen in the first half of the cycle. As the field is increased in the negative direction (parallel to the biasing direction), the domain with magnetisation parallel to the biasing direction is seen to grow as the magnetisation directions in the other domains rotate towards the biasing direction. Finally at the maximum applied field parallel to the biasing direction (l), the contrast is greatly reduced as the magnetisation direction across the element is constant and aligned with the applied field. Again the stray field contrast confirms that the element has returned to the original magnetisation direction.

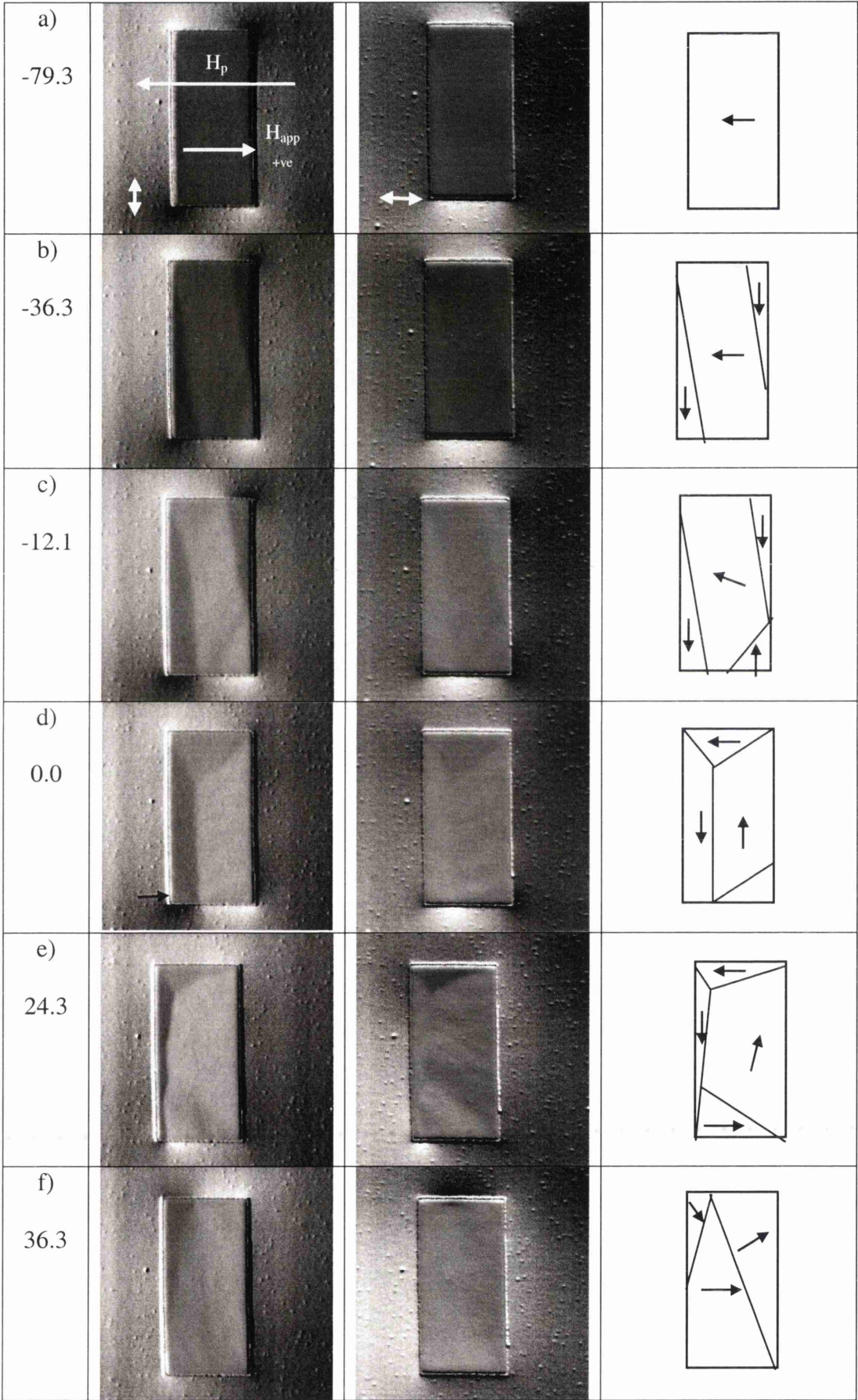


Figure 8.5 Magnetisation reversal of  $2 \times 4 \mu\text{m}^2$  rectangular spin-valve element

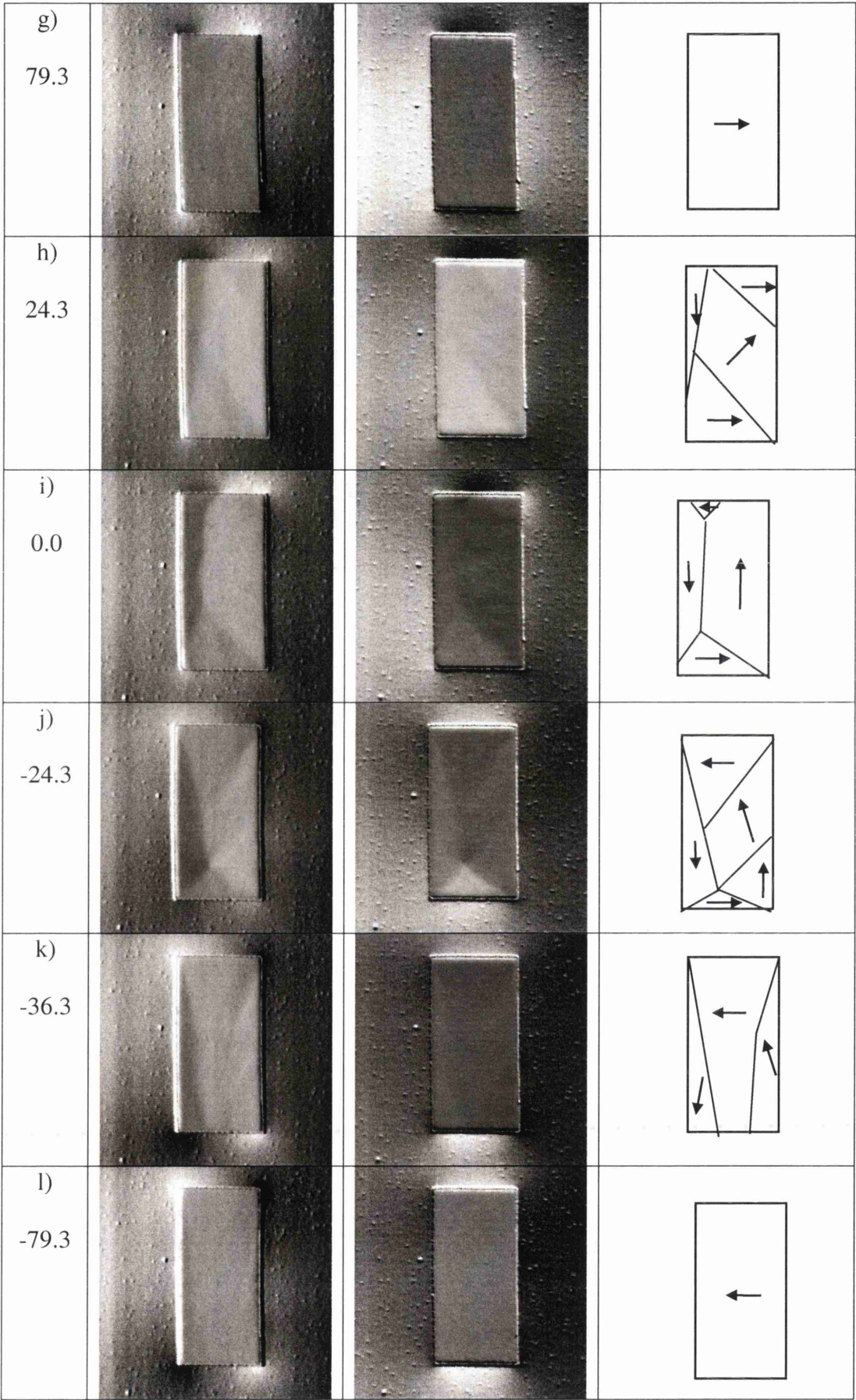


Figure 8.5 cont'd –  $2 \times 4 \mu\text{m}^2$  rectangular spin-valve element

Figure 8.6 shows a set of DPC images taken during the magnetisation reversal of a rectangular element of the same dimensions as above,  $4 \times 2 \mu\text{m}^2$ , but this time oriented with its long axis parallel to the biasing direction of the spin-valve. As the field is relaxed from parallel to the biasing direction, a slight increase in contrast indicates an increase in dispersion. Apart from the formation of small end-domains, the magnetisation within the element remains largely aligned with the biasing direction even at zero applied field (c). The shape anisotropy here supports the spin-valve biasing of the free-layer magnetisation. As the applied field is increased in the positive direction, that is opposite to the pinning direction, a complex domain structure is formed (d) as the magnetisation in different regions of the element rotates in different directions towards the applied field. This complex structure is not stable, as quickly the magnetisation across the majority of the element switches to align with the applied field as seen in (e). Two small vortex regions are seen to remain at the edges of the element where the local magnetisation rotates about a single point. Increasing the applied field further removes these vortices and the contrast decreases until at the maximum applied field (g) the magnetisation across the element is constant. Reducing the applied field from this maximum value, there is little increase in dispersion across the element, only the formation of small end domains seen in (i) at zero applied field.

The element then undergoes a rapid switching of magnetisation direction to align with the biasing direction, as by the next image (j) at  $-12.1\text{Oe}$ , the stray fields can be seen to have reversed polarity. A small vortex remains at the bottom-left corner of the element, and a small end domain at the bottom-right corner. Increasing the applied field in this negative direction, parallel to the pinning direction, removes this contrast until the magnetisation in the element is again single-domain and essentially fully aligned with the spin-valve biasing (l).

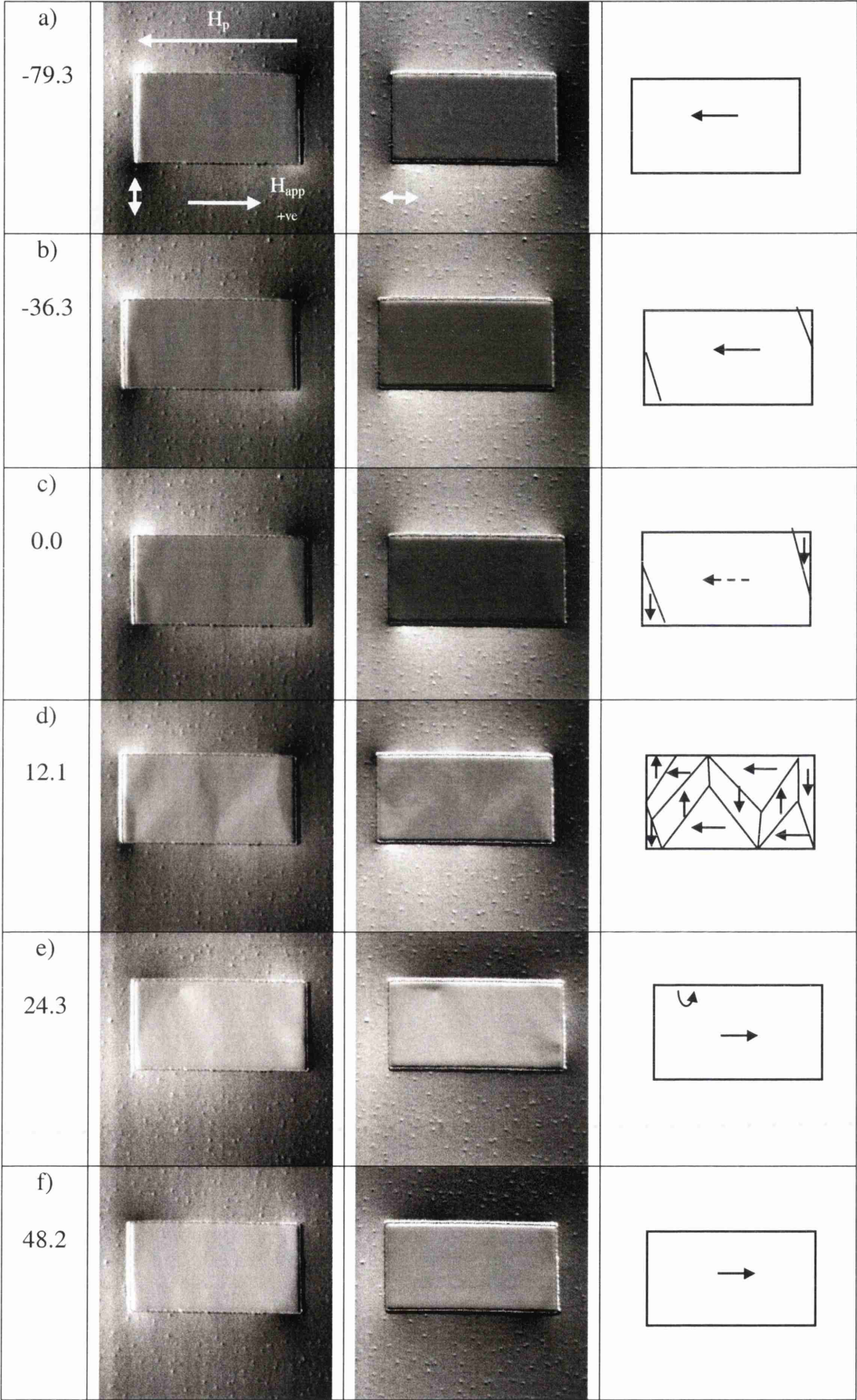


Figure 8.6 Magnetisation reversal of  $4 \times 2 \mu\text{m}^2$  rectangular spin-valve element

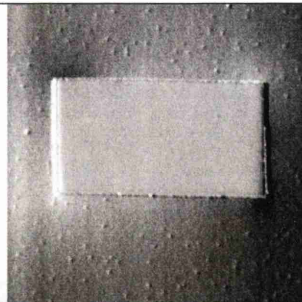
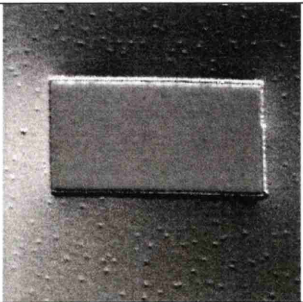
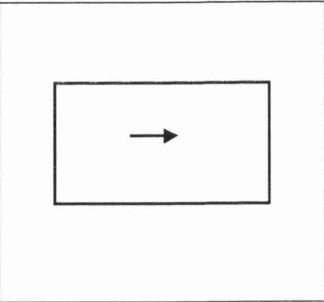
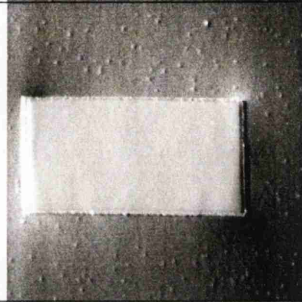
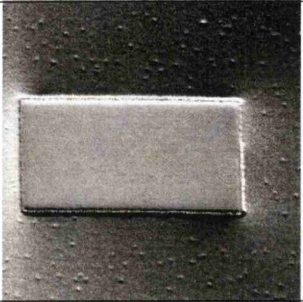
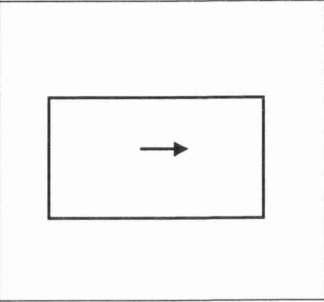
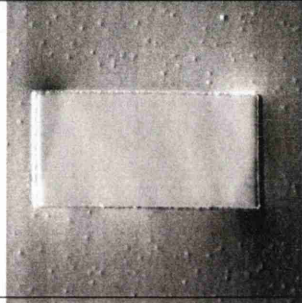
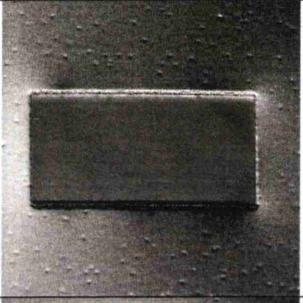
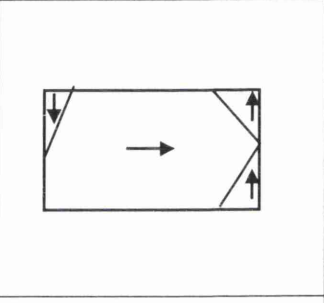
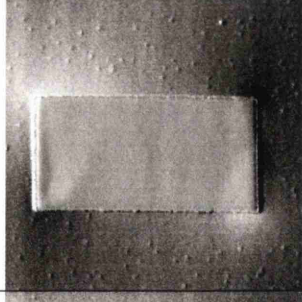
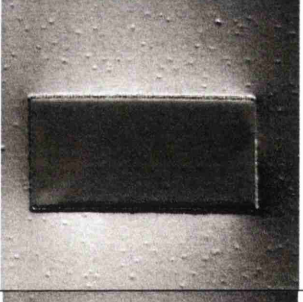
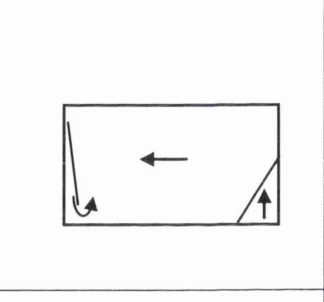
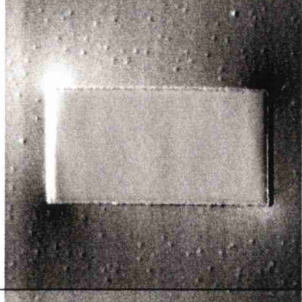
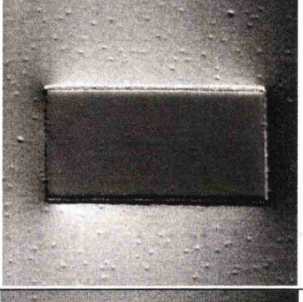
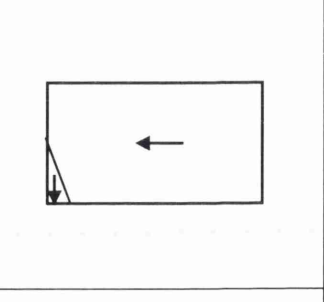
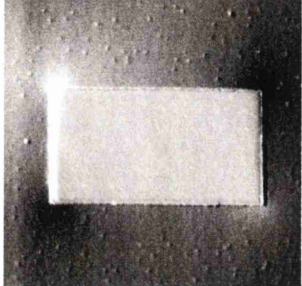
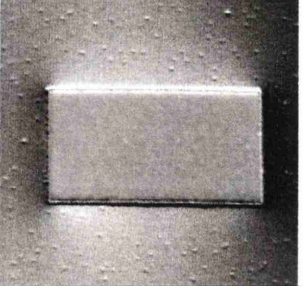
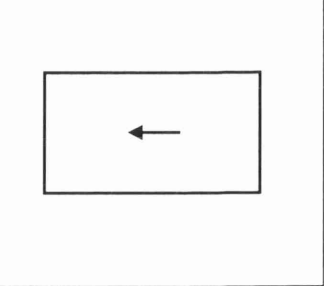
g) 79.3			
h) 48.2			
i) 0.0			
j) -12.1			
k) -48.2			
l) -79.3			

Figure 8.6 cont'd –  $4 \times 2 \mu\text{m}^2$  rectangular spin-valve element

We now consider the reversal of rectangular elements with a higher aspect ratio. Figure 8.7 shows a set of DPC images from the reversal of a  $1 \times 4 \mu\text{m}^2$  rectangular spin-valve element whose long axis is perpendicular to the pinning direction of the spin-valve. As the field is relaxed from parallel to the pinning direction, elongated domains form along the long edges of the element, with magnetisation direction aligned with the length of the element (b). By zero applied field (c) the edge domains have merged leaving the magnetisation in most of the element directed along its length, with a vortex at the bottom of the element. Increasing the applied field opposite to the pinning direction increases the dispersion within the element, and an end domain is seen to form at the top of the element (d) while the vortex remains. The end domain and the vortex remain while the majority magnetisation direction rotates towards the applied field (e) until the element becomes single domain with constant magnetisation aligned with the applied field (f). On relaxing the applied field from this maximum value, elongated edge domains quickly begin to form (g). Reducing the applied field towards zero, this edge domain continues to grow, as the magnetisation in the rest of the element begins to rotate. As the applied field is increased in the negative direction, parallel to the spin-valve pinning, a flux-closure structure is seen to form at the top end of the element (j). On continuing to increase the field in this direction, the left-hand edge domain quickly recedes and a vortex forms at the top-left corner of the element as the magnetisation in the majority of the element rotates towards the pinning direction (k). This rotation continues until the element becomes single domain with constant magnetisation parallel to the pinning direction.

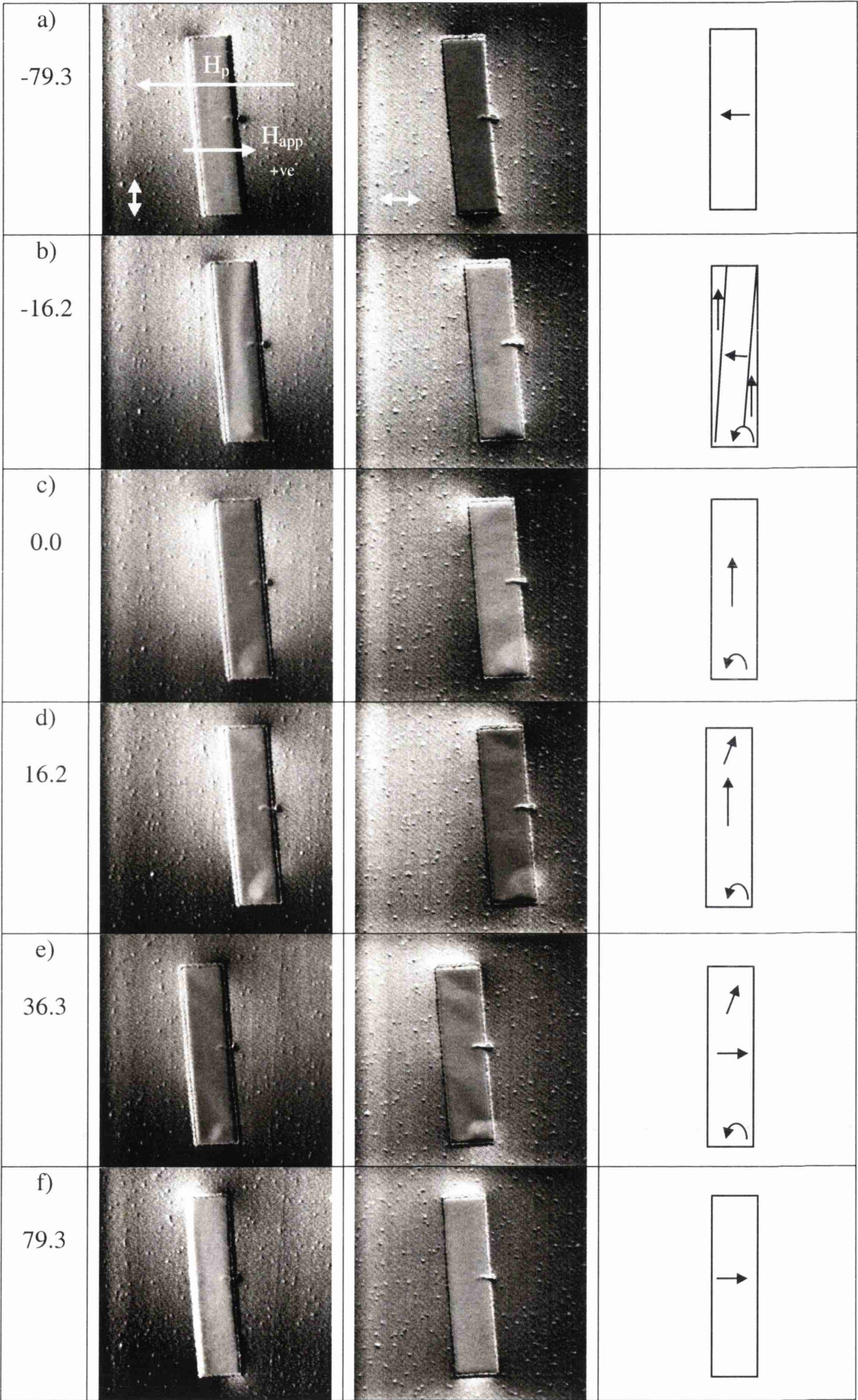


Figure 8.7 Magnetisation reversal of  $1 \times 4 \mu\text{m}^2$  rectangular spin-valve element

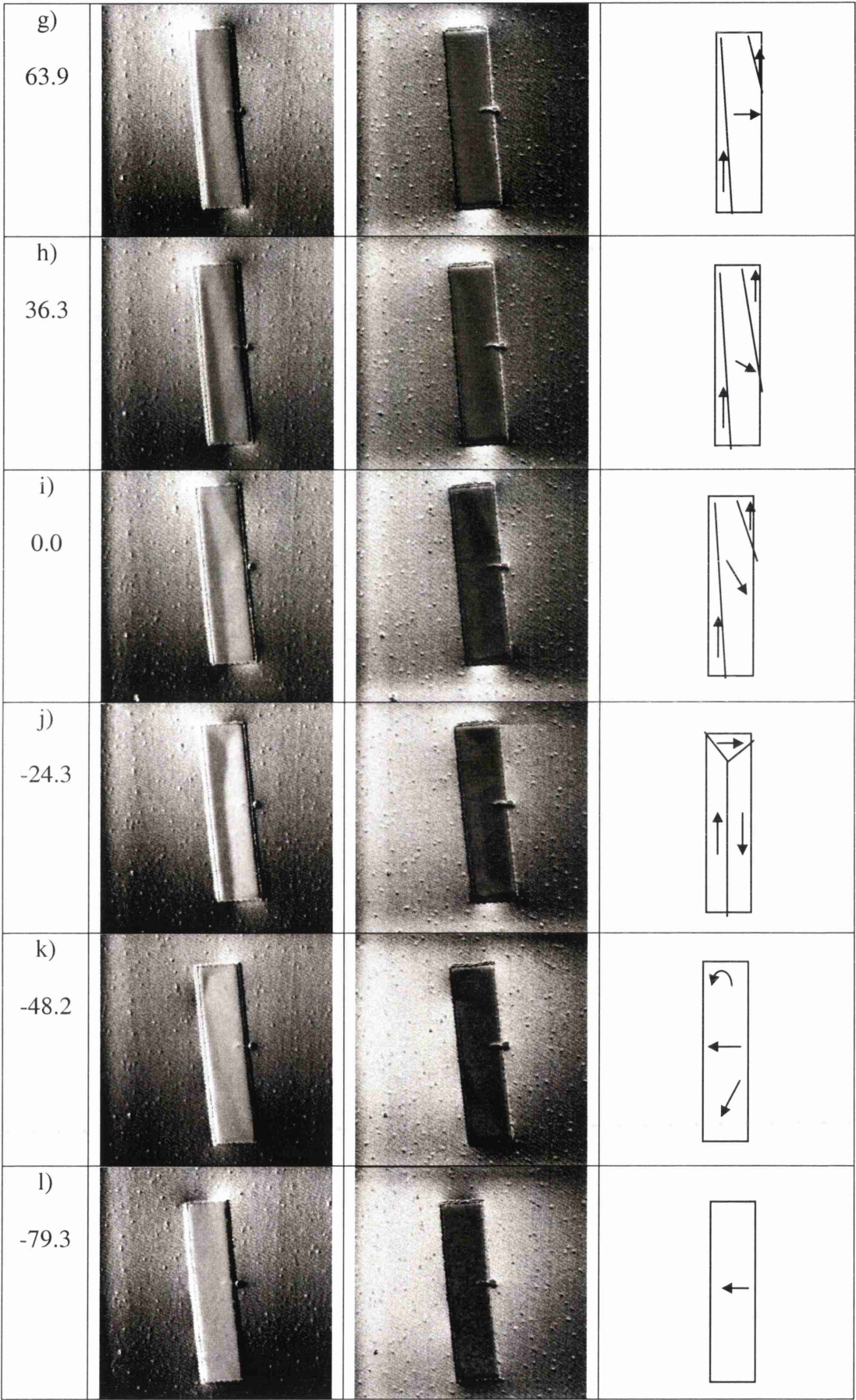


Figure 8.7 cont'd –  $1 \times 4 \mu\text{m}^2$  rectangular spin-valve element

Figure 8.8 shows a set of DPC images from the reversal of a  $4 \times 1 \mu\text{m}^2$  rectangular spin-valve element with the long axis parallel to the pinning direction. As the applied field is relaxed from parallel to the pinning direction, there is a gradual increase in the dispersion of the magnetisation direction until at zero applied field (c) small end domains begin to form. On increasing the applied field in the opposite direction, the dispersion increases further before the magnetisation direction undergoes a rapid switching between 8 Oe (d) and 16 Oe (e), leaving a small vortex in the lower left-hand corner of the element. This vortex remains as the field is increased (f), until the magnetisation fully aligns with the applied field (g). As the field is relaxed from this maximum value towards zero field, there is again an increase in dispersion within the element, and the formation of small end domains (i). The dispersion continues to increase (j) as the applied field is increased in the negative direction. The element's magnetisation direction then switches at between -24 Oe (j) and -36 Oe (k), leaving a domain wall structure at the left-hand end of the element. This structure remains as the field is increased further (l), and does not disappear until a much larger field (-150 Oe) is applied.

We see from this that the difference in reversal mechanism with orientation of these rectangular spin-valve elements is more pronounced for the elements with the higher aspect ratio. The reversal of both of the  $2 \times 4 \mu\text{m}^2$  elements tended to be smooth, with some domain formation. The element with its long axis perpendicular to the pinning direction formed a flux closure structure at zero applied field, as the easy axis of the free-layer was coincident with the length of the element. For the narrower elements, the difference in reversal mechanism between the two orientations was even more pronounced. The  $1 \times 4 \mu\text{m}^2$  element with long axis perpendicular to the pinning direction formed a flux closure structure, similar to that seen in the wider element, remaining over a range of field. The  $4 \times 1 \mu\text{m}^2$  element reversal occurred by an increase in dispersion before a rapid switching in magnetisation direction, instead of the formation of the complex domain structure seen in the wider element. This is due to the shape anisotropy in the narrower element increasing the tendency for the magnetisation to lie parallel to the length of the element.

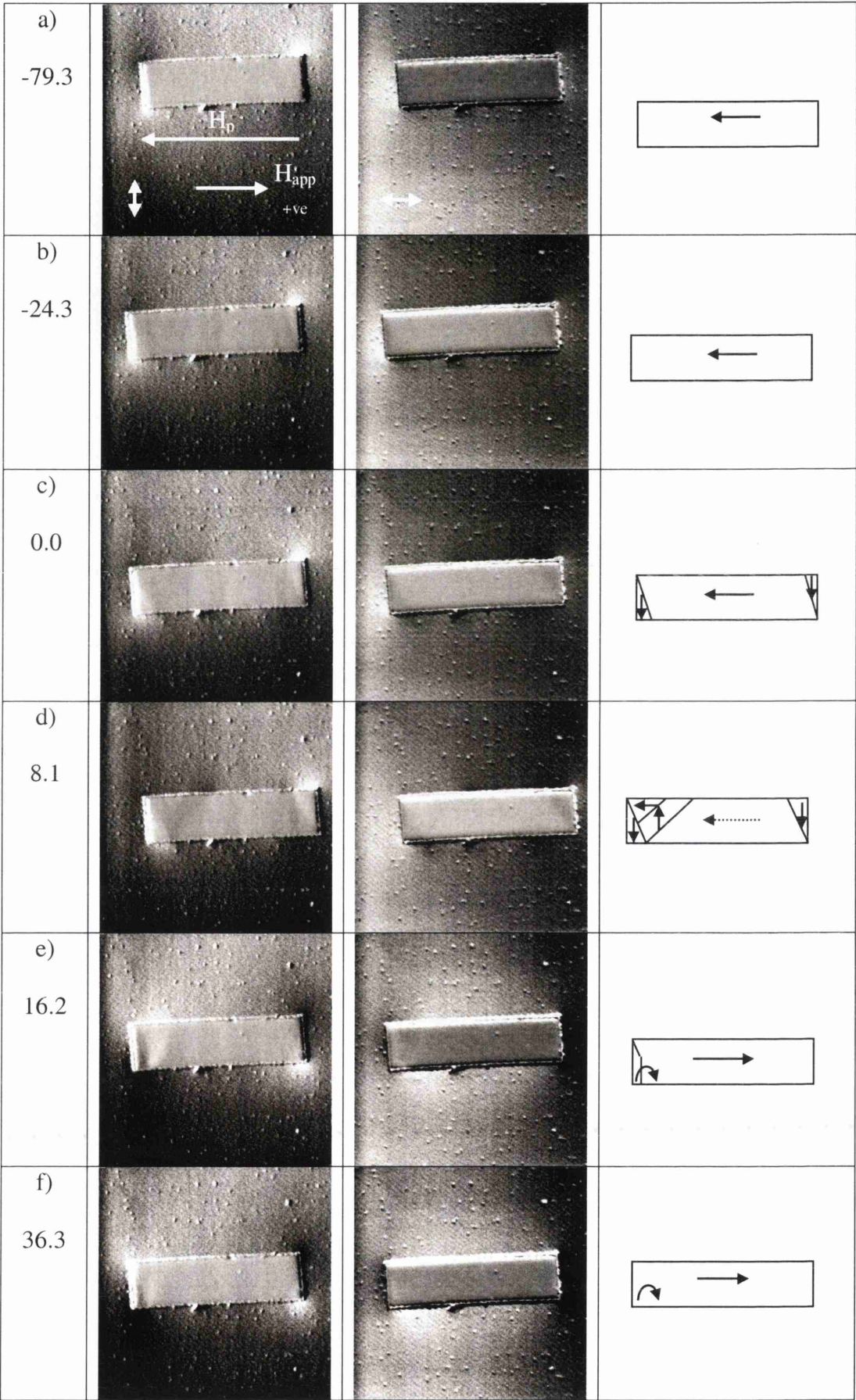


Figure 8.8 Magnetisation reversal of  $4 \times 1 \mu\text{m}^2$  rectangular spin-valve element

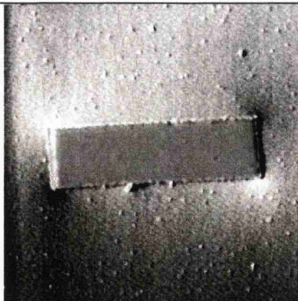
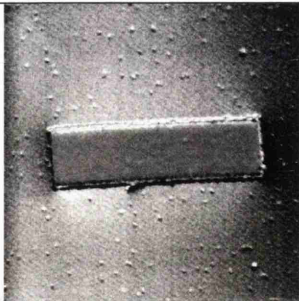
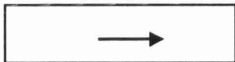
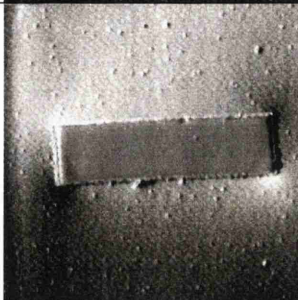
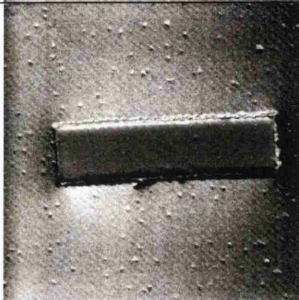
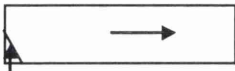
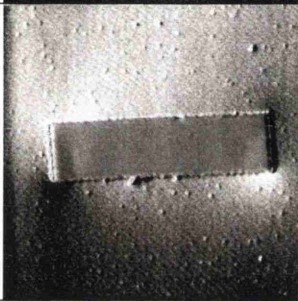
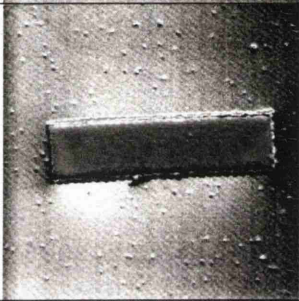
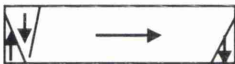
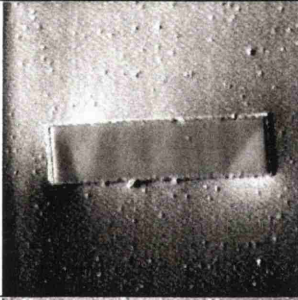
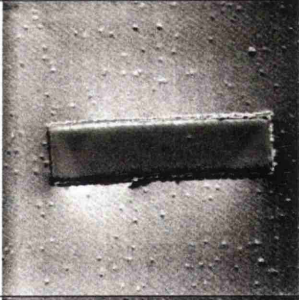
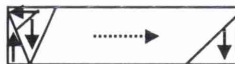
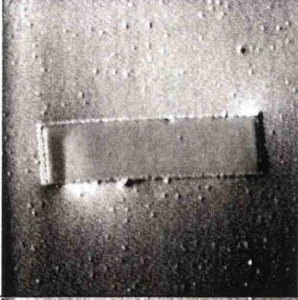
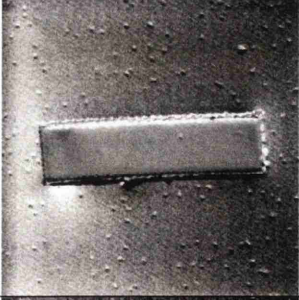

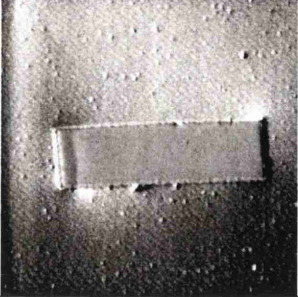
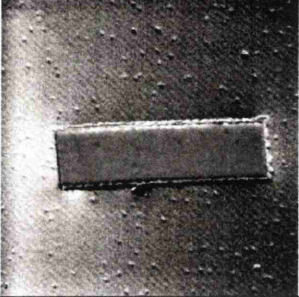
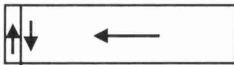
g) 79.3			
h) 36.3			
i) 0.0			
j) -24.3			
k) -36.3			
l) -79.3			

Figure 8.8 cont'd –  $4 \times 1 \mu\text{m}^2$  rectangular spin-valve element

### 8.3.2 Dependence on element end shape

In this section, a number of elements having different end shapes are considered. The elements selected all have similar dimensions and aspect ratios, with rounded ends, pointed ends and trapezoidal shapes respectively. Elements of each shape considered are oriented both parallel and perpendicular to the spin-valve biasing direction.

Figure 8.9 shows a set of DPC images taken during the free-layer reversal of a  $2 \times 4 \mu\text{m}^2$  rounded end spin-valve element whose long axis is perpendicular to the spin-valve biasing direction. As the applied field is relaxed from parallel to the pinning direction, there is a slight increase in dispersion and an elongated domain begins to form at the left-hand edge of the element (b). Another domain forms from the right-hand edge as the applied field is reduced to zero (c). On increasing the field in the opposite direction, the left-hand edge domain recedes so that the element is split into two domains with magnetisations aligned along the long axis of the element (d). The magnetisation on each side of the element rotates as the field is increased further, until the element becomes single-domain with magnetisation aligned with the applied field (f). Reducing the field from this maximum value, the dispersion increases and again domains begin to form at each long edge (g). This process continues as the applied field is reduced further towards zero field (i). On increasing the field in the negative direction, that is parallel to the pinning direction, a flux closure structure is formed near the top of the element as the magnetisation directions within the element form a loop (j). This vortex quickly moves to the top edge of the element and disappears as the field is further increased, until the element reaches a single-domain state with magnetisation aligned with the pinning direction (l).

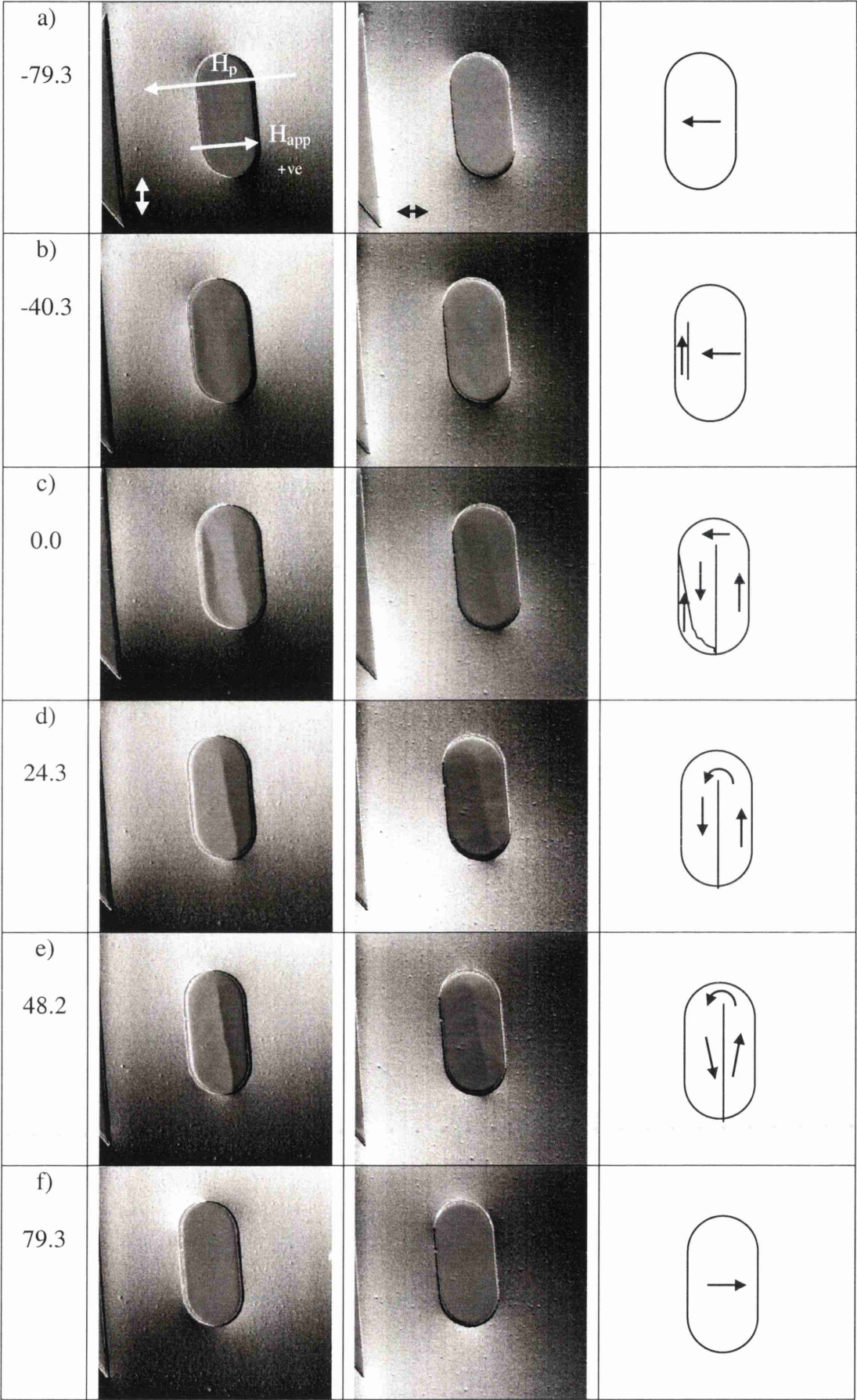


Figure 8.9 Magnetisation reversal of  $2 \times 4 \mu\text{m}^2$  rounded end spin-valve element

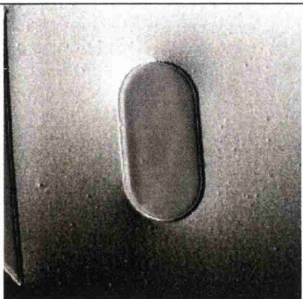
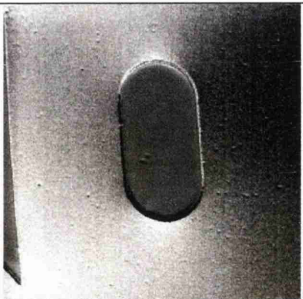
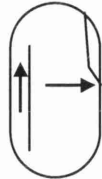
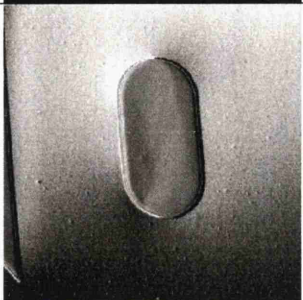
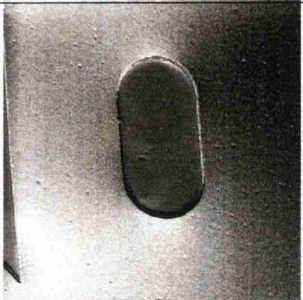
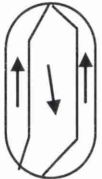
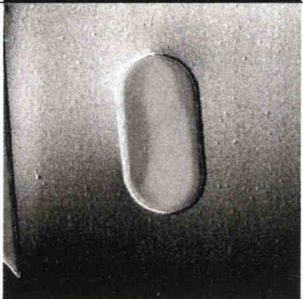
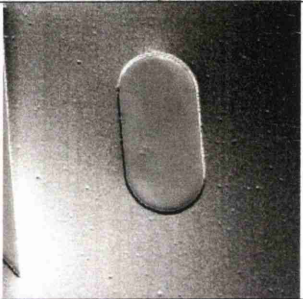
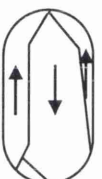
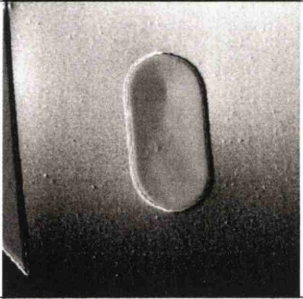
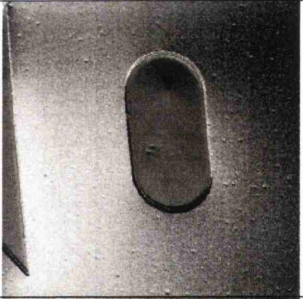
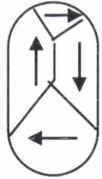
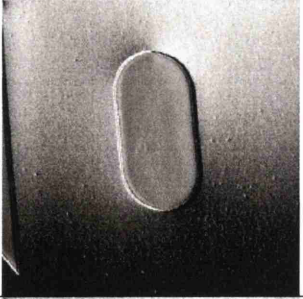
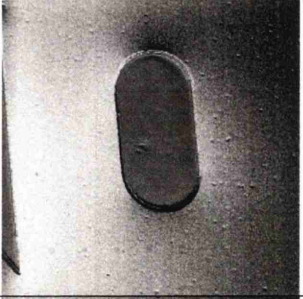
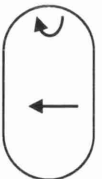
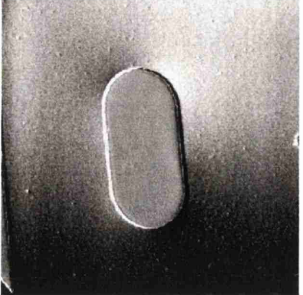
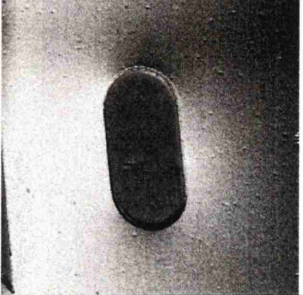
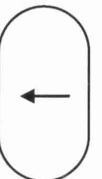
g) 40.3			
h) 24.3			
i) 0.0			
j) -24.3			
k) -48.2			
l) -79.3			

Figure 8.9 cont'd –  $2 \times 4 \mu\text{m}^2$  rounded end spin-valve element

Figure 8.10 shows a set of DPC images from the reversal of a  $4 \times 2 \mu\text{m}^2$  rounded end spin-valve element whose long axis is parallel to the pinning direction. As the applied field is relaxed from parallel to the pinning direction, there is an increase in the dispersion within the element, and end domains begin to form (b). A complex domain structure is formed as the applied field is reduced to zero (c). When the applied field is increased in the opposite direction, some of the domains grow as their magnetisation rotates towards the applied field, while the other domains recede (d). This rotation continues until the magnetisation in the majority of the element aligns with the applied field, leaving a small vortex in the bottom-left of the element (e). This vortex disappears as the field is increased further until the magnetisation across the element is constant and aligned with the applied field (f). Relaxing the applied field from this maximum value, the dispersion in the element begins to increase and again small end domains are formed (h). Another multi-domain structure has formed upon reaching zero applied field (i), with a vortex in the left-hand part of the element, and end domains forming from the right-hand side. When the applied field is once again increased in the negative direction, that is parallel to the pinning direction, the domains at the right-hand side of the element merge as the magnetisation rotates to align with the pinning direction, while the vortex at the left of the element remains (j). As the applied field is increased further in this direction, the vortex moves to the edge and disappears leaving the element single-domain and the magnetisation aligned with the biasing direction.

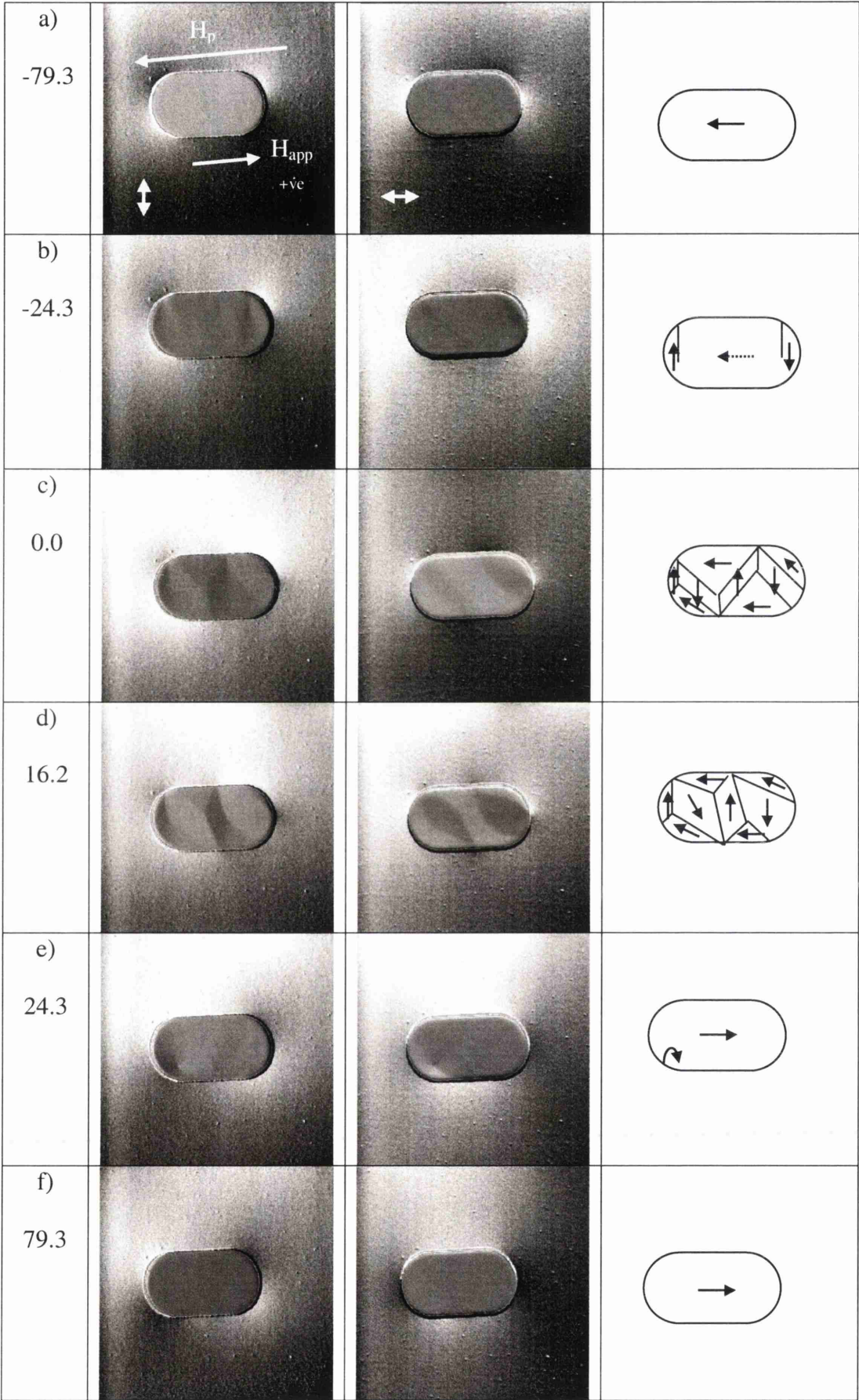


Figure 8.10 Magnetisation reversal of  $4 \times 2 \mu\text{m}^2$  rounded end spin-valve element

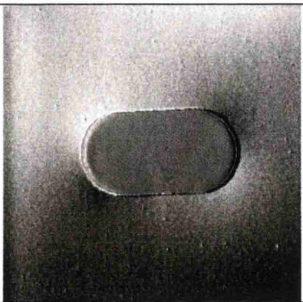

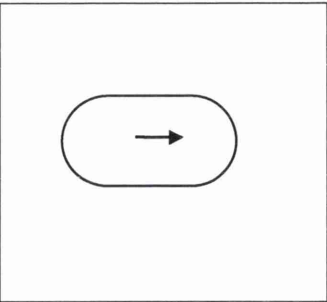
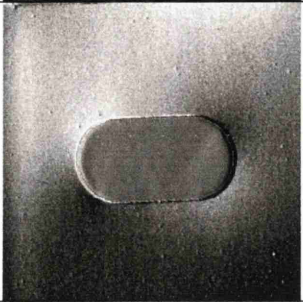
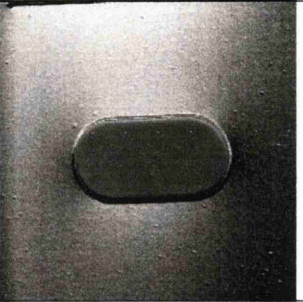
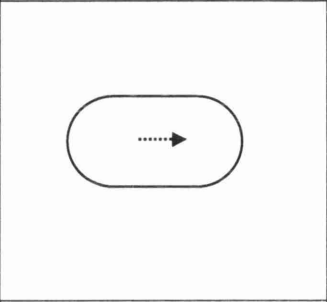
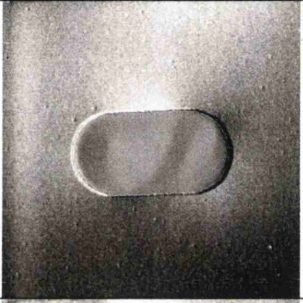
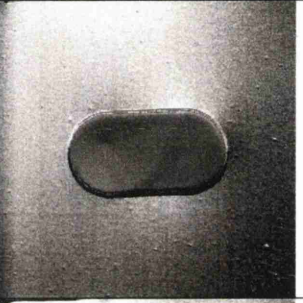
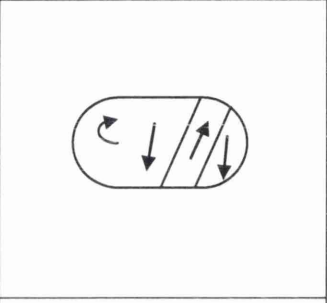
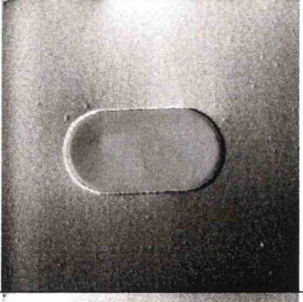
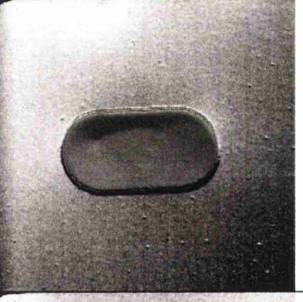
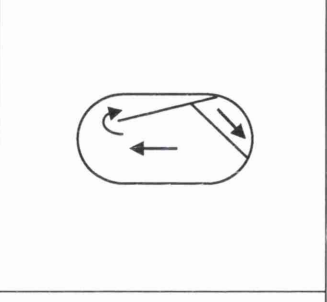
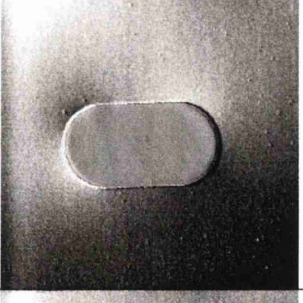
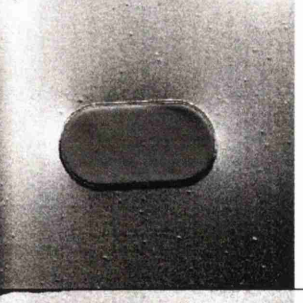
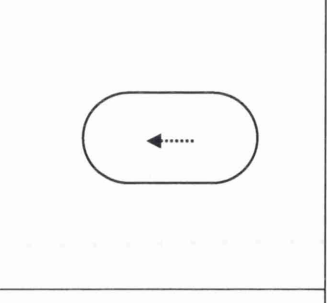

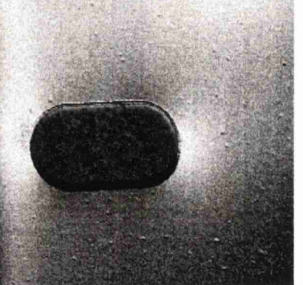
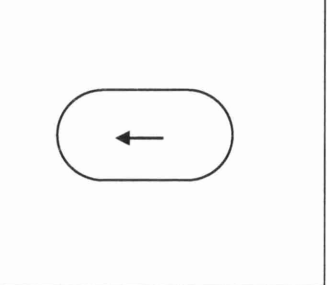
g) 40.3			
h) 16.2			
i) 0.0			
j) -16.2			
k) -36.3			
l) -79.3			

Figure 8.10 cont'd –  $4 \times 2 \mu\text{m}^2$  rounded end spin-valve element

Figure 8.11 shows a set of DPC images from the reversal of a  $2 \times 6 \mu\text{m}^2$  pointed end spin-valve element with the long axis oriented perpendicular to the pinning direction of the spin-valve. As the applied field is relaxed from parallel to the pinning direction, edge domains with magnetisation aligned with the long axis quickly begin to form (b). These domains grow inwards from either edge as the magnetisation in the central region rotates to align in the opposite direction, possibly forming a small vortex at the bottom tip of the element (c). This vortex is removed and the edge domains merge as the applied field is reduced to zero (d). At this point the magnetisation across the element is fairly well-aligned along its axis, which is coincident with the free layer easy axis, with some ripple present. Increasing the applied field in the opposite direction causes the magnetisation across the majority of the element to rotate clockwise towards the applied field while end domains form at the tips with magnetisation parallel to the edges (e). As the applied field is further increased, the magnetisation across the element continues to rotate to align with the field, while the end domains recede and all but disappear (f). Reducing the applied field from this maximum value, the end domains begin to grow again, as the dispersion increases and the magnetisation in the centre of the element rotates away from the field direction (g). As the applied field is reduced to zero, the dispersion is seen to decrease as the magnetisation rotates to align along the axis of the element (i). Increasing the field in the negative direction causes the dispersion to increase and end domains to form as the magnetisation in the centre of the element rotates away from the easy axis of the free layer and towards the pinning direction (j). The end domains recede as the magnetisation in the majority of the element aligns with the pinning direction until a single-domain state is reached (l).

In some of these images, neighbouring elements can be seen at the edges. As described in section 8.2, the patterns were designed such that the elements were no closer together than  $1.5 \times$  their width. The assumption was made that this should effectively isolate each element from its neighbours. There was no observed correlation of magnetisation between neighbouring elements during these experiments, so this assumption appears to hold true.

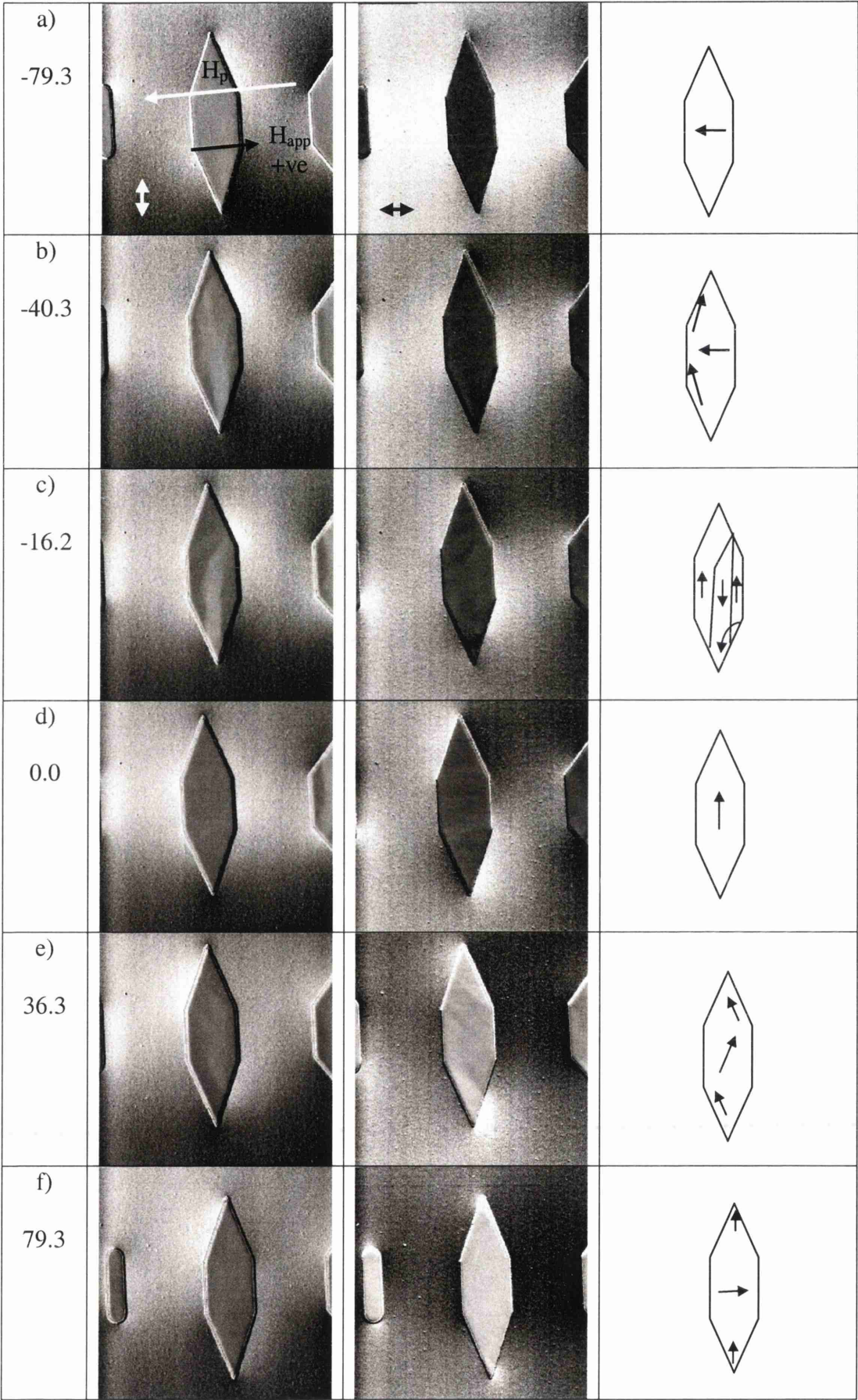


Figure 8.11 Magnetisation reversal of  $2 \times 6 \mu\text{m}^2$  pointed end spin-valve element

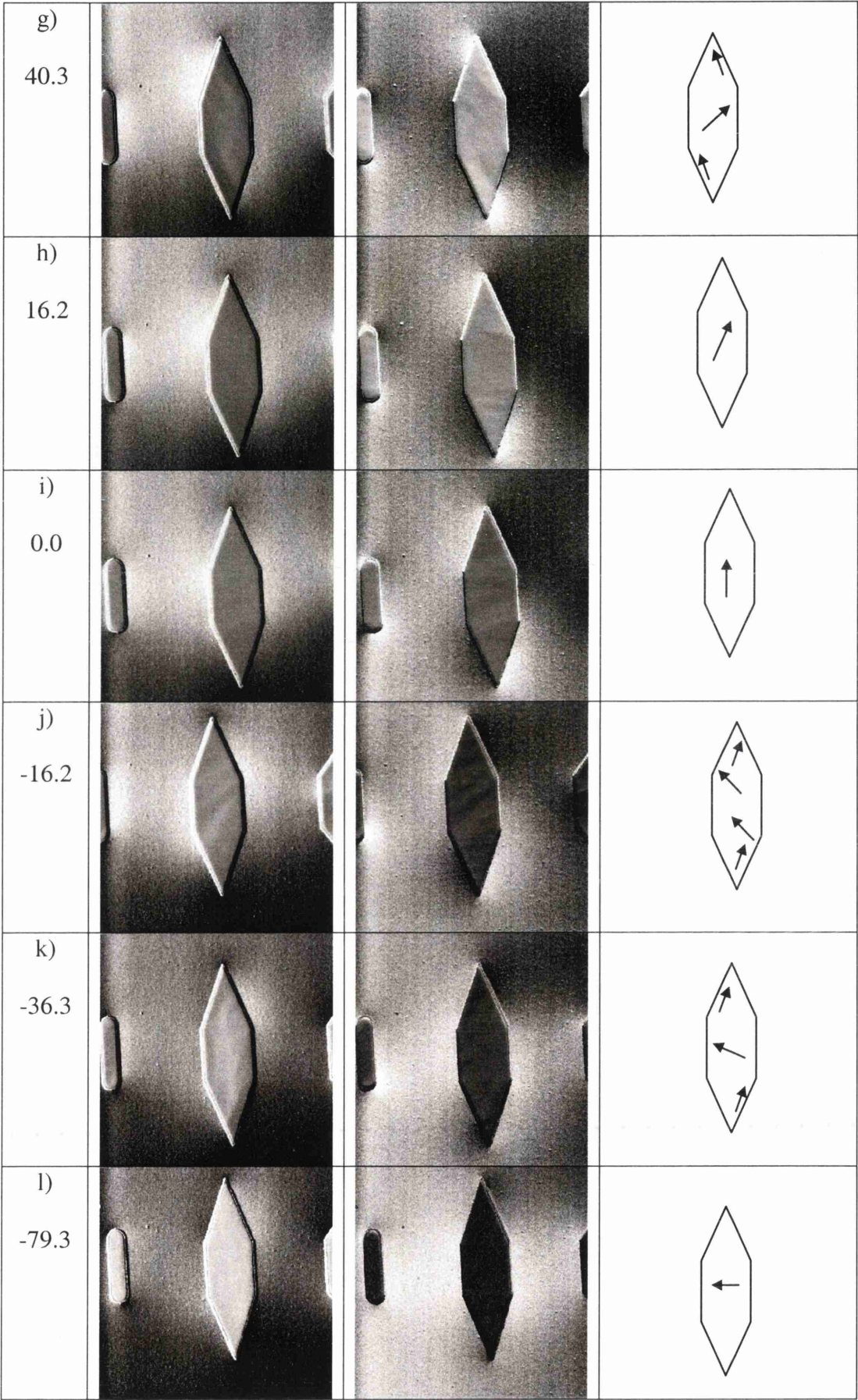


Figure 8.11 cont'd –  $2 \times 6 \mu\text{m}^2$  pointed end spin-valve element

Figure 8.12 shows a set of DPC images from the reversal of a  $6 \times 2 \mu\text{m}^2$  pointed end spin-valve element whose long axis lies parallel to the pinning direction of the spin-valve. Relaxing the applied field from parallel to the pinning direction to zero field (b), the dispersion can be seen to increase slightly. Increasing the field in the opposite direction, a distorted near-flux closure structure forms at 16 Oe (c). The flux closure domains move to the edge and disappear as the field is increased further (e), and the dispersion decreases (f). On reducing the applied field from this maximum value, the dispersion in the element increases (h), until at zero field (i) a multi-domain pattern has begun to form as the magnetisation in different regions rotates in opposite senses away from the applied field. As the field is increased in the negative direction, towards the pinning direction, the magnetisations within these domains continue to rotate, increasing the contrast levels seen in the images. Between  $-8$  Oe and  $-16$  Oe, these domains merge as the magnetisation across the majority of the element switches to align with the pinning direction once again, leaving a small vortex near the left-hand tip. On further increase of the field, the vortex disappears and the element becomes single-domain with magnetisation fully aligned with the spin-valve biasing direction.

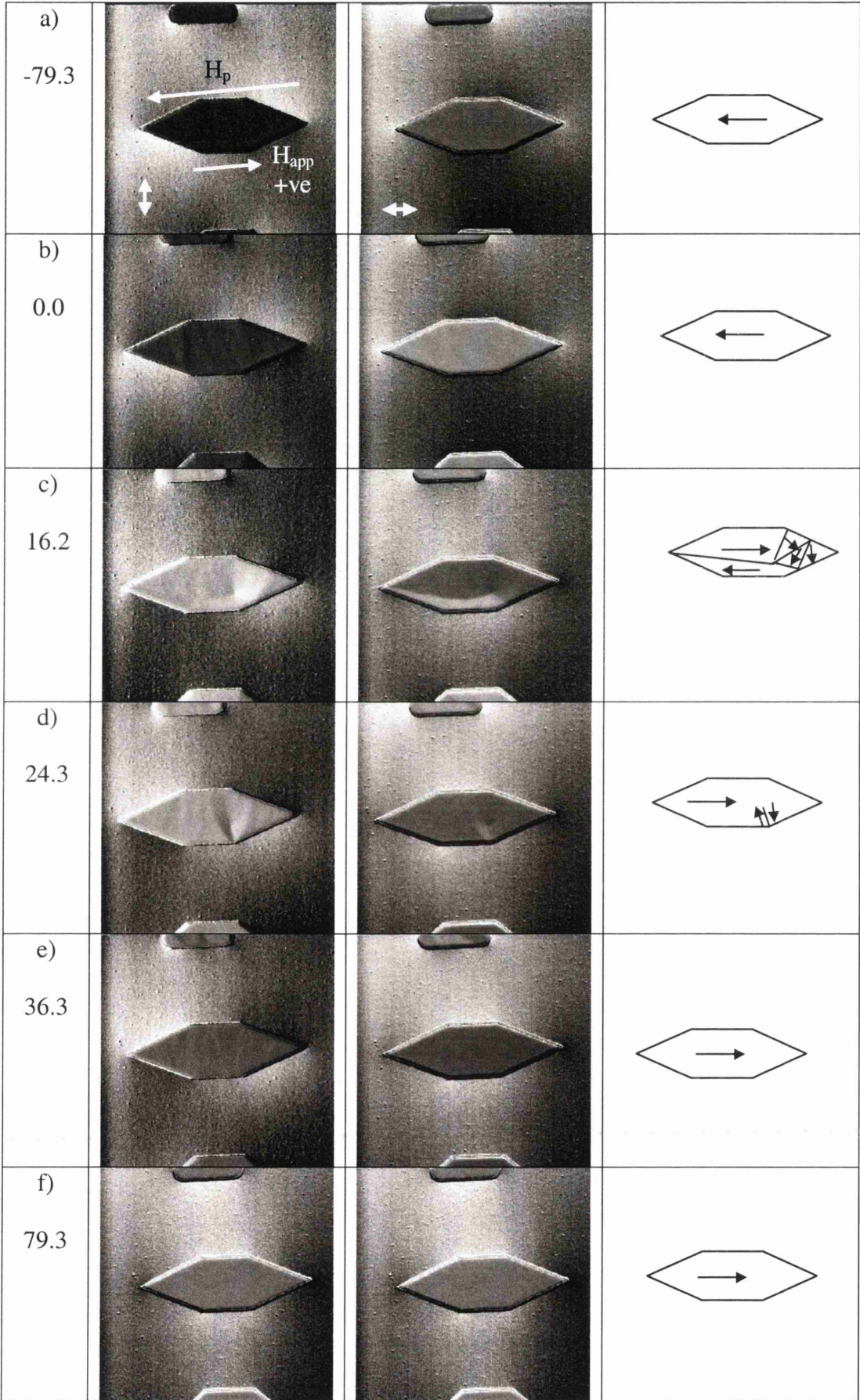


Figure 8.12 Magnetisation reversal of  $6 \times 2 \mu\text{m}^2$  pointed end spin-valve element


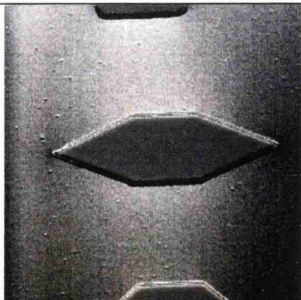
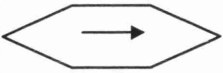
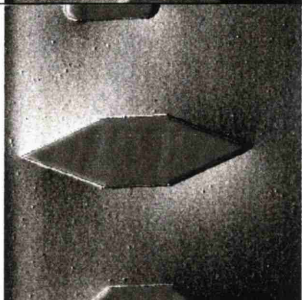

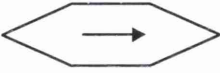
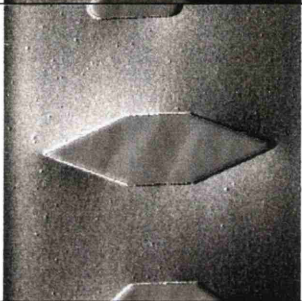
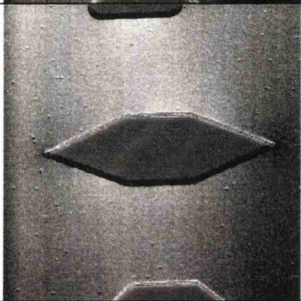

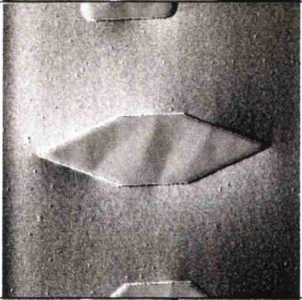
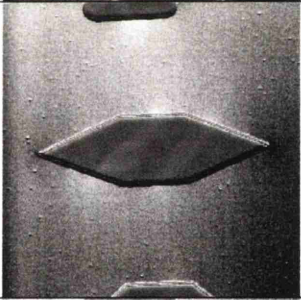

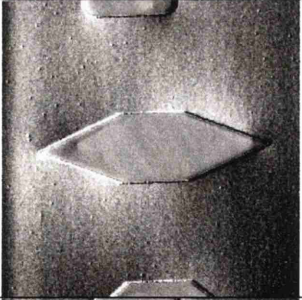
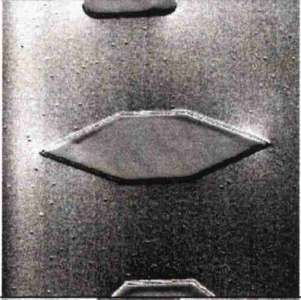

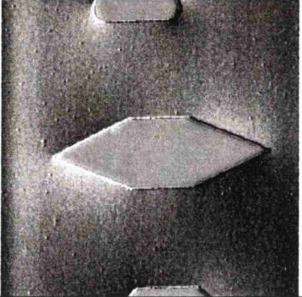
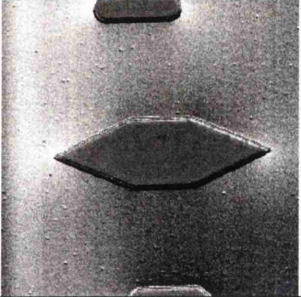
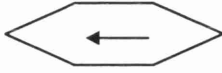
g) 40.3			
h) 16.2			
i) 0.0			
j) -8.1			
k) -16.2			
l) -79.3			

Figure 8.12 cont'd –  $6 \times 2 \mu\text{m}^2$  pointed end spin-valve element

Figure 8.13 shows a set of DPC images from the reversal of a  $2 \times 6 \mu\text{m}^2$  trapezoidal spin-valve element with the long axis oriented perpendicular to the spin-valve pinning direction. Relaxing the applied field from parallel to the pinning direction, elongated edge domains parallel to the free layer easy axis form (b). These edge domains merge as the applied field is reduced to zero (c) so that the magnetisation in the element lies parallel to its long axis with some dispersion. Increasing the applied field in the opposite direction (d), the majority of the magnetisation rotates towards the applied field with the formation of an end domain near the lower tip of the element. As the field is increased further the magnetisation continues to rotate to align with the applied field while the end domain recedes leaving a small vortex at the lower tip (e). This vortex then disappears on further increase of the field, leaving the element as a single domain aligned with the applied field (f). Reducing the field from this maximum value, the elongated edge domains reform (g), and there is an increase in the dispersion in the element. As the field is reduced further towards zero field (i), the edge domains merge while the magnetisation in the element rotates to align with the long axis of the element which is coincident with the free layer easy axis. Increasing the field in the negative direction, parallel to the pinning direction, the magnetisation in the majority of the element continues to rotate and an end domain begins to form at the upper tip (j). This end domain recedes to form a small vortex (k) at the upper tip as the field is increased further, while the magnetisation across the element aligns with the pinning direction until a single-domain state is achieved (l).

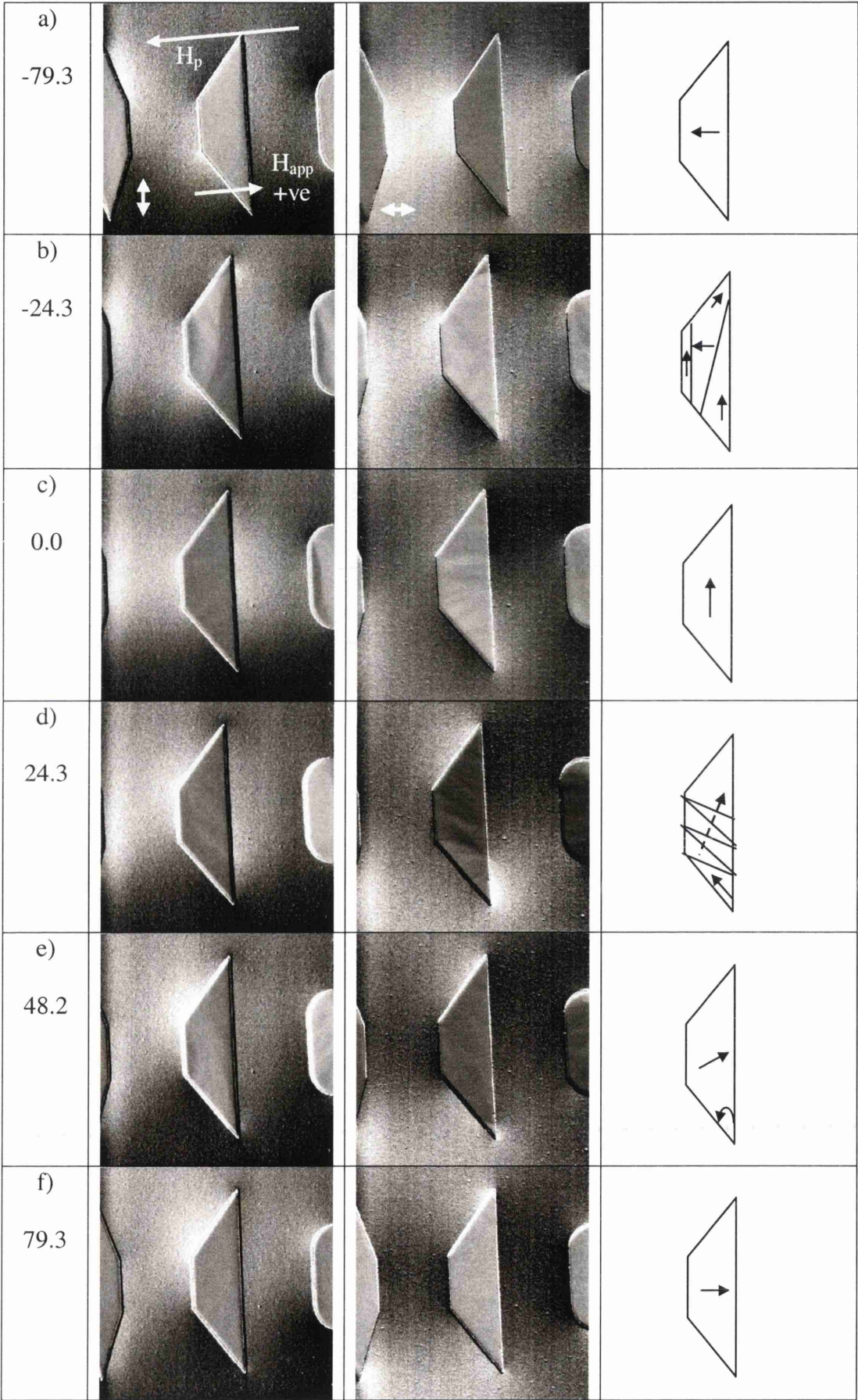


Figure 8.13 Magnetisation reversal of  $2 \times 6 \mu\text{m}^2$  trapezoid spin-valve element

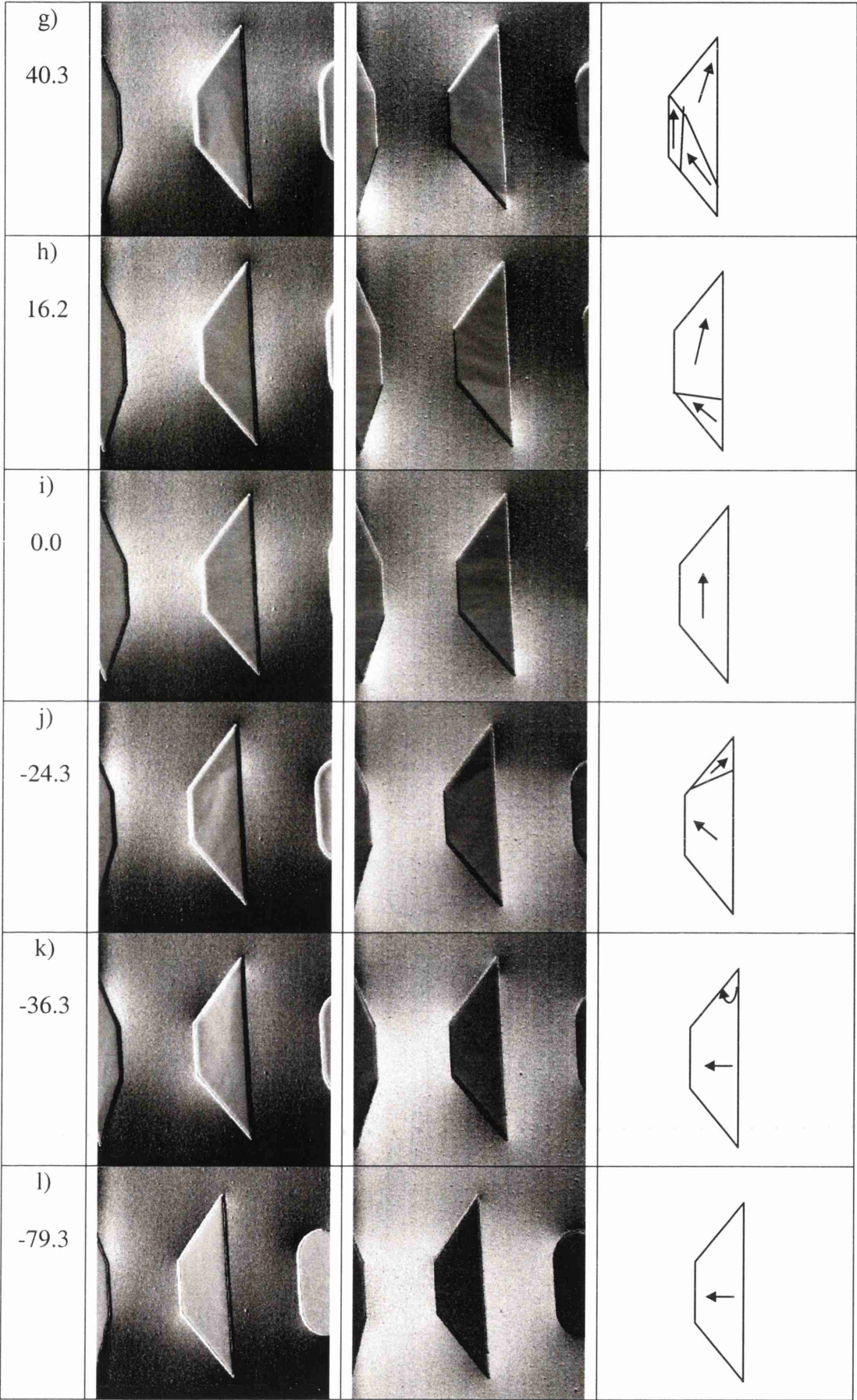


Figure 8.13 cont'd –  $2 \times 6 \mu\text{m}^2$  trapezoid spin-valve element

Figure 8.14 shows a set of DPC images from the reversal of a  $6 \times 2 \mu\text{m}^2$  trapezoidal spin-valve element whose long axis lies parallel to the biasing direction of the spin-valve. Relaxing the applied field from parallel to the pinning direction to zero field (b), there is a slight increase in dispersion, as the magnetisation tends to follow the upper edge of the element. Increasing the applied field in the opposite direction (c) and (d), the element begins to split into a complex near flux closure domain structure as the magnetisations in different regions rotate in opposite directions. These domains merge as the magnetisation across the element aligns with the applied field at 24 Oe (e). Increasing the field further reduces the dispersion as the magnetisation across the element becomes better aligned (f). Reducing the applied field from this maximum value to zero (h) causes an increase in dispersion. Increasing the field in the negative direction, parallel to the pinning direction (i), leads to the formation of a similarly complex domain structure to that seen in the first half of the cycle. These domains mostly merge as the magnetisation aligns with the pinning direction, leaving a small vortex and edge domains at the right-hand side of the element (j). The vortex and edge domains recede as the applied field is increased further, leaving the element as a single domain aligned with the pinning direction.

From these experiments, we see that for each shape of element, the orientation relative to the biasing direction of the spin-valve structure controls the reversal mechanism. For all of the end shapes, the elements oriented with their long axes perpendicular to the pinning direction showed reversal mechanisms dominated by rotation of magnetisation direction, rather than the formation of elongated edge domains as seen for the rectangular elements in the previous section. Small vortices were formed near the ends of the rounded element, while small end domains were more likely to form at the tips of the pointed and trapezoidal elements.

For the elements oriented with their long axes parallel to the pinning direction, all of the different shapes reversed with the formation of complex near flux closure domain structures as the magnetisations in different regions rotated towards one or other of the easy directions of the free layer of the spin-valve.

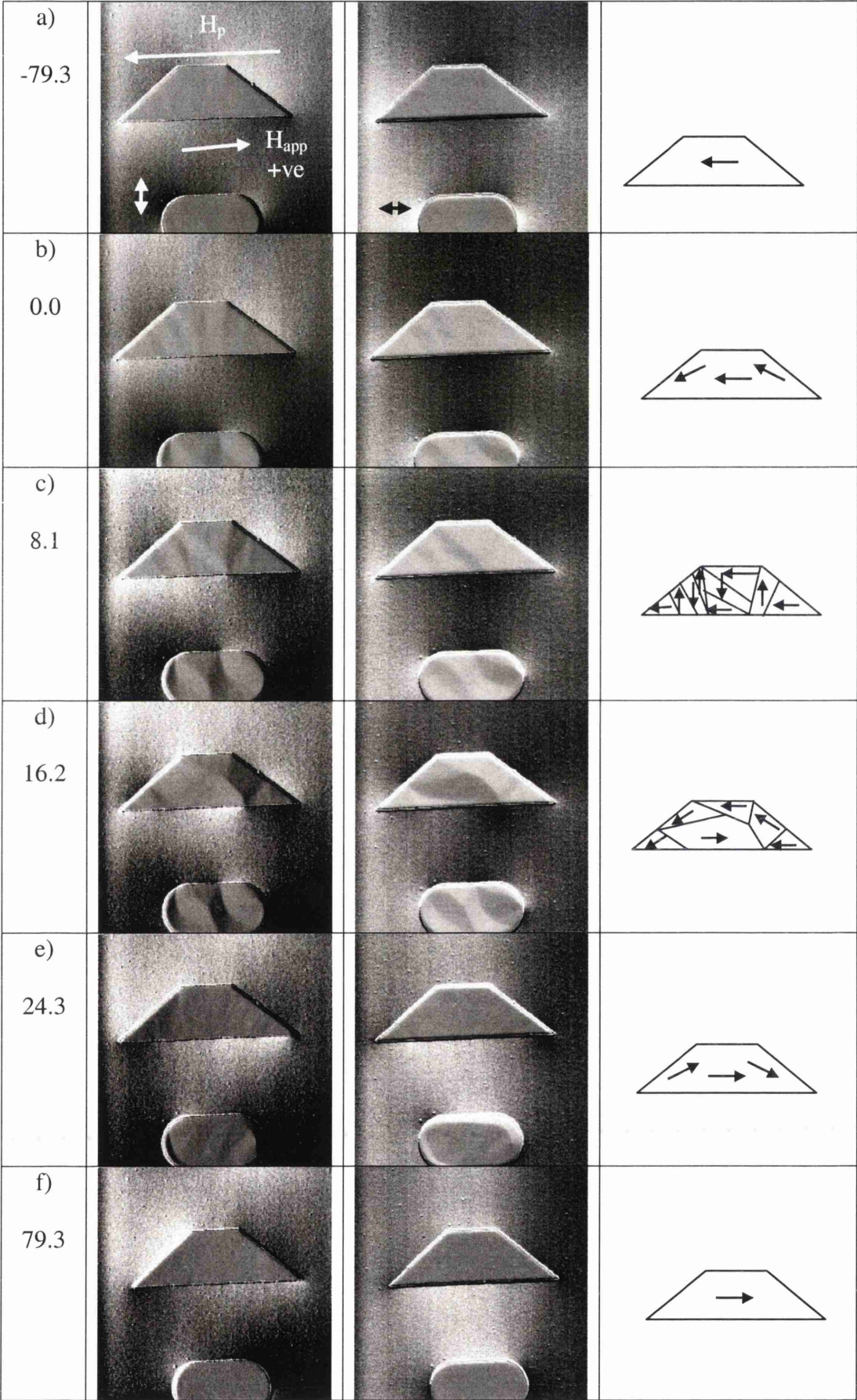


Figure 8.14 Magnetisation reversal of  $6 \times 2 \mu m^2$  trapezoid spin-valve element

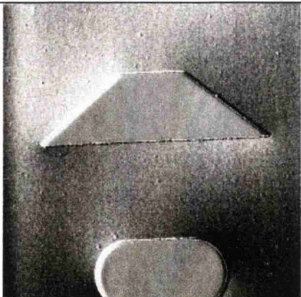
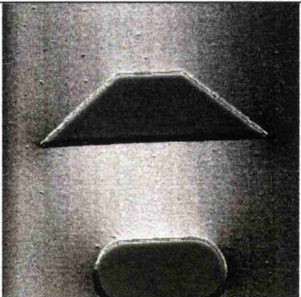
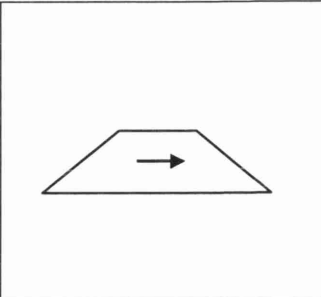
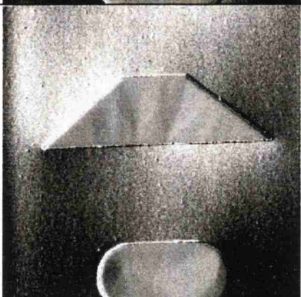
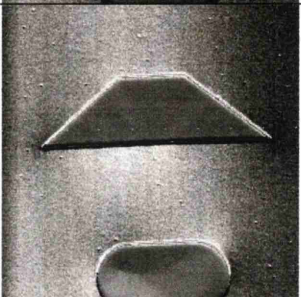
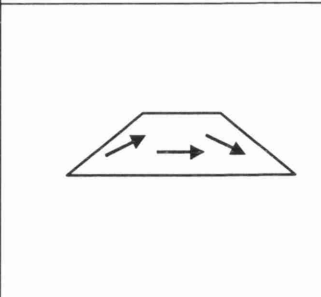
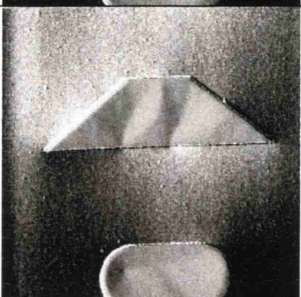
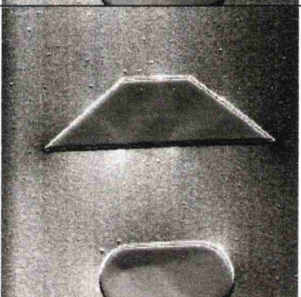
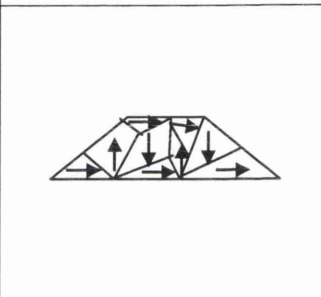
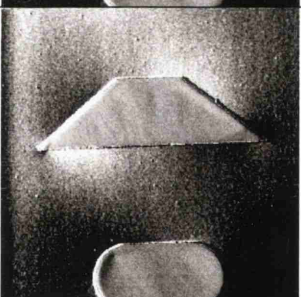
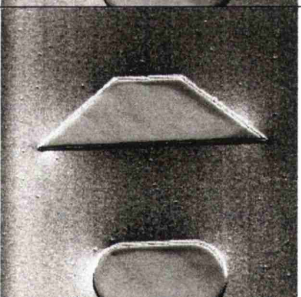
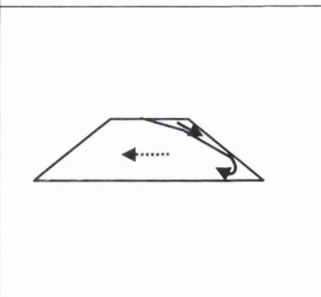
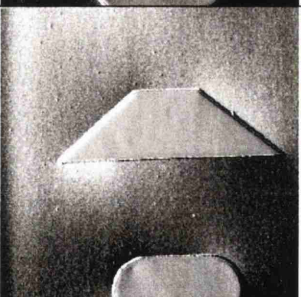
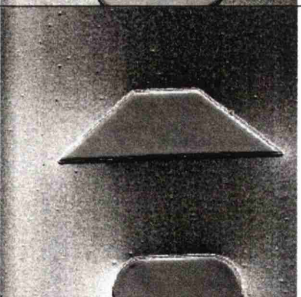
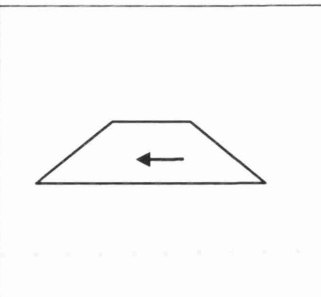
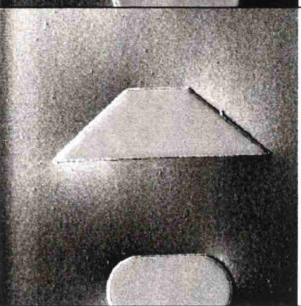
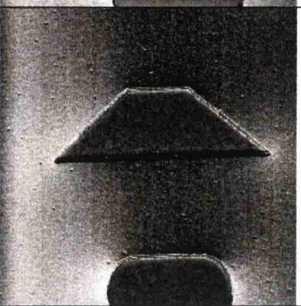
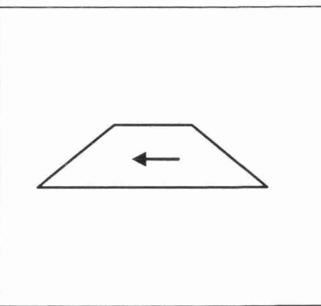
g) 40.3			
h) 0.0			
i) -8.1			
j) -16.2			
k) -48.2			
l) -79.3			

Figure 8.14 cont'd – 6x2 $\mu\text{m}^2$  trapezoid spin-valve element

## 8.4 Analysis

This Chapter introduced some of the characteristics of a patterned element of spin-valve material which have an effect on the free layer magnetisation reversal behaviour. Elements of similar dimensions were considered with orientations both parallel and perpendicular to the pinning direction of the spin-valve material, to determine the effects of different aspect ratios and different end shapes.

It could be seen that for rectangular elements, the mechanism of magnetisation reversal in an applied field was markedly different for elements of the same size and aspect ratio oriented differently relative to the pinning direction. The change in mechanism with orientation was even more pronounced for the elements with the higher aspect ratio.

Between the differently shaped elements, it could be seen that the elements oriented with their long axes perpendicular to the pinning direction of the spin-valve, that is to say aligned with the free layer easy axis, had smoother reversal mechanisms than those oriented parallel to the pinning direction. These reversals were dominated by rotation of magnetisation direction, rather than the formation of elongated edge domains and flux closure structures, as seen in the rectangular elements, which would lead to noise in a device. The trapezoidal element was seen to have the smoothest reversal of the three shapes.

The elements oriented parallel to the pinning direction all reversed via the formation of complex domain structures, similarly to the wider rectangular element. These structures formed as the magnetisation in different regions of the element rotated towards one or other easy direction.

For the elements of all shapes, oriented with their long axis perpendicular to the pinning direction, reversal occurred largely by rotation of magnetisation direction, with formation of small domain structures at the ends. In devices, domain wall formation and motion is a significant source of noise. Hence, reversal by coherent rotation will ensure a smooth repeatable response with lower noise.

## Chapter 9 Conclusions and Further Work

### 9.1 Introduction

The work described in this thesis has investigated some of the properties of magnetic sensor materials, both as continuous films and as patterned element specimens. This Chapter discusses some of the main conclusions which can be drawn from this study, and then goes on to introduce some possible further investigations which would extend the work carried out here.

### 9.2 Conclusions

#### 9.2.1 Chapter 4 Microstructure

Chapter 4 examined the physical microstructure of some of the materials investigated within this thesis. It was seen that for single layers of NiFe, the average grain size could be controlled with the thickness of the film deposited. Thicker films were seen to show an increase in grain size, corresponding with previous findings [1]. It was also shown that a Ta underlayer gave a slight increase in grain size of a NiFe film, in addition to determining the  $\langle 111 \rangle$  texturing within the film.

For the spin-valve film structure investigated, there was found to be a large spread in grain size, with the average being more than double that found in single-layer NiFe films of similar thickness. The spin-valve structure has a number of different layers, and an overall thickness in the region of 40nm. This means that the estimate of average grain size obtained from plan-view TEM micrographs gives only an approximation of the three-dimensional grain structure within the film.

These microstructural investigations were carried out as a prelude to the more detailed magnetic investigations undertaken in this study. It gave an overview of the quality and dimensions of the magnetic thin films of interest.

### 9.2.2 Chapter 5 Magnetisation of NiFe and AMR materials

The work described in Chapter 5 examined the magnetisation reversal behaviour of continuous films of single-layer NiFe, with and without the presence of a Ta seed layer to control the texturing in the film. Also investigated was the behaviour of NiFeRe, used as a SAL layer in AMR sensors, and an AMR sensor stack material.

The single layer NiFe, Ta/NiFe and NiFeRe films all underwent easy axis reversal by essentially the same mechanism. This mechanism involves an increase in dispersion in the film, followed by the rapid formation of a single domain wall parallel to the easy axis, which then sweeps across the film. For identical materials, the field at which the switching of magnetisation direction occurs is affected by the film thickness. All of these films are of soft magnetic materials, and so the switching fields are all small (of the order of a few Oe) and difficult to measure precisely.

The reversal mechanism for a NiFe single layer film with field applied along the hard axis is somewhat different. In this case, the film split into elongated domains with walls perpendicular to the applied field direction, as different regions of the film rotated in opposite senses towards the two easy directions. Different thicknesses of NiFe films, with and without a Ta seed layer, all displayed similar hard axis reversal mechanisms. The exception was for the thickest film where cross-tie walls formed.

The AMR multilayer structure was seen to undergo similar magnetisation reversal processes to those in the single layer NiFe films. The two magnetic layers in the structure were seen to act cooperatively, as if they were a single layer of soft magnetic material. The biasing effect of the soft adjacent layer (SAL) structure is entirely dependent on the presence of an electrical current passing through

patterned elements of the multilayer film. Hence, it could not be expected to observe any biasing effect in this sheet film study.

### **9.2.3 Chapters 6 and 7 Magnetisation of spin-valve materials**

Chapters 6 and 7 both considered the magnetic properties of spin-valve materials as sheet films. Chapter 6 dealt with TEM investigations of a single spin-valve structure, while Chapter 7 considered the bulk characterisation of a set of spin-valve structures obtained by varying particular layer thicknesses.

In Chapter 6, TEM techniques were used to investigate the free layer reversal mechanism of a single spin-valve structure as a function of applied field orientation, and also as a function of specimen temperature. It was shown that the free layer reversal mechanism depended strongly on the orientation at which the field was applied. When a field was applied antiparallel to the pinning direction of the spin-valve, reversal took place by the formation of very complex domain systems, including 360° walls which were difficult to remove. This would equate to a large noise signal in a device. It was possible to avoid the formation of such complex domain structures relatively simply by rotating the applied field by a few degrees away from lying antiparallel to the pinning direction.

The free-layer reversal mechanism was shown to be affected only slightly by in-situ heating within the TEM column up to 100°C. On continued heating to temperatures in excess of 200°C however, the behaviour changed markedly. Magnetic structures which appeared when the free-layer reversal was almost complete were attributed to the onset of reversal in the pinned layer. In addition, the changes that occurred at elevated temperatures proved irreversible in that the original behaviour could not be recovered on re-cooling of the specimen to ambient temperature.

The studies described in Chapter 7 demonstrated the importance of optimising the performance of a spin-valve structure by adjusting individual layer thicknesses

within the stack. It must be remembered, however, that other factors also influence the properties of a spin-valve material. Such factors include the exact deposition conditions, as well as annealing and other post-deposition processing.

It was shown that some improvements in the spin-valve stack considered were possible by altering the layers selected in this study. However, in order to optimise a spin-valve stack fully, each layer must be considered. Changing the properties of any one layer in a stack can affect the interactions between the other layers.

#### **9.2.4 Chapter 8 Patterned elements of spin-valve material**

In Chapter 8, we saw the introduction of some of the characteristics of a patterned element of spin-valve material which have an effect on the free layer magnetisation reversal behaviour. Elements of similar dimensions were considered with different aspect ratios and different end shapes. Each type of element was investigated with orientations both parallel and perpendicular to the pinning direction of the spin-valve material.

It was seen that for rectangular elements, the mechanism of free-layer reversal for the elements with higher aspect ratio showed a greater dependence on orientation relative to pinning direction than for those with a lower aspect ratio. For both orientations, the reversal mechanisms included the formation of end domains, which remained as the applied field was increased. This was particularly true for the narrower elements.

For the elements with different end shapes, the elements oriented with their long axes perpendicular to the biasing direction showed smoother reversal mechanisms than those oriented parallel to the pinning direction. These reversals were dominated by rotation of magnetisation direction, rather than the formation of complex domain structures as seen in the parallel oriented elements.

### 9.3 Future work on continuous films

The technology in the magnetic recording industry is advancing rapidly, requiring continual increases in areal densities to meet the demands for data storage. The materials investigated in this study will soon be superseded by newer materials with improved properties, in the continuing search for sensor materials to give higher amplitude signals for smaller field changes, from written bits shrinking in size.

Continuous film investigations will remain useful as a method in which to study the general magnetic behaviour of a new material before going on to look at the effects of patterning. Newer spin-valve structures, possibly with the inclusion of extra layers to increase electron scattering, tunnelling magnetoresistance (TMR) materials, and GMR multilayers are all potential candidates for use as magnetic sensors, and so would be of interest as subjects of continuous film TEM investigations. Such TEM investigations used in parallel with other magnetic metrology techniques, as used in Chapter 7, would help to give a far more complete picture of the magnetic properties of a material than available from any single technique alone.

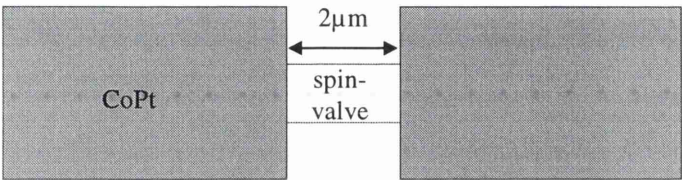
### 9.4 Future work on patterned spin-valves

Magnetic sensor devices, in which spin-valve materials are used, are patterned to dimensions in the sub-micron range. Hence it is necessary to study patterned elements of material of comparable dimensions. The investigations described in Chapter 8 of this thesis considered only isolated elements of spin-valve material of the order of microns. These investigations are extendable in the first instance by continuing experiments on the same patterned specimens. Only a small number of the spin-valve elements within each pattern design have been selected for investigation so far, and in particular the smallest elements have yet to be considered.

It would also be possible, using multi-layer lithography techniques, to include other objects on the TEM specimen in order to give a better simulation of the environment of the sensor element in a real device. Electrical contacts, permanent magnets (used to stabilise the domain structures), or small electromagnets to simulate the media fields are some possible elements which could be incorporated into a TEM specimen. Some of these techniques are already being developed elsewhere [2-4] and could provide a valuable insight into the operation of real sensor devices.

One set of experiments which had been planned during this study, but which time constraints and practical difficulties made unfeasible, was the inclusion of permanent magnets on a patterned spin-valve specimen. These permanent magnets would simulate the stabilisation magnets used in devices as part of the electrical contacts. These have the purpose of effectively pinning magnetisation direction at the ends of the sensor in order to reduce the formation and motion of domain structures within the sensor.

The proposed method was to use electron beam lithography and lift-off techniques as described in Chapter 3 to deposit CoPt pads at either end of the elements. Figure 9.1 shows an example of an element within the pattern design. Several different parameters could be varied in this experiment, including the size of the spin-valve element, and the relative dimensions of the permanent magnets.



*Figure 9.1 Spin-valve element with permanent magnet pads*

## REFERENCES

**Chapter 1 Magnetism and Magnetic Recording**

- 1 P. Weiss, J. Phys., **6**, 661 (1907)
- 2 W Heisenberg, Z. Physik, **49**, 619 (1928)
- 3 W Pauli, Z. Physik, **31**, 765 (1925)
- 4 E.C. Stoner, Phil. Mag., **15**, 1080 (1933)
- 5 H.M. Fuller, E.M. Hale, J. Appl. Phys., **31**, 238 (1960)
- 6 S. Chikazumi, J. Phys. Soc. Japan, **5**, 327 (1950)
- 7 R. Becker, Z. Physik, **62**, 253 (1930)
- 8 L. Landau, E. Lifshitz, Phys. Z. Sowjetunion, **8**, 153 (1935)
- 9 L. Néel, Compt. Rend. Acad. Sci. Paris, **241**, 533-536 (1955)
- 10 F Bloch, Z. Physik, **74**, 295 (1932)
- 11 E.E. Huber, D.O. Smith, J.B. Goodenough, J. Appl. Phys., **29**, 294 (1958)
- 12 M Prutton, Thin Ferromagnetic Films, Butterworths, 1964
- 13 W. Thompson, Proc. Roy. Soc., **8**, 546 (1857)
- 14 T.R. McGuire, R.I. Potter, IEEE Trans. Mag., **MAG-11** (4), 1018 (1975)
- 15 M.N. Baibich, J.M. Broto, A. Fert, F. Nguyen Van Dau, F. Petroff, P. Etienne, G. Creuzet, A. Friederich and J. Chazelas, Phys. Lett., **61**, 2472 (1988)
- R.L. White, IEEE Trans. Mag., **28**, 5, 2482 (1992)
- 16 R.P. Hunt, IEEE Trans. Mag., **11**, 4 (1970)
- 17 K.E. Kuijk, W.J. van Gestel, F.W. Gorter, IEEE Trans. Mag., **11**, 1215 (1975)
- 18 W Folkerts, J.C.S. Kools, Th.G.S.M. Rijks, R Coehoorn, M.C. de Nooijer, G.H.J. Somers, J.J.M. Ruigrok and L Postma, IEEE Trans. Mag., **30**, 6, 3813 (1994)
- 19 C Tsang, R.E. Fontana, T Lin, D.E. Heim, V.S. Speriosou, B.A. Gurney and M.L. Williams, IEEE Trans. Mag., **30**, 6, 3801 (1994)

## Chapter 2 Transmission Electron Microscopy – Instrumentation and Techniques

- 1 PJ Goodhew and FJ Humphreys, *Electron Microscopy and Analysis*, Taylor & Francis 1988 2<sup>nd</sup> edition
- 2 P.M. Mul, B.J.M. Bormans, L. Schapp, published in the proceedings of the 12<sup>th</sup> International Conference for Electron Microscopy (1990)
- 3 K. Tsuno and T. Taoka, *Jap. J. Appl. Phys.*, **22**, 1047 (1983)
- 4 P. Hagemann et al., *Philips Electronic Instruments*, Mahwah, New Jersey, 33 (1987)
- 5 LJ Heyderman, JN Chapman and SSP Parkin, *J. Magn. Magn. Mat.*, **138**, 344 (1994)
- 6 JN Chapman, PR Aitchison, KJ Kirk, S McVitie, JCS Kools, MF Gillies, *J. Appl. Phys.*, **83**, 10, 5321 (1998)
- 7 J.N. Chapman, *J. Phys. D: Appl. Phys.*, **17**, 623 (1984)
- 8 D Wohlleben, *J. Appl. Phys.*, **38**, 8, 3341 (1967)
- 9 JN Chapman, AB Johnston and LJ Heyderman, *J. Appl. Phys.*, **76**, 9, 5349 (1994)
- 10 AB Johnston and JN Chapman, *J. Microscopy*, **179**, 2, 119 (1995)
- 11 HW Fuller and ME Hale, *J Appl. Phys.*, **31**, 2, 238 (1960)
- 12 H. Hoffmann, *IEEE Trans. Mag.*, **MAG-4**, 1, 32, (1965)
- 13 JN Chapman and DM Donnet, in “Magnetism and Structure in Systems of Reduced Dimension” ed RFC Farrow et al., Plenum Press, New York 1993
- 14 J.N. Chapman, G.R. Morrison, *J. Mag. Magn. Mat.*, **35**, 254 (1983)
- 15 S McVitie and JN Chapman, *IEEE Trans. Mag.*, **24**, 2, 1778 (1988)
- 16 J.N. Chapman, I.R. McFadyen, S. McVitie, *IEEE Trans. Mag.*, **26**, 5 (1990)
- 17 SJ Hefferman, JN Chapman, and S McVitie, *J. Magn. Magn. Mat.*, **95**, 76 (1991)
- 18 J.N. Chapman et al., proceedings of the 2<sup>nd</sup> International Symposium on Advanced Materials (1995)

### Chapter 3 Growth and Fabrication of Specimens

- 1 M Ruhrig, B Khamsehpour, KL Kirk, JN Chapman, P Aitchison, S McVitie, CDW Wilkinson, IEEE Trans. Mag., **32**, 4452 (1996)
- 2 B Khamsehpour, CDW Wilkinson, JN Chapman, AB Johnson, J. Vac. Sci. Technol. B, **14**, 3361 (1996)
- 3 S. Thoms, Electron beam lithography training course, University of Glasgow (1997)
- 4 L. Reimer, Transmission Electron Microscopy, Springer-Verlag (1997)

### Chapter 4 Microstructure of Magnetic Films

- 1 T.R. McGuire, R.I. Potter, IEEE Trans. Mag., **MAG-11** (4), 1018 (1975)
- 2 C. Tsang, S.K. Decker, J. Appl. Phys., **53**, 3, 2602 (1982)
- 3 T.C. Anthony, J.A. Brug, S. Zhang, IEEE Trans. Mag., **30**, 6, 3819 (1994)
- 4 D.G. Neerincx et al., Thin Solid Films, (1995)
- 5 B. Dieny, B.A. Gurney, S. Lambert, D. Mauri, S.S.P. Parkin, V.S. Speriosou, D.R. Wilhoit, US Patent 5206590

### Chapter 5 Magnetisation Reversal of Single-layer NiFe and AMR stacks

- 1 R.L. Conger and F.S. Essig, J. Appl. Phys., **28**, 855 (1957)
- 2 M.F. Gillies, PhD Thesis, University of Glasgow (1996)

## Chapter 6 Free Layer Reversal of a Spin-valve with Crossed Anisotropy

- 1 B. Dieny, J. Mag. Magn. Mat., **136**, 335 (1994)
- 2 J.C.S. Kools, IEEE Trans. Mag., **32**, 4, 3165 (1996)
- 3 M. Labrune, J.C.S Kools and A. Thiaville, J. Magn. Magn. Mat., **171**, 1 (1997)

## Chapter 7 Spin-valve Stacks with Varying Layer Thicknesses

- 1 Y. Huai, J. Zhang, G.W. Anderson, P. Rana, S. Funada, C.-Y. Hung, M. Zhao, S. Tran, J. Appl. Phys., **85**, 8, 5528 (1999)
- 2 B. Dieny, M. Li, H. Liao, C. Horng, K. Ju, J. Appl. Phys., **87**, 7, 3415 (2000)
- 3 H.S. Cho, J. Chen, S. Cool, R. Michel, N. Tabat, J. Appl. Phys., **87**, 9, 4939 (2000)
- 4 H.C. Tong, C. Qian, L. Miloslavsky, S. Funada, X. Shi, F. Liu, S. Dey, J. Appl. Phys., **87**, 9, 5055 (2000)
- 5 J. Nogues, I.K. Schuller, J. Mag. Magn. Mat., **192**, 203 (1999)

## Chapter 9 Conclusions and Further Work

- 1 D.G. Neerincx et al., Thin Solid Films, (1995)
- 2 X. Portier, A.K. Petford-Long, T.C. Anthony and J.A. Brug, J Appl. Phys., **85**, 8, 4120 (1999)
- 3 X. Portier, A.K. Petford-Long, R.C. Doole, T.C. Anthony and J.A. Brug, Appl. Phys. Lett., 71, 14, 2032 (1997)
- 4 X. Portier, A.K. Petford-Long, T.C. Anthony and J.A. Brug, J. Mag. Magn. Mat., 187, 145, (1998)

